SEISMOLOGICAL APPLICATIONS OF BOUNDARY INTEGRAL AND GAUSSIAN BEAM METHODS

by

Rafael Benites Calderón

B.S. Physics, Universidad Nacional de Ingenieria

Lima-Peru, 1977

Submitted to the Department of Earth, Atmospheric, and Planetary Sciences on July 13, 1990, in partial fulfillment of the requirements for the degree of

DOCTOR OF PHILOSOPHY

at the

MASSACHUSETTS INSTITUTE OF TECHNOLOGY

July, 1990

Signature of the author_____

Department of Earth, Atmospheric, and Planetary Sciences

July, 1990

Certified by _____

Thesis supervisor

Accepted by_____

Chairman, Department Commitee

SEISMOLOGICAL APPLICATIONS OF BOUNDARY INTEGRAL AND GAUSSIAN BEAM METHODS

by

Rafael Benites Calderón

Submitted to the Department of Earth, Atmospheric,
and Planetary Sciences on July 13, 1990, in partial
fulfillment of the requirements for the degree of
Doctor of Philosophy

ABSTRACT

In the present thesis we introduce a new method based on both boundary integral and Gaussian beam methods to compute full waveform synthetic seismograms of SH waves propagating in two dimensional inhomogeneous media with irregularly shaped boundaries. In dealing with such complex media, we use the so called "single layer potential" integral representation of the scattered field, in which artificial wave sources are regularly distributed along the boundaries. Green's function for displacement and traction (acting on a plane of normal vector $\hat{n}$) at an observation point due to each wave source are computed by superposition of Gaussian beams. The total field is the sum of the incident wave and the field radiated from all sources, each multiplied by an unknown complex constant representing the strength and phase of its wave source. These constants are determined by imposing the appropriate boundary conditions in the least-squares sense. To test the method, we have computed the scattering of plane SH-waves by a semicylindrical canyon and a mountain of cosine shape; and the surface motion of a semicylindrical alluvial valley in a half-space due to incident plane wave. Our results are in excellent agreement with the available exact or other reliable numerical solutions, for the same problems.

The first application of our method is a problem of some volcanological interest, namely, the effect of hard and soft inclusions on the surface motion due to vertically incident plane waves. Both time domain and frequency domain solutions are needed to fully understand the contributions of transmission, reflection, diffraction and resonance phenomena in the whole system of inclusion and free-surface. Interestingly, both low and high velocity inclusions reduce the amplitude of the incident wave at the surface above the inclusion, suggesting a serious non-unique inverse problems using amplitude data.

The second application is two problems of interest to strong motion seismology. We found several important effects of linear increase of velocity with depth on the surface motion of mountains as well as sedimentary basins due to incident plane waves.

The third application is the deterministic study of seismic scattering in a media containing many scatterers with scale lengths comparable to the wavelength. The full waveform of multiply scattered SH waves by many cylindrical cavities in two-dimensional homogeneous media is computed. We solve scattering problems involving one, two, four, twelve and fifty cavities regularly distributed in a half-space. The validity of our results is tested using the exact solution for the case of a single cavity and using the physical interpretation in terms of ray paths associated with multiple reflection, transmission and diffraction for other cases. Finally we apply the method to compute the case of fifty cylindrical cavities, each of radius a, randomly distributed in a region $80a$ wide by $30a$ deep in a half and full spaces. The scattering loss of incident waves is estimated for wavelengths in the range from $1.7a$ to $13.3a$, using the synthetic seismograms calculated for the full-space case. We found that the value of Q^{-1} increases with kd (wavenumber$\times 2a$) in the region where $kd < 2$, peaks at $kd = 2$, and decreases proportional to $(kd)^{-1}$ for $kd > 2$.

Thesis supervisor: Professor Keiiti Aki

Title: Professor of Geophysics

This work is dedicated to the memory of my grandmother

SARA

(1906-1989)

ACKNOWLEDGEMENTS

I would like to express my deepest gratitude to my advisor, professor Keiiti Aki, for his generosity and for his guidance throughout my graduate years, which I value as a fantastic experience. This is not to say that it was an easy period in my life so far, but perhaps the most rewarding. Through his criticisms he taught me to address a new problem in a disciplined and logical manner; at the same time that allowed me to work in complete freedom. The original idea of the present study in theoretical seismology is due to Kei (see Appendix 2, 'Aki's memo'), which is just one example of his enthusiasm to pursue original ideas and share them with others. I started to work on the boundary integral- Gaussian beam method in early 1987, from "scratch". At present, after about four years and 6 months, it is rewarding to see how much I have exploited such idea. Kei's suggestions were fundamental for the progress of my research. Many times I was amazed that he could suggest the possible existence of errors in certain parts of my computer programs by just looking at the final results. I think it is going to be tough to be away from Kei's scientific judgement, for which I learned to have the highest respect. I also appreciate very much his concern and assistance in the stage of writing my thesis; without his help this would have been a very rough manuscript.

I also would like to thank Peter Molnar for his assistance during my stay at MIT. Peter and Steve Roecker were the first Americans I met in Peru, whose hard working image stimulated me to pursue a graduate course, at the time when I thought that life was over after having a secure job. Now, I may have completed the graduate course but I have no secure job anymore. However, I feel like life just starts. My gratitude is specially due to Brian Tucker, a gentleman I met in MIT and joined in his seismic experiment in La Molina, Peru. I have the fortune to keep his frienship until now.

During my years at MIT I had many friends. Among them Federico Pardo,

actually my friend since our undergraduate years in Lima. My officemates Mike Nelson and Craig Jones were very kind when I arrived at MIT, offering assistance to move my luggage around and also my first meal at a home (I do not remember which), at the time when I was staying overnight at the "barrack's", down in the basement of one of the housing buildings at MIT. Later on, in Los Angeles, Craig introduced me to the San Gabriel and Santa Monica mountains, one by one, in several hiking sessions. I also appreciate the kidness of Yves Bernabé, Paul Okubo, Scott Phillips, Helene Lyon-Caen, Joao Rosa, Peter Roberts, Barbara Sheffels and Robert Stuart. Also Tiang Qing Cao, who I got to know better in LA, where I enjoyed his wit and cleverness when we were officemates in USC. My gratitude extends to Jean Titillah and Emilio Falco for their kindness and assistance during my early days in Boston. My closest friend at that time became Kiyoshi Yomogida, with whom I got involved in many adventures, most of them "monkey business". But we also worked together, and recently we wrote a paper and plan to cooperate in the future. At present, far apart, we still keep our close friendship, the kind that will keep us fighting and critizicing each other for the rest of our lives.

At USC in Los Angeles, where I followed Kei to become a non-resident student at MIT, I met very good people, whose kindness I will always appreciate. I thank Yehuda Ben-Zion, who was the first to offer me his assistance in crucial moments for me. I also enjoyed many interesting discussions on several subjects with him. John McRaney made everything very smooth, in particular to keep my connection with MIT. I thank him not only for his help but also for his friendship.

Among the students that I met in USC at that time, I have special consideration for Syhhong Chang, a guy who is really clever, as well as gentle and sincere. I took lots of advantage of his knowledge on synthetic seismograms, digital signal processing and his skills with computers. Also, I would like to mention Xiao-Fei Chen, in my opinion, the smartest student of seismology I ever met. Discussions with him are always illustrative. Thanks are extended to Y. Zeng, J. Chin, J. Peng, Su-Feng and H-C Chiu. To all of them, thanks for those fantastic fish meals

at Monterrey Park. I am also grateful to the friendship of K. Mayeda, S. Koyanagi, and S. Steacy. Thanks to Mustaq Khan, for making things easier in the computer and for his willingness to help. I deeply appreciate the effort that Valerie Ferrazzini put to prepare my slides for thesis defense. Of course, I have to thank Valerie not only for this, but also for her friendship, interesting conversations and many pounds of caffeine consumed from drinking her coffee in the last three years.

Kei brought many good scientists to visit USC, and my contact with them meant a lot of benefit to me. In particular, I learned from working closely to Hiroshi Kawase, Kojiro Irikura, Francisco Sanchez-Sesma and Michel Campillo. I also had great discussions with T. Miyatake and Y. Hisada. I wish some day I can work with them too. I met Anshu Jin for the first time in MIT. Now at USC, I would like to thank her frienship, personal warmth and for her help to prepare some of my figures in the final form for thesis. I think I am going to miss her when I am out of USC.

I thank Susana Moncayo, from the Organization of American States (OAS) for her kind assistance in matters related to my fellowship, and to Dr. Leonidas Ocola, from the Geophysical Institute of Peru.

I express my deep gratitude to my parents, Tomás and Violeta, for providing their children with such a solid home, and to my brothers Walter, David, Tomás and Orlando, for their constant support. They are my strength. Similarly to Armando Turín for his assistance when we needed it. Finally, I thank my wife Elena Turín for sharing my ideals and goals, getting along easily with my kind of life and always illuminating our home with a big smile.

This research was financially supported by NSF grant BCS-8819988, and DOE grant DE-FG03-87ER13807.

TABLE OF CONTENTS

CHAPTER I

INTRODUCTION

1.1 Purpose

In this thesis we use the boundary integral method (BIM) and the Gaussian method for obtaining solutions to problems involving scattering of seismic waves incident upon complex subsurface structures. The examples of problems that we solved here are mainly from two research areas in Seismology, namely the so-called "site effect", or the amplification effect of the near-surface on strong ground motion during earthquakes, and the scattering and attenuation of short period (less than 1 sec.) seismic waves in the heterogeneous lithosphere.

As a result of geological processes such as weathering, erosion and deposition, the near surface structures may be composed of soft soil layers and/or exhibit strong lateral and vertical variation of the seismic wave velocities. These geological conditions cause complex wave phenomena such as resonance of waves trapped in the soft layers, and interference of the scattered waves generated by the irregularities. The accurate quantification of the site effects has been the subject of extensive experimental and theoretical work since Takahasi and Hirano (1941) observed the ground response of sites with different geological conditions for the same earthquake and interpreted observed response in terms of an explicit formula for the amplification factor of a soft soil layer over a half-space with a flat interface for incident plane S waves. Seismologists and earthquake engineers have been developing methods that could reliably predict the ground displacement, velocity, acceleration and their variation in space, time and frequency

domains, in terms of input wave fields and geological structures of the site. The goal is to assess effects of the local site conditions on the strong ground motion parameters for a large earthquake. Literatures on the state of the art methods to evaluate site effects have recently been reviewed by Aki (1988). While most of these methods consider the effect of complex geometry of structures in 2-D, and sometimes in 3-D, they usually neglect the effect of velocity and density gradients with depth. Other methods applicable to the study of effects of these gradients usually neglect the effect of the lateral variation of topography and interface by simplifying the problem to 1-D (e.g. Idriss and Seed 1968). The understanding of realistic situations requires the combination of both effects. For instance, observations made by Tucker et. al. (1984) at ridge sites that showed an amplification factor up to 8 could be predicted neither by inhomogeneous models with 1-D geometry nor by homogeneous models with 2-D geometry, and it was concluded that accurate predictions required a model that included both the ridge topography and the near-surface velocity gradient (Bard and Tucker, 1985). Also, as pointed out by Bard and Gariel (1986-a), sediment-filled basins present strong vertical variations of the seismic wave velocities with depth, as a result of soil compaction.

A usual approach to solve this problem is to simulate the gradient with a stack of thin homogeneous layers whose velocity increases stepwise with depth, and use an hybrid scheme that combines both Finite Element and Boundary Element methods to treat layered basins (Fukuwa et. al. 1985). However, there is a difficulty arising from this procedure. The velocity discontinuities at each interface of the stack of layers introduce impedance contrast effects not present in the case of smooth increase of

velocity, leading to incorrect values of the resonant peaks of the overall response of the inhomogenoeus structure, in particular for high frequencies. Moreover, when the velocity gradient is strong the number of homogeneous thin layers in the stack must be increased in order to reduce the interface impedance contrast effects. This makes the procedure highly costly and cumbersome.

The response of an inhomogeneous layer over a homogeneous half-space to incident plane waves has resonant peaks at different frequencies than the resonant peaks of the homogenoeus layer (Burridge et.al. 1980), and the former peaks have slightly greater amplitudes, for any incidence angle. Bard and Gariel (1986) was the first to study the effects of irregular boundaries of a surface layer with velocity variation within the layer. They computed the effects of linear velocity gradient on the response of 2-D basins, by incorporating the analytical solution of the wave equation in inhomogeneous unbounded media into the Aki-Larner (1970) technique. They considered a velocity gradient of about 12 m/sec/m and frequencies in the range of 0 to 15 Hz. Their method gave results in a good agreement with those obtained for the model that replaces the gradient with a nine homogeneous layers stacked in a 60 m depth range, for frequency 15 Hz. However the agreement breaks down as the number of layers decreases to five. They found that these velocity gradients do not alter much the general qualitative behavior of the basin with respect to the homogeneous case. In other words, 2-D resonance and local surface waves are still observed, but the amplification factor obtained may be much larger than the one obtained by neglecting either the 2-D heterogeneities or the velocity gradient. In addition, it appears that the edges of the valley undergo larger differential

motions, in comparison to the basin with a homogeneous sedimentary layer.

The method developed in this thesis is intended to offer an alternative way to solve the above problem. It is essentially a boundary integral formulation of the scattering problem, where the wave field is expressed as the superposition of seismic sources distributed along the free surface and interface. The field due to each source, or Green's function, is calculated for unbounded media and is approximated by the superposition of Gaussian beams.

In the past, integral equation techniques to solve a particular differential equation under certain boundary conditions were considered analytical rather than numerical. They were developed, for instance, to obtain closed form solutions for Laplace's equation type problems (Kellog 1953), potential problems (Smirnov 1964) and diffraction of acoustic waves problems, which are governed by Helmholtz equation (Morse and Ingard 1968). In the pre-computer era their applications were limited to some particular geometries that conform to a suitable coordinate system (Morse and Feshbach 1953). With the help of modern computers and by incorporating the variational principle, these techniques were combined with other approximate methods such as the so-called "collocation" and least squares methods (Brebbia 1978), and gave rise to a new class of powerful hybrid methods applicable to a wide variety of problems. The method proposed here belongs to this class. Our assumption is that if the wave field of a single point (line) source in inhomogeneous full-space can be well represented by a superposition of Gaussian beams, then it can be used in a boundary integral method scheme, which has been proved extensively to be effective in dealing with problems involving boundaries with irregular geometry.

A Gaussian beam is a high-frequency approximate solution of the wave equation, introduced into Seismology by Červený et. al. (1982) and Červený and Pšenčík (1983 a,b). A method that uses a superposition of Gaussian beams has been developed to evaluate the seismic field in smooth media, i.e. media for which its material properties and geometrical features vary slowly in space within a wavelength; or equivalently, that the wavelengths considered are much shorter than the scale length of heterogeneities. Within the limits imposed by these restrictions, the method has been tested and succesfully applied to a variety of geophysically interesting cases, by Nowack and Aki (1984), Červený and Pšenčík (1984), Madariaga (1984) and Madariaga and Papadimitriou (1985), Yomogida (1985), and more recently by George (1987). In all these works, when the medium contains planar or curved interfaces, boundary conditions are satisfied locally, for each beam, at the point where its ray hits the interface. New initial conditions are set for the reflected and transmitted beams, and again these are propagated individually towards the next boundary. At the end, direct, transmitted and reflected beams that pass close to the receiver are superimposed. A difficulty of this approach is that the results are very sensitive to the smoothness of the media and to the choice of the initial value (at the source) of each beam parameter. The application of this approach to compute the response of subsurface structures with strong lateral heterogeneities and large impedance contrasts may be cumbersome and lead to incorrect results. In particular, the correct description of the resonance phenomena in a soft layer would require many accurately calculated reflected and transmitted rays.

The above problem is eliminated in our approach by representing the

reflected and transmitted fields by seismic wave sources located at both sides of an interface and determining their strengths to satisfy the boundary conditions at the interface. From each source Gaussian beams having the same beam width are radiated at angle increments, to synthesize the wavefield in each medium. The boundary conditions are then matched globally along the interface, in the least-squares sense. The smoothness of the medium is required to guarantee that each point along a given interface is densely illuminated with the beams radiated from the sources distributed along the interface. The choice of the initial beam width does not affect seriously the overall results because its effects are smoothed by the least-squares procedure to find the multiplicative complex constant that represents the strength of each source interacting with all other sources and with the input motion. In this thesis, our method is applied only to antiplane, or SH, waves in a layer with a simple 2-D shape having velocity which varies linearly with depth, but it is straightforward to extend it to P and SV waves in multiple layers with irregular boundaries with more general variation in velocity. All we need is to establish the appropiate source distribution to represent the elastic wave scattering from the irregular boundaries and implement a one-point ray tracing to construct Green's function for each source. The rest of our algorithm remains the same for any case.

Regarding the second class of problems mentioned at the beginning of the present Chapter, namely seismic scattering and attenuation in the lithosphere, we have used the boundary integral method to solve deterministically multiple scattering problems involving SH waves in media with many inclusions. Our solution for the total field includes all scattered waves

all inclusions, and is computed for incident wavelengths comparable with the size of the inclusion. The wavefield is again represented by the distribution of artificial wave sources along the surface of all inclusions, and the boundary conditions are satisfied in the least squares sense. For the solution of this problem we used exact Green's function for homogeneous unbounded media. Our purpose was to compute the attenuation factor of the primary wave in media where the inclusions are distributed randomly. This problem has been addressed e.g by Varadan et. al. (1978) who studied SH waves scattered by cylinders of arbitrary cross-section, using T-matrix representation of the wavefield (Waterman 1969) and statistical approach based on an average procedure, and by Matsunami (1988, 1990), who studied scattering attenuation in duralumin plates with randomly distributed holes, using ultrasonic techniques. The relevance of the problem to the study of seismic scattering and attenuation in the lithosphere is well known as reviewed in Wu and Aki (1988, parts I, II, III), Toksöz and Johnston (1981), and Herraiz and Espinosa (1987).

Although the particular model studied in this thesis, namely, cavities of circular shape in a homogeneous medium, is not directly applicable to the lithosphere, we believe that by solving the wave scattering problem deterministically including all multiple scattering effects, we are able to assess the applicability of various approximate methods developed to compute scattering and attenuation for more realistic earth models. For example, analytical solutions have been obtained for random media characterized by spatial autocorrelation of various forms such as the exponential and Gaussian, using the first Born approximation (Chernov 1960). The same random media characterization was used by Frankel and Clayton (1984, 1986) in

their finite difference simulation of scattering. Their results on scattering loss of incident wave per unit distance of propagation showed disagreement with the results obtained under the Born approximation. In the present thesis we shall compare the frequency dependency of the scattering loss of incident waves obtained by various approximate methods with our solution.

1.2 Scope and Chapter Contents.

The basic formulation of our method is described in Chapter II, giving first a brief summary of both the boundary integral formulation of the wave scattering problem and the Gaussian beam solution for an SH wave. Then, we describe the procedure to combine them in compliance with the boundary conditions of the problem. An important step in this procedure is to represent the traction as superposition of Gaussian beams of the same type as those used to represent displacement. Instead of developing a new asymptotic expansion for stress, we differentiate the Gaussian beam for displacement with respect to the vector normal to the boundary and superimpose them in a similar manner as for displacement. This approximation appears to be accurate as long as the number of beams used to represent displacement is increased for traction. In this Chapter II we also test the method by solving problems with known exact solutions and those obtained by other reliable approximate methods. We have chosen examples involving only homogeneous media for this purpose. First we deduce an explicit expression for the Gaussian beam representation of displacement and traction in homogeneous media, using a geographical coordinate system. We compute the wavefield (Green's function) due to a line source in unbounded medium using superposition of these Gaussian beams, for various choices of the initial beam width, radiation angle range and total number of beams in

a synthesis. Their effects are studied by comparing displacement and stress fields with the corresponding exact solutions given by the Hankel functions of first and second kind, (order zero), respectively. Those values are adjusted in order to best fit both solutions (beam superposition and exact formula) in the spatial range considered in the testing examples. We choose as testing examples the scattering by ridge, canyon and alluvial valley, all of which have the cylindrical shape with a semi-circular cross-section. Results are given in frequency domain.

In Chapter III we have applied the boundary integral-Gaussian beam method to calculate the effects of a cylindrical inclusion on the surface ground motion of a homogeneous half-space. The inclusion is considered either "hard" or "soft" when its velocity is larger or smaller than, respectively, that of the half-space. Our results are given in frequency and time domains. We found a surprising result that both soft and hard inclusions cause deamplification of surface motion above the inclusion. The effect is attributed to scattering and trapping of energy in the case of soft inclusion, and to scattering and defocusing in the case of hard inclusion.

In Chapter IV we apply the method to the scattering of SH waves in inhomogeneous media with irregular topography and interface. We describe the algorithm to find Green's function in media with linear velocity gradient by superposition of Gaussian beams. The computation of radiation angles for given source-receiver positions, the ray-centered coordinates without involving ray tracing, and the summation of Gaussian beams is performed by a computer program subroutine called INGREEN. Amplitude and phase of Green's function for displacement and traction are shown for various choices of the velocity gradient. The scattering problem is solved for a

ridge in the inhomogeneous half-space and for an inhomogeneous cylindrical alluvial basin embedded in a homogeneous half-space, for various values of velovity gradient and frequency.

Chapter V is devoted to application of the boundary integral method to compute synthetic seismograms in media with many inclusions. For simplicity we consider cylindrical cavities in full and half spaces for the incident SH plane wave or point(line) source. The seismograms are computed for wavelengths ranging from $30a$ to a, where a is the radius of the cavities. The validity of our solution was tested succesfully against known analytical solution for the case of a single cavity, and by measuring normalized residual tractions along cavity boundaries for many cavities. We analyzed the scattering due to cavities distributed at regular spatial intervals, and identified various phases associated with ray paths for multiply reflected and diffracted waves. Finally, we compute synthetic seismograms for scattered wave field generated by many cavities randomly distributed in full and half spaces. We used the seismograms obtained for the full space case to compute the attenuation factor Q^{-1} of the direct wave due to scattering loss. The resulting scattering Q^{-1} as a function of incident wave number k times the diameter $d = 2a$ showed a peak around $kd = 2$, and Q^{-1} decreased proportionally to k^{-1} for $kd > 2$, in agreement with the result based on the Born approximation as well as the simple argument based on ray theory.

CHAPTER II

DESCRIPTION AND TESTING OF THE METHOD

2.1 Introducction

This Chapter has two main purposes. The first is to give the theoretical formulation of our method starting with some basic concepts of both the boundary integral and Gaussian beam methods that are relevant to the problems addressed in this work. The second is to test the method by solving some problems with known analytical solutions, or with available solutions by other reliable numerical methods. In section 2.2 we introduce the so-called "single layer potential" of the wavefield for scattering problems, based on wave source distribution (Ursell, 1973). Briefly explained, the boundary conditions of the problem are imposed on the integral representation of the wavefield, leading to an integral equation in which the kernel, or Green's function, incorporates the values of the wavefield at the boundaries into the solution for the total wavefield. In general, the integral equation is solved numerically by means of discretization of the boundary. This and other boundary methods have emerged from the integral representation of the wavefield in heterogeneous media (see for instance Mow and Pao, 1971), where the heterogeneities are homogeneous region of different elastic properties enclosed by boundaries. They have been succesfully applied to solve various types of wave propagation problems in Engineering and Seismology (Brebbia 1978, Dravinsky 1982, Kawase 1988). From the computational point of view, the use of boundary integral is for most cases more convenient than Finite Element and Finite Differences methods since we do not have to discretize the whole body but only the boundaries.

While the boundary methods share a common foundation, they differ on their discretization scheme and the way in which Green's function is evaluated. We use a discretization based on distribution of point (line) sources along the boundary of two different media for homogeneous and inhomogeneous media. Our Green's function can be exact for homogeneous media, or computed by superposition of Gaussian beams for inhomogeneous media, and the boundary conditions are imposed in the least-squares sense. Criteria to select the source distribution for optimal compliance of the boundary conditions are given. We use first the simple case of an irregular free-surface topography to introduce the boundary integral method, and extend it to more complicated structures involving different media and irregular interfaces.

In section 2.3 we formulate the Gaussian beam solution in a way that is more appealing to geometrical intuition, instead of presenting the involved mathematical procedure to obtain the asymptotic expansion of the ansatz solution of the Elastodynamic equation, which has been extensively described earlier (see for instance Červený 1982). Here we follow the approach developed by Madariaga (1984) for Gaussian beams in vertically heterogeneous media, which is suitable for the later formulation of our method. The final expression for the Gaussian beam, however, corresponds to the paraxial ray solution given by Červený et.al. (1982). We give in addition some differentiation formulas to compute the shear stress field in terms of the same Gaussian beams that represent displacement field. All formulas are given in terms of the ray-centered coordinates (s, n). The wavefield produced by a point(line) source in 2-D vertically inhomogeneous media is then constructed by superposition of Gaussian beams, departing from the source

point with regular take off angle intervals. In section 2.4 we develop an expression for the Gaussian beam solution of both displacement and stress fields in homogeneous media in terms of cartesian coordinates (x, z), and confirm the validity of the superposition to represent a point(line) source using an analytical solution given by Hankel function.

Our second purpose in this chapter is to check the accuracy of the method when Green's function is computed by superposition of Gaussian beams. This is done in section 2.5. We have selected three examples of wave propagation in media with strong lateral heterogeneities, which have already been solved analytically (closed form) or by using other well tested numerical methods. In subsection 2.5.1 we calculate the response of a semicylindrical canyon of radius a to incident SH waves for various frequencies, and compare it with the closed form solution given by Trifunac (1973). In 2.5.2 this example is used to study the effect introduced in the solution by selecting different values of the initial beam width, number of sources, number of beams and the range of their radiation angle. In 2.5.3 we calculate the response of a half-space whose free-surface topography is a cosine shaped mountain. The solution is compared with that obtained by Bouchon (1973) using the Aki-Larner technique (Aki and Larner 1970), which has been proved to be accurate for the cases studied. Additionally the values of traction residual at the free surface are used, as a measure of the accuracy of the solution. In subsection 2.5.4 we solve the case of a semicylindrical alluvial valley in a half-space bedrock, for different values of impedance contrast and frequency. Results are compared with the corresponding Boundary Element solution (Kawase 1988).

2.2 The Boundary Integral method

Let us consider the medium to be a homogeneous full-space with a two-dimensional inclusion of an arbitrary cross-sectional shape C (see Figure 2.1). Referring to a cartesian coordinate system x-z (z-positive down), a plane SH wave v_0 is incident from below. Also, let us start for the sake of simplicity, with the case in which the inclusion is a cavity. The total wavefield v at an observation point P (position vector $\vec{r}_P$) will be $v(\vec{r}_P) = v_0(\vec{r}_P) + v_s(\vec{r}_P)$, where v_s is the wavefield scattered by the cavity. As mentioned in the introduction, the scattered field can be written as

$$v_s(\vec{r}_P) = \int_C \sigma(\vec{r}_Q) G(\vec{r}_P|\vec{r}_Q) ds \tag{2.1}$$

where $\sigma(\vec{r}_Q)$ is the strength of the source located at $\vec{r}_Q$ on the boundary, C is the curve representing the boundary of the cavity, ds is an element of arc of C and $G(\vec{r}_P|\vec{r}_Q)$ is Green's function. This integral representation of the wavefield is called single layer potential by some authors (Copley 1967, Burton and Miller 1971, Ursell 1973) corresponding to the role of potential density $\sigma(\vec{r}_Q)$ at the boundary points. Similarly, a "double layer potential"

$$\int_C \gamma(\vec{r}_Q) \frac{\partial}{\partial \hat{n}} G(\vec{r}_P|\vec{r}_Q) ds$$

will represent a dipole distribution, where $\gamma(\vec{r}_Q)$ is the strength of the dipole at the point Q on the boundary, and $\hat{n}$ is the outward unit vector normal to C. The word "potential" is taken from the potential theory developed by Kupradze (1979) to deal with elliptic partial differential equations of second order. In the general formulation of boundary integral equation methods developed to solve wave propagation problems, equation (2.1) is classified as "indirect" integral representation because the scattered wavefield v_s is given in terms of the unknown values of the distribution density σ (or γ for

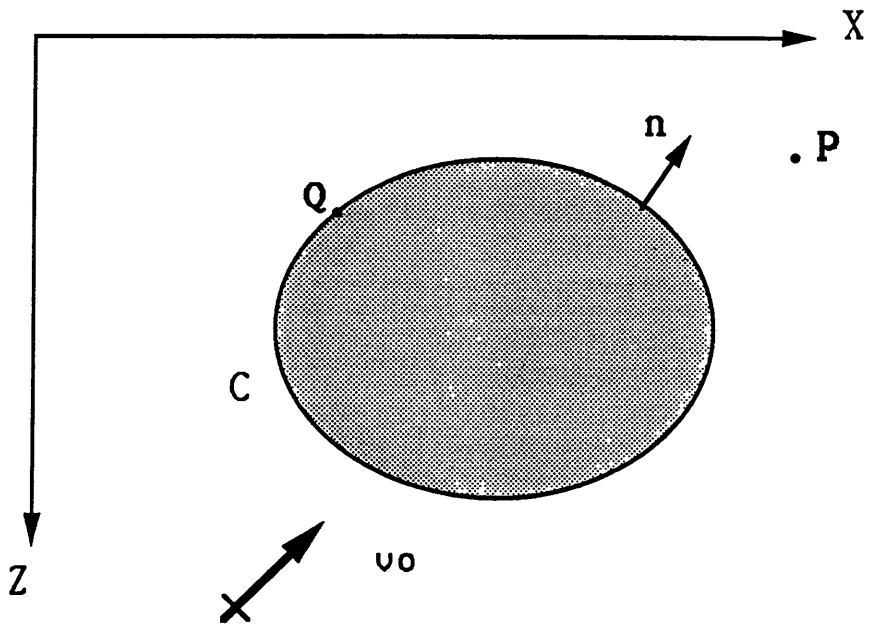

FIGURE 2.1 A cavity enclosed by the boundary C in an elastic full-space. The incident wave v_0 is plane wave or point(line) source. Point Q on the boundary corresponds to the location of a wave source representing waves scattered by the boundary. The total field, i.e. incident and scattered waves, are observed at point P.

dipole) at the boundary. Applying the boundary condition

$$\frac{\partial v}{\partial \hat{n}}\Big|_C = 0$$

to (2.1), it is found that $\sigma(\vec{r}_Q)$ satisfies the integral equation (Smirnov 1964)

$$\int_C \sigma(\vec{r}_Q)\frac{\partial}{\partial \hat{n}} G(\vec{r}_P|\vec{r}_Q)ds = -\frac{\partial v_0(\vec{r}_P)}{\partial \hat{n}}$$

On the contrary, the "direct" integral representation gives v_s in terms of the known values of the displacement and traction fields at the boundary (Brebbia 1978). To evaluate the integral in (2.1) we resort to the following discretization scheme. Let us assume that instead of the continuous wave source distribution we select N points along the boundary of the inclusion and assign a line source at each point. The strength σ is thus written as

$$\sigma(\vec{r}_Q) = \sum_{j=1}^{N} A_j \delta(|\vec{r}_Q - \vec{r}_{Q_j}|) \tag{2.2}$$

where $\vec{r}_{Q_j}$ is the vector position of the $j-th$ source. Inserting (2.2) in (2.1)

$$v(\vec{r}_P) = v_0(\vec{r}_P) + \int_C \sum_{j=1}^{N} A_j \delta(|\vec{r}_Q - \vec{r}_{Q_j}|)G(\vec{r}_P|\vec{r}_Q)ds$$

$$v(\vec{r}_P) = v_0(\vec{r}_P) + \sum_{j=1}^{N} A_j \int_C \delta(|\vec{r}_Q - \vec{r}_{Q_j}|)G(\vec{r}_P|\vec{r}_Q)ds$$

$$v(\vec{r}_P) = v_0(\vec{r}_P) + \sum_{j=1}^{N} A_j G(\vec{r}_P|\vec{r}_{Q_j}) \tag{2.3}$$

A_j is a complex constant that represents the strength of the source located at the $j-th$ point on the boundary. Since equation (2.3) is derived for a given ω, it should be written as

$$v(\vec{r}_P;\omega) = v_0(\vec{r}_P,\omega) + \sum_{j=1}^{N} A_j(\omega)G(\vec{r}_P|\vec{r}_{Q_j};\omega) \tag{2.4}$$

In general, the appropiate number of sources assigned to the cavity may vary according to the shape of its cross-section and to its size relative to the input wavelength.

The problem has been reduced to determine the constants $A_j(\omega)$. This is done by imposing the boundary conditions in the least-squares sense (Sanchez-Sesma and Rosenblueth 1979), i.e. by minimizing the total quadratic error of the values of shear traction $\mu \frac{\partial v}{\partial \hat{n}}$ along the boundary:

$$L = \int_C \left| \mu \frac{\partial v}{\partial \hat{n}} \right|^2 ds \tag{2.5}$$

where μ is the shear modulus and $\hat{n}$ the outward normal vector to C at P. The minimum value of L is found from $\frac{\partial L}{\partial A_j} = 0$, which leads to the linear system:

$$\sum_{j=1}^{N} \Gamma_{ij} A_j = b_i \tag{2.6}$$

where

$$\Gamma_{ij} = \int_C \frac{\partial G_i^*}{\partial \hat{n}} \frac{\partial G_j}{\partial \hat{n}} ds$$

and

$$b_i = - \int_C \frac{\partial G_i^*}{\partial \hat{n}} \frac{\partial v_0}{\partial \hat{n}}$$

$(^*)$ stands for complex conjugate, $i, j = 1, 2, ..., N$ and $G_\alpha = G(\vec{r}_P | \vec{r}_{Q_\alpha})$. In (2.6) Γ_{ij} represents the mutual interaction of all sources and b_i represents the interaction of each source with the incident wave.

This formulation can be extended to include other type of heterogeneities. For example, let us take the media shown in Figure 2.2 (a) for a buried inclusion, (b) for valley and (c) for layer, which are refered as "interior" regions in a half-space. In this case the heterogeneities are the interface C_2 separating two different media of shear rigidities μ_1 and μ_2 and

shear velocities β_1 and β_2 respectively, and the free-surface topography C_1. Using (2.1), the fields inside and outside the interior regions in Figure 2.2 are represented by

$$v_2(\vec{r}_P;\omega) = \sum_{m=1}^{M} A_m G_2(\vec{r}_P|\vec{r}_{Q_m};\omega) \tag{2.7}$$

$$v_1(\vec{r}_P;\omega) = v_0(\vec{r}_P) + \sum_{n=1}^{N} B_n G_1(\vec{r}_P|\vec{r}_{Q_n};\omega)$$

respectively, where M is the number of sources corresponding to the interior region and N the number of sources corresponding to the half-space. The coefficients A_m and B_n are obtained following the least-squares procedure described before; that is by minimizing the quadratic error corresponding to mismatch of boundary conditions. In the present case these are free-traction along C_1 and continuity of displacements and tractions along C_2:

$$\mu_1 \frac{\partial v_1}{\partial \hat{n}}\Big|_{C_1} = 0$$

$$v_1 = v_2\Big|_{C_2}$$

$$\mu_1 \frac{\partial v_1}{\partial \hat{n}} = \mu_2 \frac{\partial v_2}{\partial \hat{n}} \quad \Big|_{C_2}$$

The errors in displacement and tractions corresponding to mismatch of the boundary conditions are

$$\theta_1 = \mu_1 \frac{\partial v_1}{\partial \hat{n}}\Big|_{C_1}$$

$$\theta_2 = v_1 - v_2\Big|_{C_2}$$

$$\theta_3 = \mu \frac{\partial v_1}{\partial \hat{n}} - \frac{\partial v_2}{\partial \hat{n}} \quad \Big|_{C_2}$$

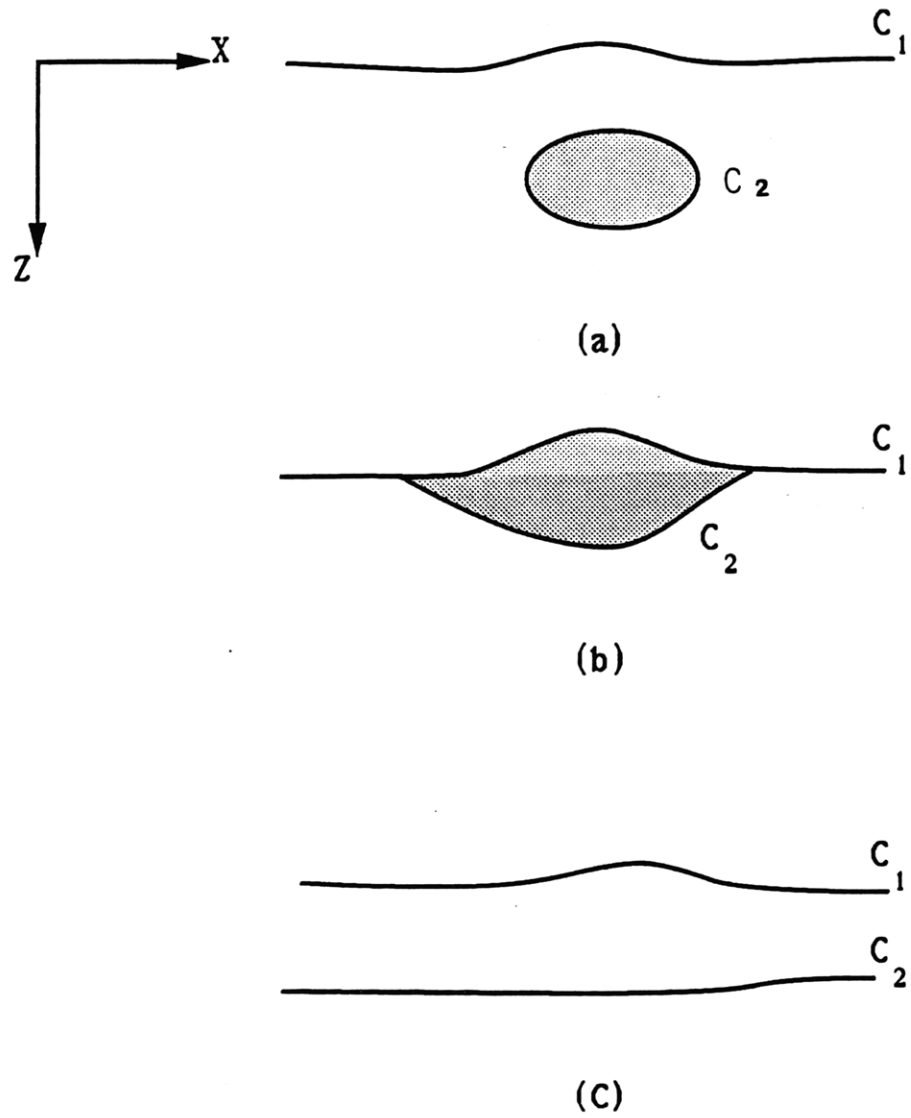

FIGURE 2.2 (a,b,c,) show examples of structures with lateral heterogeneities for which the method introduced in this thesis can be applied to compute the scattering in the case of incident SH waves. C_1 defines the free surface topography and C_2 defines either the depth of the interface or the shape of the inclusion.

where $\mu = \mu_1/\mu_2$, is the ratio of the rigidities of media 1 and 2; and the functional to be minimized

$$L = \int_{C_1} \theta_1^2 ds_1 + \int_{C_2} [(\frac{\omega}{\beta_1})^2 \theta_2^2 + \theta_3^2] ds_2 \qquad (2.8)$$

The weight $(\omega/\beta_1)^2$ for θ_2^2 is used to equalize the units and degree of variability of each term in L (Sanchez-Sesma and Esquivel, 1979, (Brebbia and Dominguez 1989). It is important to point out here that whenever an interface between two different media is present, the selected points along the boundary represent the locations of two different sources; one for radiation into each medium. Thus, if we selected M points along C_2 , the corresponding number of unknowns is $2M$, and the total number of unknowns is $N + 2M$.

2.3 SH Gaussian beam in vertically inhomogeneous media

In this section we first describe the approach of Madariaga (1984) to construct a Gaussian beam in 2-D media in which seimic wave velocity β varies only with depth. We use this formlulation to represent Green's function to be used in the boundary integral scheme. The line source is constructed by superposition of beams of the same initial width, which are shot from the source point at regular take-off angle intervals, with a sufficient number of beams to densely illuminate the observation point. In the second part of this section we develop a Gaussian beam representation of shear stress by taking appropiate spatial derivatives of the corresponding Gaussian beam displacement field.

2.3.1 Gaussian beam theory

As illustrated in Figure 2.3, a central ray is defined as having origin at x=0, and z=0 and horizontal slowness $p_0 = \frac{sin(\phi_0)}{\beta_0}$. To construct a Gaussian

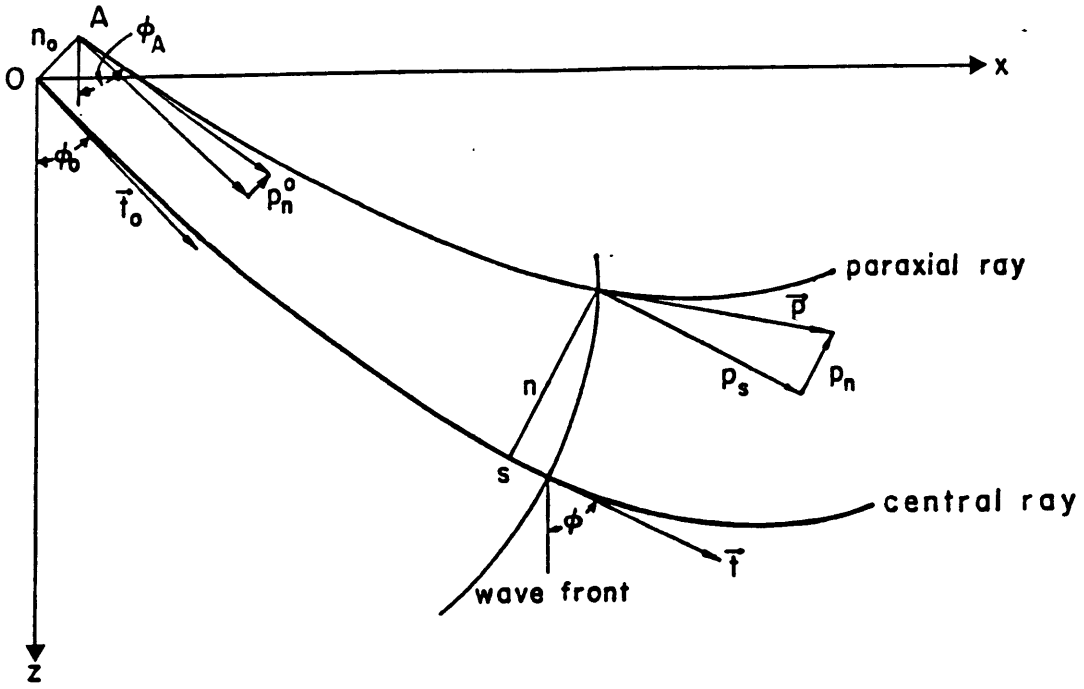

FIGURE 2.3 Geometry of the pararaxial ray corresponding to a central ray deparing from O with take-off angle ϕ_0 used in the text to develop the Gaussian beam solution. The paraxial ray is obtained by perturbation of origin and slowness of the central ray (from Madariaga 1984).

beam attached to this ray we consider a paraxial ray, i.e., a ray originated from point A with a small perturbation of position and slowness of the central ray. The perturbation in slowness is given by $\vec{p}_n^0$, perpendicular to the unit vector $\vec{t}$ tangent to the central ray at O. Therefore, the slowness of the paraxial ray at A is $\vec{p} = \vec{p}_0 + \vec{p}_n^0$. After a certain time of propagation the slowness $\vec{p}$ of the paraxial ray has components p_s and p_n at a point whose coordinates in the so-called ray-centered coordinate system (s, n) attached to the central ray, where s is the distance measured along the central ray and $n = n(s)$ is the lateral displacement of the paraxial ray, measured along normal to the central ray at s (Červený 1982). To the first order Taylor expansion, we have $p_s = \frac{1}{\beta}(1 - p_0 \frac{\partial \beta}{\partial z} n)$. Since $p_n = 0$ at the central ray, it is assumed that on the first order approximation $p_n = C(s)n$ at the paraxial ray, where $C(s)$ is proportional to the curvature of the wave front. Let $\tau(s, 0)$ be the travel time over a length s along the central ray; then the corresponding travel time along the paraxial ray will be delayed by $\int_0^n p_n \, dn$. Putting $p_n = C(s)n$ into the integral

$$\tau(s, n) = \tau(s, 0) + \frac{1}{2} C(s) n^2 \tag{2.9}$$

where $\tau(s, 0) = \int_0^s ds/\beta(s)$ The values of $n(s)$ and $p_n(s)$ can be found by solving the dynamic ray tracing equations (DRT)

$$\frac{dn}{ds} = \beta p_n \tag{2.10}$$

$$\frac{dp_n}{ds} = -\frac{n}{\beta^2} \frac{d^2\beta}{dn^2}$$

(Červený and Pšenčık, 1979). The initial conditions are $p_{n_0} = C(0)n_0$, where $n_0 = n(0)$ is the initial displacement of the paraxial ray (see Figure

2.3). Once the DRT equations are solved for $n(s)$ and $p_n(s)$ the asymptotic ray amplitude, or geometrical solution, for the paraxial ray in the case of an SH wave is given by

$$v(s,n;\omega) = \left[\frac{\rho(0)\beta(0)n(0)}{\rho(s)\beta(s)n(s)}\right]^{1/2} e^{i\omega\tau(s,n)}; \quad s \geq 0 \tag{2.11}$$

where ρ is density (Červený and Pšenčík, 1979).

In vertically inhomogeneous media the DRT equations can be transformed into simple 1-D form by inserting $d/ds = \cos\phi(d/dz)$ and $d/dn = \sin\phi(d/dz)$ into equation (2.10), i.e.

$$\frac{dn}{dz} = \frac{\beta}{\cos\phi} p_n \tag{2.12}$$

$$\frac{dp_n}{dz} = -\frac{p^2}{\cos\phi}\frac{d^2\beta}{dz^2} n$$

where $p = \sin\phi/\beta$ is the ray parameter. In this particular case we can obtain closed form solutions for n and p_n by eliminating $p_n = \frac{\cos\phi}{\beta}\frac{dn}{dz}$ from equations 2.12

$$\frac{d}{dz}\left(\frac{\cos\phi}{\beta}\frac{dn}{dz}\right) = -\frac{p^2}{\cos\phi}\frac{d^2\beta}{dz^2} n \tag{2.13}$$

A trial solution $n_a = \cos\phi$ satisfies equation 2.13, since $\frac{d\phi}{dz} = \frac{p}{\cos\phi}\frac{d\beta}{dz}$, we have

$$\frac{d}{dz}\left(\frac{\cos\phi)}{\beta}\frac{dn_a}{dz}\right) = \frac{d}{dz}\left(-\frac{p^2}{\beta}\frac{d\beta}{dz}\right) = -p^2\frac{d^2\beta}{dz^2}$$

which is identical to the right hand side term, if $n_a = \cos\phi$. Since all parameters vary only with z, a second solution can be found from $n_b = \cos\phi f(z)$. After inserting it into 2.13, it is found that

$$f(z) = \int_0^z \frac{\beta}{\cos^3\phi} dz \tag{2.14}$$

Complete solutions for $n(s)$ and $p_n(s)$, where $s = s(z)$ are then

$$n(s) = A\cos\phi + B\cos\phi f(z) \tag{2.15}$$

$$p_n(s) = -Ap^2\frac{d\beta}{dz} + \frac{B}{\cos\phi}[1 - p^2\frac{d\beta}{dz}\cos\phi f(z)]$$

A and B are real unknowns, to be found from the initial conditions. The corresponding expression for $C(s)$ (from $p_n = C(s)n$) is:

$$C(s) = -\frac{p^2}{\cos\phi}\frac{d\beta}{dz} + \frac{B}{\cos^2\phi[A + Bf(z)]} \tag{2.16}$$

The initial conditions in the vertically inhomogeneous medium are chosen in such a way that (2.15) may represent either a plane wave or a point source at the origin (Červený et. al. 1982). For a plane wave, $n(0) = 1$ and $p_n(0) = 0$, i.e. the paraxial ray shifts its origin in the direction n with respect to the central ray, and takes off with the same initial angle as the central ray. In this case $A = 1/\cos\phi_0$, $B = p^2\frac{d\beta}{dz}\big|_{z=0}$ and

$$n^P(s) = \frac{\cos\phi}{\cos\phi_0} + p^2\frac{d\beta}{dz}\Big|_{z=0}\cos\phi \tag{2.17}$$

$$p_n^P(s) = p^2\frac{d\beta}{dz}\Big|_{z=0}[\frac{1}{\cos\phi} - p^2\frac{d\beta}{dz}f(z)] - \frac{p^2}{\cos\phi_0}\frac{d\beta}{dz}$$

where the upperscript P stands for "plane wave". For a point(line) source $n(0) = 0$ and $p_n(0) = 1/\beta_0$. The paraxial ray takes off from the origin of the central ray but with different initial take-off angles. In this case $A = 0$, $B = \frac{\cos\phi_0}{\beta_0}$ and

$$n^L(s) = \frac{\cos\phi_0\cos\phi}{\beta_0}f(z) \tag{2.18}$$

$$p_n^L(s) = \frac{\cos\phi_0}{\beta_0}\Big[\frac{1}{\cos\phi} - p^2\frac{d\beta}{dz}f(z)\Big]$$

where the upperscript L stands for line source.

A Gaussian beam is defined as the paraxial ray (defined by equation 2.11) where n and p_n are obtained by a linear combination of the corresponding solutions for plane wave and point(line) source, through a complex parameter ϵ, i.e.

$$n(s) = \epsilon n^P(s) + n^L(s) \tag{2.19}$$

$$p_n(s) = \epsilon p_n^P(s) + n^L(s)$$

In this case the quantities $C(s)$ and $\left[\frac{\rho(0)\beta(0)n(0)}{\rho(s)\beta(s)n(s)}\right]$ defined in equations (2.9) and (2.11) respectively, become complex. The asymptotic wave function corresponding to an SH Gaussian beam is written as

$$v(s,n;\omega) = \frac{1}{J^{1/2}} e^{i\omega\tau(s,n)};\ s \geq 0 \tag{2.20}$$

where

$$J = \left[\frac{\rho(s)\beta(s)n(s)}{\rho(0)\beta(0)n(0)}\right]$$

is called "spreading" in ray theory.

In a media with more general inhomogeneity the Gaussian beam may be constructed in a similar way as described above, i.e. through a linear combination of solutions of the DRT equations for initial conditions corresponding to plane wave and point(line) sources.

The SH wavefield observed at a point P due to a source located at Q in a 2-D vertically inhomogeneous media, can be constructed by superposition of Gaussian beams of the type (2.20), i.e.

$$v^{SH}(\vec{r}_P;\omega) = A(\vec{r}_Q)\int_\Omega \frac{1}{J^{1/2}} e^{i\omega\tau(s,n)} d\phi \tag{2.21}$$

where $\vec{r}_P$ and $\vec{r}_Q$ are the vector positions of points P and Q respectively, $A(\vec{r}_Q)$ is the strength or excitation function at the source point Q, Ω is

the radiation angle range, and (s, n) represent the ray centered coordinates of point P with respect to each ray. This expression shall be used to compute displacement Green's function in our boundary integral scheme for scattering problem.

2.3.2 Gaussian beam representation of traction

To satisfy continuity conditions for the displacement and traction in problems where boundaries are present, we need to calculate the shear stress acting at a point P on a plane with normal $\hat{n} = (n_x, n_z)$ due to a source at Q. In order to use equation (2.21) as the wavefield due to the source at Q, we have to find a representation of shear stress in terms of the same Gaussian beams used to represent displacement. We shall do this by taking the space derivative $\partial/\partial\hat{n}$ of v in (2.20), where we will take $\hat{n}$ as the outward vector normal to the boundary. However we must keep in mind that the asymptotic procedure that leads to the expression of v in equation(2.20) may have to be modified for its derivative. For instance, any of the spatial derivatives may introduce an additional factor of $O(\omega)$. The effect of boundaries in Gaussian beam propagation has been studied by Červený and Pšenčík (1984) by modifying the solution at the interface to locally satisfy the boundary conditions. Their method is similar to the one first proposed by Popov and Pšenčík (1978) to calculate ray amplitudes in media with curved interfaces. Basically they establish a set of differential equations in the neighborhood of the point where the ray intersects the interface, to calculate new initial conditions for the reflected/transmitted beam. An important assumption is that the irregularity of the interface must be smooth, that is, its radius of curvature must be greater than the wavelength of the incident field.

Madariaga and Papadimitriou (1985) used the complex travel time $\tau(s,n)$ at the interface to calculate the geometrical spreading of the reflected/transmitted beam in terms of the spreading of the incident beam. The amplitudes are then multiplied by the corresponding plane wave reflection/ transmission coefficients. Recently George (1987) derived explicit expressions for the reflection and transmission coefficients for an incident SH-Gaussian beam in terms of both interface and (parabolic) wavefront curvatures. Continuity of displacement and traction is applied locally at the interface, in the neighborhood of the intersection point with the central ray. According to George, these formulas are still valid when the curvature of the interface is comparable to the wavelength.

In our scheme we need no modification to the asymptotic solution, because we try to match boundary conditions globaly using the distribution of unknown sources along the boundary instead of continuing beams to reflected and transmitted waves by locally satisfying boundary conditions.

Since all our application problems are formulated in a cartesian system represented by geographical coordinates x, z, and

$$\frac{\partial}{\partial \hat{n}} = n_x \frac{\partial}{\partial x} + n_z \frac{\partial}{\partial z} \quad ;$$

explicit formulas for the derivatives $\frac{\partial v}{\partial s}\frac{\partial s}{\partial q}$, and $\frac{\partial v}{\partial n}\frac{\partial n}{\partial q}$, $q = (x, z)$ are necessary. The derivatives $\frac{\partial s}{\partial q}$ and $\frac{\partial n}{\partial q}$ depend upon the characteristics of the medium. Let us assume that the ray centered coordinates s and n can be expressed in terms of x, z using a suitable coordinate transformation. From equation (2.20)

$$\frac{\partial v}{\partial s} = [i\omega \frac{\partial \tau}{\partial s} - \frac{1}{2J}\frac{\partial J}{\partial s}]v$$

Using the definition of $\tau(s,n)$ (equation 2.9)

$$\frac{\partial v}{\partial s} = \left[i\omega\left(\frac{s}{\beta_0} + \frac{1}{2}\frac{\partial C}{\partial s}n^2\right) + \frac{1}{4}\left(\frac{1}{n}\frac{\partial n}{\partial s} + \frac{1}{\beta}\frac{\partial \beta}{\partial s}\right)\right] v \tag{2.22}$$

Similarly

$$\frac{\partial v}{\partial n} = i\omega\frac{\partial \tau}{\partial n}v$$

or,

$$\frac{\partial v}{\partial n} = i\omega C(s)nv \tag{2.23}$$

The term $\frac{1}{2J}\frac{\partial J}{\partial s}$ can be simplified if we assume that the density ρ in the definition of J (equation 2.20) is constant, then

$$\frac{1}{2J}\frac{\partial J}{\partial s} = \frac{1}{2\beta}\frac{\partial \beta}{\partial s}$$

The shear stress field at a point P acting in the direction of $\hat{n}$ due to a line source located at point Q can be constructed by superposition of these Gaussian beams,

$$\sigma^{SH}(\vec{r}_P, \vec{r}_Q; \hat{n}) = \mu A(\vec{r}_Q)\int_\Omega \frac{\partial v}{\partial \hat{n}}d\phi \tag{2.24}$$

where μ is the rigidity of the medium and ϕ is the take off angle covering the radiation Ω at regular intervals.

2.4 SH-Gaussian beams in homogeneous media

The solution for a Gaussian beam in homogeneous unbounded media can be readily obtained from the formulation in the previous section, by puting $d\beta/dz = 0$. The function f in (2.14) becomes $f(s) = \beta_0 s/\cos^3\phi_0$ (z = s in homogeneous media), where β_0 is the constant shear wave velocity. From (2.17), since $\phi = \phi_0$,

$$n^P = 1$$

$$p_n^P = 0$$

From (2.18)

$$n^L = As$$

$$p_n^L = 1/\beta_0$$

where $A = 1/\cos\phi_0$ The corresponding Gaussian beam DRT solutions are (from 2.19)

$$n = \epsilon + s$$

$$p_n = 1/\beta_0$$

where we have chosen $A = 1$. In some Gaussian beams literatures (e.g. Červený 1982, Nowack and Aki 1984), the complex parameter ϵ is chosen in the form of $s_0 - i\frac{\omega}{2\beta_0}L_M^2$, where s_0 is the point along the central ray where the beam is narrowest, and L_M is the half-width of the beam at s_0, as shown in Figure 2.4 (a). We also use parameter L_0 which is related to L_M by $L_M = (2\beta_0/\omega)^{1/2}L_0$. Here, we will set the location of the beam waist at $s_0 = 0$ and the beam width to be minimum at the origin of the central ray. Using these parameters, we have

$$n = s - iL_0^2 \tag{2.25}$$

$$p_n = 1/\beta_0$$

Inserting (2.25) to $n(s)$ in the expression for J in (2.20)

$$J = \frac{s - iL_0^2}{-iL_0^2} \tag{2.26}$$

which becomes the geometrical spreading for a ray in homogeneous media originating from $s = 0$ if $L_0 = 0$. In general, J is a complex number. Also,

inserting (2.25) in the expression for $C(s) = p_n/n$, we have $C(s) = p_n/n = 1/\beta_0(s - iL_0^2)$. Taking into account that the travel time $\tau(s,0) = s/\beta_0$ in homogeneous media, equation (2.9) can be written as

$$\tau(s,n) = \frac{1}{\beta_0}\left(s + \frac{1}{2}\frac{n^2}{s - iL_0^2}\right) \tag{2.27}$$

$\tau(s,n)$ is also a complex quantity. Both (2.26) and (2.27), along with (2.20) define completely the Gaussian beam v in homogeneous media. Let us summarize these concepts. Refering to Figure 2.4 (a), the beam is defined for a central ray with origin at $s = s_0 = 0$, and $v(s,n;\omega)$ represents the shear wave field at an observation point whose ray centered coordinates with respect to the central ray are s and n, measured along and normal to the ray, respectively. The real part of $\tau(s,n)$ measures the travel time from 0 to s along the central ray and the additional time due to the curvature of the wave front at n. Its imaginary part describes the bell-shaped amplitude distribution of $v(s,n)$ with respect to n increases (hence the name Gaussian beam).

In a Cartesian system representing geographical coordinates (Figure 2.4 (b)) , the beam solution in a homogeneous medium can be expressed in terms of x and z (z positive down) by using the following formulas (Benites and Aki, 1988):

$$s = (x - x_0)\sin\phi + (z - z_0)\cos\phi \tag{2.28}$$

$$n = -(x - x_0)\cos\phi + (z - z_0)\sin\phi$$

Let us rewrite equation (2.21) for the wave field at $P = (x,z)$, due to a line source at $Q = (x_0, z_0)$

$$v^{SH}(x,z;\omega) = \frac{i}{4\pi}\int_\Omega \frac{1}{J^{1/2}} e^{i\omega\tau(x-x_0,z-z_0,\phi)}\, d\phi \tag{2.29}$$

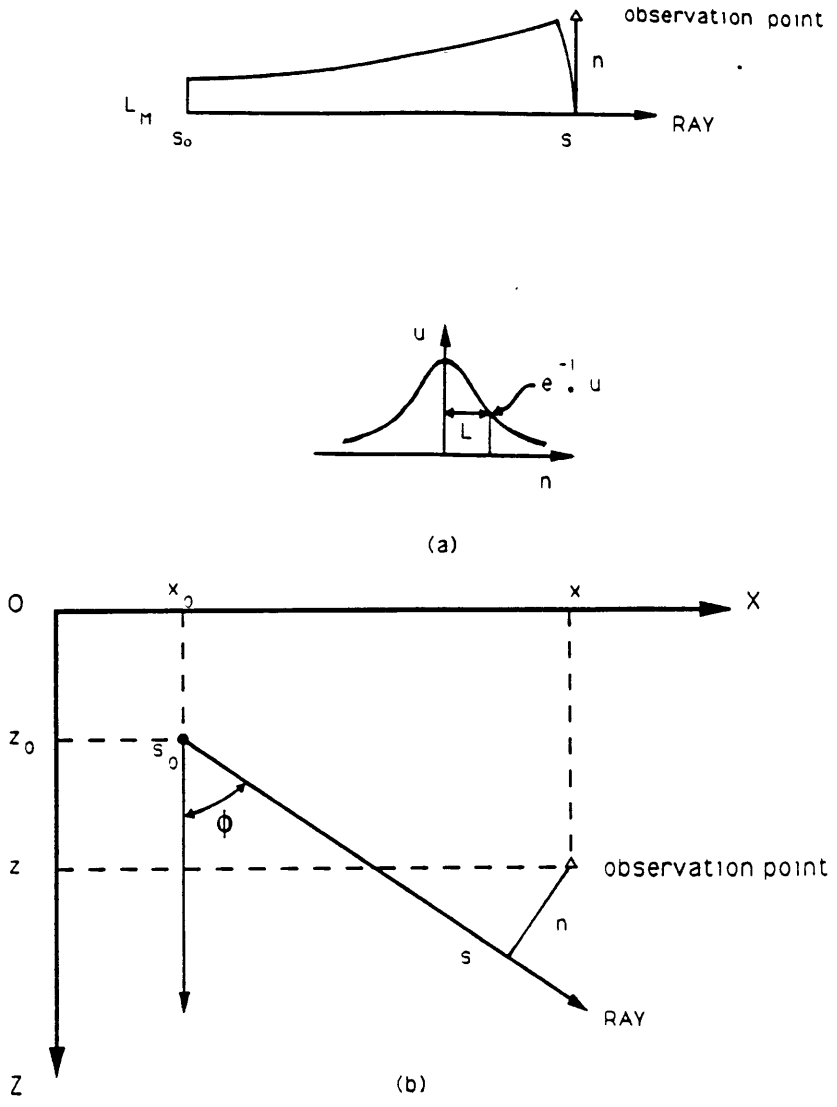

FIGURE 2.4 (a) The Gaussian beam solution attached to the central ray. The ray centered coordinates (s, n) are measured along and perpendicularly to the ray, respectively. L_M is the initial beam's half width, measured at s_0. The amplitude distribution across the ray and along n is shown below. L is the effective half-width of the beam at s, where the amplitude decreases by a factor of $1/e$. At $s = s_0$, $L = L_M$. (b) A Gaussian beam in geographical coordinates (x, z). The beams are radiated from the source at (x_0, z_0) towards the observation point, at regular angles ϕ, measured with respect to the vertical.

where the excitation constant $A(x_0, z_0) = i/(4\pi)$, according to the Fourier transformed expansion of a line source into Gaussian beams (Červený et.al., 1982). On the other hand, the exact solution for line source in unbounded homogeneous media (Brekhovskikh, 1960) is

$$w^{SH}(x, z; \omega) = \frac{i}{4\pi} \int_{\Phi} e^{i\frac{\omega}{\beta_0}[(x-x_0)\sin\phi + (z-z_0)\cos\phi]} d\phi \qquad (2.30)$$

where Φ is the contour going from $-\frac{\pi}{2} - i\infty$ to $\frac{\pi}{2} + i\infty$. The path Ω for (2.29) is restricted to the real axis and the integrand (plane wave) in (2.30) is replaced by a Gaussian beam in (2.29). Although the Gaussian beam is an approximate solution of the wave equation, it does not form a complete function basis to represent the total wavefield of the line source. Therefore, the observation point P must be densely illuminated with beams radiated from Q in order to have an accurate representation of the field. Another important point to mention is that while $w^{SH}(x, z; \omega)$ has a singularity at $P = Q$, $v^{SH}(x, z; \omega)$ is non-singular everywhere thus deviating from w_{SH} in the close neighborhood of the source. This effect , however, becomes rather advantageous when it is used in the boundary integral method, as we will see in the next section.

In our scheme, line sources distributed along the irregular boundaries of the medium represent the scattered field. To match the boundary conditions, the total field at some point of the boundary is constructed by adding the contributions of all sources at that point. Since the Gaussian beam amplitude decays quickly with distance from the central ray, the main contribution comes from those rays passing near the observation point. Therefore, the radiation angle ϕ of the beams should be selected in such a way that the observation points are covered nearly uniformly by the

beams. The case of an observation point located below the source is shown in Figure 2.5. The procedure to select ϕ can be divided into the following three steps. First the radiation range Ω is chosen arbitrarily, subject to the condition $0 \leq \Omega \leq \pi$. Second, the angle α of the straight line joinning the source and the observation point is determined and the initial and final shooting angles are defined as $\phi_0 = \alpha - \Omega/2$ and $\phi_1 = \alpha + \Omega/2$ respectively. Third, the range Ω is discretized at equal intervals and the beams are shot counterclockwise starting from ϕ_0. In this way, the number of beams on both sides of the observation point will be equal for any choice of Ω. In Figure 2.5, the line A-A' is perpendicular to the line joining source and station. We should mention that in general, the value of Ω and the number of beams per source may change from source to source, depending on the geometrical characteristics of the boundary. For instance, a source positioned at a corner may require a wider Ω and denser distribution of beams than the source for a flat surface.

The line source representation by the Gaussian beam superposition has been shown to give satisfactory results for an appropriate choice of L_0, given β_0 and frequency (see for instance Nowack and Aki, 1984). We shall now check the accuracy of our Gaussian beam representation for line source for traction. Let us first obtain the expressions for shear stress in homogeneous media using the formulae given in section 2.3. Operating (2.22) and (2.23) on the Gaussian beam for expression defined by (2.21), with J and τ given in (2.26) and (2.27) respectively; and using (2.28), we have

$$\frac{\partial v}{\partial \hat{n}} = n_x\left(\frac{\partial v}{\partial s}\sin\phi - \frac{\partial v}{\partial n}\cos\phi\right) + n_z\left(\frac{\partial v}{\partial s}\cos\phi + \frac{\partial v}{\partial n}\sin\phi\right) \qquad (2.31)$$

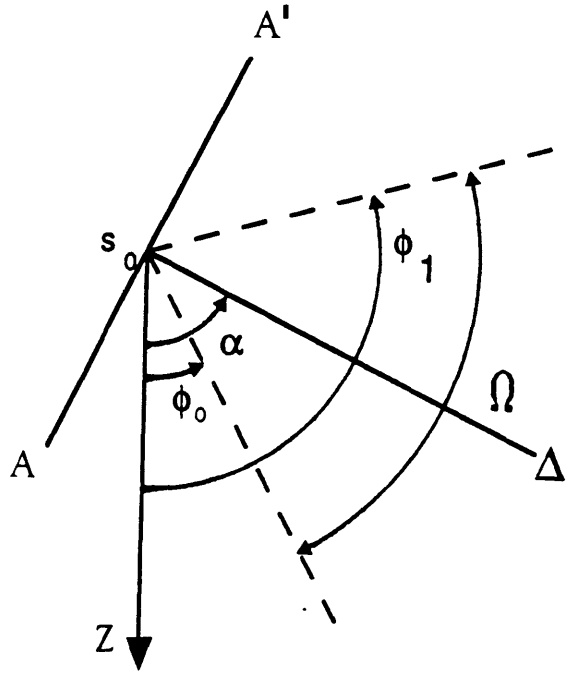

Δ : observation point

$\Omega = \phi_1 - \phi_0$

FIGURE 2.5 The diagram illustrate the case when the observation point is below the source in the geographical coordinate system. The beams are radiated from ϕ_0 to ϕ_1, covering a wide angle range Ω to densely illuminate the station. Ω is bisected by the line joinning the source and the observation point, so that the beams are always equally distributed around the receiver. The angle Ω cannot be larger than AOA' (180^0, plotted here only for display).

where:

$$\frac{\partial v}{\partial s} = [\frac{i\omega}{\beta_0} - \frac{1}{2}\frac{1}{(s - iL_0^2)} - \frac{i\omega}{2\beta_0}\frac{n^2}{(s - iL_0^2)^2}]v$$

$$\frac{\partial v}{\partial n} = -\frac{\omega}{\beta_0}\frac{n}{(s - iL_0^2)}v$$

After some algebra we find that $\frac{\partial v}{\partial \hat{n}}$ can be rewritten as the summation of the following four terms:

$$\frac{i\omega}{\beta_0}(n_x \sin\phi + n_z \cos\phi)v \tag{2.32}$$

$$-\frac{1}{2}(n_x \sin\phi + n_z \cos\phi)\frac{v}{(s - iL_0^2)}$$

$$-\frac{i\omega}{2\beta_0}(n_x \sin\phi + n_z \cos\phi)\frac{n^2 v}{(s - iL_0^2)^2}$$

$$+\frac{\omega}{\beta_0}(n_x \cos\phi - n_z \sin\phi)\frac{nv}{(s - iL_0^2)}$$

The first term of (2.32), multiplied by μ, can be regarded as the stress obtained by operating $\frac{\partial}{\partial \hat{n}}$ over the integrand of the plane wave expansion (2.30) and replacing each plane wave by a Gaussian beam. The other terms can be interpreted as coupling effect of the wavefront curvature and the plane normal to $\hat{n}$ at P. For the beam whose central ray is in the neighborhood of the obsservation point, the ray centered coordinate n is small and the contributions of the first two terms to the sum (2.32) are predominant. For beams away from the observation point n is large and the magnitude of the contributions of the four terms decreases due to the exponential decay with n^2.

Figure 2.6 shows the normalized shear stress Green's function calculated by both Gaussian beam superposition and analytical solution at 70 observation points along 10 km of the horizontal line $z = 1$ km, due to a

source located at $x = 5$ km, $z = 0$ km. Our purpose here is to find the values of L_0 and the number of beams N that best fit the exact solution, and observe the effects of different choices of L_0 and N. The analytical solution is given by:

$$\sigma(x,z,\omega) = \mu(n_x \sin\phi + n_z \cos\phi)\frac{i\omega}{4\beta_0} H_1^{(2)}(\frac{\omega}{\beta_0} r) \qquad (2.33)$$

where $H_1^{(2)}$ is the Hankel function of first order and second kind; and $r = [(x - x_0)^2 + (z - z_0)^2]^{1/2}$. Frequency is fixed at 1 Hz, $\beta_0 = 1$ km/s and the radiation angle range at $\Omega = 180^0$. In Figure 2.6 (a - d) the value of L_0 is fixed at 0.4 km$^{1/2}$, which yields $L_M = 0.2$ km, whereas the number of beams N increases from 20 to 100. In (e)and (f) the number of beams is kept at 100 whereas L_0 is chosen as 0.6 and 0.3 km$^{1/2}$ respectively. From the comparison of both solutions we estimate the accuracy of the beam superposition approach. It is observed that for a fixed $L_0 = 4$ km$^{1/2}$ the accuracy increases with the number of beams N, becoming stable for N greater than about 50. The values for which the Gaussiam beam solution best fit the analytical solution are $L_0 = 0.4$ km$^{1/2}$, $N = 100$ (d). However the accuracy is poor if we choose $L_0 = 0.6$ km$^{1/2}$ (e) or $L_0 = 0.3$ km$^{1/2}$ (f) once $N = 100$ is fixed. In (e) the wavefront is almost planar at the observation points above the source ($s \simeq 1$ km) and all beams in their neighborhood contribute with the same intensity. In (f) on the other hand, the beams are too narrow and only a few number around the observation point contribute significantly to the field. Note that the superposition becomes unstable for points far away from the source, resembling the solution for 20 beams in (a).

We conclude that the shear stress field due to a line source can be approximately represented by superposition of Gaussian beams of the same

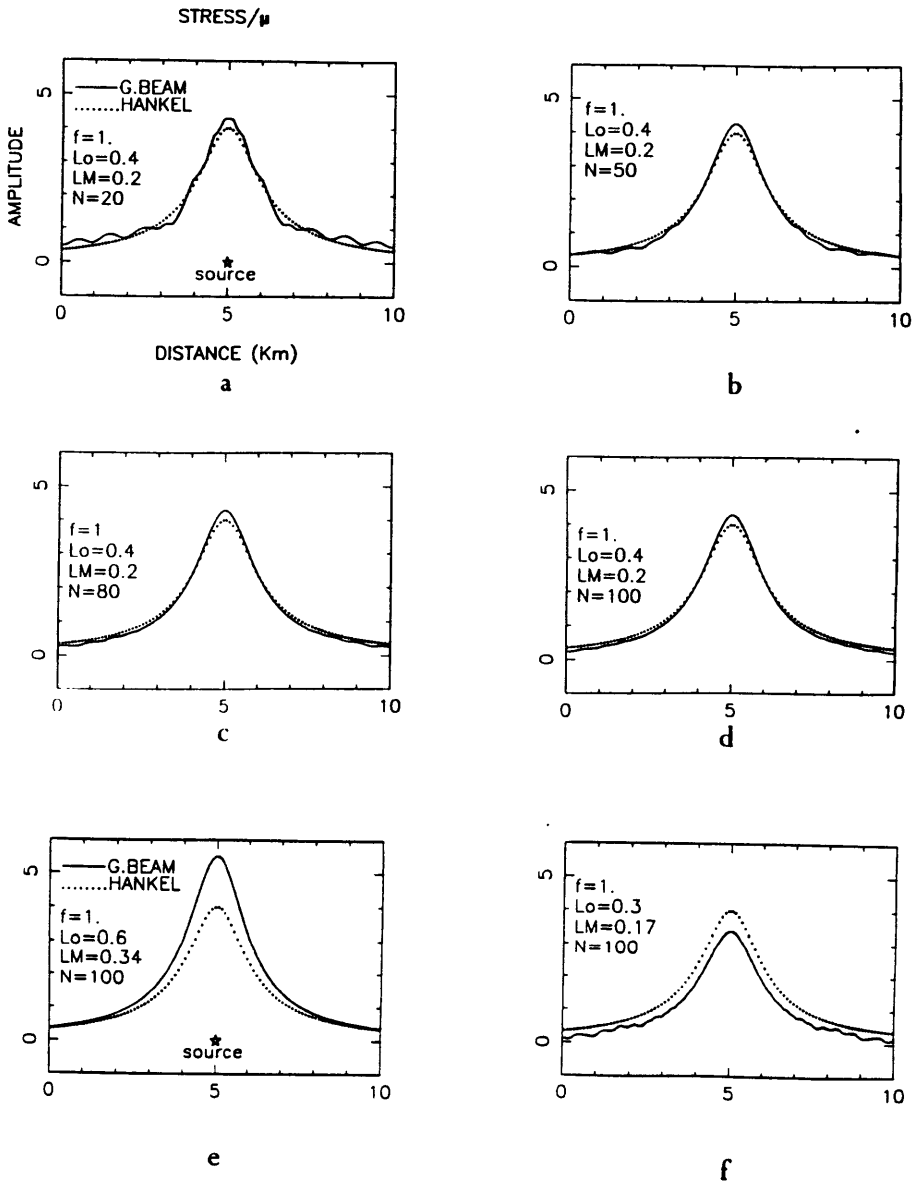

FIGURE 2.6 Amplitude distribution of the normalized stress (with respect to the rigidity μ) calculated along 10 km of the line $z = 1$ km, due to a line source located at $x = 5$ km, $z = 0$ km. (a,b,c,d) show the effect on the amplitude when the number of beams is increased from 20 to 100, keeping $L_0 = 0.4$ km$^{1/2}$. (e,f) show the effect of choosing $L_0 = 0.6$ km$^{1/2}$ and 0.3 km$^{1/2}$ respectively, keeping the number of beams equal to 100.

type used to represent the displacement field. The accuracy of this representation increases with the number of beams used in the superposition, and is not singular at the source point since the Gaussian beams have no singularities anywhere. In a boundary integral scheme, this property of the Green's function representation is extremely convenient because there is no further need to smooth Green's functions to obtain discretized matrix equations.

2.5 Test using problems with known solutions

To check the accuracy of our boundary integral-Gaussian beam method, we have selected three examples of wave propagation in elastic structures with strong lateral heterogeneities, which have already been solved analytically (closed form) or by using other well tested numerical methods.

2.5.1 Semicylindrical canyon

In the first example we calculate the response of a semicylindrical canyon of radius a. The exact solution in frequency domain was given by Trifunac (1973). The solution in time domain was given by Kawase (1988). Figure 2.7 (a) shows the comparison between both Gaussian beam and analytical solutions for vertical incidence, for varius normalized frequencies η (ETA) which is defined to be $\eta = 2a/\lambda$, where λ is the wavelength. We have used $a = 2.5$ km. The actual frequency can be calculated from $f = \frac{\beta}{2a}\eta$. The same comparison for 30^0 incidence and $\eta = 2$ is shown in Figure 2.7 (b). The Gaussian beam results were obtained using 20 sources ($N_s = 20$), 100 beams per source ($N_b = 100$), $\Omega = 180^0$ and $L_0 = 0.4$ km$^{1/2}$. The sources were located along a semicircle of radius $r_s = 0.9a$, concentric to

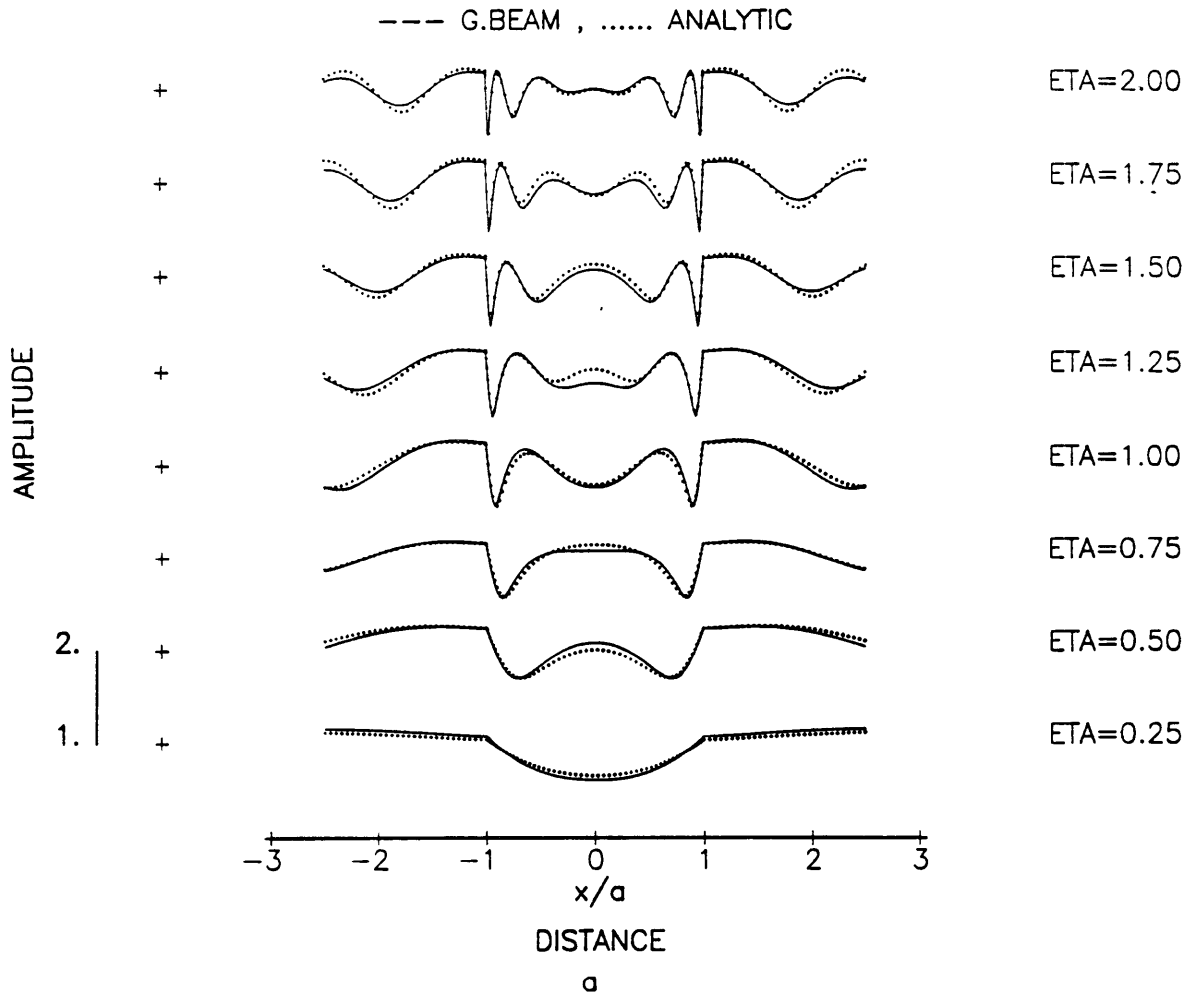

FIGURE 2.7 (a) shows the response of a circular canyon to incident SH waves, for the values of η as in Trifunac (1973). We used the number of sources $N_s = 20$, the number of beams per source $N_b = 100$ and the radiation angle $\Omega = 180^0$. The sources were located at a semicircle of radius $r_s = 0.9a$ The amplitude of the responses is normalized with respect to the response of the half-space without the canyon.

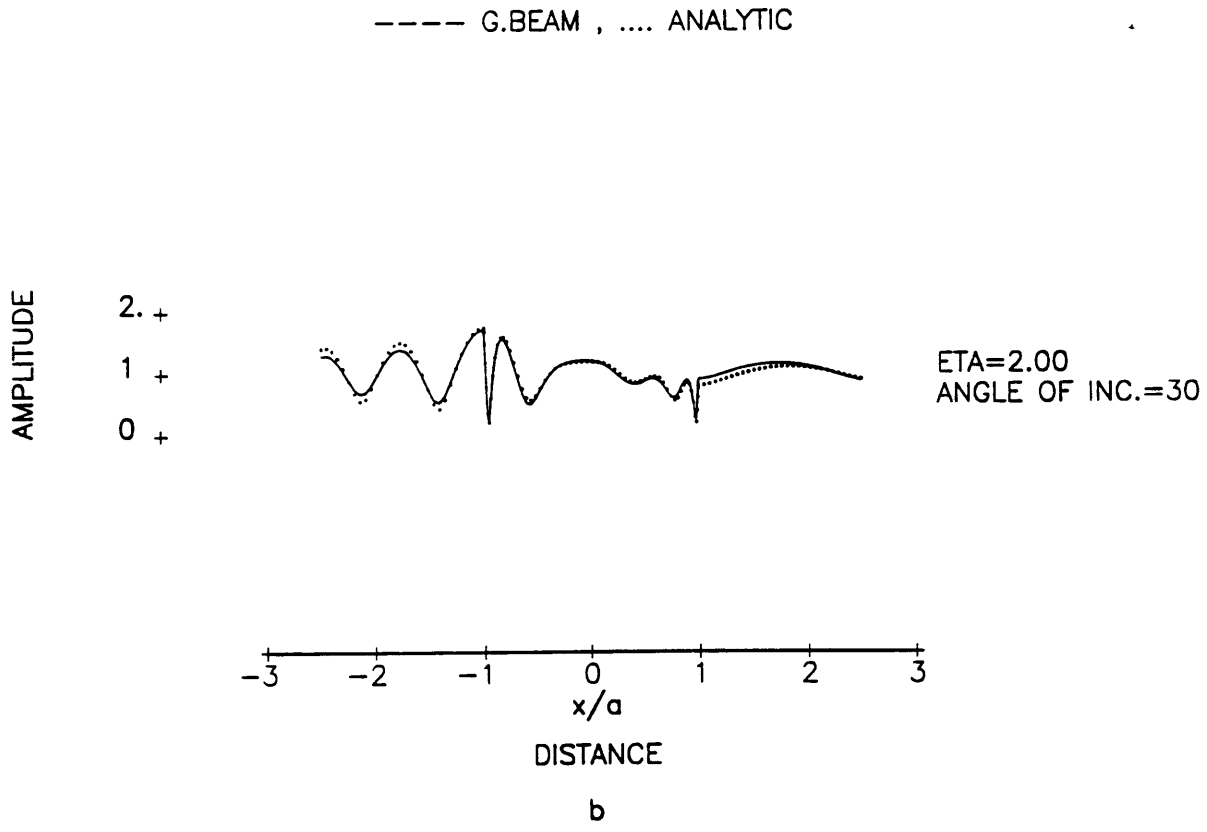

FIGURE 2.7 (b) shows the same response for 30^0 incidence.

the canyon. The wave field reflected at the surface is calculated by using the image source.

2.5.2 Effects of N_s, N_b, Ω, r_s and L_0

Let us use this example (for $\eta = 2$ and normal incidence) to check the effects on the solution due to different choices of N_s, N_b, Ω, r_s and L_0 In Figure 2.8 (a) we choose $N_s = 10$, keeping all other quantities the same as before. Results show minor disturbance of the response at the center and edges of the canyon, which disappears when the number of sources is increased beyond 15. For the results shown in (b) we set $N_s = 25$ and decreased both N_b and Ω down to 50 and 60^0 respectively. The result is again in good agreement with the analytical solution, but in this case the computational time was reduced to about 35 percent of the corresponding case shown in (a). It must be noted here that most of the computational effort is expended, rather, in constructing the Gaussian beam representation of the displacement and stress fields of each source, than in solving the linear system (2.6). Now we choose $r_s = a$ (other quantities are the same as in (a)). Results are significatively disturbed, as shown in (c), although the solution does not blow up, as it does when exact Green's function is used, without an appropiate elimination of the singularity at the source point. This effect does not disappear for any choice of N_s, N_b, Ω or L_0 . Finally, we found that the results are not strongly sensitive to changes in L_0 in the range from $L_0 = 0.2$ km$^{1/2}$ to $L_0 = 1.0$ km$^{1/2}$, as it is shown in Figure 2.9. This independency on L_0 is demonstrated in the case of a line source shown in Figure 2.6 (e) and (f). The amplitude of the stress field varies roughly linearly with L_0 for observation points right above the source, when L_0 was chosen between 0.3 and 0.6 km$^{1/2}$. A similar result for displacement field

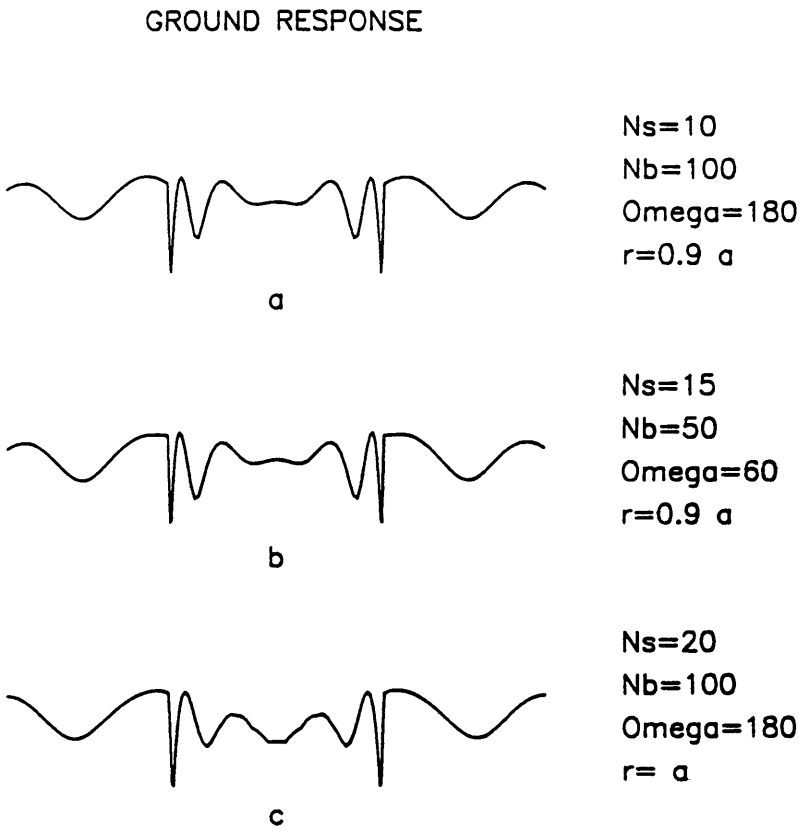

FIGURE 2.8 Effect introduced on the solution for the response of the circular canyon, for $\eta = 2$ and vertical incidence, when a $N_s = 10$, keeping the values of N_b, Ω, r_s and L_0 the same as in Figure 5, (b) N_b and Ω are decreased to 50 and 60^0 respectively, and $N_s = 15$. This case is an example of "trade-off" selection of these parameters in turn to decrease the computer time expended to construct Green's function without affecting the final solution, (c) the artificial sources are located exactly at the border of the canyon, keeping the values of N_s, N_b and Ω the same as in Figure 2.7. This case suggests that high instability of the final solution may occur when the observation points coincide with the source locations.

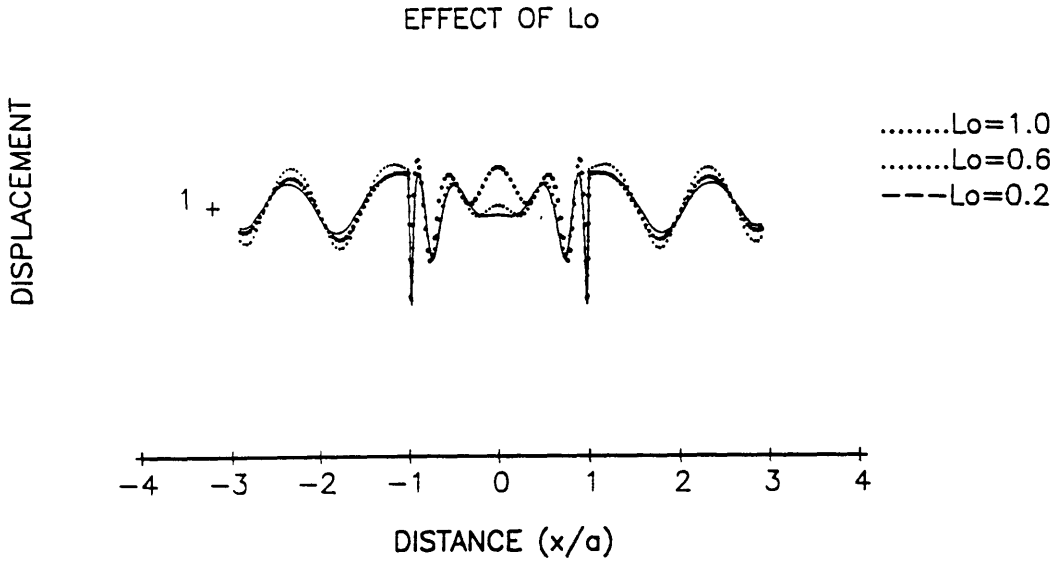

FIGURE 2.9 Effect of the beam parameter L_0 on the solution for the circular canyon, $\eta = 2$. All other quantities are the same as in Figure 2.7. $L_0 = 0.6$ km$^{1/2}$m gives the correct solution. Variations of L_0 to up to 66.6solution.

was also observed by Nowack and Aki (1984, Fig. 5-e), for the station above the source. In our method this means that matrices Γ_{ij} and b_i (equation 2.6) are both multiplied by a constant factor roughly proportional to the selected value of L_0, without altering the solution of the equation.

2.5.3 Mountain

In the second example we consider a mountain of cosine shape. Bouchon (1973) studied this problem using the Aki-Larner method for P, SV and SH incident waves. The response at the free surface is given for different ratios of height to half-width (h/a) of the ridge. The geometry of the problem in this case does not allow the use of image source scheme; so the artificial sources are distributed along the entire surface. The results shown in Figure 2.10 (a),(b),(c) were obtained using 80 sources and 100 beams per source. As in Bouchon (1973) for the SH case, (a) and (b) correspond to $h/a = 0.4$, and 0.8, respectively, and $\lambda = 5h$. (c) shows the response for $h/a = 1$ and $\lambda = a$ using our method. Since an exact solution is not available for this case, the accuracy of our results is also estimated from the compliancy of the boundary conditions. This is demonstrated below for each of the response's curves mentioned above, showing the fractional residual traction along the free surface, defined as the total traction divided by the traction due to the incident wave in full-space.

2.5.4 Semicylindrical alluvial basin

In our third example we calculate the diffraction and scattering due to a semicylindrical alluvial basin over a half-space bedrock. This problem was solved analytically (closed form) by Trifunac (1971). We used 60 artificial sources of beams along the interface, and image source scheme.

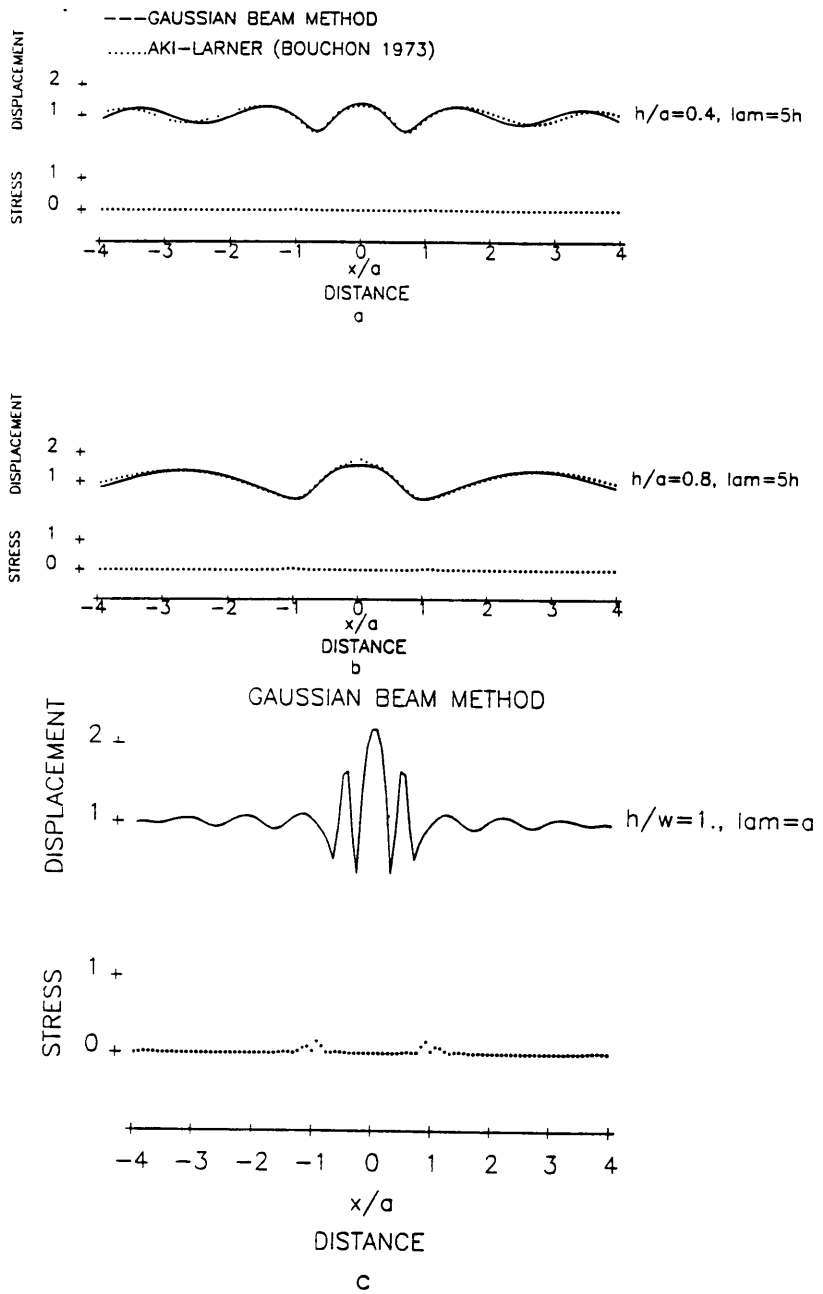

FIGURE 2.10 The response of a half-space whose free surface topography is a ridge of cosine shape. The response is calculated for different values of the ratio height to half-width of the ridge (h/a). (a) and (b) are calculated using the Gaussian beam method, and the corresponding cases given by Bouchon (1973) are shown below. (c) shows the response when the wavelength is equal to the half-width of the mountain ($h/a = 1$). In each of these cases the residual stress is shown below the response, to estimate the accuracy in fulfiling the boundary conditions.

In Figure 2.11 (a),(b) the Gaussian beam results are compared with the corresponding boundary element method solutions (Kawase 1988), which are in good agreement with the analytic solution given by Trifunac (1971) for $\beta_v/\beta_r = 1/2$, $\rho_v/\rho_r = 1/1.5$, and several values of η, where subcripts r and v stand for rock and basin, respectively. Similar comparison is shown in Figure 2.12 (a),(b),(c), for $\beta_v/\beta_r = 1/3$ and $\rho_v/\rho_r = 1/1.5$.

In summary, the above test examples show that the results obtained using our Gaussian beam method are in excellent agreement with those obtained by exact or other approximate methods. Its performance at low frequencies is remarkably good, in spite of the fact that it uses a high-frequency asymptotic solution of the wave equation to represent the field. In fact, the performance of this method for any frequency depends strongly upon the source distribution, provided that full space Green's function for each source is accurately computed by the superposition of Gaussian beams, as shown in Figure 2.6 (d). Let us take the case of the semicircular canyon to describe our criterion for the choice of the source interval. We have selected $\eta = 2$ as the highest non-dimensional frequency for which the scattering problem is to be solved and used this value to calculate the number of sources. The wavelength corresponding to this frequency is $\lambda = a$. We assume that the boundary conditions can be accurately matched in this case by assigning six sources per wavelength, which yields a source interval $\delta = a/6$. The total amount of sources necessary to cover the entire length of the semicircle, distributed at an equal interval δ, can be calculated from $\pi a/(a/6) = 6\pi$ or, approximately, twenty sources. Actually, a minimun of four sources per wavelength, or approximately a total of ten sources, still yields an acceptable solution (Sanchez-Sesma and Rosenblueth 1979),as

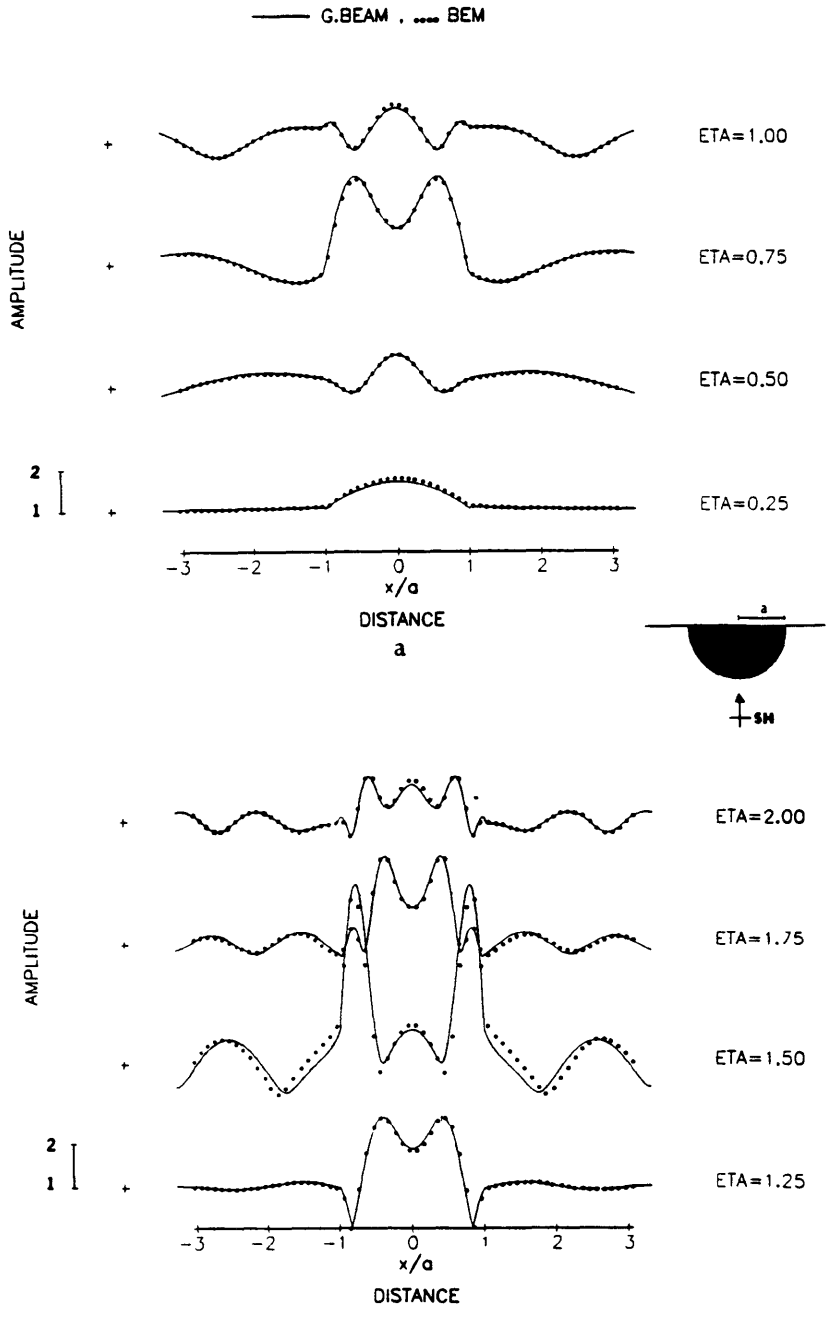

FIGURE 2.11 The cylindrical alluvial valley case. (a),(b) show the response calculated with Gaussian beams for values of η up to 2, compared with the corresponding solution using Boundary Element method. Here also $\eta = 2a/\lambda$, and the velocities and densities of both media are related (v: valley, r: rock) by $\beta_v/\beta_r = 1/2$, $\rho_v/\rho_r = 1/1.5$,

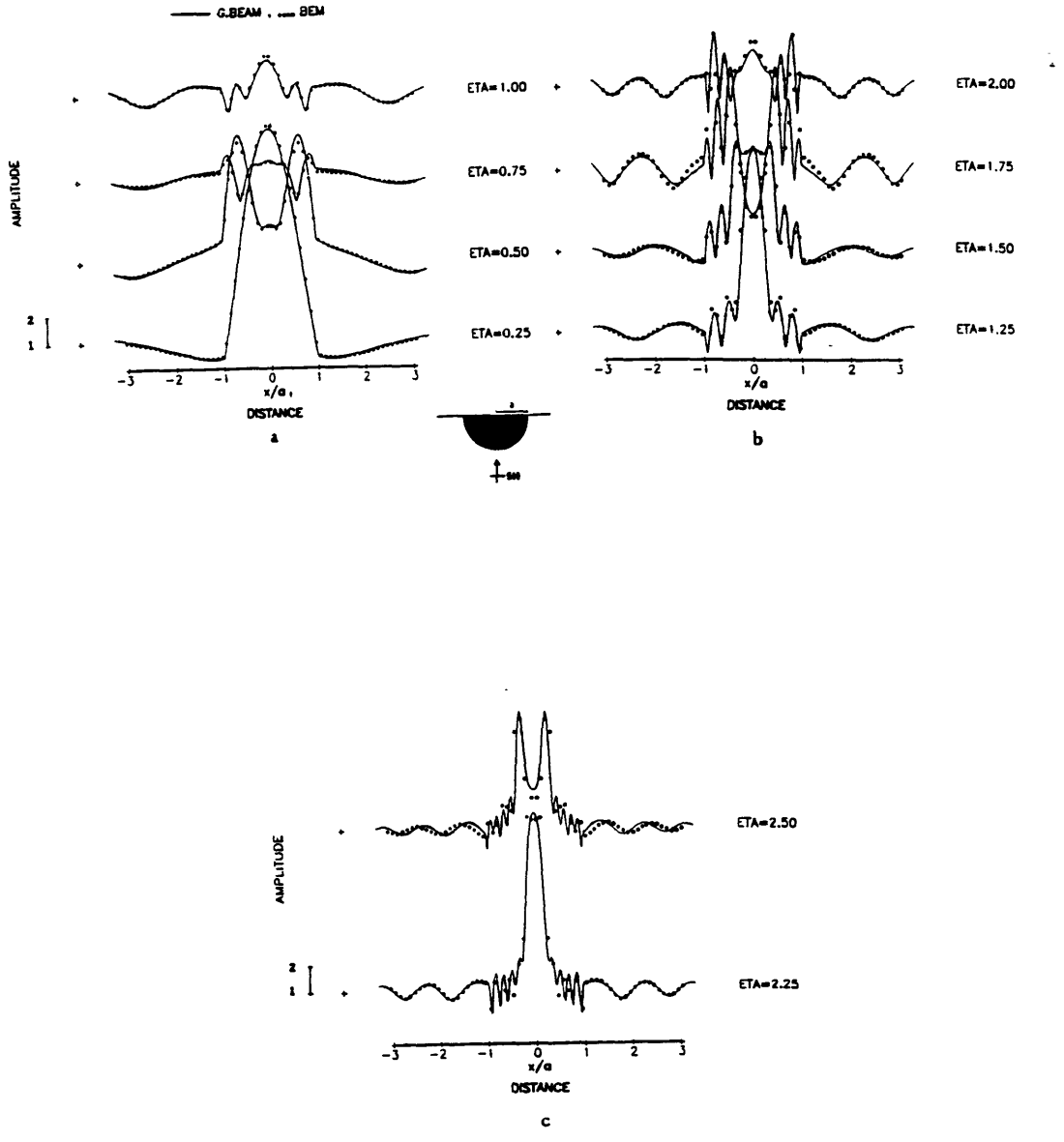

FIGURE 2.12 (a), (b), (c) show the response of the cylindrical alluvial valley for high velocity contrast, $\beta_v/\beta_r = 1/3$. Density contrast is 1/1.5. (c) shows the response for η larger than 2 (high frequency). The sharp features of the response amplitude are accuratelly calculated by our metod.

shown in Figure 2.8 (a). The accurate solution obtained for the lowest frequency $\eta = 0.25$, or $\lambda = 4a$ is due to the fact that we have used twenty sources per wavelength, which is five times the minimum amount of sources necesary to match the boundary conditions.

2.6 Conclusions

We have shown that our new method based on Gaussian beam superposition can accurately calculate the scattering of plane SH-waves by a semi-cylindrical canyon, a cosine shaped mountain and a semicylindrical soft basin in a homogeneous half-space. The accuracy of our method is confirmed by the excellent agreement between the Gaussian beam solutions and solutions obtained by exact and/or other well tested approximate methods.

The novelty of the method and its power to deal with strong lateral heterogeneities lie in our global approach to match boundary conditions instead of the traditional local approach in formulating transmitted and reflected Gaussian beams. Our boundary point (line) source scheme allows the global solution of the boundary conditions in the least-squares sense, including the effect of lateral variation of the interface. However, this requires an accurate representation of the tractions at the boundaries in terms of the same Gaussian beams used to represent displacement field. Here we have demonstrated that this is possible by increasing the number of beams to represent the displacement field. Our use of Gussian beams in the boundary integral method has an important advantage that Green's function represented by superposition of Gaussian beams are not singular anywhere. This is important to avoid the need for smoothing matrix elements when the integration path includes the point where the source

is located. We also confirmed that the method gives stable results with respect to the choice of L_0.

The most important outcome of the present Chapter is the validity of the use of Gaussian beams in calculating Green's function to be used in the boundary integral method of solving the seismic scattering problems. Since the Gaussian beam solutions can be readily obtained for inhomogeneous media, we believe that our method can be extended to a medium consisting of inhomogeneous layers with irregular interface and topography in a straight-forward manner. This problem will be addresed in Chapter IV.

CHAPTER III

APPLICATION TO SOFT AND HARD INCLUSIONS BURIED IN A HALF-SPACE

3.1 Introduction

In this Chapter III we apply the boundary integral-Gaussian beam method to study the surface motion, in frequency and time domains, of a homogeneous two dimensional half-space containing a soft or a hard inclusion when a plane SH-wave is incident from below. The shape of the inclusion is assumed to be cylindrical with circular cross-section, although there is no restriction for the formulation with other shapes.

To the author's knowledge, no explicit closed form solution for the above problem exists, although the analytic solution for the case of full-space containing such an inclusion is known (Mow and Pao 1971, pp.279). In a study related to upper mantle seismic tomography, Wielandt (1987) analyzed the effects of diffraction on the travel times of teleseismic waves propagating through an inclusion, in order to estimate the error in observed arrival times which can be caused by diffracted waves of larger amplitude with faster velocity than the direct wave. He used a closed form solution of Helmholtz equation for pressure wavefield in a full space with an spherical inclusion, considering plane wave incidence. Chapman and Phinney (1972) treated a similar problem for elastic waves and obtained high and low frequency asymptotic solutions.

On the other hand, numerical techniques applicable to wave scattering by inclusions in a half-space are available. Dravinski (1983), for instance, developed a boundary integral method based on the representation of the

complete elastic wavefield by means of dilatational potential ϕ and equivoluminal potential ψ , applicable to 2-D cases for multiple cylindrical inclusions embedded in a half-space. He focused mainly on the study of ground motion on the free-surface, in frequency domain, for the case of one and two inclusions with elliptic cross-section and for obliquely incident P, SV, and SH waves. Results show that the amplitude distribution of the ground motion depends strongly on the type of incident wave, depth of inclusion, angle of incidence, frequency and on the separation distance between inclusions (in the case of two inclusions).

As the results in this chapter demonstrate, our approach of studying both in frequency and time domains helps capturing the physics of various aspects of wave phenomena.

3.2 Formulation

Refering to Figure 3.1 and to equations (2.7) (Chapter II) for two regions separated by a closed boundary, we define the fields inside and outside of the inclusion, respectively as:

$$v^{(I)}(x,z;\omega) = \sum_{m=1}^{M} A_m v_m^{(I)}(x,z;\omega) \tag{3.1}$$

$$v^{(E)}(x,z;\omega) = v^0 + \sum_{n=1}^{N} B_n v_n^{(E)}(x,z;\omega)$$

where $v_m^{(I)}$ and $v_n^{(E)}$ represent Green's function for medium I (interior) with source point(line) located at a point (x_m, z_m) of medium E (exterior), and for medium E with source(line) point at (x_n, z_n) of medium I (interior), respectively, M and N are the number of point(line) sources distributed along the interface, in the inclusion and in the half-space respectively. Functions

INCLUSION

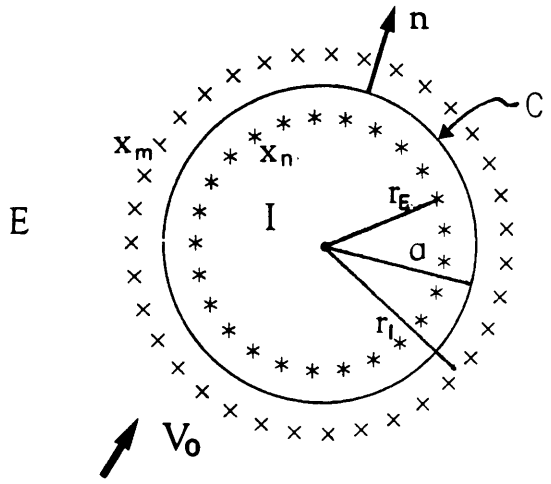

FIGURE 3.1 Elastic inclusion in a half-space, enclosed by C. The wave sources to represent the scattered wavefield inside the inclusion are distributed in the exterior region E, on a circle of radius $r_i = 1.1a$, marked with 'x'. The wave sources to represent the wavefield are distributed in the interior region I, on a circle of radius $r_E = 0.9a$, marked with '*'. The normal $\hat{n}$ is taken as the outward normal to the region where the sources are distributed.

$v_m^{(I)}$ and $v_n^{(E)}$ are constructed by superposition of Gaussian beams for homogeneous media, defined by equation (2.29). The complex constants A_m represent the strength of the sources of Green's function for the inclusion and B_n the strength of the sources for the half-space Green's function. The observation point is at (x, z).

Using the least-squares procedure described in section 2 of Chapter II to satisfy continuity of displacement and traction along the boundary, the constants A_m and B_n are obtained from the following system of simultaneous equations:

$$\sum_{m=1}^{M} A_m R_{km}(1,1) - \sum_{n=1}^{N} B_n R_{kn}(1,2) = S_k^0 \tag{3.2}$$

$$\sum_{m=1}^{M} A_m R_{lm}(2,1) - \sum_{n=1}^{N} B_n R_{ln}(2,2) = S_l^0$$

with $k,m = (1,M)$ and $l,n = (1,N)$. The R's and S's are matrices whose complex valued elements represent the interaction of all sources with each other and with the incident wave, respectively. They are given by:

$$R_{km}(1,1) = \int_C [\alpha^2 v_k^{(I)*} v_m^{(I)} + \mu \frac{\partial v_k^{(I)*}}{\partial \hat{n}} \frac{\partial v_m^{(I)}}{\partial \hat{n}}] ds \tag{3.3}$$

$$R_{kn}(1,2) = \int_C [\alpha^2 v_k^{(I)*} v_n^{(E)} + \mu \frac{\partial v_k^{(I)*}}{\partial \hat{n}} \frac{\partial v_n^{(E)}}{\partial \hat{n}}] ds$$

$$R_{lm}(2,1) = \int_C [\alpha^2 v_l^{(E)*} v_m^{(I)} + \mu \frac{\partial v_l^{(E)*}}{\partial \hat{n}} \frac{\partial v_m^{(I)}}{\partial \hat{n}}] ds$$

$$R_{ln}(2,2) = \int_C [\alpha^2 v_l^{(E)*} v_n^{(E)} + \mu^2 \frac{\partial v_l^{(E)*}}{\partial \hat{n}} \frac{\partial v_n^{(E)}}{\partial \hat{n}}] ds$$

$$S_k^0 = \int_C [\alpha^2 v_k^{(I)*} v^0 + \mu \frac{\partial v_k^{(I)*}}{\partial \hat{n}} \frac{\partial v^0}{\partial \hat{n}}] ds$$

$$S_l^0 = \int_C [\alpha^2 v_l^{(E)*} v^0 + \mu^2 \frac{\partial v_l^{(E)*}}{\partial \hat{n}} \frac{\partial v^0}{\partial \hat{n}}] ds$$

with $\alpha = \omega/\beta_E$, $\mu = \mu_I/\mu_E$, μ_I and μ_E are the rigidities of the inclusion and the half-space respectively, and β_E is the shear wave velocity in the half-space. C denotes the integration path along the boundary of the inclusion; and $()^*$ stands for complex conjugate.

3.3 Numerical examples

In our first example we study the surface motion of a half-space containing a soft cylindrical inclusion due to plane waves incident from below. As we find from our results, the incident wave is first reflected (back to the half-space) and refracted (into the inclusion) by the boundary of the inclusion. The refracted waves are, in turn, transmitted out of the inclusion and also multiply reflected inside. The energy carried by the waves confined to the inside of inclusion are referred here as "trapped" energy. We have computed the seismic motion on the free surface, as shown in Figure 3.2 (a) for vertical incidence, and (b) for 30^0 incidence angle. The depth h of the center of the inclusion is twice its radius a, the ratios of the velocity and density of soft inclusion to those of half-space are $\beta_I/\beta_E = 1/2$ and $\rho_I/\rho_E = 1/1.5$, respectively. We have used $M = 40$ and $N = 30$ sources, located along circles concentric to the boundary of the inclusion, of radii $r_I = 1.1a$ and $r_E = 0.9a$ respectively. The Gaussian beam parameter is chosen to be $L_0 = 0.16a$ and we have used 100 beams per source. The amplitude distributions shown in Figure 3.2 for several values of the non-dimensional frequency $\eta = 2a/\lambda$ are normalized with respect to the amplitude of the ground motion of the half-space without the inclusion. In (a), amplification of the ground motion is observed in the region $|x/a| > 2$

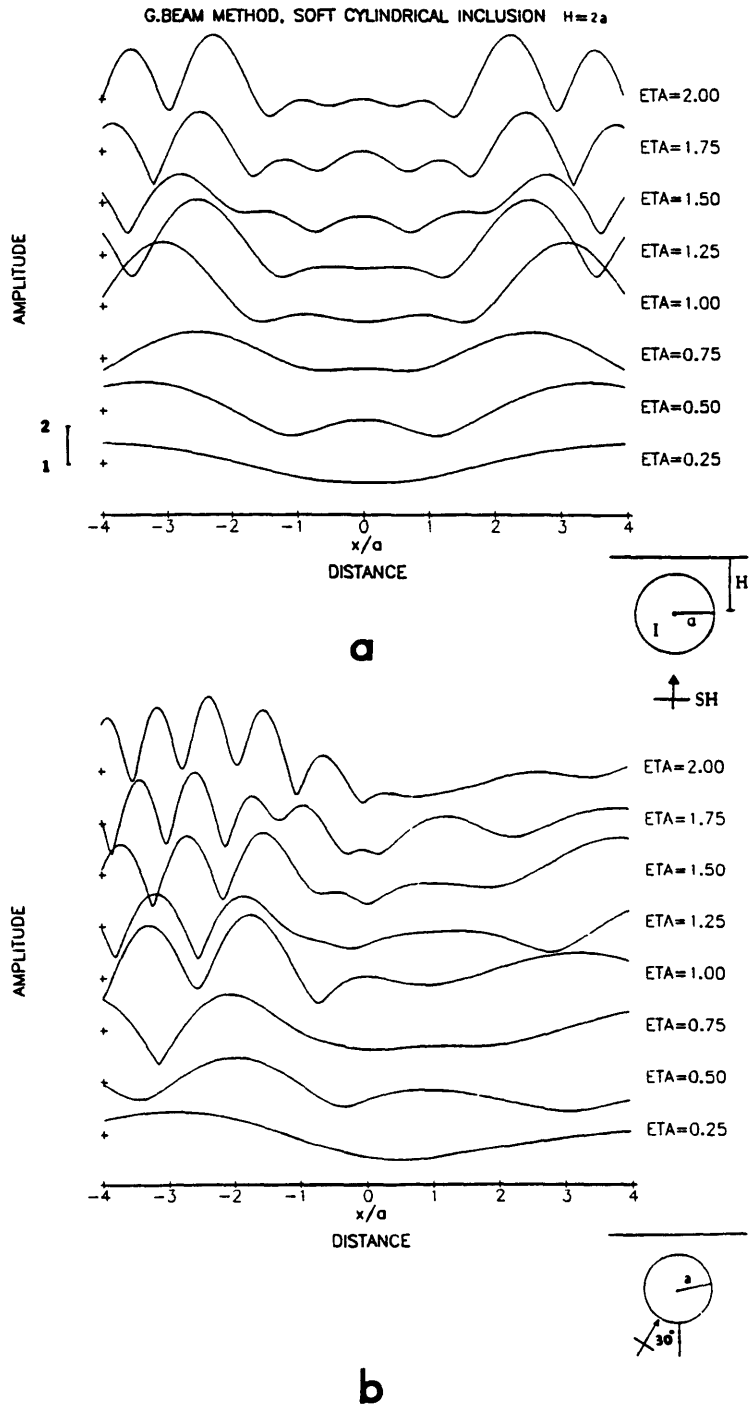

FIGURE 3.2 Response of a half-space containing a totally embedded soft inclusion. The incidence of the SH plane waves is vertical in (a) and 30^0 in (b). The depth of the inclusion is equal to $2a$, measured from the surface to the center of the inclusion. $\eta = 2a/\lambda$, $\beta_{incl}/\beta_{hs} = 1/2$ and $\rho_{incl}/\rho_{hs} = 1/1.5$. We have used a total of 60 sources to represent the scattered field. The response amplitude is normalized with respect to the response of the half-space without the inclusion.

on the surface, where the reflected waves from the boundary contructively interfere with the incident wave. This amplification effect appears to be stronger for larger values of η. On the other hand, a deamplification of ground motion is observed at the surface immediately above the inclusion, in the region $|x/a| \leq 2$. In the case (b) of inclined incidence, the interference between incident and reflected waves causes amplification in the region $x/a < -1$ (from the direction of wave incidence) and, at lesser extent, at $x/a > +3$. The region within $-1 < x/a < 3$ shows deamplification.

The deamplification effect observed in the shadow of inclusion both for normal incidence (a) and inclined incidence (b) maybe due to the reflection of the incident wave at the boundary of the inclusion, or the energy trapped inside the inclusion, or both. With only amplitude information as shown in Figure 3.2, it is difficult to find which. The time domain solution, which includes both amplitude and phase information, is needed to resolve this question.

Figure 3.3 shows the motion at $z = 2a$, along the horizontal line passing through the center of the inclusion. The motion is plotted for various non-dimensional frequency η over the whole range inside the inclusion. The amplitude of motion is shown in the unit ten times greater that in Figure 3.2, indicating an order of magnitude greater motion inside the inclusion as compared to the motion on the surface.

To see if any focusing effect due to the low velocity inclusion may be produced by increasing the depth of the inclusion, and decreasing the velocity and density contrast, we tried the depth $h = 4a$ and the velocity and density ratios $\beta_I/\beta_E = 1/1.2$ and $\rho_I/\rho_E = 1/1.1$ respectively. Results for η up to 4 are shown in Figure 3.4 (a), (b). We see no strong focusing

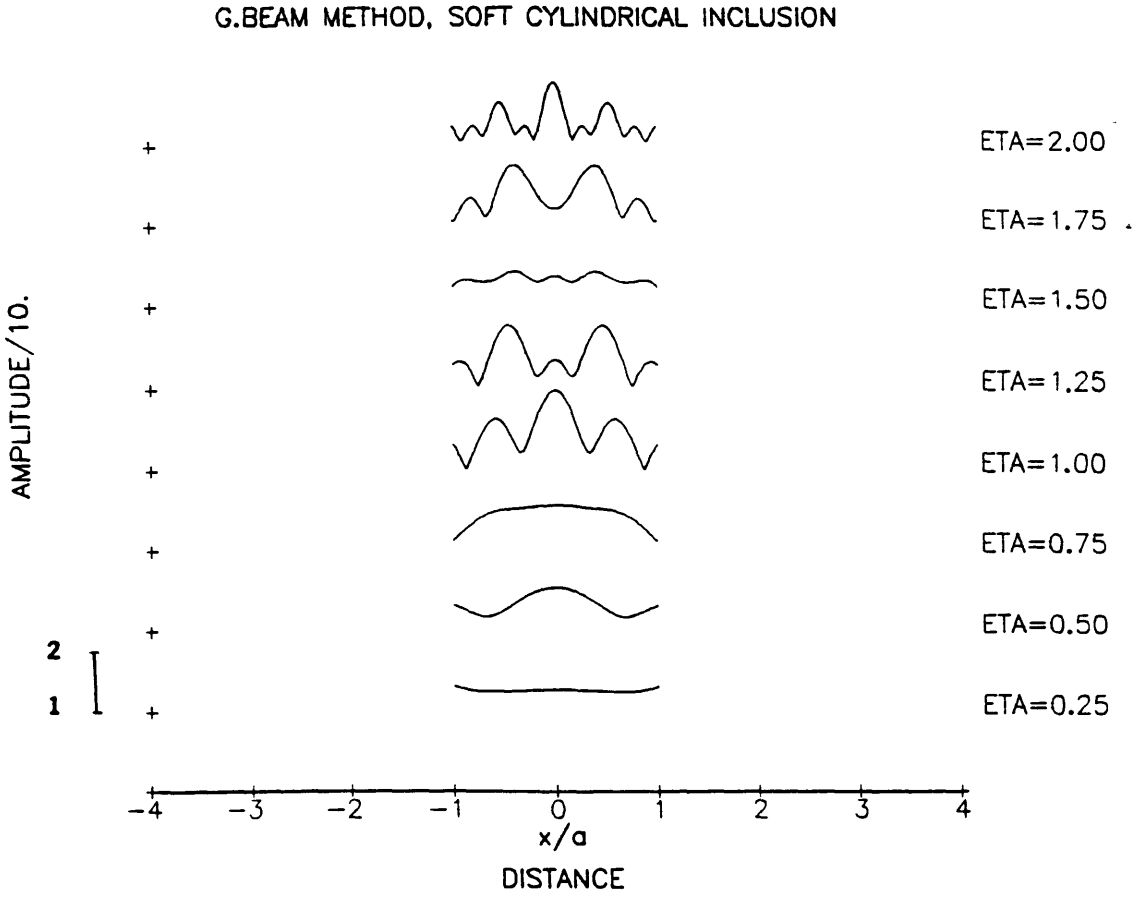

FIGURE 3.3 Amplitude distribution inside the inclusion, along a horizontal line at depth $2a$. The elastic parameters, the depth of the inclusion and the range of variation of η are the same as in Figure 10. The vertical scale is 10 times larger. It can be estimated from these results that the amplitudes inside the inclusion are of one order of magnitude larger than on the surface. Also, the shape of this amplitude distribution suggests the existence of natural vibratory modes caused by resonance.

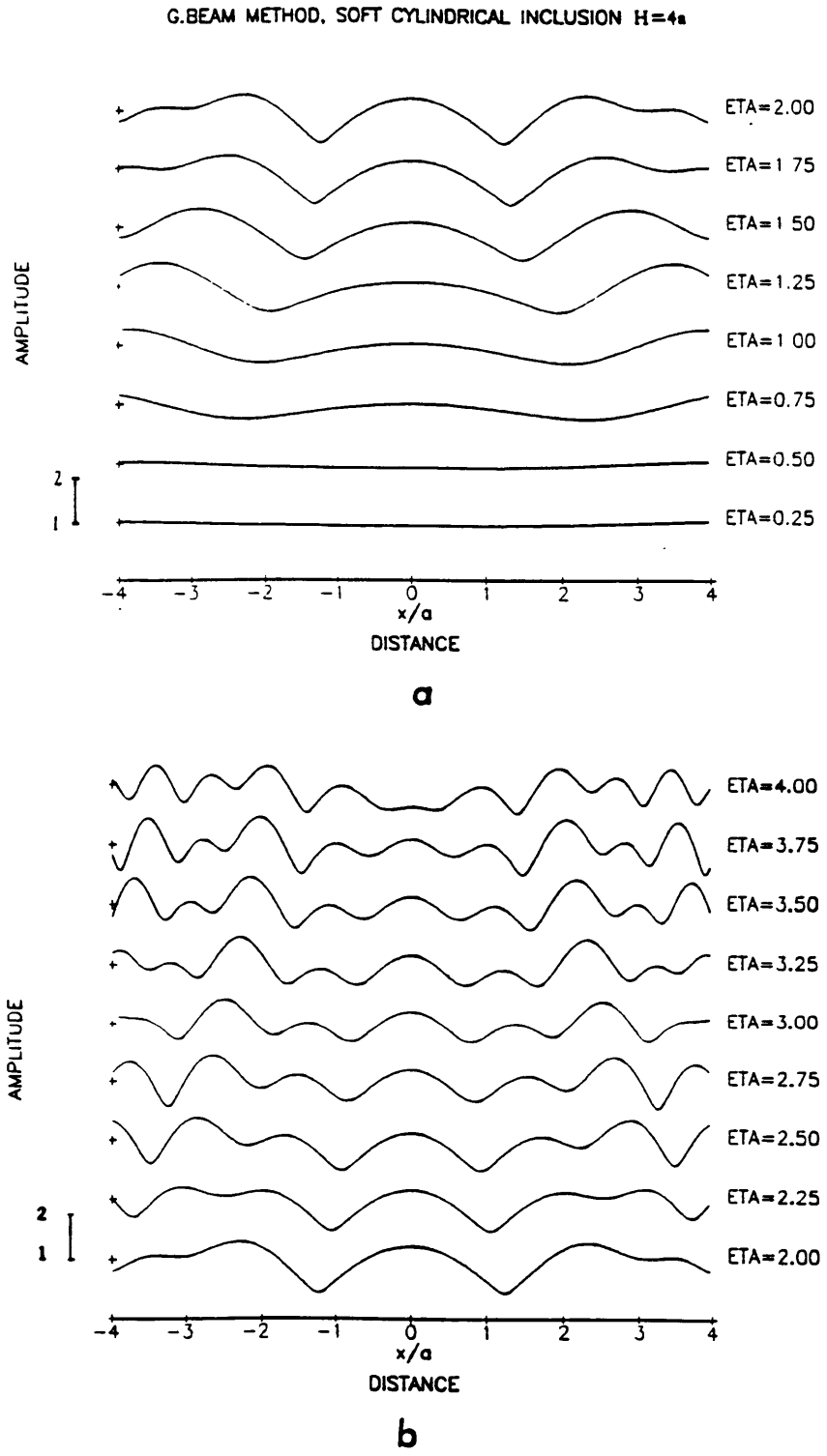

FIGURE 3.4 (a), (b) response for deeper inclusion ($H = 4a$) and lower velocity and density contrast between the soft inclusion and the half-space. Incidence is vertical. Apparently, no focusing effect occurs in this case for values of η up to 4.

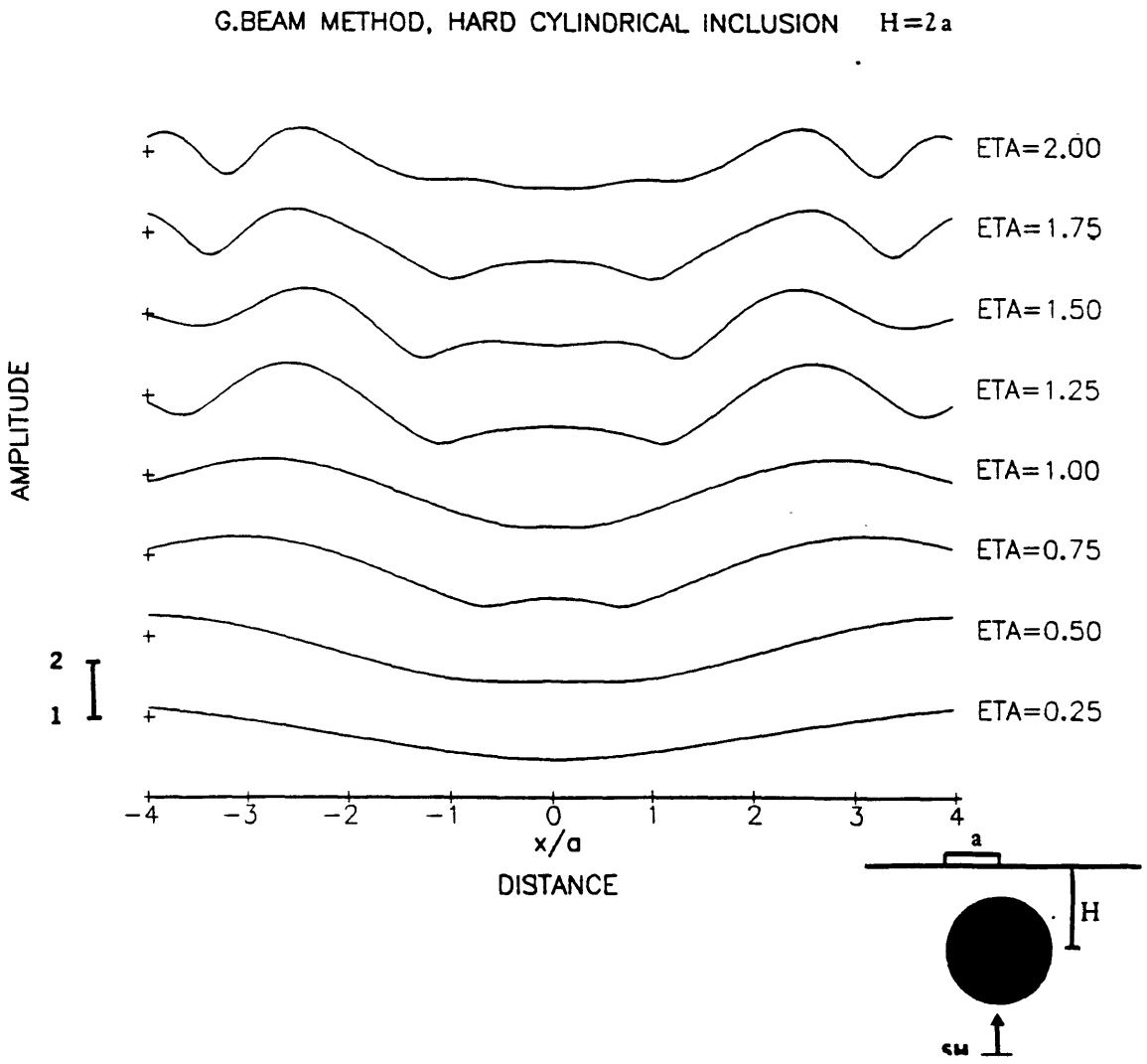

FIGURE 3.5 - Surface response of a half-space containing a hard cylindrical inclusion. These results were obtained by switching the velocities and densities between the half-space and the soft inclusion in Figure 11. Incidence is vertical. The amplitude distribution in this case is quite similar to the case of the soft inclusion, particularly for low frequencies.

effect on ground motion at the free surface in these cases.

For comparison with the effect of a buried soft inclusion on seismic motion on the surface, let us study now the case of a hard inclusion, with the same medium parameters but switched between the half-space and the inclusion. Results for normal incidence of plane waves are shown in Figure 3.5. Surprisingly the general pattern of amplitude distribution in this case is quite similar to that in the case of a soft inclusion, i.e., we observe again amplification in the region $|x/a| > 2$ and deamplification in the region $|x/a| \leq 2$. This is a surprise because ray-theoretically, we expected defocussing for a hard inclusion and focussing for a soft inclusion, for receivers on the surface immediately above the inclusion. This result poses the question of serious non-uniqueness if we wanted to determine whether the inclusion has higher or lower velocity than the half-space from the observed amplitude at the surface. Detailed studies of spectrum and wave forms, however, give a unique answer, as demonstrated below.

Figure 3.6 (a), (b) shows the spectra as a function of non-dimensional frequency η, for the case of a hard and that of a soft inclusion, respectively, at five stations located on the surface at $x = 0, a, 2a, 3a, 4a$; marked with solid triangles in the inset. The spectra was computed for 80 frequency points, at the spacing of 3/80 in η. We note that the spectra shown in (a) and (b) are remarkably different. Let us first look at the case of hard inclusion. Its spectrum shows no significant peaks up to $\eta = 2$ at any station. For the station immediately above the inclusion (STA 1) the whole spectrum varies smoothly and with low amplitudes for this range of frequency, indicating a true shadow zone for η up to 2. For $\eta \simeq 2$ there is a rather broad peak of small amplitude. The period of this peak is $T \simeq a/\beta_E = 2a/\beta_I$,

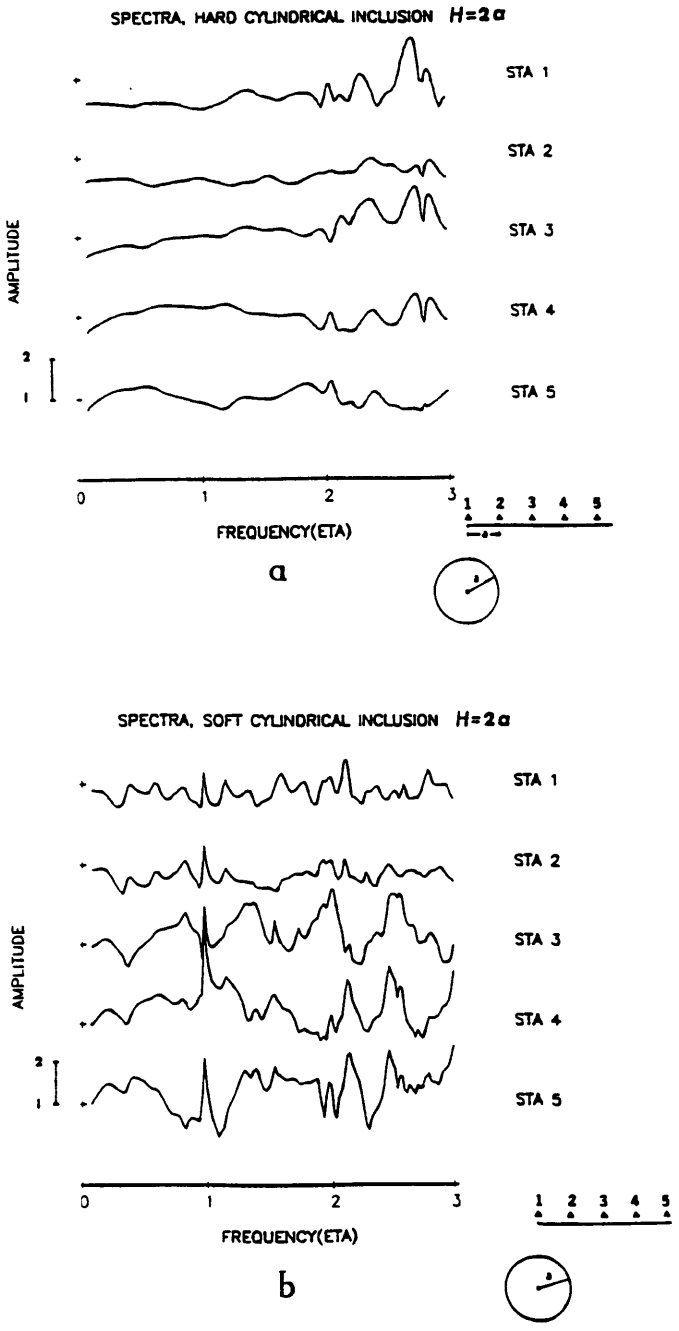

FIGURE 3.6 Amplitude spectra as a function of η at five stations located at distance intervals a on the surface of a half-space containing a hard inclusion (a), and soft inclusion (b), for vertical incidence. The spectra for hard inclusion appears to be smoother than the spectra for soft inclusion. In (a) the spectrum at observation points away from the inclusion show more defined peaks for η greater than 2, due to the interaction between incident and scattered waves. In (b) observe a well defined peaks at $\eta = 0.97$ and broader peaks at 1.15, 2.0 and 2.15. These peaks may be caused by energy radiated from the inclusion for the values of η corresponding to resonance inside the inclusion.

which corresponds to the two way travel time between the free-surface and the top boundary of the inclusion. As we shall see in our time domain solution, the wavefield in the region immediately above the inclusion is due to waves that have been transmitted through the inclusion with velocity β_I and to difracted waves travelling along the boundary also with velocity β_I, i.e., both faster than the incident wave. Several spectral peaks appear for values of η larger than 2, at all stations, probably due to the constructive interference of waves scattered by the inclusion (by reflection, refraction and diffraction) and the incident waves. The strongest peak occurs at STA 1 for η around 2.75.

The spectrum for the soft inclusion (Figure 3.6 b) shows a well defined narrow peak at $\eta = 0.97$ ($\lambda = 2a/0.97$) for all stations. Other peaks can be observed around $\eta = 1.15, 2., 2.15$, although they are broad and not as well defined as the first. These peaks are related to the resonance modes trapped in the soft inclusion. For instance, comparing the spectrum calculated at STA 1 with that at the point $x = 0, z = a$ immediately above the inclusion shown in Figure 3.7, we observe that spectral peaks occur at about the same frequency for both. The first peak at both observation points occurs for $\eta \simeq 1$, corresponding to the period $T = 2a/\beta_E = 4a/\beta_I$. This period corresponds to the mode with a loop at the center of the inclusion and nodes at the boundary. The presence of the free-surface, impedance contrast between the half-space and the inclusion and 2-D resonance inside the inclusion add complexity to the observed spectra. In fact the 2-D resonace peaks of an inclusion in general do not coincide with those determined from a simple 1-D model even in the full space (Mow and Pao, 1971). The study to estimate to what extent these factors affect the spectra for soft inclusion

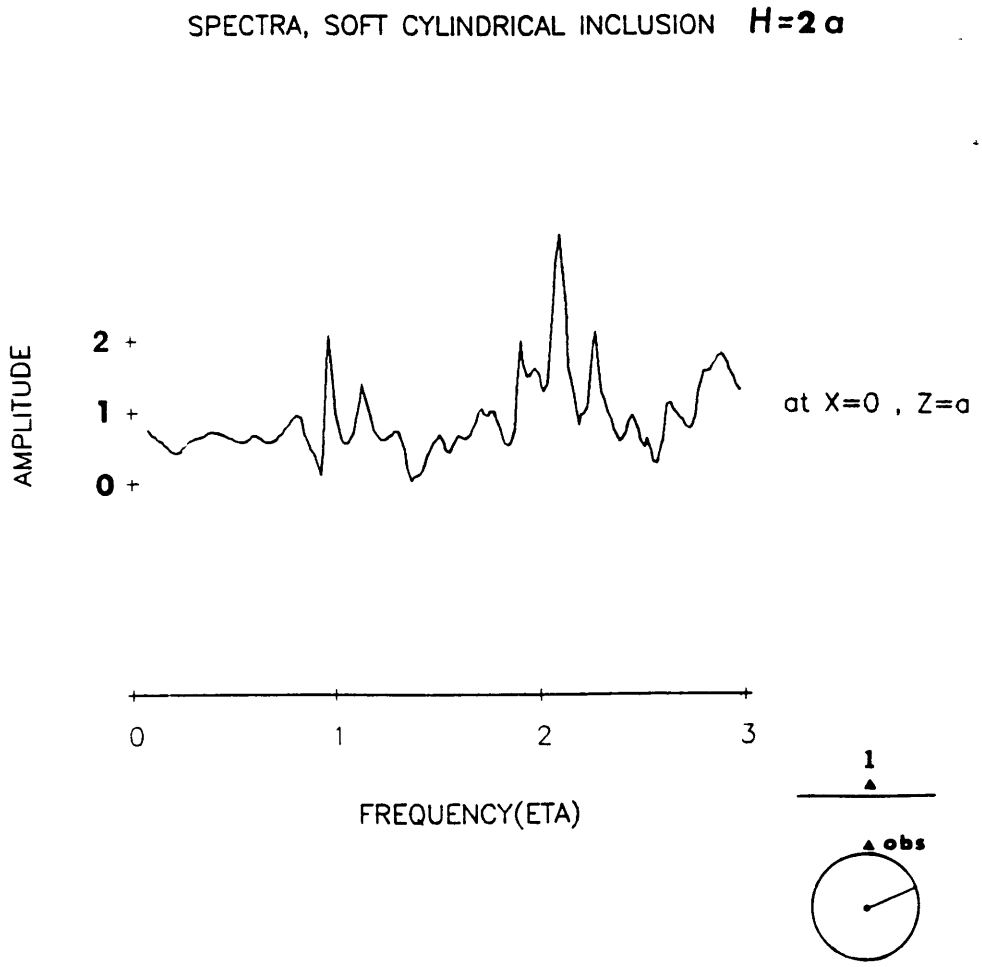

FIGURE 3.7 - Amplitude spectrum at the vertical top of the soft inclusion. Well defined peaks occur at the same frequencies observed in the spectrum of each station at the surface of the half-space in Figure 3.6 (b), suggesting that those peaks correspond to the resonant modes excited by the trapped waves inside the inclusion.

is described next.

In order to analyze the effect of the free-surface, we increased the depth of the center of soft inclusion to $h = 4a$, and computed the spectra at the same five stations considered above, keeping velocities and densities of both half-space and inclusion exactly the same as for Figure 3.6 (b). Results are shown in Figure 3.8. The peak for $\eta \simeq 1$ dissapears, because of the greater distance from the inclusion. On the other hand, a peak occurs at $\eta = 0.33$ in the spectrum at all stations. This peak cannot be due to resonance inside the inclusion, but probably to waves propagating back and forth between the free-surface and the top boundary of the inclusion.

Let us now study the case with stronger velocity and density contrast between the inclusion and half-space, choosing $\beta_I = 0.1\beta_E$ and $\rho_I = 0.5\rho_E$, i.e. for a large impedance contrast between half-space and inclusion. Results for the depth of the inclusion the same as in Figure 3.6 (b) are shown in Figure 3.9 (a), in which we have increased the number of frequency (η) points to 200, i.e., the frequency interval is now 3/200 in η. We observe a well defined peak at $\eta = 0.16$ in the spectra of all stations. Other peaks are commonly observed at $\eta = 0.38$ and $\eta \simeq 1$. The results for the increased depth of the center of the inclusion $h = 4a$ (same as the case of Figure 3.8) are shown in Figure 3.9 (b), where we observe well defined peaks at $\eta = 0.08$, $\eta = 0.16$ and $\eta = 0.38$, at all stations. The sharpness and the large amplitude of the peak at $\eta = 0.16$ in both (a) and (b) (larger than any other peak in the spectra) suggests that this may correspond to the fundamental mode of resonance inside the inclusion. A second mode may correspond to $\eta = 0.38$ in (b), which appears not well defined in (a). Although we could consider the peak at $\eta = 0.16$ to be insensitive to variations of depth of the

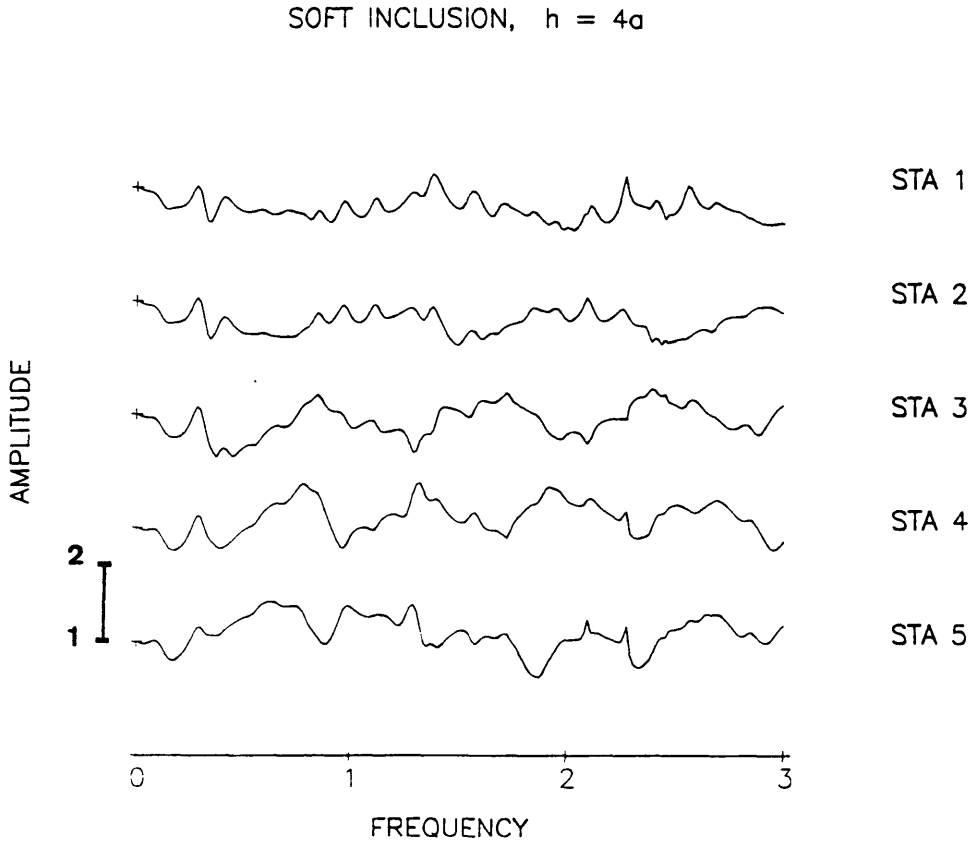

FIGURE 3.8 Spectra for soft inclusion at the same locations described for Figure 3.6, but the depth of the inclusion is twice larger. The sharp peak observed in 3.6 dissapeared, suggesting the effect of the free-surface.

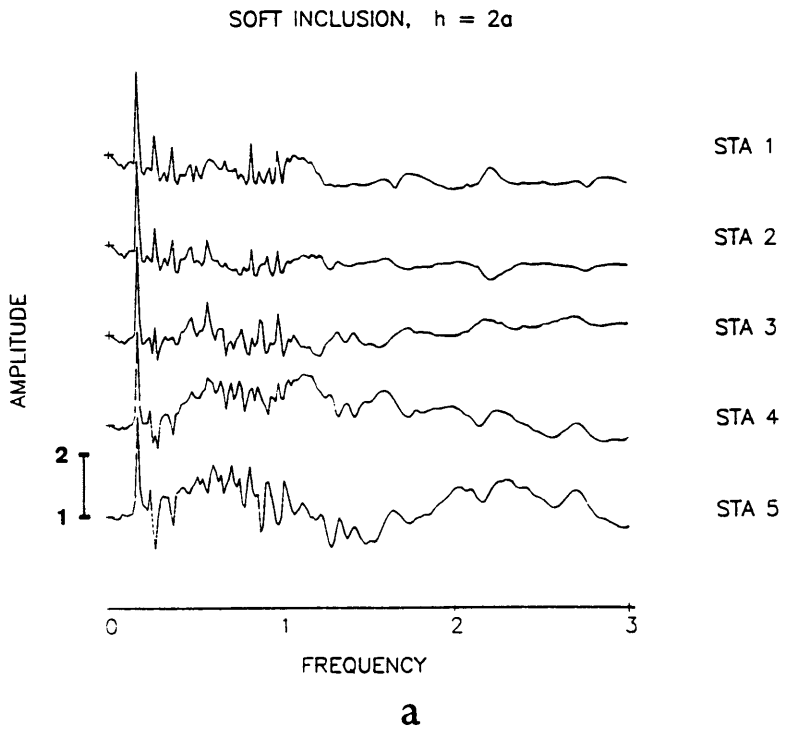

a

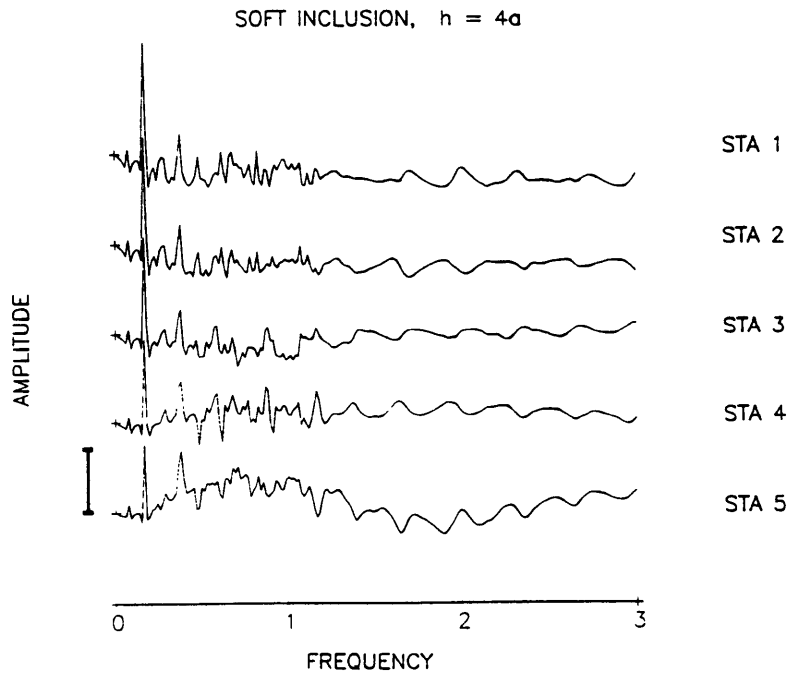

b

FIGURE 3.9 (a) Same location of the soft inclusion and stations as in Figure 3.6, but velocity inside the inclusion is 10 timessmaller than that of the half-space. Note that the sharp peak occurs at much lower frequency (η) than the peak for the soft inclusion in Figure 3.6. In (b) the inclusion is deeper, but a sharp peak appears at the same frequency as that in (b), suggesting that the effect of the free-surface decreases as impedance contrast increases.

inclusion, as compared with the earlier case of smaller impedance contrast, we note that there is still some effects due to the free-surface, by comparing the spectra (a) and (b) (Figure 3.9) computed at each station. These complexities suggest some coupling between the resonance in the inclusion and that set up between the free-surface and the top of inclusion.

From the above examples on spectral computations of the ground motion at the surface of a half-space with an inclusion, we conclude that the free-surface plays an important role on the build-up of resonance of trapped modes inside the inclusion, in particular for shallow depths and small impedance contrasts between the half-space and the inclusion. The reason is that reflected waves at the free-surface back to the half-space also contribute to trapped modes (in addition to the incident wave), by refraction at the boundary of the inclusion. This effect appears to be smaller when the impedance contrast between the inclusion and half-space is larger, so that the fundamental resonance peak appears as a dominant feature in the spectra, regardless of the position of the inclusion with respect to the free-surface. The detection at the surface of spectral peaks corresponding to the resonance inside a buried soft inclusion is extremely interesting in view of the recent report by Biswas et. al. (1990) about the narrowly peaked site amplification effect of Hawaiian stations near the active rift zone presumably containing magma body on the T-phase generated by distant earthquakes.

3.4 Synthetic Seismograms in Time Domain

Now let us compute the solution in time domain for both the soft and hard inclusion cases treated in the previous section. We choose radius $a = 1$ (unit of distance), half-space shear wave velocity $\beta_E = 1$ (unit

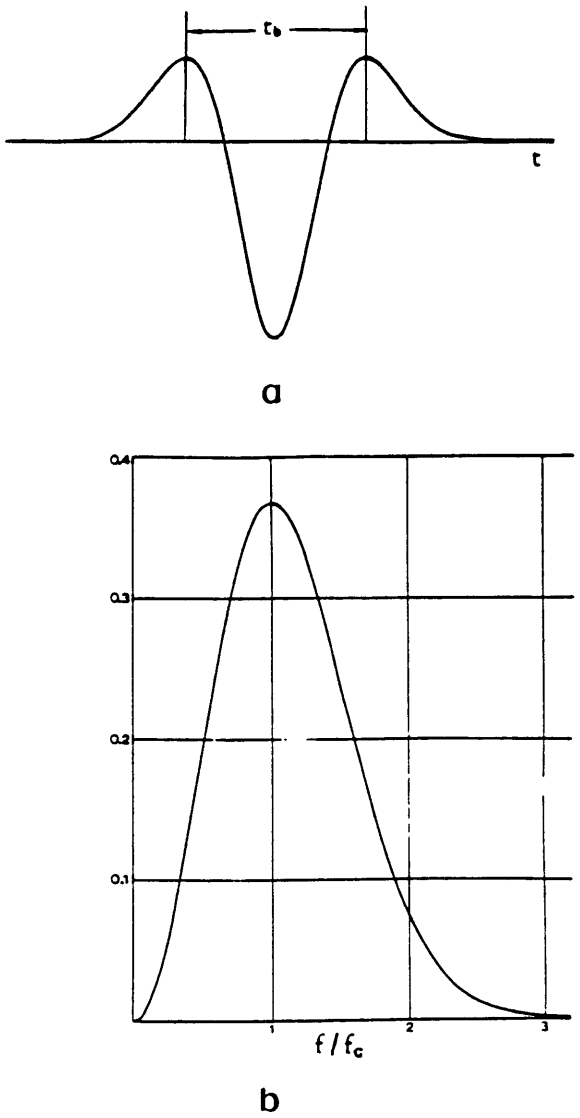

FIGURE 3.10 (a) Ricker wavelet of characteristic frequency f_c. (b) spectrum of Ricker wavelet.

of distance/time). The synthetic seismograms are computed by inverse Fourier transform of the ground response spectrum for 100 frequencies, in the non-dimensional frequency range from $\eta = 0.02$ to $\eta = 5$. The input source-time function is the symmetric Ricker wavelet,

$$s_R(t) = (\frac{u^2}{4} - \frac{1}{2})\frac{\sqrt{\pi}}{2} \exp(-\frac{u^2}{4}) \tag{3.4}$$

whose spectrum is

$$S_R(\omega) = \frac{f^2}{f_c^2} \exp(\frac{-f^2}{f_c^2}) \tag{3.5}$$

where $u = 2\sqrt{6}(t - t_0)/t_b$, t_0 being the arrival time of the center of the wavelet, t_b the time interval between the two peaks of the wavelet, also called "breadth" of the wavelet (see Figure 3.10), f is frequency, and $f_c = \sqrt{6}/\pi t_b$ is the characteristic (peak) frequency of the wavelet. Both f and η are related by $f = \beta\eta/2a$.

Figure 3.11 (a) shows the synthetic seismogram section for the case of the soft inclusion and vertical incidence. The seismograms shown in the right part of (a) are synthesized for 100 stations, deployed along the line A-A', shown in the left part of (a), covering a range of $8a$. The center of the inclusion is located at $x/a = 0$ and $z/a = 2$ (x-positive to the left). Breadth of the Ricker wavelet is 0.78 a/β seconds, which corresponds to a characteristic wavelength of a in the half-space. We observe the arrivals of phases corresponding to the direct wave d, the reflected waves r at stations located in the region $|x/a| > 2$, and phases R, Rs, all marked by arrows. As observed for the frequency response (Figure 3.2), the direct wave identified in the time domain is also strongly attenuated at stations just above the inclusion. The field in the region $|x/a| = 1$ is due mainly to diffraction along the border of the inclusion (see ray diagram (b)). The time delay for

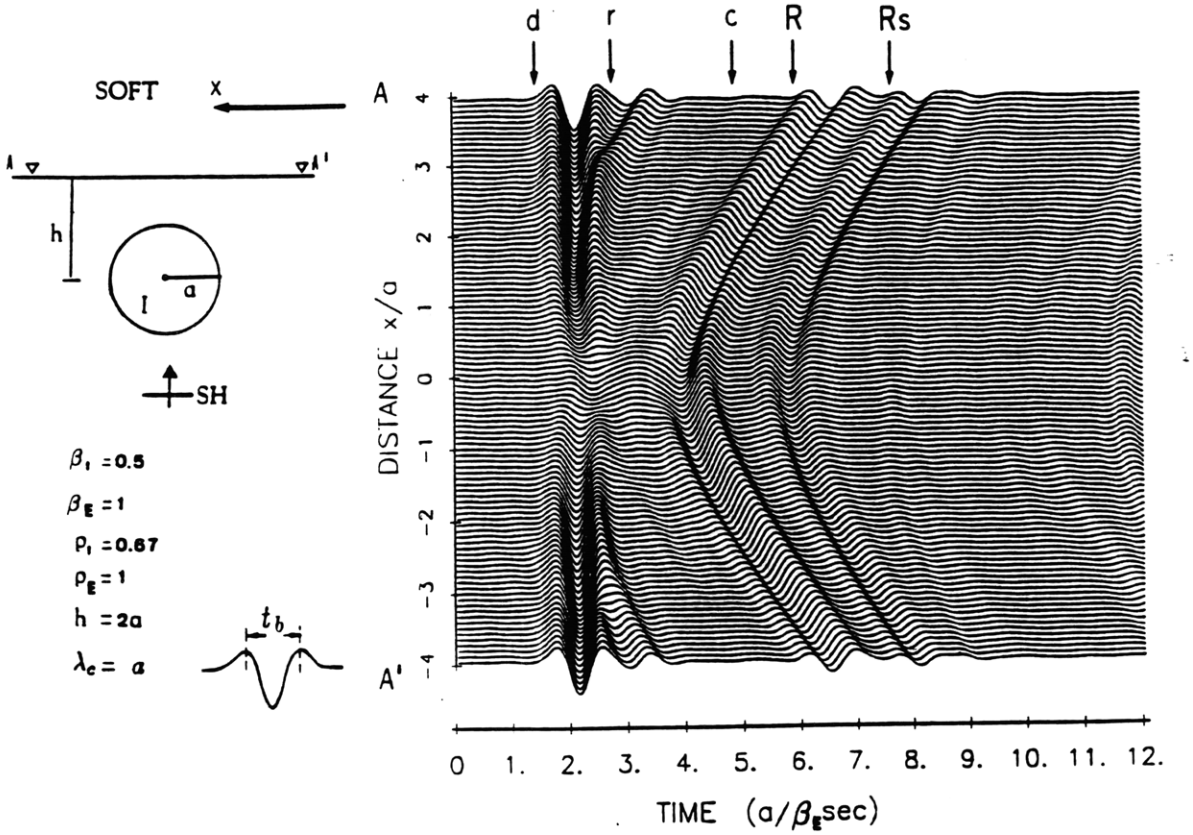

a

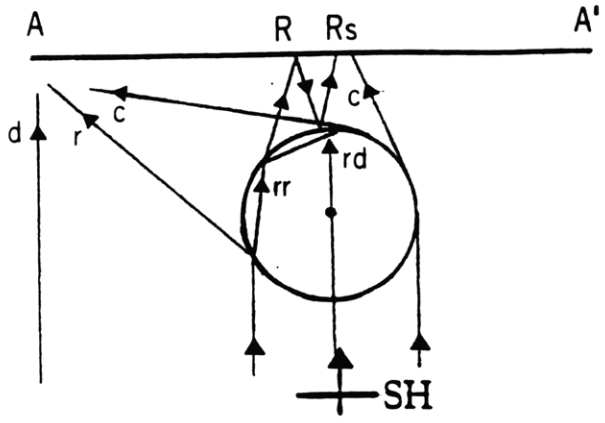

b

FIGURE 3.11 (a) Synthetic seismograms (full waveform) for scattered waves by a soft inclusion, upon the incidence of a plane wave, for a Ricker wavelet source time function. (b) ray diagram corresponding to the observed phase arrivals in (a). (c) seismograms for deeper inclusion. Note the effect of the free-surface on the delay of the pulse R_s.

these waves with respect to the direct wave in the absence of inclusion is about $0.4a/\beta_E$ seconds at $x = 0$. These diffracted waves reach all stations, appearing as a minor feature marked as phase c in the seismograms. Phase R, which arrive later than phase c, is the wave transmitted through the inclusion, marked as rr or rd, shown in the ray diagram (b). The wave rd travelling vertically is delayed by $2a(1/\beta_I - 1/\beta_E)$ or $2a/\beta_E$ seconds with respect to the incident wave in the absence of inclusion for the station at $x/a = 0$. At other stations this delay includes the one proportional to the travelling path outside the inclusion, which determine the wavefront well defined in the seismograms. For large x, phase R is propagating horizontally with the half-space velocity β_E. Phase Rs corresponds to the reflection of phase R at the free-surface and the inclusion boundary. It arrives at about $2a/\beta_E$ seconds after R, since the two-travel time path between the top boundary and the free surface is $2a$. In order to clarify the nature of R_s, we calculated the seismograms shown in Figure 11 (c), where the depth of the inclusion is increased to $h = 4a$ and accordingly, we observe the time interval between R and R_s equal to $4a/\beta_E$. Note that in this case the wavefronts become more curved than in (a). Also, note in both (a) and (c) that the amplitude of Rs is smaller than that of R, reflecting the assumed 1/2 impedance contrast ratio and to other factors such as the wavelength λ and the size of the inclusion.

The resonance of trapped modes inside the soft inclusion is not evident in our synthetic seismograms. Also, it is difficult to depict it with the ray diagram shown in Figure 3.11 (b). Assuming that resonance can be built by two trapped rays travelling in opposite directions (one dimensional model), the period corresponding to one resonant mode will be $T = 2a/\beta_I$ or $4a/\beta_E$,

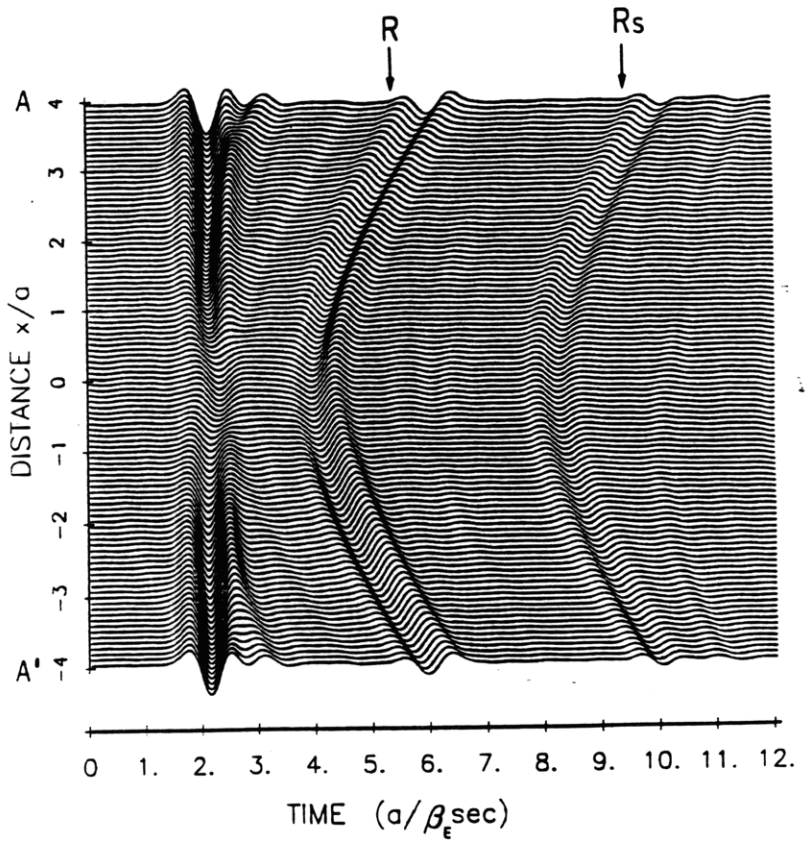

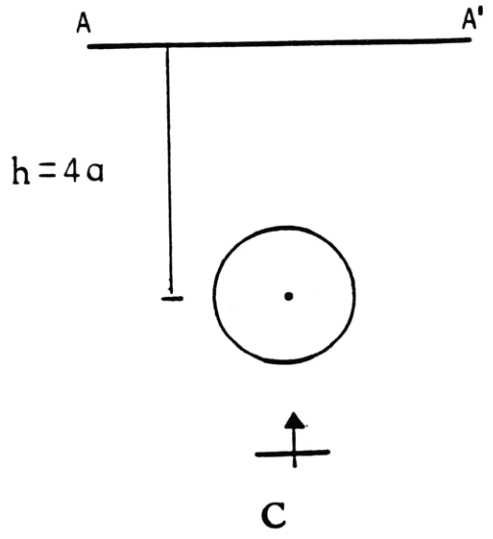

FIGURE 3.11 (c) seismograms for deeper inclusion. Note the effect of the free-surface on the delay of the pulse R_s.

which is the time delay by a trapped wave to travel back and forth over one diameter. Looking at the seismogram section shown in Figure 3.11 (a), we observe no clear periodicity corresponding to such mode, though the total duration of the seismogram, $12a/\beta_E$, may allow to see at least the first two periods.

Some of the peaks identified earlier in the frequency response correspond to a very long period. For example, the peak identified at $\eta = 0.16$ in the spectra shown in Figure 3.9 (a) and (b) correspond to the period $T = 12.5a/\beta_E$ seconds. In order to observe such periodicity we need to calculate synthetic seismograms much longer than those in Figure 3.11. We do not intend to compute a longer seismogram to show more details of the resonance phenomena in this case, but emphasize that to study resonance phenomena it is more important to compute the frequency domain solution than the corresponding time domain, because the computation of periodic pulses that synthezise narrow peaks of the spectra would require a long duration seismogram.

Figure 3.12 (a) shows the synthetic seismograms for the case of hard inclusion. The model parameters are shown at its left. We observe the arrival of the direct phase d, reflected phase r , refracted phases denoted as f_1, f_2 respectively, and phases corresponding to multiple bouncing between the top boundary of the inclusion and the free-surface, two of them marked as $s1$ and $s2$. As in the case of soft inclusion, the direct wave is again attenuated at stations immediately above the inclusion in the region $|x/a| < 1$. This attenuation in this case is partly due to reflection at the inclusion boundary and partly due to defocusing of the refracted wave, as depicted in diagram (b). Refracted phase f_2 arrives earlier than phase r in the

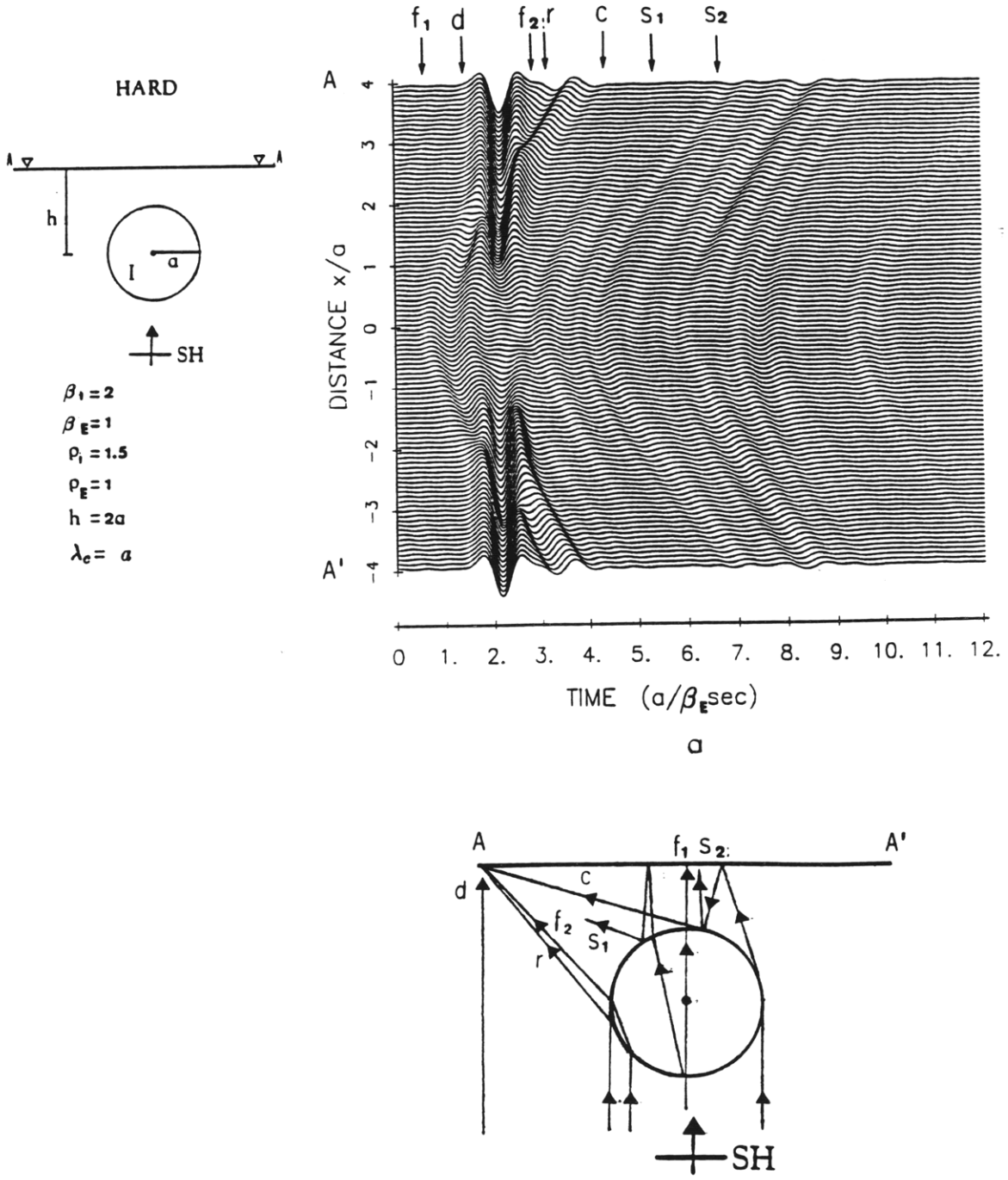

FIGURE 3.12 (a) Synthetic seismograms of the scattering for a hard inclusion upon the incidence of a plane wave. In both, soft and hard inclusions the dominant feature of the seismogram sections is the strong attenuation of the primary wave at stations right above the inclusion. (b) ray diagram.

region $|x/a| > 2$, since it travels along a faster path inside the inclusion. The refracted phase f_1 arrives a/β_E seconds before the direct wave (in the absence of inclusion) at the station $x/a = 0$. Its wavefront is clearly defined in the seismograms at stations within the region $|x/a| < 2$. The amplitude of this phase is about one-fourth of that of the incident wave. How much of this reduction is due to defocusing and how much to the reflection?. From the ray theory, the refracted direction with respect to the inward normal to the boundary at the incidence point is smaller for the case in which the wave is transmitted from hard to soft media than for the opposite case. As a result, refracted waves into soft inclusion have larger amplitudes and travel longer paths than those refracted by the hard inclusion. By comparing Figures 3.11 (a) and 3.12 (a) we find amplitude reduction of direct waves for both soft and hard inclusions. Focusing, therefore, is not the main factor controlling the amplitude of direct waves. We also observe diffracted waves c similar to those observed for soft inclusion but faster and with reversed polarity. In addition, as illustrated in Figure 3.12, phase s_1 arrives at about $2a/\beta_E$ seconds after f_1. Phases s_2 corresponding to reflection of diffracted waves at the free-surface and top boundary of the inclusion arrives about a/β_E seconds after s_1.

The most interesting difference between the cases of hard and soft inclusion shows up in the waves marked as R and R_s for the latter, and as s_1 and s_2 for the former. All of them form well defined wavefronts propagating away from the general region inside or above the inclusion. These waves are stronger for the case of soft inclusion than for the case of hard inclusion, because of the following two reasons. First, as we mentioned earlier, the ray theoretical condition favors the concentration of wave energy toward $x = 0$

for the soft inclusion, while the hard inclusion tends to divert wave energy away from $x = 0$. Secondly, the seismic motion within a soft inclusion may be sustained by trapped modes which behave as inhomogeneous waves in the half-space. For the hard inclusion, all motions set up inside it will be quickly lost as radiated waves into the half-space.

3.5 Conclusions

We have applied the boundary integral-Gaussian beam method to compute surface ground motion of a half-space with a buried cylindrical inclusion due to vertically incident plane SH waves. The computed wavefield is complete including all multiply reflected, refracted and diffracted waves by the boundary of the inclusion. We found a surprising result that both soft and hard inclusions cause deamplification of surface motion at stations immediately above the inclusion, due mainly to scattering by the boundary of inclusion in both cases, and to less extent, to wave energy trapping by the soft inclusion and defocusing by the hard inclusion. The computed amplitude spectra for hard and soft inclusions are significant different, being smoother for the former, and showing many spectral peaks for the latter. Some of the spectral peaks for soft inclusion is attributted to resonance of trapped modes inside the inclusion. We found that this resonance phenomenon is affected by the presence of free-surface, for example, the peak for a shallower inclusion occurring at higher frequencies than the corresponding peak for a deeper inclusion. The effect of the free-surface decreases as the impedance contrast between the half-space and the inclusion increases. Larger impedance contrasts yield narrower resonant peaks, as expected for a trapped mode.

Finally, from the analysis of the synthetic seismograms, we found that

the frequency domain solution is more appropiate than the time domain solution to analyze resonance phenomena, because the resolution necessary to define a sharp peak in the spectra requires long duration seismograms. On the other hand, the time domain solution gave a clear physical picture of the reflection, refraction and diffraction of waves, and helped to understand the essential difference in wave phenomena between the scattering due to a hard inclusion and a soft inclusion buried in a half-space.

CHAPTER IV

GROUND MOTION AT MOUNTAINS AND VALLEYS WITH VERTICAL SEISMIC VELOCITY GRADIENT

4.1 Introduction

In this Chapter IV we apply the full power of our method to study the ground motion in two-dimensional structures that exhibit irregular topography and interface, and whose shear wave velocity varies linearly with depth, for incident plane waves. In our first example of application, the model is a half-space whose free-surface topography is a ridge of cosine shape, with vertical shear wave velocity gradient. In the second, the model is a semi-cylindrical sedimentary basin in a homogeneous half-space, in which the shear wave velocity of the sediment increases linearly with depth. Our results are given in frequency and time domains. To our knowlegde, the present work is the first study on these subjects.

The ground motion at elevated free-surface topographies of homogeneous half-space has been studied extensively from observations (Davis and West 1973, Tucker et. al. 1984) and by theoretical modeling using finite difference method (Boore 1972, 1981, Jih et. al.1986), the Aki-Larner (1970) method (Bouchon 1973 and Bard 1982) and the boundary method using point sources by Bouchon (1985). The results of 2-D modeling of ridge in a homogeneous half-space in general predicts amplification of ground motion at its top, there are considerable discrepancies between the observed ground motion amplification factor and the one obtained by modeling (Bard 1982). For instance, ridge effects observed by Tucker et. al. (1984) show large amplification factors (4 to 8), while the corresponding theoretical pre-

diction using the Aki-Larner method yields only a factor equal to 2. This discrepancy has been attributed to combined effects of vertical variation of seismic velocities and lateral resonance pattern due to repeated neighboring topographies. Bard and Tucker (1985) made a parameter sensitivity study of such effects in order to explain the results observed by Tucker et. al. (1984). They used several models of isolated ridges and groups of neighboring ridges, which were either homogeneous or covered by a low velocity surface layer. They showed that although the models with the low velocity layer improved the agreement of the predicted ground motion with the observed, none of them satisfactorily fit the observed. They concluded that more accurate prediction would require a model that includes both effects of ridge topography and near surface velocity gradient.

The case of a homogeneous half-space containing a sedimentary basin, in which the shear wave velocity of the sediment increases linearly with depth has been treated by Bard and Gariel (1986). The purpose of their study was to investigate to which extent the velocity gradient modified the behavior of the groung motion response calculated for a homogeneous basin (Bard and Bouchon 1985), in particular for an incident plane SH wave. They used a technique based on the modified Aki-Larner method in which the expression for a plane harmonic wave in homogeneous media $e^{ikx \pm i\nu z}$ (ommiting the factor $e^{i\omega t}$), where k and ν are the horizontal and vertical wavenumbers respectively and the $\mp$ sign refers to plane waves going up and down respectively, is replaced by a $e^{ikx}Z(z,k)$, where $Z(z,k)$ is the exact solution of the wave equation in media with a linear increase of velocity with depth. This technique is applicable to shallow valleys with smooth interface irregularity, for which the Rayleigh-ansatz error described

in Aki and Larner (1970), is small. They concluded that neglecting the velocity gradient leads to significant underestimation of surface amplification, particularly at the edges of the basin, where large differential motion is developed. Bard and Gariel (1986) also applied their method to study the ground motion observed in the Chusal valley (Soviet Union) by King and Tucker (1984), and obtained a satisfactory fit of the theoretical results with the observations. Other studies have considered steep 2-D basins composed of several sedimentary homogeneous layers and incident SH, P-SV plane waves (Fukuwa et. al. 1985), using a hybrid method in which the field exterior to the basin is computed using a boundary element scheme and the interior field by the finite element method. We will see that although this method deals quite satifactorily with the case of the basin composed of several homogeneous layers, it failed to simulate the case of the basin with continuous vertical variation of velocity for high frequencies.

In our study, in addition to the vertical variation of velocity, we investigate the effect of the slope of both the ridge topography and the interface between the basin and the half-space. We believe that our method is particularly suited for these problems because it combines the power of the boundary integral representation to deal with steep boundary shape, and that of the Gaussian beam method to describe wave propagation in inhomogeneous media. In section 4.2 we develop expressions for the Gaussian beam representation of displacement and traction in media where velocity increases linearly with depth. We use the formulas for calculating the complex travel time and spreading in vertically inhomogeneous media already obtained in Chapter II. Here, the ray centered coordinates (s, n) of the observation point with respect to each ray departing from the source point

can be computed exactly, taking advantage of the fact that in such media ray paths are segment of circles uniquely determined from the geographical coordinates of observation and source points, and the take-off angles of the rays. In section 4.3 we describe the Gaussian beam superposition to compute Green's function for both displacement and traction due to a point(line) source, in the vertically inhomogeneous media considered. It was not easy to implement a general computer routine to perform this superposition for any pair of observation-source points, because our analytical solutions for the ray centered coordinates are a multiple valued function of their positions with respect to an absolute system of geographical coordinates. In this thesis we have developed a computer program subroutine called INGREEN, which carries out the Gaussian beam superposition and provides the displacement and traction Green's functions, in such a way that it can be easily incorporated into the boundary integral scheme. Tests of accuracy for both the ray centered coordinates and the wave field computed for small velocity gradient are also given in this section. In section 4.4 we apply the method to compute the ground response of a vertically inhomogeneous half-space with ridge topography, for several ridge aspect ratios, i.e. the ratio of height h to half-width a, for several values of the non-dimensional frequency $\eta = 2a/\lambda$ (λ wavelength) and several choices of the velocity gradient. Similarly, in section 4.5 we study the response of a semi-cylindrical sedimentary basin with vertical heterogeneity, for small and large velocity gradients.

4.2 Gaussian beam for displacement

The medium considered in this section has a linear seismic wave

velocity- depth dependency defined by

$$\beta(z) = \beta_0 + g(z - z_0) = \beta_0[1 + \delta(z - z_0)] \tag{4.1}$$

where g, the velocity gradient, is a constant with the units of reciprocal of time, and $\delta = g/\beta$. Refering to Figure 4.1, consider a ray with its source point at (x_0, z_0) and take-off angle ϕ_0 (positive z is taken downward). The shear wave velocity at the source point is β_0. The ray path in this media is an arc of a circle whose radius R and center (x_c, z_c) are determined from (x_0, z_0) and ϕ_0 :

$$R = (\beta_0/g)\sin\phi_0 \tag{4.2}$$

$$x_c = x_0 + R\cos\phi_0$$

$$z_c = z_0 - \beta_0/g$$

The center of the circular ray path is located on the line normal to the ray direction at its source point and at a vertical distance β_0/g from the source point. Then the ray centered coordinates (s, n) of any observation point (x, z) can be expressed as

$$n = R - d \tag{4.3}$$

$$s = R(\phi - \phi_0)$$

where $d = [(x - x_c)^2 + (z - z_c)^2]^{1/2}$ and $\phi = \tan^{-1}(z - z_c)/(x - x_c)$

The intersection point (x^*, z^*) on the ray at which the normal to the ray passes through the observation point can be obtained as

$$x^* = x_0 + \frac{\beta_0}{g\sin\phi_0}(\cos\phi_0 - \cos\phi) \tag{4.4}$$

$$z^* = z_0 + \frac{\beta_0}{g\sin\phi_0}(\sin\phi - \sin\phi_0)$$

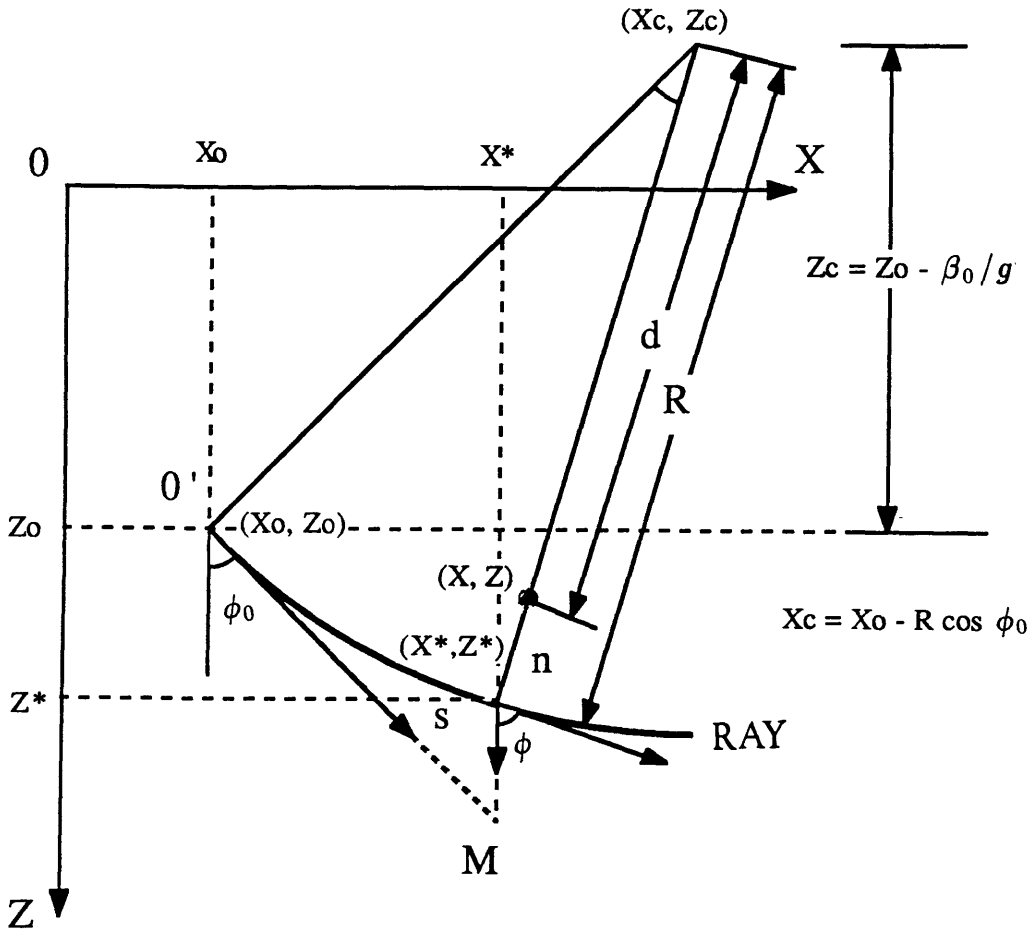

FIGURE 4.1 Ray path in media with linearly increasing velocity (with depth). The Take-off angle ϕ_0, source point coordinates (x_0, z_0) and observer position coordinates (x, z) determine completely the ray-centered coordinates (s, n).

and the travel time from the origin (x_0, z_0) to the intersection point (x^*, z^*), along the ray is

$$\tau(s,0) = \begin{cases} \frac{1}{g}\ln\left(\beta/\beta_0\right), & \text{when } \phi = 0, \pi, 2\pi; \\ \frac{1}{g}\ln[\tan(\phi/2)/\tan(\phi_0/2)], & \text{otherwise.} \end{cases}$$

The corresponding DRT solutions are determined by the procedure introduced in Chapter II, section 2.3. Recalling equations 2.15 and putting $d\beta/dz = g$, we obtain

$$n(s) = A\cos\phi + B\cos\phi.f(z) \tag{4.6}$$

$$p_n(s) = -Ap^2g + \frac{B}{\cos\phi}[1 - p^2g\cos\phi.f(z)]$$

In this case the evaluation of $f(z)$ from equation (2.14), namely,

$$f(z) = \int_{z_0}^{z} \frac{\beta_0 + g(z - z_0)}{\cos^3\phi} dz$$

is straightforward. We use $\beta = \sin\phi/p$ to obtain $d\phi = pg/\cos\phi$; and insert both in the equation for $f(z)$, resulting in

$$f(z) = \frac{1}{p^2g}\int_{\phi_0}^{\phi} \frac{\sin\phi}{\cos^2\phi} d\phi$$

or

$$f(z) = \frac{\beta_0^2}{g\sin^2\phi_0}\left(\frac{1}{\cos\phi} - \frac{1}{\cos\phi_0}\right) \tag{4.7}$$

Thus, we have

$$n(s) = A\cos\phi + \frac{B\beta_0^2}{g\sin^2\phi_0}\left(1 - \frac{\cos\phi}{\cos\phi_0}\right) \tag{4.8}$$

$$p_n(s) = -Agp^2 + \frac{B}{\cos\phi_0}$$

As described in section 2.3 (Chapter II), for the plane wave source we have $A = 1/\cos\phi_0$, $B = gp^2$. Putting them into (4.8),

$$n^P(s) = 1 \tag{4.9}$$

$$p_n^P(s) = 0$$

For the point source, $A = 0$, $B = \frac{1}{\beta_0}\cos\phi_0$, and we have

$$n^L(s) = \frac{\cos\phi_0 \cos\phi}{\beta_0 gp^2}\left(\frac{1}{\cos\phi} - \frac{1}{\cos\phi_0}\right) \tag{4.10}$$

$$p_n^L(s) = 1/\beta_0$$

These solutions for both plane wave and point source, differ from the corresponding solutions in the homogeneous case only in the value of n^L. For the homogeneous case $n^L = s$ (see section 2.4). We can find a simple geometrical meaning of n^L in the inhomogeneous case by taking into account equation (4.4) and rewriting n^L as

$$n^L = \frac{x^* - x_0}{\sin\phi_0} \tag{4.11}$$

This is the length of the line O'M in Figure 4.1, which corresponds to the straight line ray path in the homogeneous case, for the same shooting angle.

As described in section (2.3), the DRT solution for the Gaussian beam is obtained by a linear combination of the DRT solutions corresponding to plane wave and point(line) source

$$n^G = \epsilon + \frac{x^* - x_0}{\sin\phi_0} \tag{4.12}$$

$$p^G = 1/\beta_0$$

Where ϵ is a complex constant. The constant ϵ is chosen as in section 2.4, i.e. $\epsilon = -iL_0^2$, assuming that the beam waist is at the source point (x_0, z_0). From $C(s) = p_n/n$ (section 2.3),

$$C(s) = \frac{p_0/2}{\epsilon \sin \phi_0 + x^* - x_0}$$

According to the definition given in section 2.3, the Gaussian beam for displacement is now given by

$$v(s, n, \omega) = \frac{1}{J^{1/2}} e^{i\omega\tau(s,n)} \tag{4.13}$$

where

$$J = \frac{\beta}{\epsilon\beta_0}(\epsilon + \frac{x^* - x}{\sin \phi_0})$$

$$\tau(s, n) = \frac{1}{g} \ln \frac{\tan(\phi/2)}{\tan(\phi_0/2)} + \frac{pn^2/2}{\epsilon \sin \phi_0 + x^* - x}$$

This expression is different from the one given by Madariaga (1984), who used the WKB solution $n_{WKB} = \cos\phi/\cos\phi_0$, $p_{WKB} = -gp^2/\cos\phi_0$ for the Gaussian beam, instead of the plane wave source $(n^P = 1, p_n^P = 0)$.

The expressions for both spreading J and travel time τ in equation (4.13) contain a complex factor $q = \epsilon + (x^* - x_0)/\sin\phi_0$, which yields indeterminate values for a Gaussian beam propagating vertically; i.e. $x^* = x_0$ and $\phi_0 = 0$ or π. In this case it is simpler to recall equations (4.6) and find first the DRT solutions for the Gaussian beam. Let us take first the case of $\phi = 0$, and put $p = \sin\phi/\beta = 0$ in equation (4.6)

$$n(s) = A + Bf(z) \tag{4.14}$$

$$p_n(s) = \frac{B}{\cos\phi}$$

From equation (2.14)

$$f(z) = \int_{z_0}^{z} \beta dz = \int_{z_0}^{z} [\beta_0 + g(z - z_0)]dz$$

or

$$f(z) = \beta_0(z - z_0) + \frac{1}{2}g(z - z_0)^2$$

The corresponding DRT solutions are

$$n(s) = A + B[\beta_0(z - z_0) + \frac{1}{2}g(z - z_0)^2 \tag{4.15}$$

$$p_n(s) = B$$

For plane wave source $n(0) = 1$, $p_n(0) = 0$, or $A = 1$ and $B = 0$, and $n^P(s) = 1$ and $p_n^P(0) = 0$. For point source $n(0) = 0$ and $p_n(0) = 1/\beta_0$, or $A = 0$ and $B = 1/\beta_0$, and $n^L(s) = (z - z_0)[1 + \frac{1}{2\beta_0}(z - z_0)]$ and $p_n^L(s) = 1/\beta_0$. The DRT solutions for the corresponding Gaussian beams are

$$n^G(s) = \epsilon + (z - z_0)[1 + \frac{1}{2\beta_0}(z - z_0)] \tag{4.16}$$

$$p_n^G(s) = 1/\beta_0$$

Then

$$C(s) = \frac{\beta_0/2}{\epsilon + (z - z_0)[1 + \frac{1}{2\beta_0}(z - z_0)]}$$

The complete expression for $\tau(s, n)$ requires to find the travel time along the ray $\tau(s, 0) = \int_0^s ds/\beta(s)$, or (since $s = z$) $\tau(s, 0) = \int_{z_0}^{z} dz/[\beta_0 + g(z - z_0)]$ We obtain

$$\tau(s, 0) = \frac{1}{g} \ln\left(\frac{\beta}{\beta_0}\right)$$

Finally, the formulas for $J(s)$ and $\tau(s, n)$ for a vertically propagating Gaussian beam are:

$$J(s) = \frac{\beta}{\epsilon\beta_0}\{\epsilon + (z^* - z_0)[1 + \frac{g}{2\beta_0}(z^* - z_0)]\} \tag{4.17}$$

$$\tau(s,n) = \pm\frac{1}{g}\ln\left(\frac{\beta}{\beta_0}\right) + \frac{n^2/2}{\epsilon + (z^* - z_0)[1 + \frac{g}{2\beta_0}(z^* - z_0)]}$$

where '+' and '-' correspond to $\phi_0 = 0$ and $\phi_0 = \pi$, respectively, and we have taken $z = z^*$. These formulas for J and τ do not present the indeterminate problem.

4.3 Gaussian beam for traction

Let us now follow a similar procedure used for homogeneous media (Chapter II) to represent traction in our inhomogeneous media, and start with the general expression for the derivative of the Gaussian beam displacement $v(s,n,\omega)$

$$\frac{\partial v}{\partial \xi} = \left(\frac{1}{2J}\frac{\partial J}{\partial \xi} + i\omega\frac{\partial \tau}{\partial \xi}\right)v(s,n,\omega) \tag{4.18}$$

where ξ represents x or z, and

$$\frac{\partial}{\partial \xi} = \frac{\partial}{\partial \phi}\frac{\partial \phi}{\partial \xi} + \frac{\partial}{\partial n}\frac{\partial n}{\partial \xi}$$

The derivatives involved in equation (4.18) are:

$$\frac{\partial J}{\partial \phi}^{-1} = -\frac{\epsilon\beta_0}{\beta^2 q^2}\left(q\cos\phi + \beta\frac{\sin\phi}{g\sin\phi_0}\right)$$

$$\frac{\partial \tau}{\partial \phi} = \frac{1}{g\sin\phi} - \frac{n^2\sin\phi}{2gq^2\sin\phi_0)}$$

$$\frac{\partial \tau}{\partial n} = \frac{n/\beta_0}{\epsilon\sin\phi_0 + x^* - x_0}$$

$$\frac{\partial \phi}{\partial x} = sgn\frac{\sin\phi}{d}$$

$$\frac{\partial \phi}{\partial z} = sgn\frac{\cos\phi}{d}$$

$$\frac{\partial n}{\partial x} = -\cos\phi$$

$$\frac{\partial n}{\partial z} = \sin\phi$$

$$sgn = \begin{cases} 1, & \text{if } x \le x_c; \\ -1, & \text{if } x > x_c \end{cases}$$

where $q = \epsilon + (x^* - x_0)/\sin\phi_0$.

If the propagation is vertical, the derivatives in (4.18) are:

$$\frac{\partial J^{-1}}{\partial z} = -\frac{\epsilon\beta_0}{\beta^2 q^2}\{gq + \beta[1 + \frac{g}{\beta_0}(z^* - z_0)]\} \tag{4.19}$$

$$\frac{\partial \tau}{\partial z} = sgn\frac{g}{\beta} - \frac{1}{2\beta_0 q^2}[1 + \frac{g}{\beta_0}(z^* - z_0)]n^2$$

where

$$q = \epsilon + (z^* - z_0)[1 + \frac{g}{2\beta_0}(z^* - z_0)]$$

and

$$sgn = \begin{cases} 1, & \text{if } \phi_0 = 0; \\ -1, & \text{if } \phi_0 = \pi \end{cases}$$

Using the above spatial derivatives, traction is computed as in section 2.3 (Chapter II).

The accuracy of the displacement and traction fields of Gaussian beam in the media considered above depends to a large extent on the accuracy of computation of the angle ϕ for given source point, observation point, and central ray (see Figure 4.1). Since ϕ is determined by the multivalued function $\tan^{-1}$ of the source and observation points coordinates (equation 4.3), it is important to construct an algorithm capable of systematically and correctly compute its value for arbitrary positions of source and observation points, values of the velocity gradient g and rays with different take-off

angles. This is done in the next section, along with the Gaussian beam superposition.

4.4 Beam superposition. Subroutine INGREEN.

The analytical procedure described in the previous section to construct a Gaussian beam in vertically linear inhomogenous media has to be adapted for superposition of many such beams in order to represent Green's function as described in sections 2.3 and 2.4 to be used in the boundary integral scheme described in section 2.2. The superposition for displacement and traction are given by equations (2.21) and (2.24) respectively, where the radiation angle range Ω is chosen and discretized in such a way that the observation point is uniformly and densely illuminated with beams departing from the source. Since in our boundary integral scheme many sources and observation points are spatially distributed, the algorithm that carries out the superposition has to be capable to deal with all possible situations emerged from the relative source-receiver position and the take-off angle of the ray at the source, without yielding non-unique solutions for the ray-centered coordinates. In this process we must be careful in determining the angular quadrant, (in our geographical coordinate system) corresponding to the value of ϕ, which in fact determines the ray centered coordinates (s, n) of the observation point with respect to a given ray, and the intersection point (x^*, z^*) of the ray with the perpendicular line passing through the observation point. In addition, we must choose the appropriate sign of n for the computation of traction, although this is not important for the displacement since n always appears squared in its Gaussian beam expression.

The superposition of Gaussian beams is carried out by the subroutine

INGREEN, which computes the displacement and traction fields at an observation point (x, z) (along a surface direction in the case of traction) due to a line source at (x_0, z_0) in a 2-D full-space with linear increase of shear wave velocity with depth. Once the number of beams and the radiation angle Ω have been selected, INGREEN discretize the radiation angle range Ω and computes the take-off angles ϕ_0 measured counter-clockwise with respect to the vertical (z-positive down) in a similar way as the one described in Chapter II (section 2.4, Figure 2.5). For each ray shot at angle ϕ_0 it computes the angle ϕ (counter-clockwise from the vertical) according to the formula

$$\phi_i = (i-1)\frac{\pi}{2} + (-1)^i(i-2)\tan^{-1}\left|\frac{z-z_c}{x-x_c}\right|; \quad 0 \leq \phi_0 \leq \pi \tag{4.20}$$

$$\phi_i = (i/2+1)\pi + (-1)^i(i-2)\tan^{-1}\left|\frac{z-z_c}{x-x_c}\right|; \quad \phi_0 > \pi$$

where $i = 1, 2, 3$ for positions 1, 2, 3 respectively, as shown in Figure 4.2, where position 2 corresponds to $x = x*$. Then it computes the ray-centered coordinates (s, n), the intersection point (x^*, z^*) and the travel-time along the ray from the source point (x_0, z_0) to (x^*, z^*). The sign of n is defined by

$$n = \begin{cases} (R-d), & \text{if } 0 < \phi_0 < \pi; \\ -(R-d), & \text{if } \phi_0 > \pi \end{cases} \tag{4.21}$$

Finally, after computing the Gaussian beam corresponding to each ray according to equations (4.13) and (4.17-4.19) in section 4.2, the superposition is performed for displacement and traction.

It is desirable to check the results given by INGREEN before incorporating it into the boundary integral scheme. This can be done for simple cases involving one point(line) source and one or several observation points,

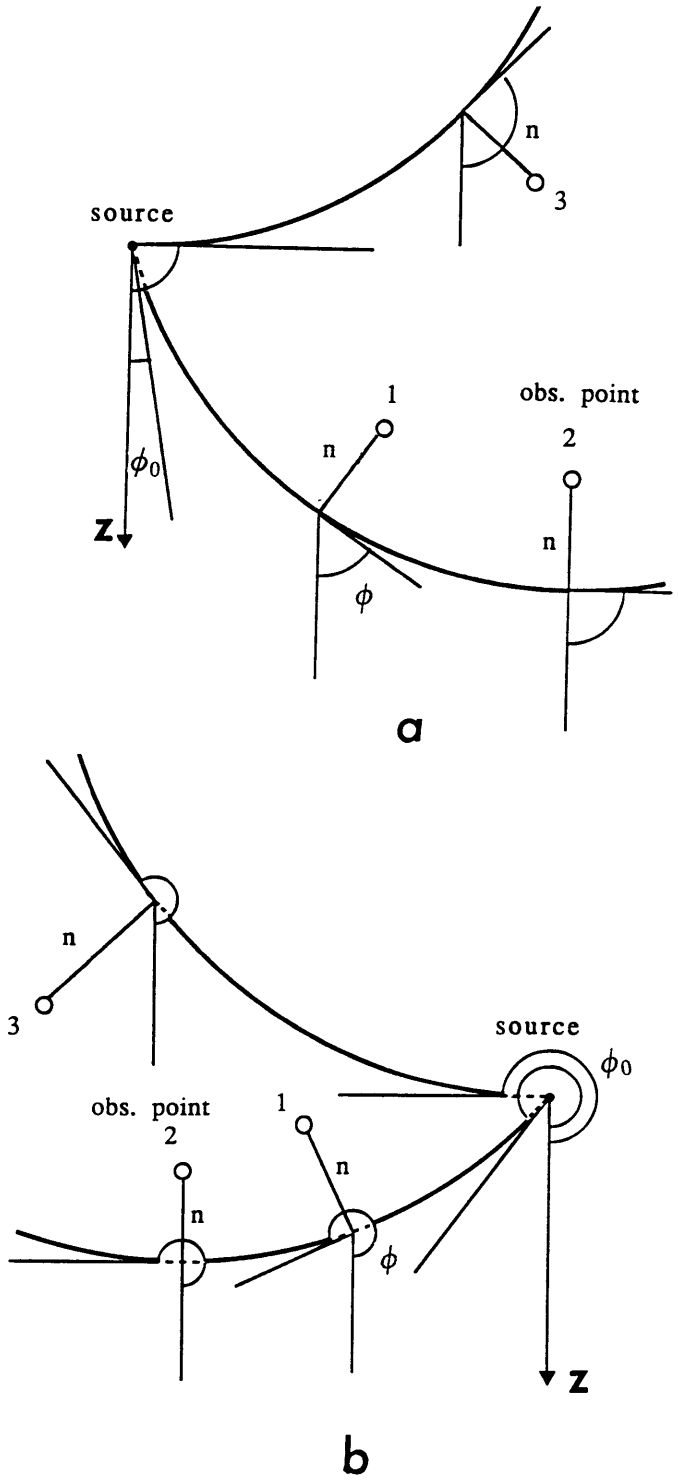

FIGURE 4.2 (a) The observation point, marked with 'o', at three possible positions, marked 1, 2, 3, with respect to the source and to the ray, when the take-off angle of the ray is (a) less than π and (b) greater than π. All angles are measured from Z axis, counterclockwise.

similarly to those computed for the homogeneous case (section 2.4, Figure 2.6). First, the accuracy of calculation for the intersection points (x^*, z^*) by INGREEN is demonstrated in Figure 4.3 (a)-(e), for several arbitrary positions of source and observation points located within an spatial range of 10 km wide and 5 km depth (full-space), for 30 rays departing from a source, and for velocity gradients from 0.0001 sec^{-1} (nearly homogeneous) to 1.0 sec^{-1} (100 % velocity change). The rays are traced only for display, since ray tracing is not needed in our case. The path of these rays are computed by an analytic formula, equation (4.2). The set of intersection points is refered as the "locus" curve, perpendicular to the rays. On the right side of the figure is the travel-time computed along each ray from its origin to the corresponding intersection point, plotted as a function of the take-off angle ϕ_0 (defined in Figure 4.2) in radians, where angles greater than 2π are shown as $\phi_0 - 2\pi$.

Next we calculate amplitude and phase for both displacement and traction acting on a surface with normal $\hat{n} = (0, 1)$, at observation points distributed along a line of length 10 km at a distance 1 km below the source point, due to a single line source in full-space, for several values of the velocity gradient. The geometry is depicted in Figure 4.4. Since for vertically inhomogenous media we have no analytical solution to compare our results with, we compute first the case where $g = 0.001\text{sec}^{-1}$, and compare our results with those corresponding to analytical solutions for homogeneous media, as we did in Chapter II. Then we compute the cases for which $g = 0.1$ km^{-1}, $g = 0.5$ km^{-1} and $g = 1.$ km^{-1}, keeping other parameters exactly the same as for the homogeneous case, and check the results with physical arguments regarding the effect of the velocity gradient.

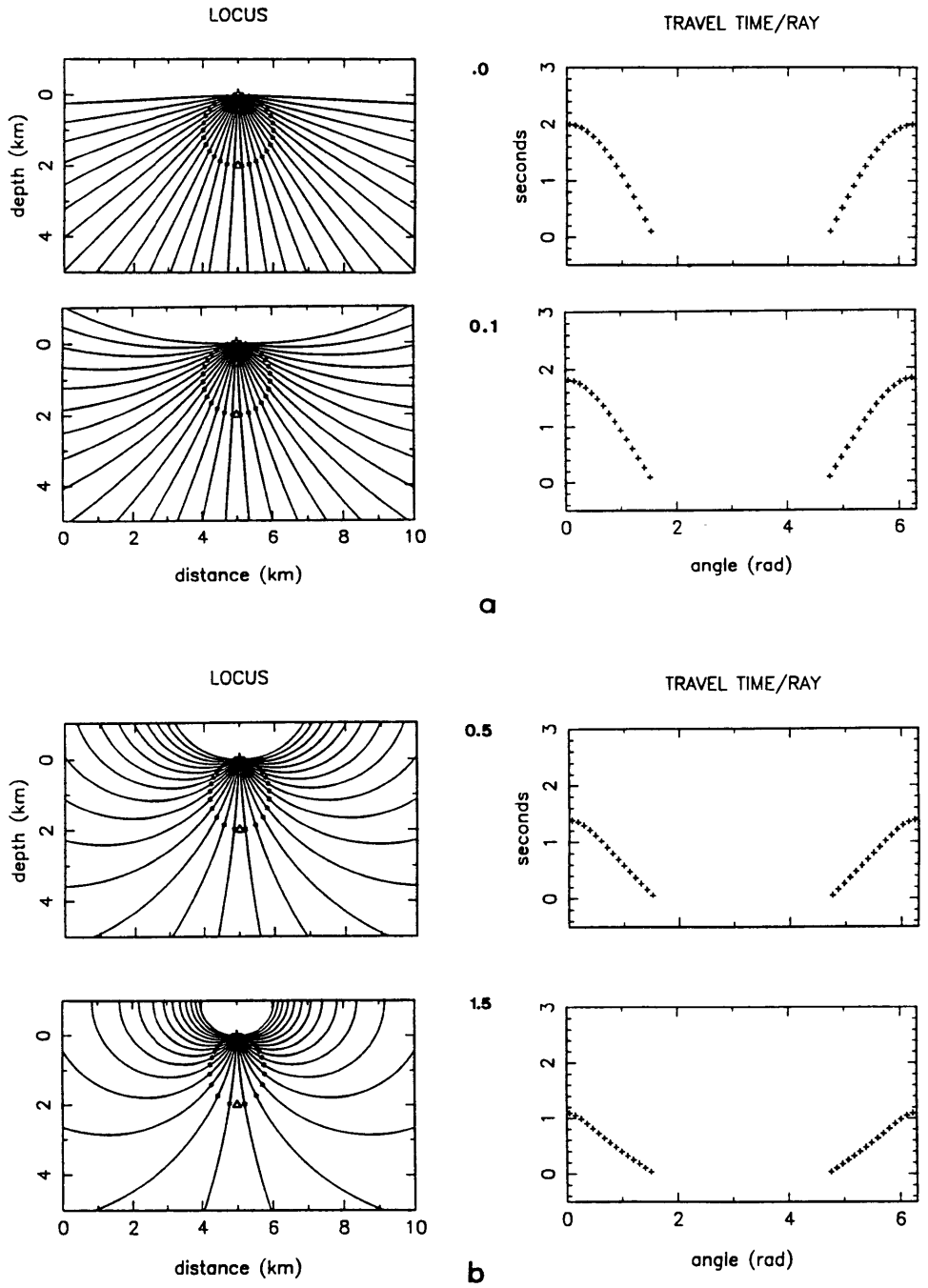

FIGURE 4.3 (a), (b) illustrate the accuracy of computation of the intersection points on the ray where the normal to the ray passes through the station (locus). The numbers indicate the value of the velocity gradients, in units $\sec^{-1}$ according to $\beta(z) = \beta_0 + g(z - z_0)$. For instance, if $\beta_0 = 1$ km/sec, $g = 1$ $\sec^{-1}$ means that the velocity increases 100% in one km depth. At the left, travel-times are plotted as function of the take-off angle, in radians.

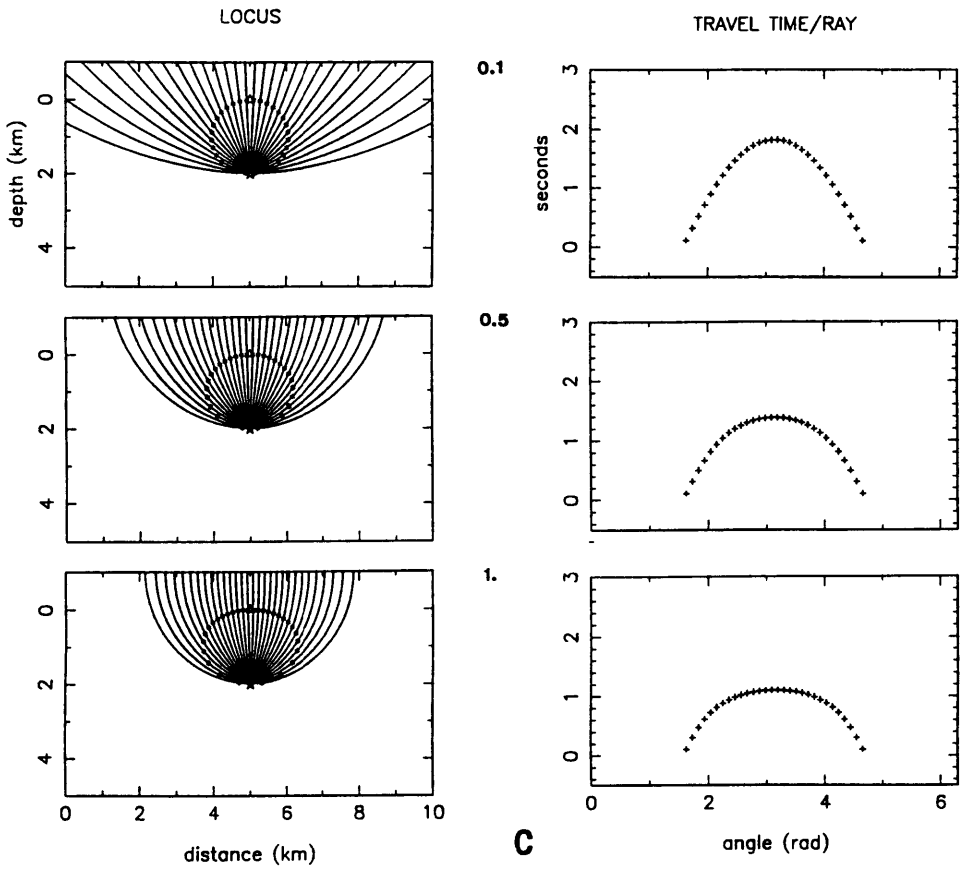

FIGURE 4.3 (c) same as in (a) and (b) but the source below the receiver.

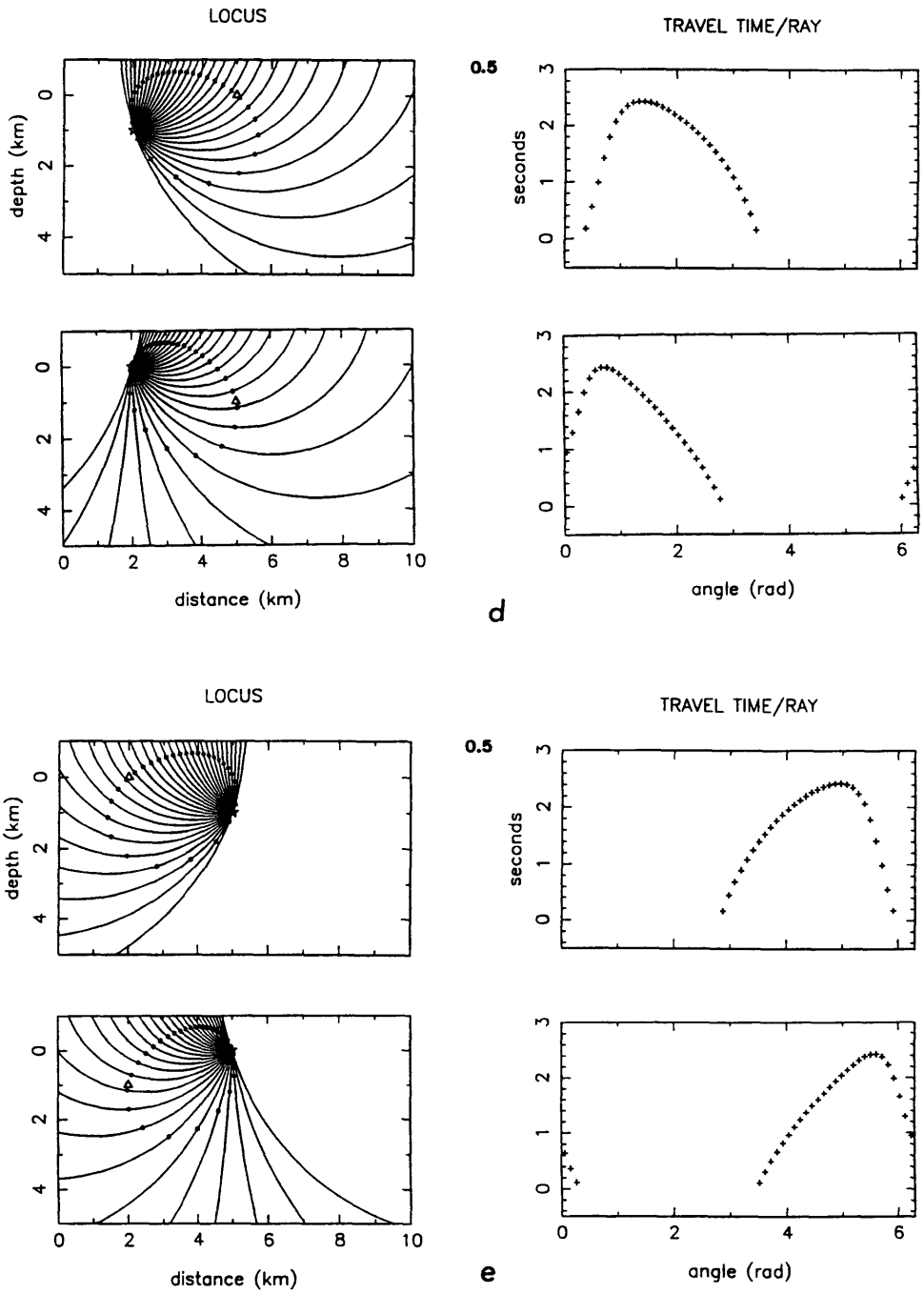

FIGURE 4.3 (d), (e) source at the sides of the receiver.

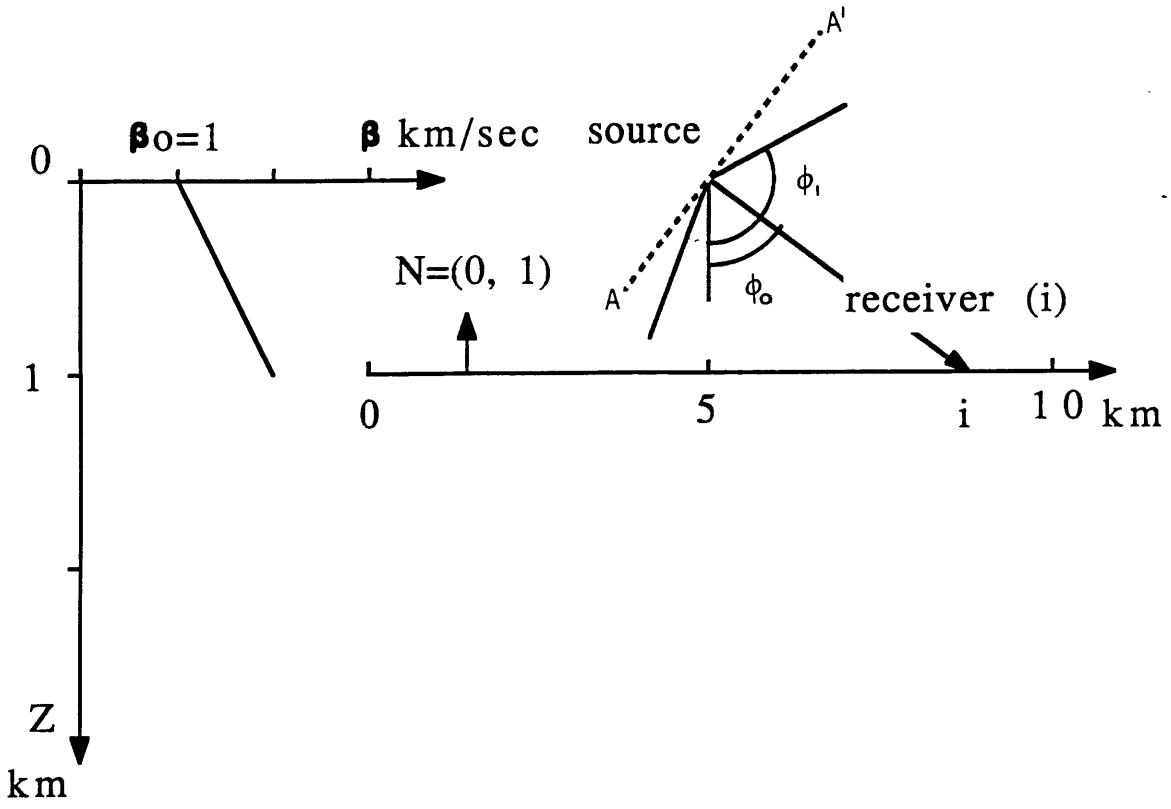

FIGURE 4.4 Geometry of the test problem (section 4.3). The superposition of beams with take-off angles between ϕ_0 and ϕ_1 is carried out for each observation point i.

The results for the nearly homogeneous case mentioned above are shown in Figure 4.5, (a) for the exact solution and (b) for the Gaussian beam, where the source is located at $x_0 = 5$ km, $z_0 = 0$ km, and the observation points are located along the line $z = 1$ km. Frequency is 1 hz. In (b) we have used 100 beams, each with parameter $L_0 = 0.3$ km$^{-1/2}$ and radiation angle range $\Omega = 180^0$. The amplitude factors 50 for displacement and 10 for traction in the figure are used for the purpose of plotting only (the fields are not normalized); they do not play any role in the computations. Note that the agreement between the analytical and Gaussiam beam solutions for both displacement and traction acting on the surface with normal $\hat{n} = (0, 1)$ (and their respective phases) is satisfactory. The agreement can be improved by adjusting the initial beam parameter L_0, however this adjustment will not affect the final solution of a particular problem using the boundary integral-Gaussian beam method, as demonstrated in section 2.4. We observe that for both analytical and Gaussian beam solutions, the phase of either displacement or traction wavefields varies smoothly and nonlinearly with distance. The separation distance between two points whose wavefield is 2π out of phase (or "jump" interval) tends to decrease from points in the near field towards those in the far-field, down to a constant value proportional to the separation distance between observation points. This is barely observed within the spatial range considered for Figure 4.5, because the wavefront of the cylindrical wave originated at the point(line) source becomes planar at the far-field.

In Figure 4.6 (a), (b) we have computed the cases in which the values of the gradient are 0.1 sec^{-1}, 0.5 sec^{-1} and 1.0 sec^{-1} respectively, keeping all other parameters the same as for Figure 4.5 (see their corresponding ray

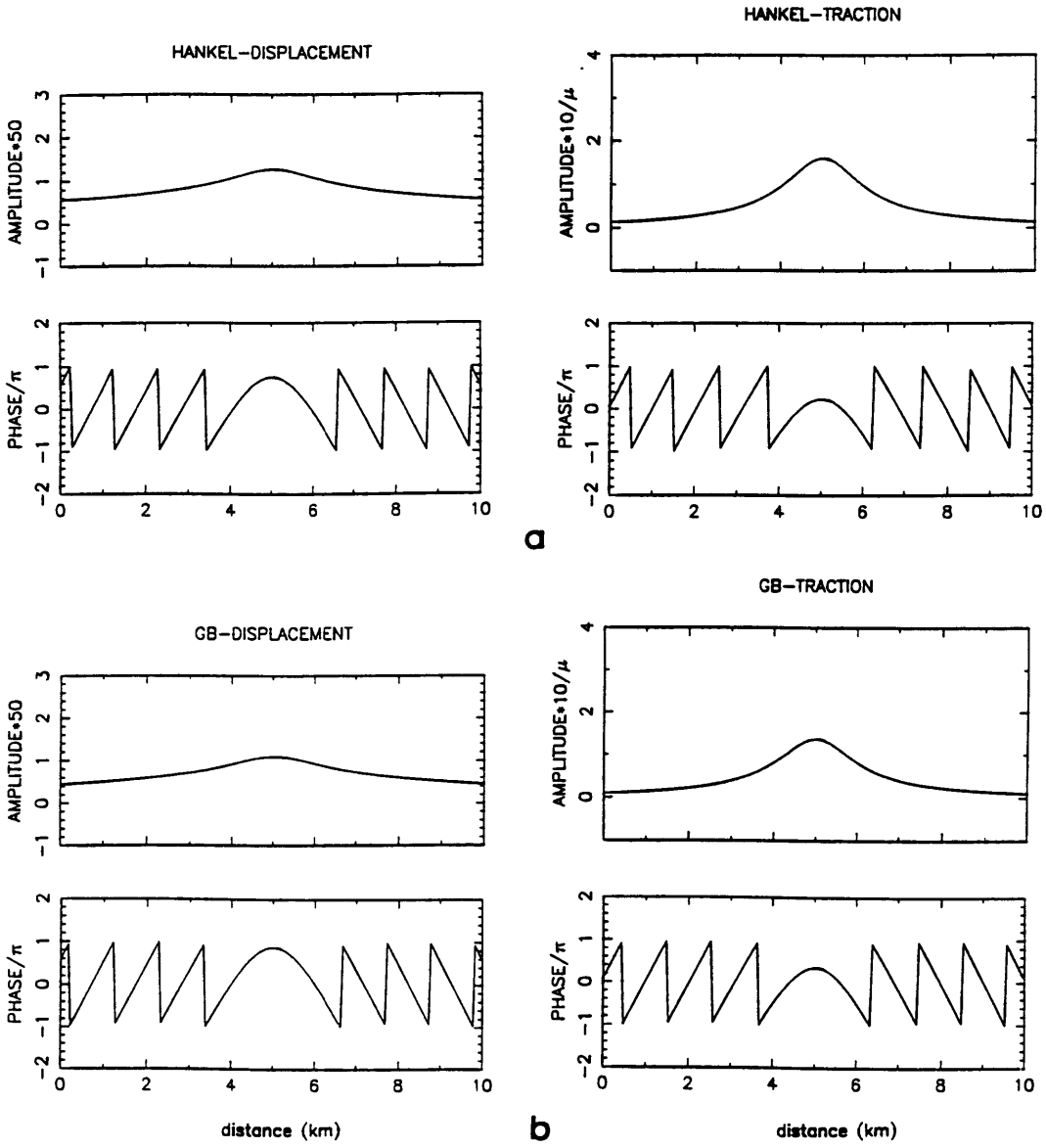

FIGURE 4.5 Displacement and traction amplitude distribution along the observation line depicted in Figure 2.4 for homogeneous media, computed (a) using exact solution (Hankel function), (b) by superposition of Gaussian beams, using INGREEN with $g = 0.001$ sec^{-1}. The phase of each amplitude distribution is plotted below.

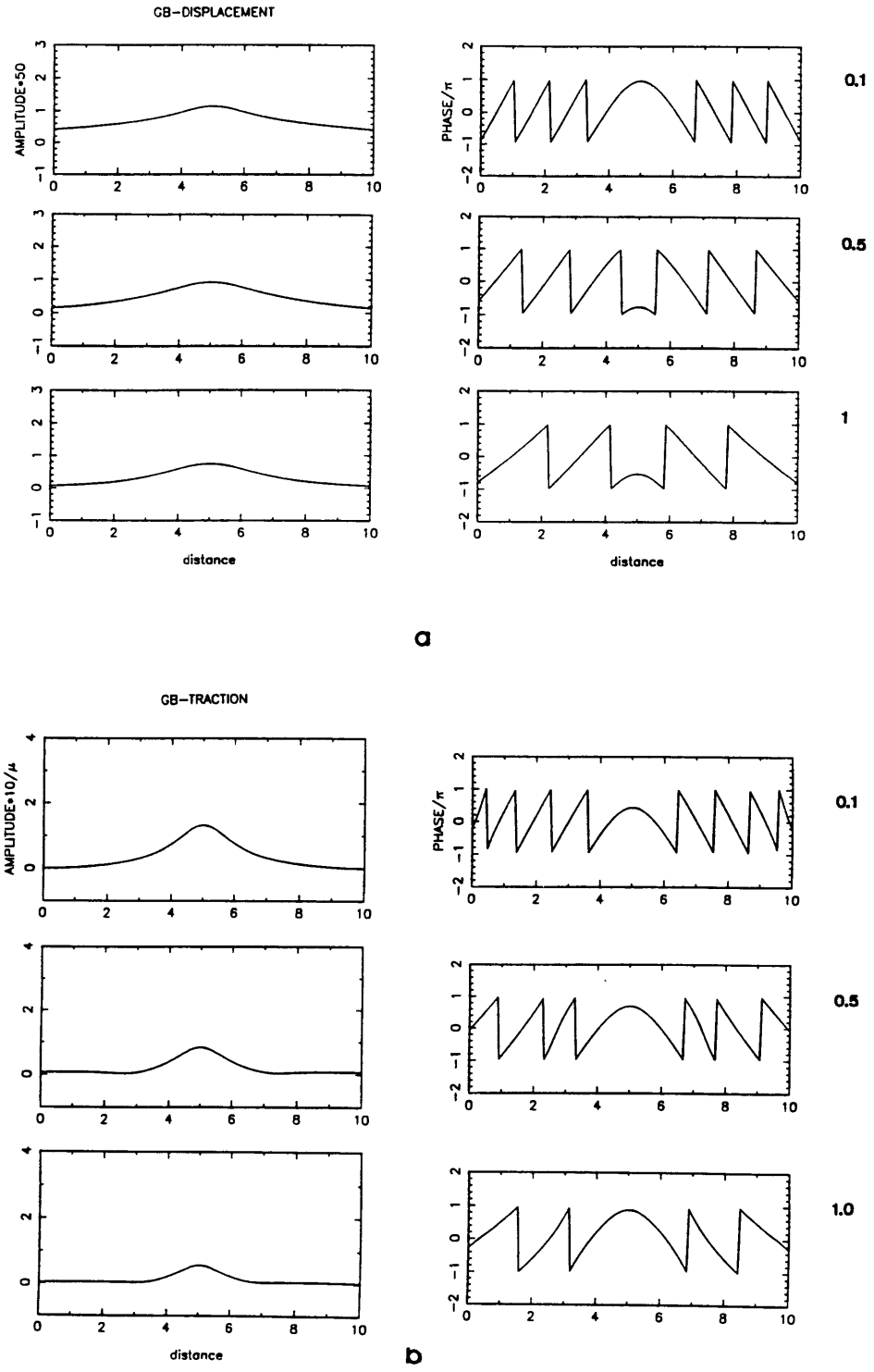

FIGURE 4.6 (a) displacement amplitude and phase distribution along the observation line depicted in Figure 2.4 for inhomogeneous media, computed using INGREEN. (b) Traction amplitude and phase distribution along the same observation line as in (a).

paths, locus and travel-times at selected observation points in Figure 4.3). (a) corresponds to the displacement field and phase for those three values of g; and similarly (b) corresponds to the traction field. For $g = 0.1$ sec^{-1} the results are only slightly different than those for homogeneous media, but for $g = 0.5$ and 1.0 sec^{-1} the amplitudes become smaller and somewhat localized. Also the phase becomes more non-linear and with less number of 2π jumps as g increases, which reflects the effect of shorter travel times of faster waves than for the homogeneous case.

Next we compute the case in which the source is at $x_0 = 5$ km, $z_0 = 1$ km, and the observation points are located along the line $z = 0$ km, i.e. the observation line is 1 km above the source point rather than below as in the case of Figure 4.6. The ray paths, locus and travel time for selected observation points were already shown in Figure 4.3. Results are shown in Figure 4.7 (a) for displacement amplitude and its phase, and (b) for traction amplitude and its phase. Comparing each case with their counterpart in Figure 4.6, we observe that the amplitudes become larger for both displacement and traction as g increases. This is due to the focusing effect as obvious from the pattern of rays shown in Figure 4.3. On the contrary, for the case shown in Figure 4.6 the defocusing effect tends to lower the amplitude with increasing g. The phase of the displacement field is exactly the same for both cases, because travel-times are equal. The phase of traction, however, is different, because of the difference in wavefront.

Thus, our subroutine INGREEN computes Green's function for a vertically heterogeneous media with linearly increasing velocity with depth by the superposition of Gaussian beams. Considering 100 beams in the superposition, the computational time (in terms of CPU time) is about 30%

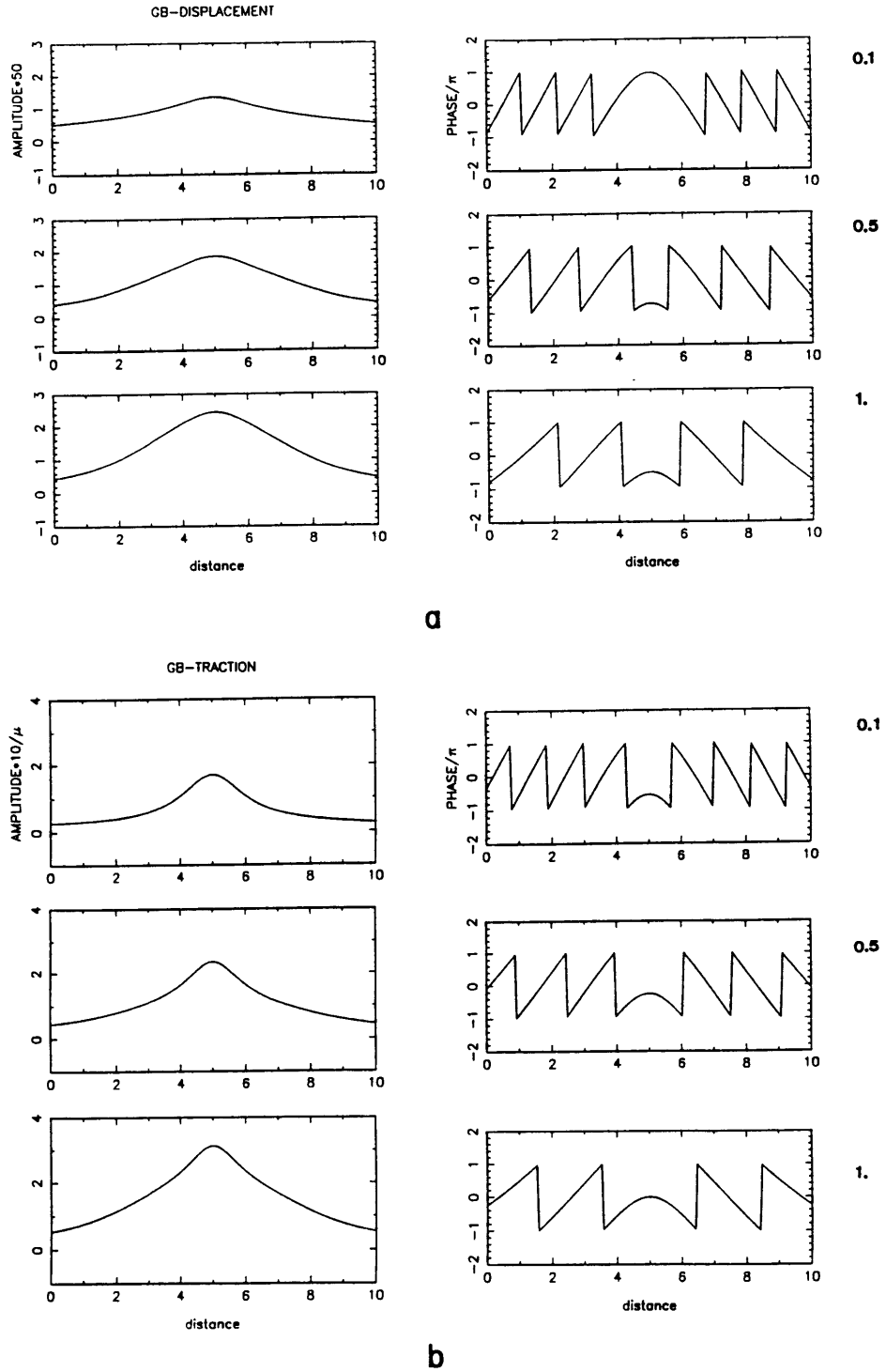

FIGURE 4.7 In this case, the observation line depicted in Figure 2.4 is 1 km above the source. (a) corresponds to the displacement amplitude and phase distribution along the observation line for inhomogeneous media, using INGREEN. (b) Traction amplitude distribution and its phase along the same observation line.

larger than the corresponding Hankel function for the homogeneous case, using the same computer. Green's function for displacement and traction calculated by INGREEN will be used in the boundary integral method as described in section 2.2 (e.g equations 2.4 and 2.7) to solve the problems of wave scattering by mountains and valleys, in the next two sections.

4.5 Inhomogenous mountain

In this section we compute the scattering of plane SH waves in vertically inhomogeneous 2-D media whose free-surface topography is a cosine shaped ridge (Figure 4.8 (a)). The vertical position z (positive down) are measured with respect to $z_0 = 0$ at the top of the ridge. The height and half-width of the ridge are h and a respectively, and the shear wave velocity is β_0 at the top of the ridge and β_h, at the bottom, thus the gradient is $g = (\beta_h - \beta_0)/h$. The density is assumed to be uniform. The same gradient continues to the depth $D = 5a$ i.e. $4a$ below the bottom of the ridge. At that depth we place a horizontal interface, below which the medium is homogeneous, with the same velocity as the inhomogeneous medium at the interface. We assume that the density below the interface is also uniform and equal to that above the interface. The aim of this "transparent" interface is to model a plane SH wave incident upon the ridge in the inhomogeneous medium. Since the wavelength λ of the incident wave varies as it travels in the inhomogeneous medium, we take its value at the bottom of the ridge, λ_h, to define the non-dimensional frequency $\eta = 2a/\lambda_h$, in order to study the response of the mountain for several values of η, as we did in section 2.4 for the homogeneous case. That is, if we wanted to study the case of $\lambda_h = a$, the incident wavelength in the lower (homogeneous) medium has to be $\lambda_D = (\beta_D/\beta_h)a$. We define the local wavelength λ_z at

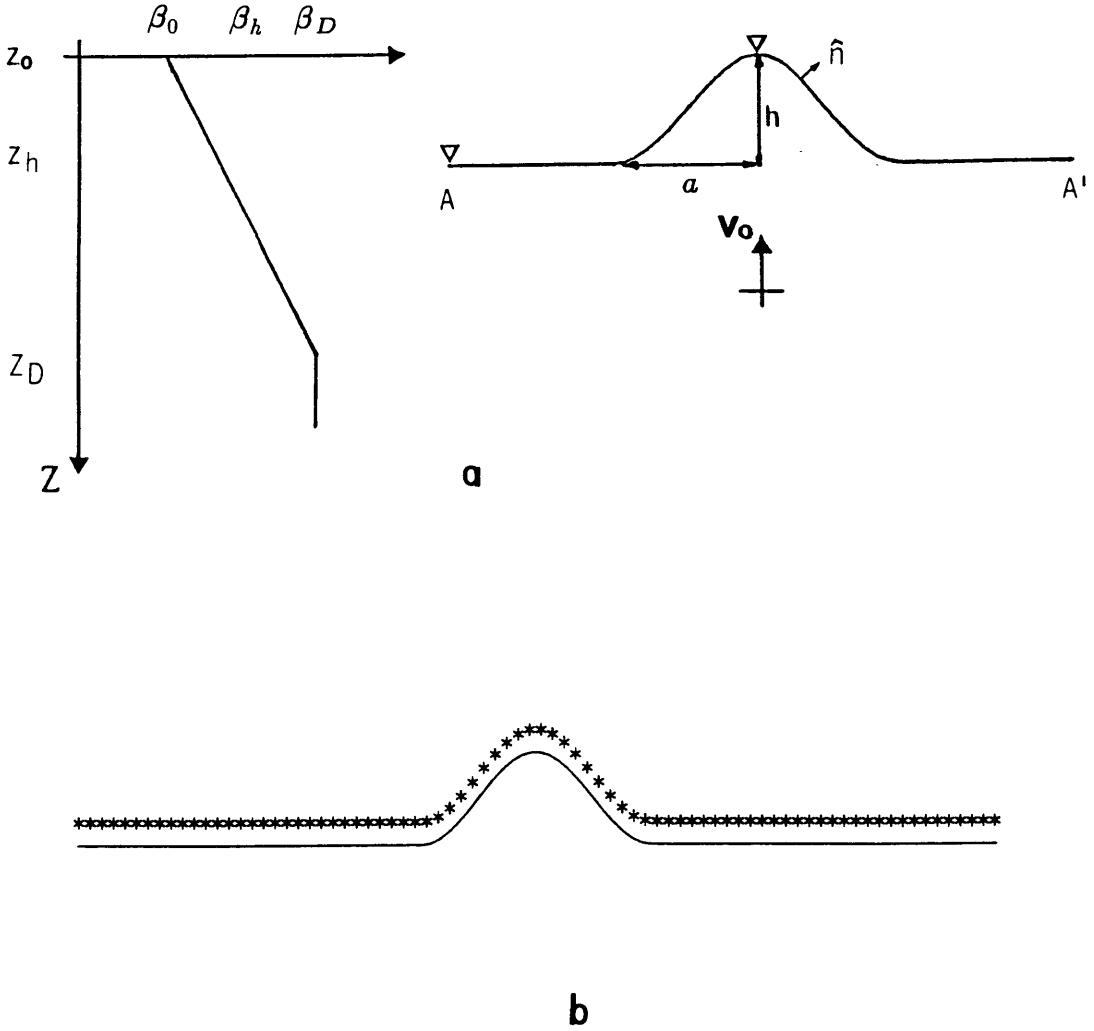

FIGURE 4.8 (a) Shear wave velocity distribution with depth for the case of mountain. (b) wave source distribution along the topography to represent the scattered field.

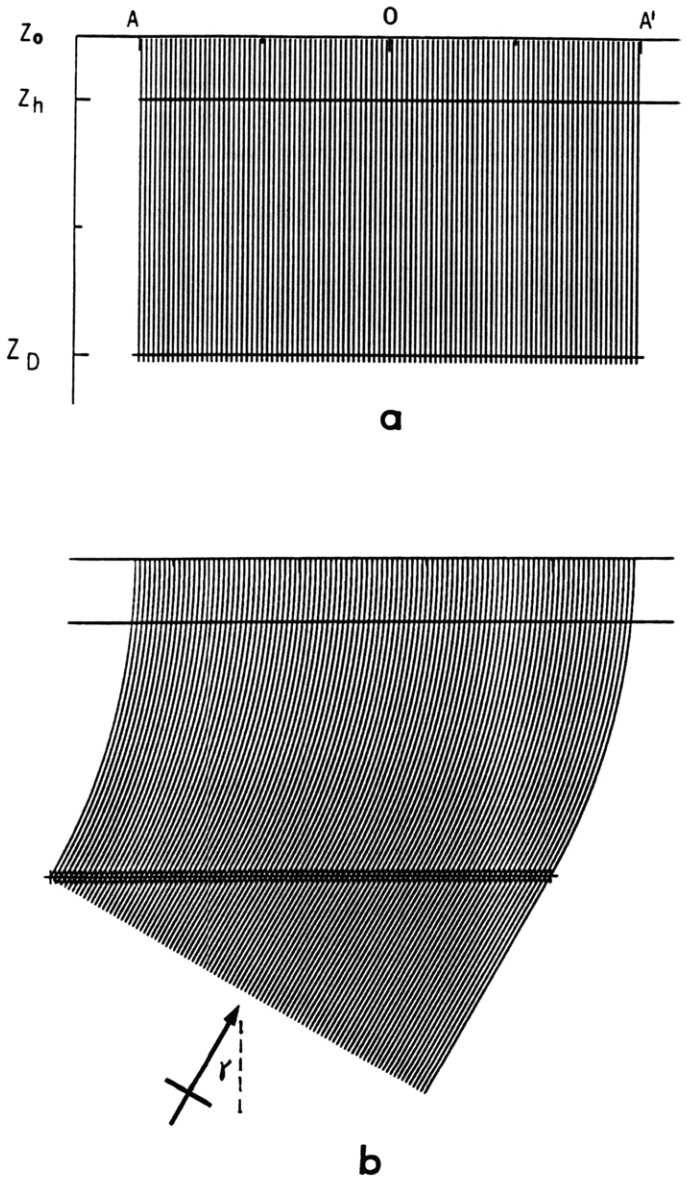

FIGURE 4.9 The incident plane wave for the mountain problem. The mountain range is between A and A', centered at O, its top is at z_0 and its bottom at z_h. The field due to the incident wave is computed by Gaussian beams attached to the rays shown in this figure, considering that the mountain is at the top of an inhomogeneous layer over a homogeneous half-space. The flat interface between both media is at z_D. The incident plane wave in the homogeneous media is expanded in Gaussian beams and each is continued into the inhomogeneous layer, (a) for vertical incidence and (b) for inclined incidence.

an arbitrary depth z in the inhomogenous medium as $\lambda_z = (\beta_z/\beta_h)\lambda_h$.

With regards to the distribution of sources along the free-surface topography, as mentioned in section 2.4, we need at least four point(line) sources per wavelength in order to satisfy the boundary conditions at any point on the surface. This means that the distribution of sources would be denser towards the top of the ridge. We will use a regular distribution by selecting an equal interval between any pair of adjascent sources as $\delta_s = \lambda_0/4$, where λ_0 is the wavelength at the top of the ridge. Since λ_0 is the smallest wavelength, the compliance of the boundary conditions everywhere is guaranteed.

4.5.1 Ground motion in frequency domain

We have distributed 80 sources along the surface topography of the mountain (marked by '*' in Figure 4.8 (b)), which extends from $-4a$ to $4a$. The ridge is centered at $x = 0$. This choice of distance range is to avoid the error introduced by truncating the source distribution at the edges of the mountain. Here, these sources are located at a distance $0.9a$ above the mountain. Since the Gaussian beam Green's function has no singularity at the source point, we can put them exactly on the surface. We avoid that, however, because of a slightly unstable solution. The expression for the total field is given by equation (2.4), for which $G(\vec{r}_P|\vec{r}_{Q_j};\omega)$ (refer to section 2.2 for definition of the variables) is computed by INGREEN, using 100 beams with initial beam parameter $L_0 = 0.2a$ (with units of square root of length) and radiation angel $\Omega = 180^0$, i.e., with a take-off angle interval of 1.8^0. The value of L_0 is chosen from the definition $L_0 = (\pi/\lambda)^{1/2} L_M$, where L_M is the half-beam width (see section 2.3), assuming that $\lambda = \lambda_h = a$ and that $L_M = 0.1a$. The incident wave is computed also by superposition

of Gaussian beams, in the following way. We consider first a plane wave $\exp(ik_0 x + i\nu_0 z)$ incident with an angle γ in the lower medium , where $k_0 = (\omega/\beta_D)\sin\gamma$ and $\nu_0 = (\omega/\beta_D)\cos\gamma$. γ is measured with respect to the vertical, counterclockwise. This plane wave is expanded into parallel Gaussian beams, according to Ĉervený (1982), then each beam is continued into the inhomogeneous medium individually, as shown in Figure 4.9 (a) and (b), for vertical and inclined incidence. The travel time from the interface to the observation line $z = h$ is the same for all rays, so that the phase difference for non-vertical incidence will be due only to delay in the lower homogeneous medium. Finally, the wavefield at each observation point on the surface topography is computed by summing the contribution of each beam. This process is well known and accurate (Nowack and Aki, 1984) and therefore will not be discussed here. Let us just mention that we have constructed the incident wave using a modified version of INGREEN, so that we can also get tractions acting on any surface.

Let us first describe the amplitude distribution of the ground motion at the free-surface in frequency domain for various values of the velocity gradient g, the non-dimensional frequency $\eta = 2a/\beta_h$ and the "aspect ratio" h/a of mountain. In examples that follow, a and β_h are fixed parameters, h is given in terms of a and aspect ratio, and β_0 is given in terms of β_h and g. The amplitude of the ground motion is normalized to the amplitude of the response of a homogeneous with velocity β_h half-space without the ridge. In Figure 4.10 the ground motion amplitude is shown (a) for $\beta_0 = \beta_h/1.001$, and (b) for $\beta_0 = \beta_h/2$ The aspect ratio is 0.4 and $\eta = 2a/\lambda_h = 1$, both chosen to be the same as in Bouchon (1973). Since $h = 0.4a$, $g = 0.0025\beta_0/a$ for (a) and $g = 2.5\beta_0/a$ for (b). The fractional residual traction, defined

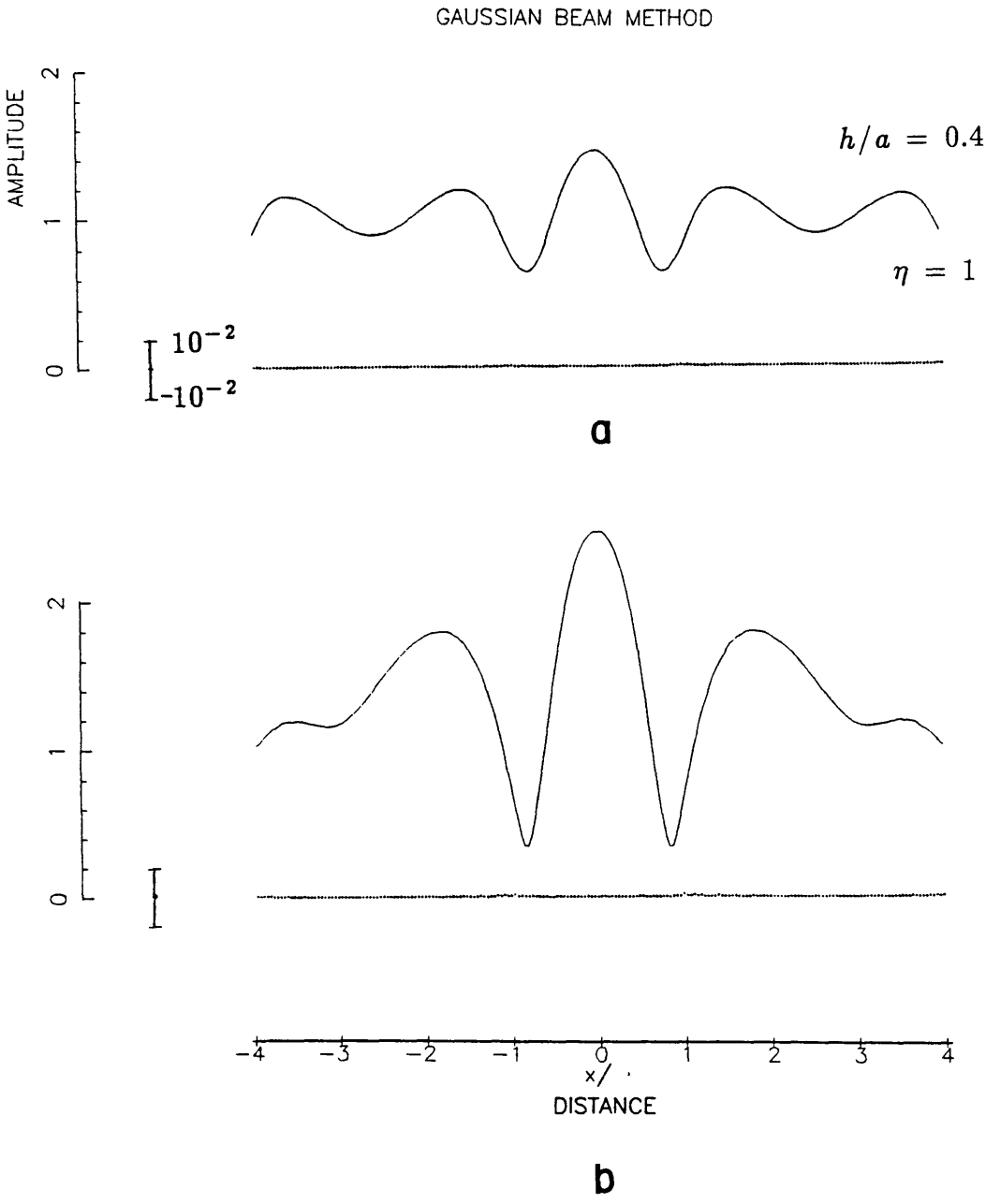

FIGURE 4.10 Response of the ridge (a) homogeneous case; (b) inhomogeneous, when the velocity at the top of the ridge is 0.5 times the velocity at the bottom, or $g = 1/h$ sec^{-1}. Aspect ratio $h/a = 0.4$, and the wavelength is equal to the width of the ridge. The dotted line in the figure below is the fractional residual traction.

as the total traction at the free-surface divided by the traction due to the incident wave, is shown by the dotted line below the curve for ground motion amplitude, to demonstrate the compliancy of the boundary conditions. We observe that the ground motion is in general amplified in comparison to that in (a), nearly twice as large at the top of the ridge. In both cases the residual traction is of the order of 10^{-3}. In Figure 4.11 (a) and (b) we computed the similar cases to those in Figure 4.10 (a) and (b) respectively, but for $h/a = 0.8$ and $\eta = 0.5$, so that $g = 0.001\beta_0/0.8a = 0.00125\beta_0/a$ for (a) and $g = \beta_0/0.8a = 1.25\beta_0/a$ for (b). The amplification effect is also observed here, although with a factor $\simeq 1.6$. Residual tractions are of the order of 10^{-2} in both (a) and (b), and we note that in (b) these are slightly spread towards the slopes of the ridge, where the space interval between the distributed sources is larger than those on the flat and top parts of the mountain. The residuals can be reduced by increasing the number of sources along the slope. Nevertheless, for the results shown in (b) our choice of sources is enough to guarantee their accuracy.

Final example for assessing the effects of velocity gradient for the case of $\beta_0 = \beta_h/2$ and aspect ratio $h/a = 1$ is shown in Figure 4.12; for non-dimensional frequency $\eta = 2$. Comparing it with the corresponding homogeneous case shown Figure 2.10 (c), the amplification on the top of the ridge is a factor of 1.5 this case.

Now, we would like to make a parameter sensitivity study of the effects of the ridge's shape, velocity gradient and incident wave frequency on the ground motion response along the mountain topography. First, we fix the values of the aspect ratio, β_h and velocity gradient, and calculate the ground response for several values of η. Then the process is repeated for different

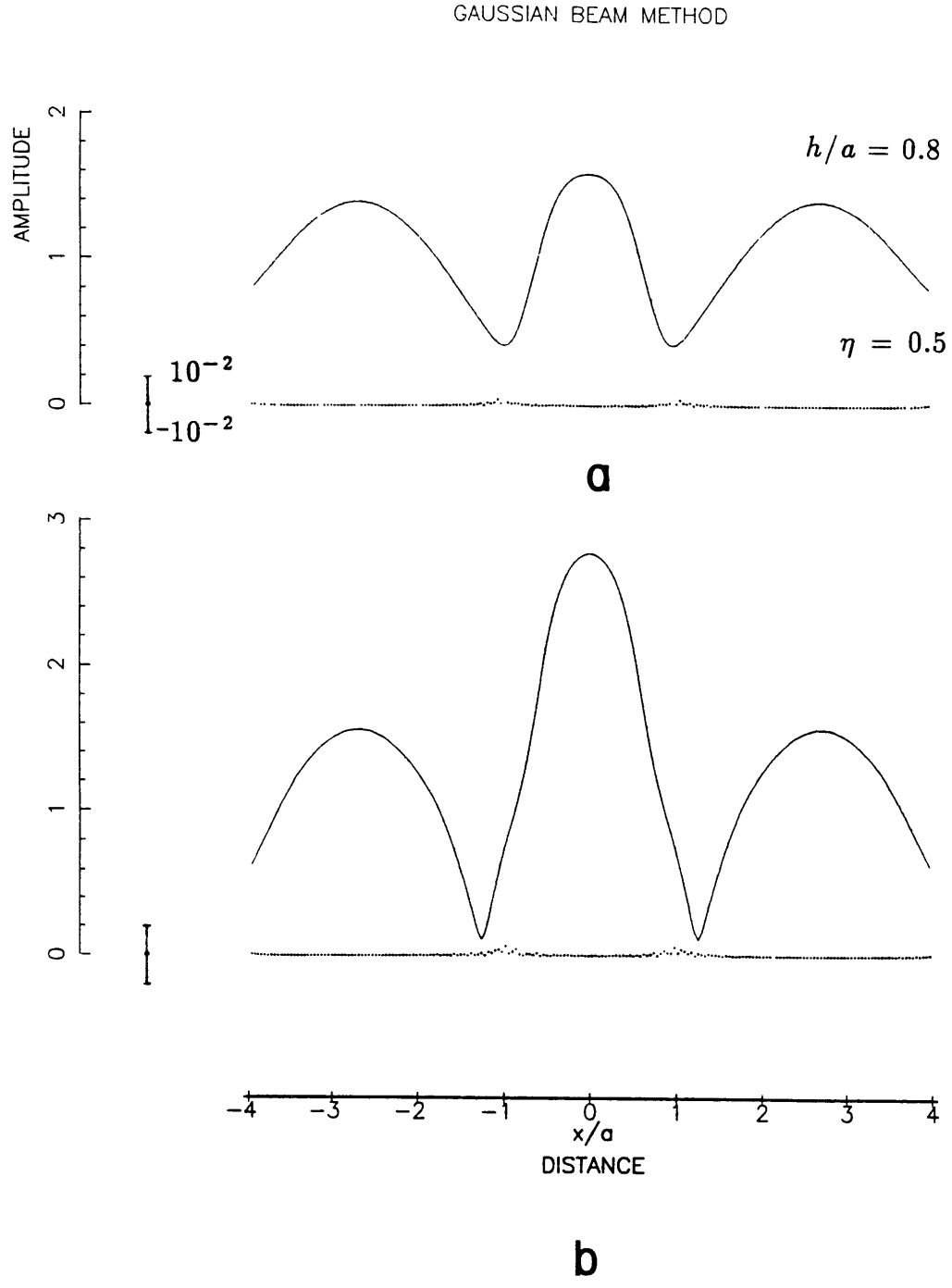

FIGURE 4.11 Same as for Figure 4.10, but for aspect ratio $h/a = 0.8$.

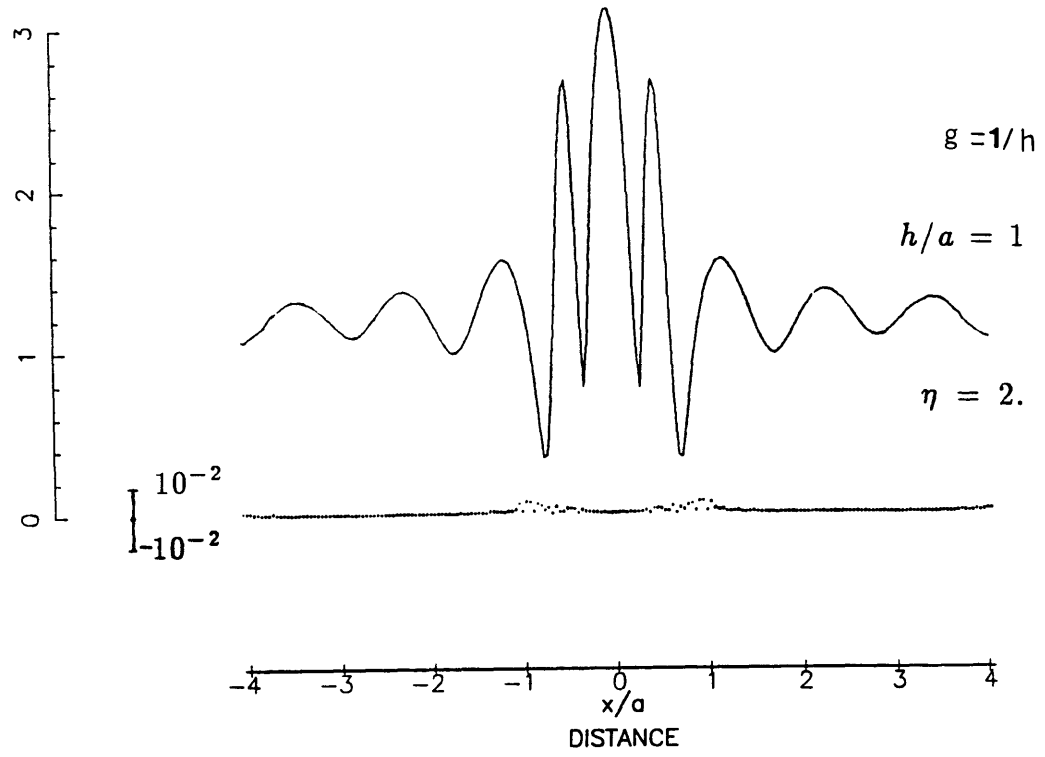

FIGURE 4.12 Steep ridge, $h/a = 1$, velocity on the top of the ridge is 0.5 of that at the bottom, and wavelength at the bottom is equal to a.

values of aspect ratio and velocity gradient, keeping β_h the same. Results of the amplification distribution of the ground motion are shown in Figures 4.13 (a)-(e), and 4.14 (a)-(c), for η up to 4, or $\lambda_h = a/2$. In all these figures we observe a systematic amplification at the top of the ridge for all non-dimensional frequencies, except for $\eta = 0.25$ (or $\lambda_h = 8a$). When the gradient is $\simeq 0$ and the aspect ratio is fixed, we obtained the well known result that the amplification factor at the top of the ridge increases with η (Bouchon 1973, Bard 1982). In fact, note in Figures 4.13 (a) and 4.14 (a) that our results agree with those of Bouchon (1973) for the corresponding case of $\eta = 1$ and $\eta = 0.5$, respectively. From our results, we estimate that the amplification factor in the homogeneous case is close to 3 for $\eta = 2$. When the velocity gradient is introduced, for fixed aspect ratio, η and β_h, the ground motion is amplified in general, and particularly strongly at observation points within the ridge region. This can be observed, for instance, by comparing the results in Figure 4.13 for the same η. Taking $\eta = 2$ as example, we estimate that the amplification factors at the top of the ridge for $\beta_0 = (2/3)\beta_h$ and $\beta_0 = 0.5\beta_h$ are about two and three times larger than that for the homogeneous case, respectively (or four and six times larger, respectively, than the response of the half-space with neither ridge nor velocity gradient). This result seems to be robust, independent of the aspect ratio up to 0.8, as we observe by comparing (a) and (b) of Figure 4.14. A similar conclusion can be obtained by taking as example other values of η. In addition we observe in (a), (b) and (d) of Figure 4.13 that the amplitude outside the ridge appears to vary less as the gradient increases. Finally, the amplification/deamplification pattern observed along the slopes of the ridge appears not to be affected by either the velocity

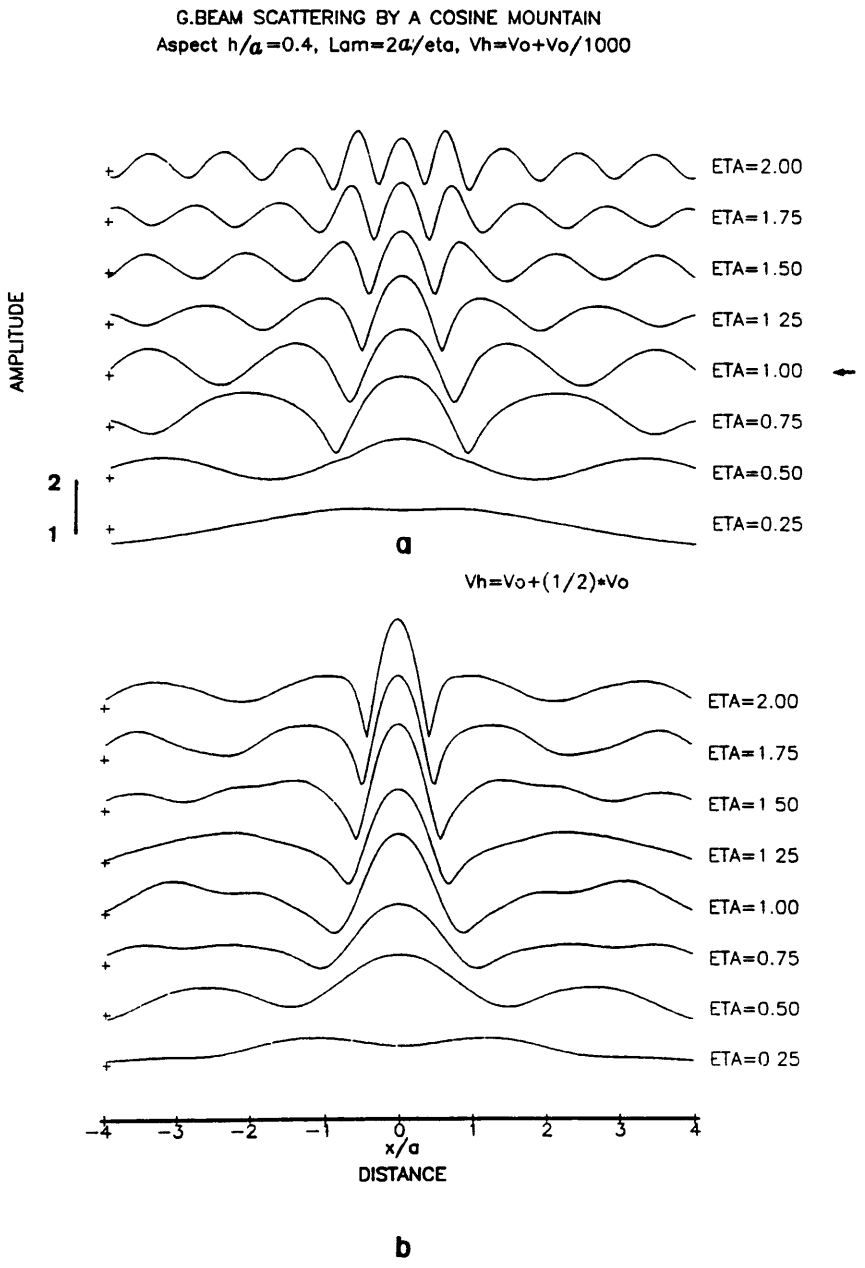

FiGURE 4.13 (a) The response of the mountain with aspect ratio $h/a = 0.4$, for the homogeneous case, and for several values of $\eta = 2a/\lambda$. The arrow points the similar solution obtained by Bouchon (1973). (b) inhomogeneous case, velocity on the top of the ridge in 2/3 of that on the bottom.

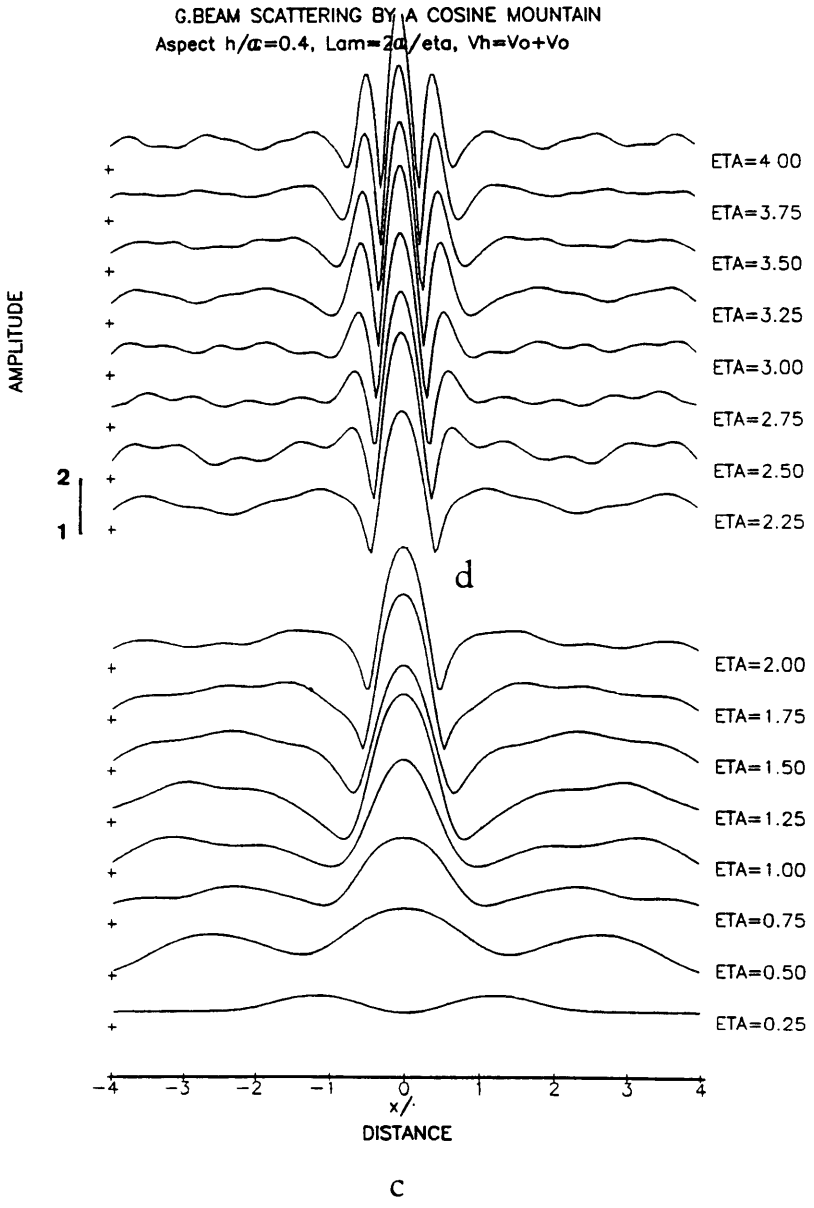

FIGURE 4.13 (c) the same ridge as in (a), but with velocity on the top equal to 1/2 of that on the bottom. (d) same as in (c) but for larger η's (high frequency).

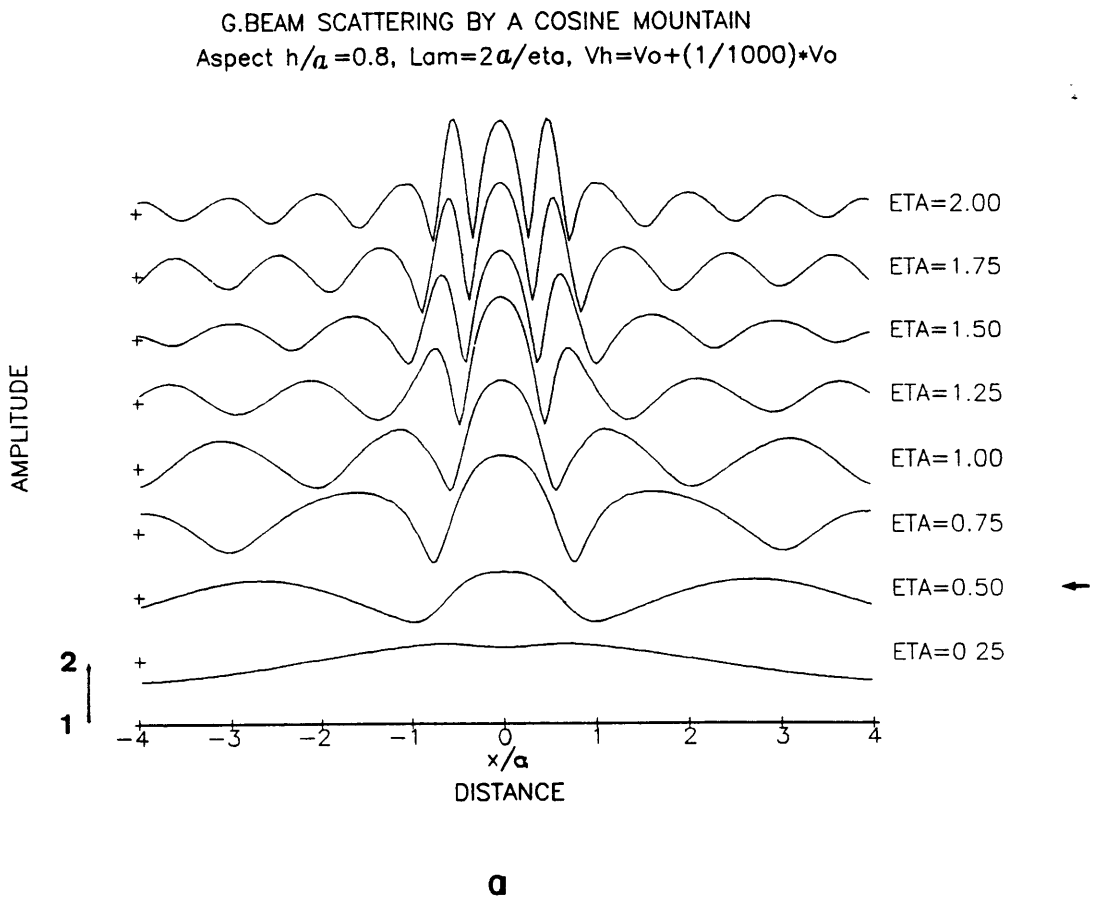

FIGURE 4.14 The aspect ratio $h/a = 0.8$, (a) homogeneous. The arrow points the solution for similar problem obtained by Bouchon (1973).

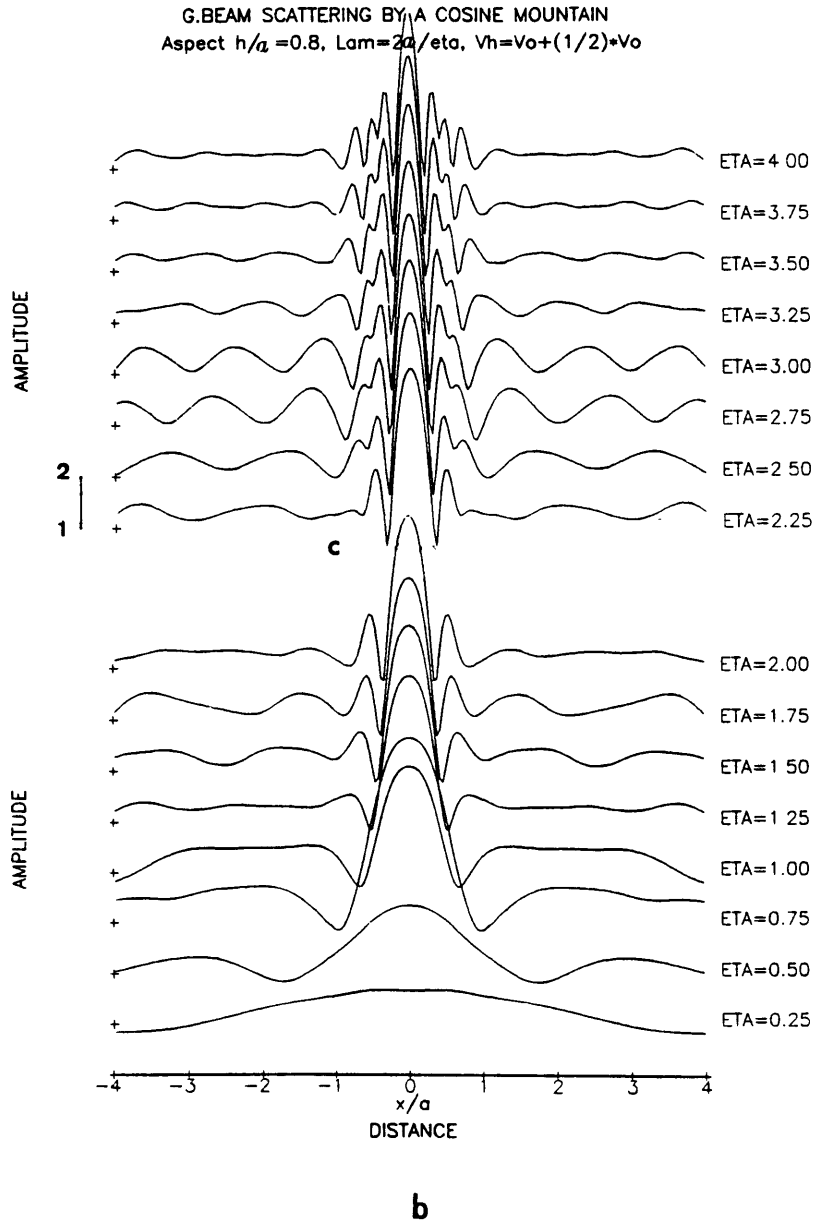

FIGURE 4.14 (b), (c) correspond to the inhomogeneous case, with velocity at the top of the ridge equal to 2/3 of that in the bottom.

gradient or aspect ratio, but rather by the non-dimensional frequency η.

We conclude that an intensive amplification occurs for the ground motion at the top of a ridge when the velocity increases with depth. For example, the amplification factor at the top of the ridge, which is about two for the homogeneous case when the wavelength of the incident wave is comparable with the half-width of the ridge, was found to be close to seven when the velocity of the shear wave at the bottom of the ridge was twice the velocity at its top. This intensive effect of the ridge with a velocity gradient depends on the non-dimensional frequency, but is not strongly dependent on the aspect ratio of the ridge.

4.5.2 Ground motion in time domain

Time domain synthetic seismograms are obtained by inverting Fourier transform evaluated at 100 non-dimensional frequencies $\eta = 2a/\lambda_h$, and using Ricker wavelet source time function, as it was described in Chapter III (section 3.4). Refering to Figure 4.8, the seismograms are synthesized at 100 stations covering a distance $8a$ along the free-surface topography (AA' in the figure), at equal intervals. Their duration is given in the unit of time needed by the wave to propagate the ridge half-width a with velocity β_0, i.e. the velocity at the top of the ridge. The characteristic wavelength of Ricker wavelet λ_c is selected to be equal to a.

Results for a ridge whose aspect ratio is 0.4 are given in Figure 4.15, for $\lambda_c = a$ and for $g = 0$, 0.25, 0.5 and 1 (unit of time)$^{-1}$, with $\beta_0 = 1$ unit of distance/time. The velocity β_h at the bottom of the ridge is therefore $\beta_h = 1. + 0.4ga$. We should mention that the origin times of these four seismograms sections have been adjusted for plotting, in such a way that the arrival of the incident wave outside the ridge region be simultaneous.

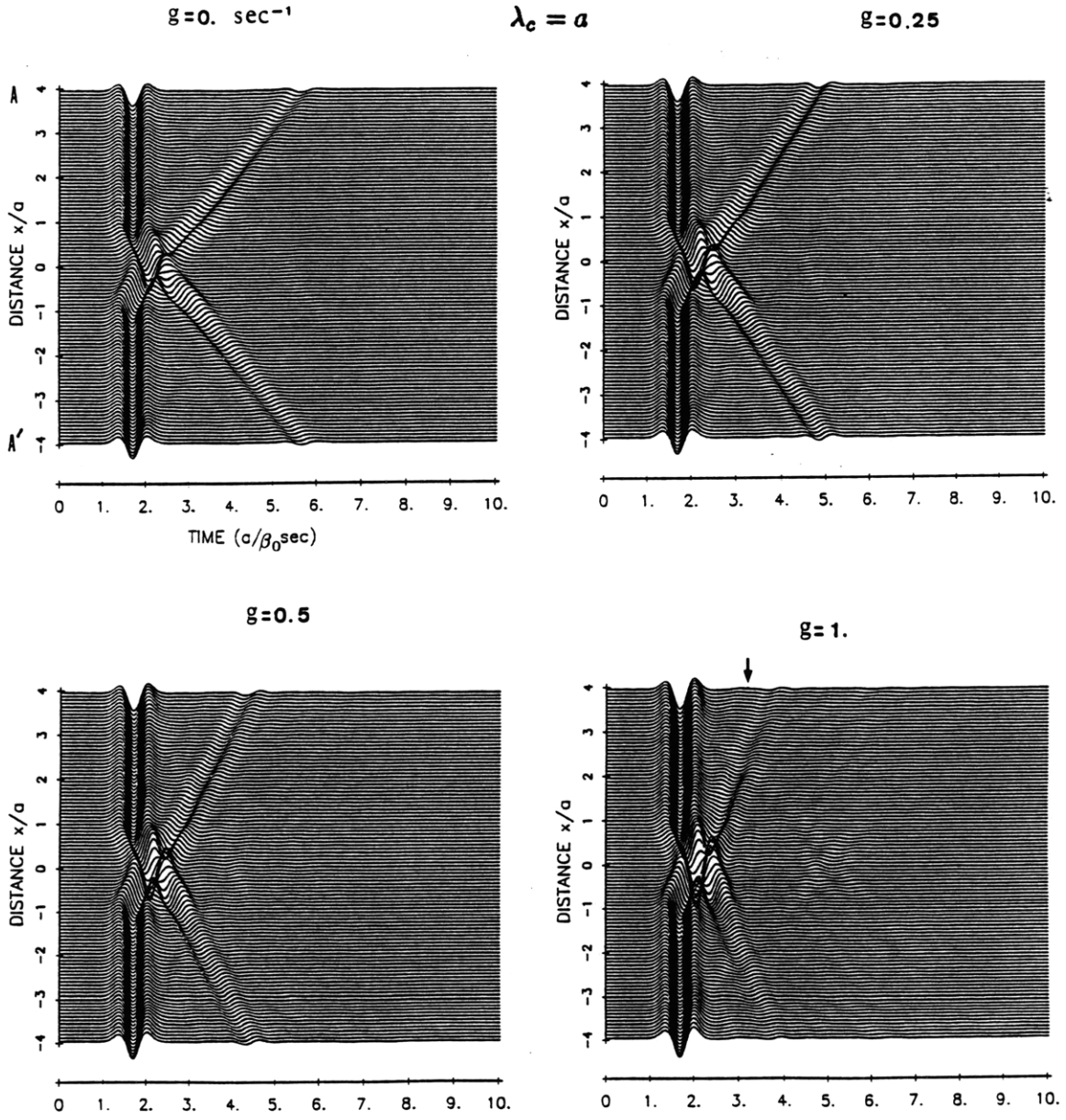

FIGURE 4.15 Synthetic seismograms for a ridge of 0.4 aspect ratio. $g = 0$ ($\sec^{-1}$) corresponds to the homogeneous case. $g = 0.25$ ($\sec^{-1}$) corresponds to velocity at the bottom equal to 1.25 times that at the top, similarly $g = 0.5$ and $g = 1$ ($\sec^{-1}$) to 1.5 and 2 times the velocity at the bottom, respectively.

We observe two dominant features in these seismogram sections, the first is the amplification of the waveform at stations close to the top of the ridge, being largest at the top; and the second is the wave scattered by the ridge, propagating outwards along the free-surface, without significant attenuation.

Regarding the first, the amplification of the waveforms observed for the homogeneous case has been reported by several authors, e.g. Bard (1982), who obtained waveforms similar to those shown in our figure, using the Aki-Larner (1970) method. Bard attributes this amplification to constructive interference of waves inside the ridge. For the inhomogeneous case, it appears that the gradient only enhances this amplification without affecting significatively the shape of the waveforms. As observed for the ground motion in frequency domain, there is also a systematic amplification with increasing velocity gradient g. The amplification effect due to g is also observed in Figure 4.16, where $h/a = 1$, keeping $\lambda_c = a$. (a) is for homogeneous (b) for $g = 1$ (unit of time)$^{-1}$ (origin time is not adjusted in this case). Although the amplitude of the waveform observed at the top of the ridge is larger for the inhomogeneous case than for the homogeneous by a factor of about 1.4, this amplification factor appears to be smaller than that for the corresponding cases for $h/a = 0.4$ shown in Figure 4.15., which we esimate $\simeq 2$. We observe also that the amplification at stations on the slopes of the ridge is relatively small compared with that on the top, in all cases. This characteristic of the motion on the flanks of mountais has been reported in some observations (e.g.Davis and West 1973) and in studies using theoretical modeling, considering homogeneous media (Bard 1982).

The second feature mentioned above, that is, the scattered wave by

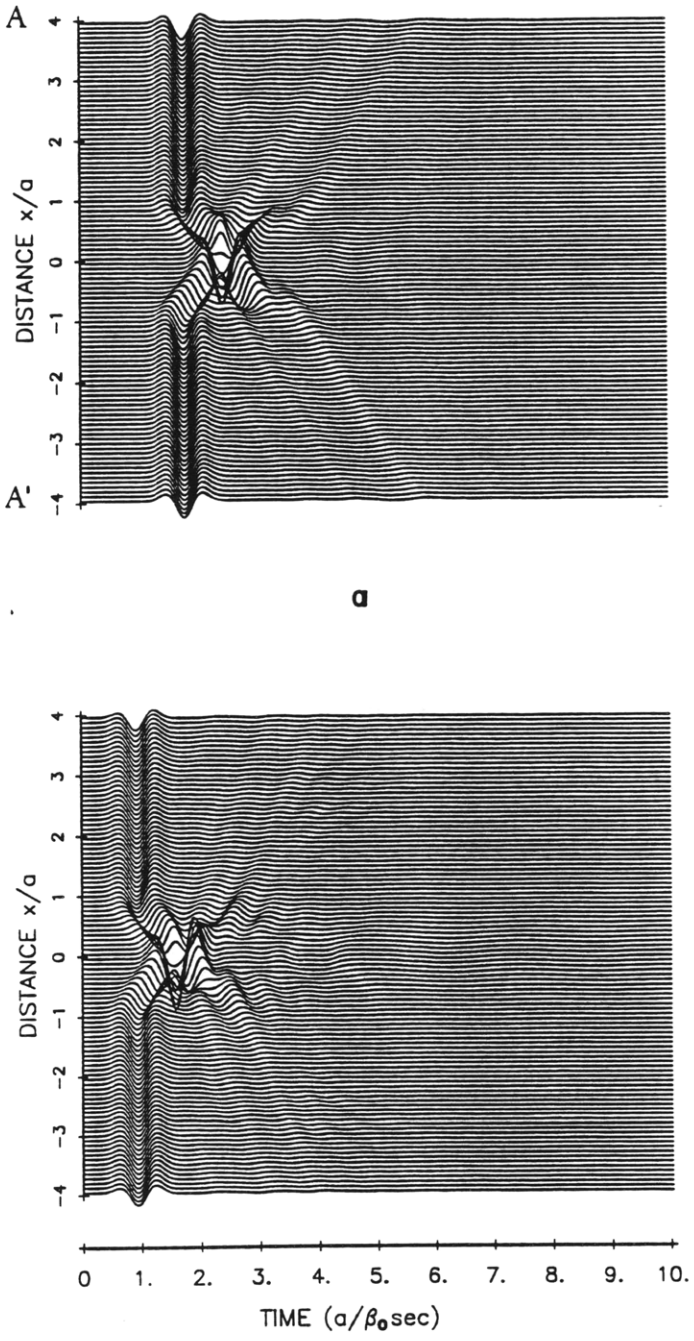

FIGURE 4.16 Synthetic seismograms for a ridge of aspect ratio equal to 1, for (a) $g = 0$ sec^{-1}, and (b) $g = 1$ sec^{-1}, $\beta_0 = 1$ unit distance/time.

the ridge, is examined more closely next. Due to the complexity of the waveform at stations within the ridge region, we plot the seismograms of only 17 stations distributed at equal intervals, five of them on the ridge in such a way that one is on the top and four on the flanks. We choose the seismograms of Figure 4.15 corresponding to $h/a = 0.4$, $\beta_0 = 1$ unit of distance/time, and $g = 0$ and 1 (unit of time)$^{-1}$, shown in Figure 4.17 (a) and (b) respectively. The total duration has been increased to $16a/\beta_0$ for both. The scattered wave appears to be originated by reflection of the incident SH wave at a certain point R, and subsequent diffraction at point S of the ridge topography, as illustrated by the ray diagram below each seismogram section. Thereafter, the wave propagates outward along the free-surface. Note that points R and S represent any points in the ridge where this phenomenon occur. The velocity of this wave, measured from the seismogram section, is the same as the SH velocity at the bottom of the ridge. We demonstrate this by measuring in Figure 4.17 (a) the velocity of the scattered wave from the slope of its trace within the time interval of about $1.7a/\beta_0$, marked by two arrows, i.e., $2.9a/(1.7a/\beta_0 \times 1.6) \simeq 1$unit of distance/time. Similarly, for the case shown in Figure 4.17 (b) the velocity of the scattered wave is $2.9a/(0.9a/\beta_0 \times 1.6) \simeq 2.$, where $0.9a$ is the time interval marked by two arrows. We conclude that the scattered wave is an SH (body) wave propagating along the free-surface. In both cases (a) and (b) the amplitude of the scattered SH wave is $\simeq 1/4$ of the amplitude of the incident wave, keeping the same waveform, and attenuating slightly away from the center of the ridge. We observe that there is a constructive interference between the incident and the scattered waves at the ridge top causing amplification. The amplitude at the top of the ridge for the in-

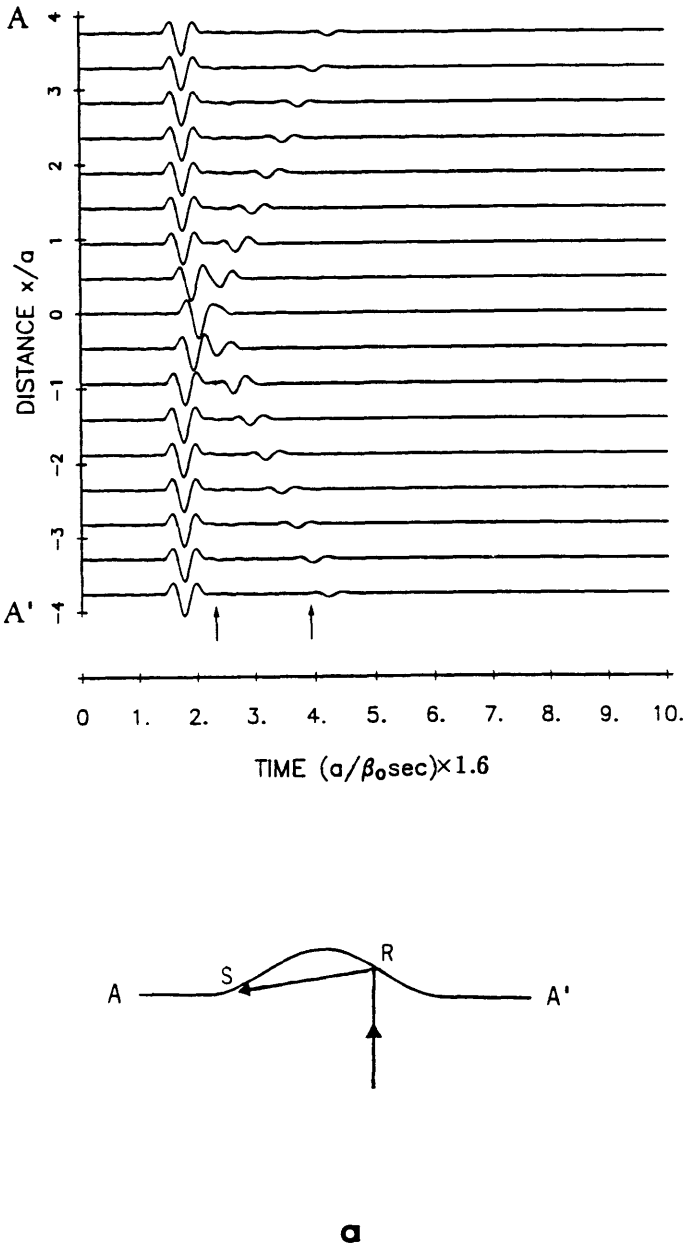

a

FIGURE 4.17 (a) seismograms at 17 stations for the homogeneous case. Aspect ratio is 0.4. The velocity of the scattered wave, measured from the slope of its trace between the arrows is equal to the velocity at the bottom of the ridge.

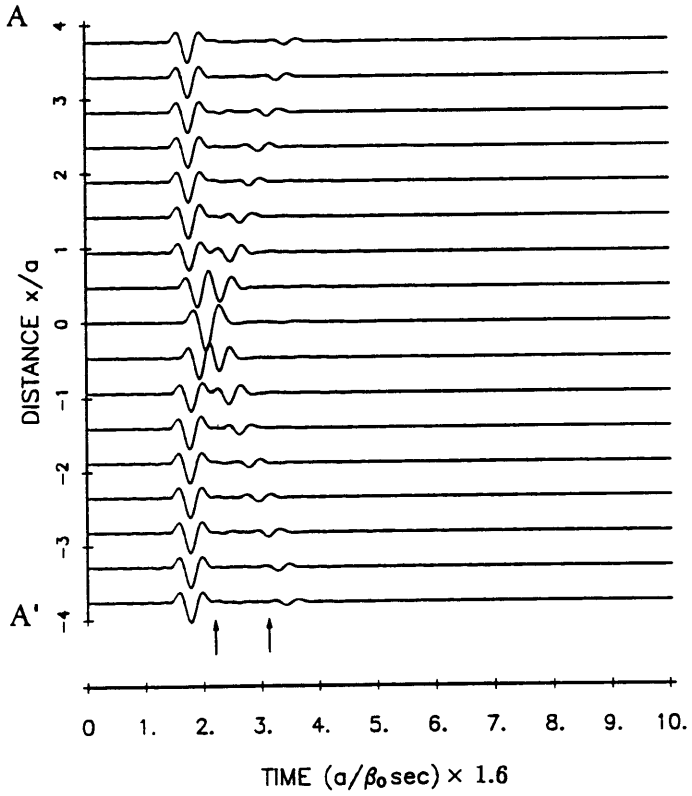

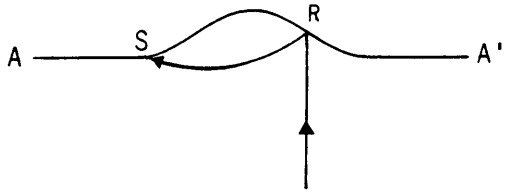

b

FIGURE 4.17 (b) the inhomogeneous case, when velocity at the bottom is twice the velocity at the top of the ridge. As in (a), the velocity of the scattered wave, measured from the slope of its trace between the arrows is equal to the velocity at the bottom of the ridge.

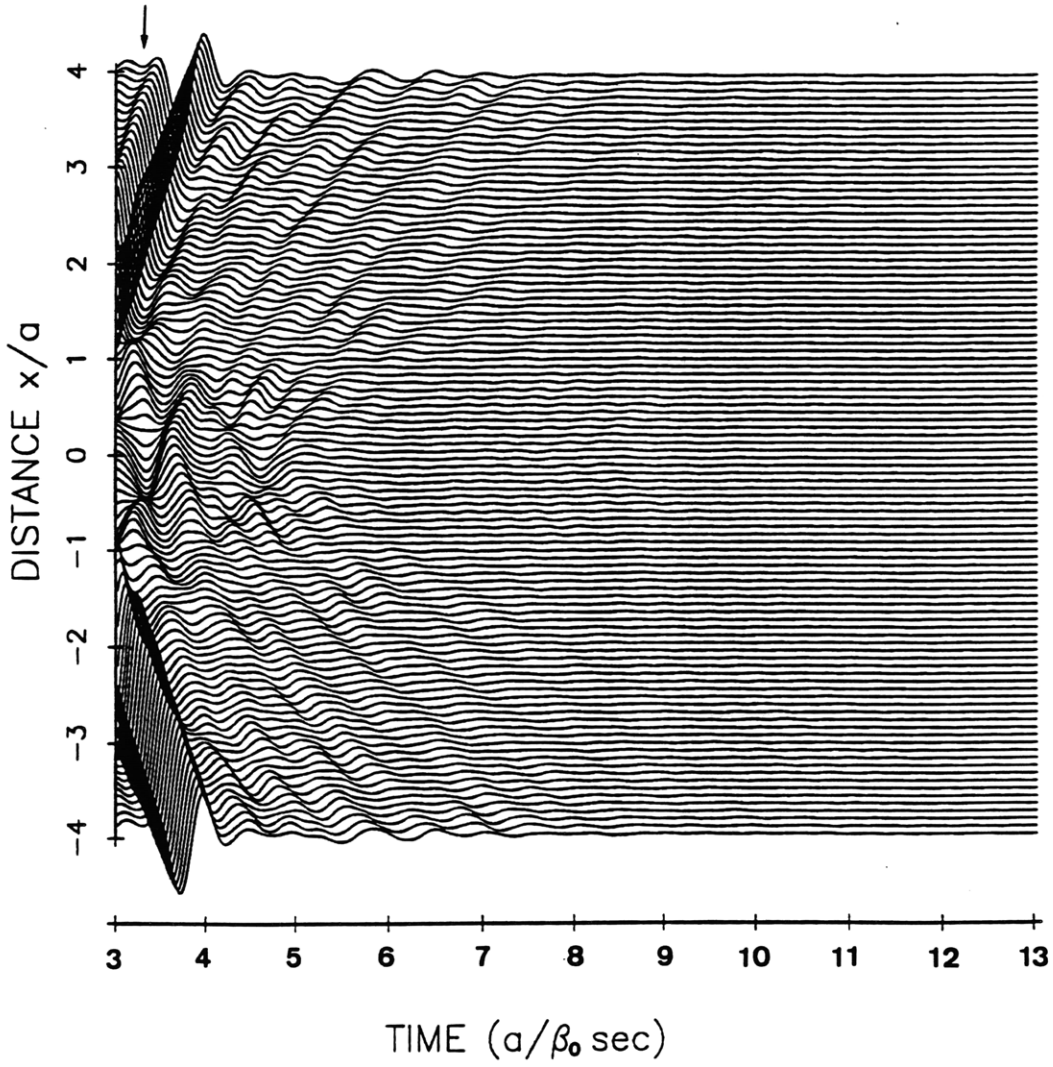

FIGURE 4.18 The seismogram for $g = 1$ (unit of time)$^{-1}$ in Figure 4.15 is blown-up after the time marked by an arrow.

homogeneous case is about 1.3 times that of the homogeneous case. The amplification at stations on the flanks of the ridge is about the same in both cases. Comparing these results with those for a higher aspect ratio ridge, as the one shown in Figure 4.16, we observe that the amplitudes of the scattered SH wave outside the ridge are much smaller than those for lower aspect ratio ridge. The motion on the flank of ridge is, on the other hand, greater for higher aspect ratio ridge. When $\beta_0 = 1$ unit of distance/time, and the gradient is $g = 1$ (unit of time)$^{-1}$, the amplitudes of the scattered wave outside the ridge are even smaller than those for the homogeneous case, but the seismograms at stations inside the ridge show more arrivals, suggesting multiple reflection-diffraction phenomena.

The presence of the vertical inhomogeneity may give rise to surface Love waves. We suspect this from the barely observed arrivals in Figure 15, for $g = 1$ (unit of time)$^{-1}$ and $\beta_0 = 1$ unit of distance/time. This arrivals are not present in the case of $g = 0$ (unit of time)$^{-1}$, but appear gradually as g increases. We have blown-up these arrivals, starting from $t = 3.4a/\beta_0$ (marked with arrow), that is to include the arrival of the scattered SH wave. Results are shown in Figure 4.18. It appears that in effect, these arrivals correspond to Love waves. We need to calculate phase velocity of Love waves to confirm it.

4.6 Inhomogeneous sedimentary basin

In this section we compute the ground motion of a sedimentary basin in which shear wave velocity increases linearly with depth, embedded in a homogeneous half-space. The geometry of the problem is depicted in Figure 4.19, along with the source distribution. To represent the field outside the basin (exterior) we have used the sources marked with '*' distributed along

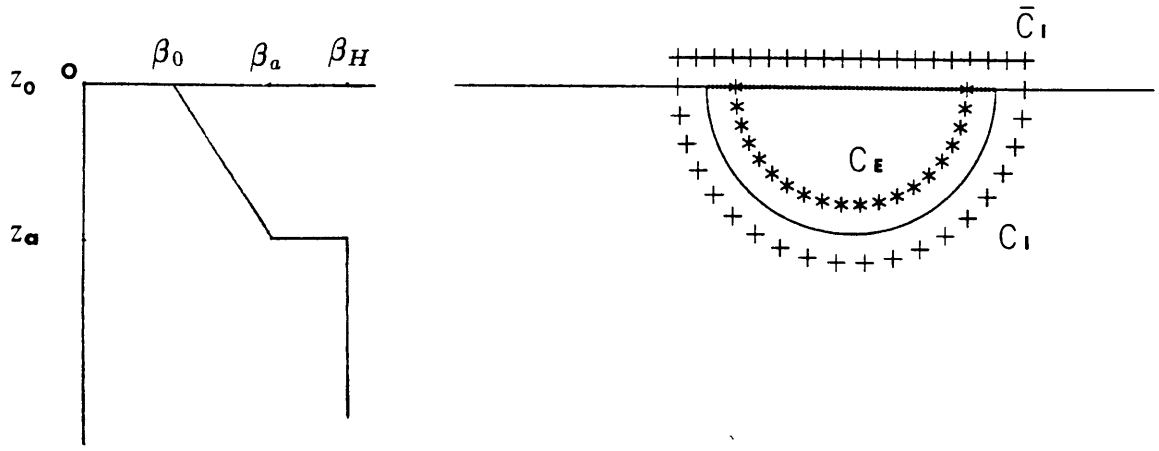

FIGURE 4.19 Source distribution along the interface with the half-space and free-surface of the semi-cylindrical inhomogeneous basin. The sources represent scattered fields in the exterior region (C_E), interior (C_I and $\bar{C}_I$). At the left is the velocity distribution with depth. a is the radius of the basin.

the semi-circle C_E in the figure. For the field inside the basin we use the sources marked with '+' distributed along the free-surface $\bar{C}_I$ and along the semi-circular interface with the homogeneous half-space. The wavefield in both regions is expressed by equations (3.1) (refer to Chapter III for more detail about source distribution for interior and exterior fields), where $v_m^{(I)}$ is computed by INGREEN (section 4.4) and

$$v_n^{(E)}(x,z;\omega) = \frac{i}{4}[H_0^{(2)}(kr) + H_0^{(2)}(kr_-)] \tag{4.21}$$

where $H_0^{(2)}$ is Hankel function of second kind, order zero, $i = \sqrt{-1}$, $k = \omega/\beta$ is wavenumber, $\beta = \beta(z)$, and

$$r = \sqrt{(x - x_E)^2 + (z - z_E)^2}$$

$$r_- = \sqrt{(x - x_E)^2 + (z + z_E)^2}$$

where (x_E, z_E) is the position of the source distributed along the semicircle C_E. (x,z) is the position of an arbitrary observation point, and r_- is the vector position of its image source $(x_E, -z_E)$. $v_n^{(E)}$ in equation 4.21 is 2-D Green's function for a homogeneous half-space.

The boundary integral scheme for the inhomogeneous basin described above requires a much more involved algebra than those for the homogeneous basin (section 2.4) and embedded inclusions (section 3.2, equations 3.2 and 3.3). In the present case, we must include the integral of the total field along the free-surface of the basin in order to satisfy boundary conditions. In Chapter II we overcame this problem for the valley by adopting a image source scheme, which allowed automatically the compliance of the boundary conditions along the free-surface in both the half-space and the

valley, so that the distribution of sources and integration paths (see equation 2.6) were restricted only to the curved interface between valley and half-space. Similarly in the case of inclusions. Here it is not possible to adopt such a scheme for the basin, therefore we must distribute sources along its free surface and incorporate them into our least squares method to determine their strengths, as described in section 2.2. In this section we shall write neither the algebra nor the elaborated equations, as we did for the inclusion in section 3.2, but refer to Appendix 1 in this thesis. Let us only mention that now we have nine submatrices of the type R (see equation 3.2 and 3.3) and one more integral (along $\bar{C}_I$) incorporated into their expressions and in those for the source terms S^0.

4.6.1 Ground motion in frequency domain:

Comparison with the finite element method.

We compute the ground motion along the free-surface of a semi-cylindrical inhomogeneous basin in a half-space of radius a, in which the shear wave velocities at the top (β_0) and bottom (β_a) of the basin are 1 and 2 unit of distance/time, and in the half-space (β_h) 3 unit of distance/time. That is, $g = 1$ (unit of time)$^{-1}$ in the basin and a strong jump of velocity at the bottom of the basin. Densities ρ_s and ρ_H of sediments and half-space respectively are assumed uniform and their values are related by $\rho_s/\rho_H = 0.667$. Results are shown in Figure 4.20, for several values of $\eta = 2a/\lambda_a$. These are to be compared with the results of Figure 2.12 (Chapter II) corresponding to the case of a similar basin whose shear wave velocity is constant and equal to 1 unit of distance/time, and the half-space velocity is 3 units of distance/time.

We observe that the response is in general strongly affected by the

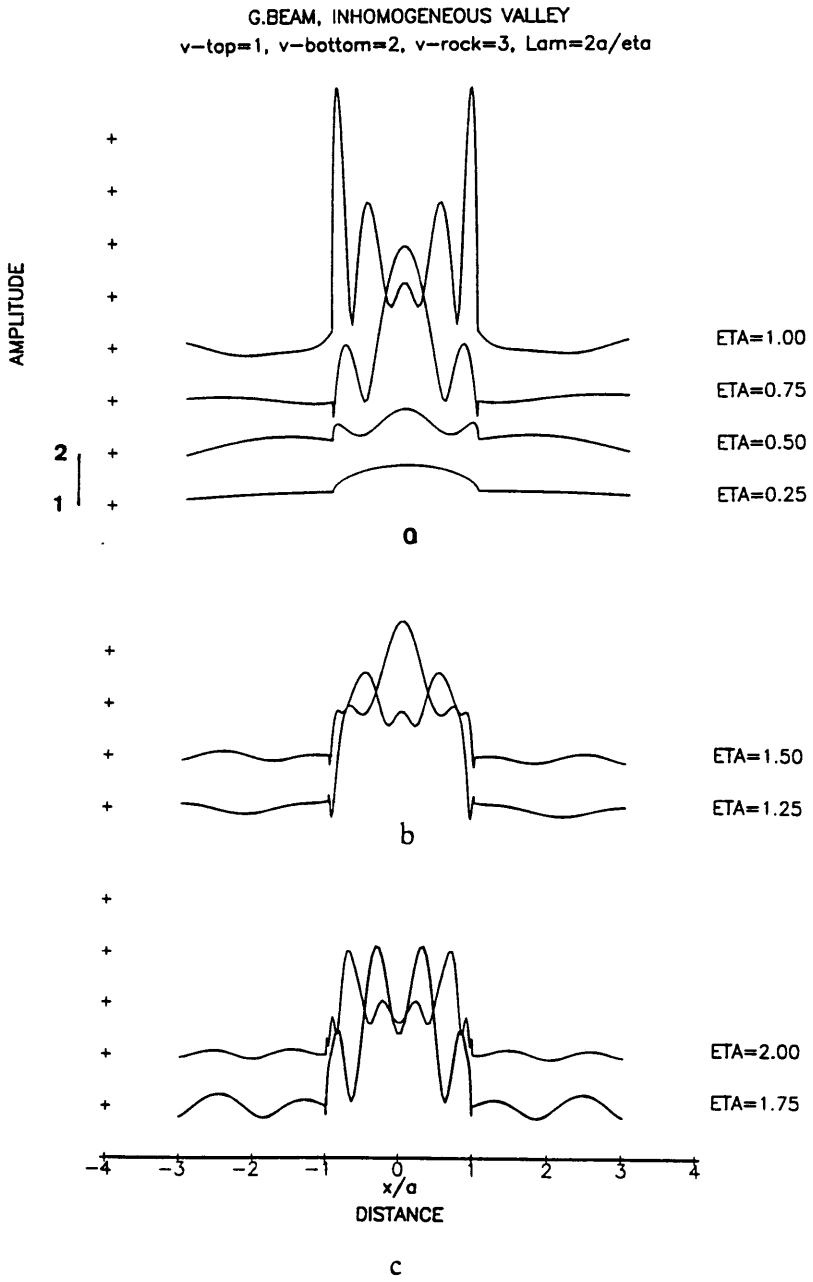

FIGURE 4.20 (a), (b), (c) response of the inhomogeneous basin for several η's, computed with boundary-integral Gaussian beam method.

velocity gradient, but the effect is not systematic. In fact, for some frequencies, e.g. $\eta = 0.25$ the motion is deamplified by a factor of $\simeq 6$. The amplitude distribution of the ground motion at the edges of the basin becomes more pronounced with the gradient, for all frequencies, reaching its maximum amplitude for $\eta = 1$, or $\lambda_a = 2a$. On the contrary, the amplitude outside the basin becomes smoother with the increased gradient. These characteristics of the motion can be observed more clearly in Figure 4.21 (a)-(d), which shows the effect of the velocity gradient on the response of the basin for $\eta = 1$, by increasing the velocity at the bottom of the basin β_h from 1 at intervals of 0.1 unit of distance/time. We observe that area of amplification within the basin systematically becomes wider as β_a increases, covering the basin range for $\beta_a = 1.6$ and thereafter amplifying the motion at the edges more than at any other parts of the basin. This dependence of the ground motion with velocity gradient was also noted by Bard and Gariel (1986), who modeled inhomogeneous basins with sinusoidal interface with the half-space.

The accuracy of our results are checked by comparing them with those obtained by solving an identical case using a hybrid method based on boundary element representation of the wavefield for the homogeneous half-space and finite element computation of the field in the basin. The method was developed by Toshiaki Sato (1984) and used in problems of Eartquake Engineering (Fukuwa et. al. 1985). Figures 4.22 (a)-(e) showing the results for the cylindrical basin using this method are courtesy of T. Sato and H. Kawase (personal communication). The finite element mesh for the basin is shown in Figure 4.22 (a), providing 10.67 elements per wavelength in the basin for $\eta = 2$. The coarse mesh attached to the left of the basin is used

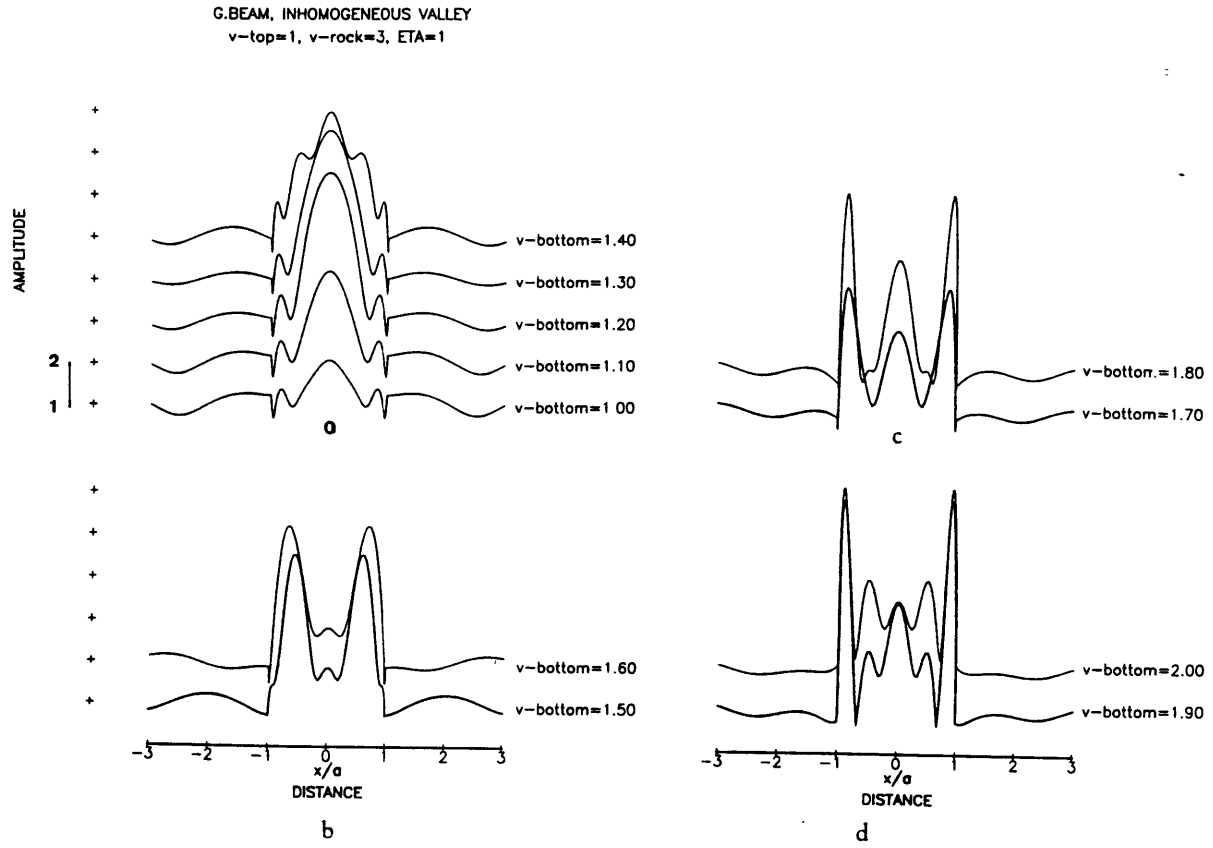

FIGURE 4.21 (a)-(d) response of the basin for $\eta = 1$, gradually increasing the velocity at the bottom, from 0 to 2.00.

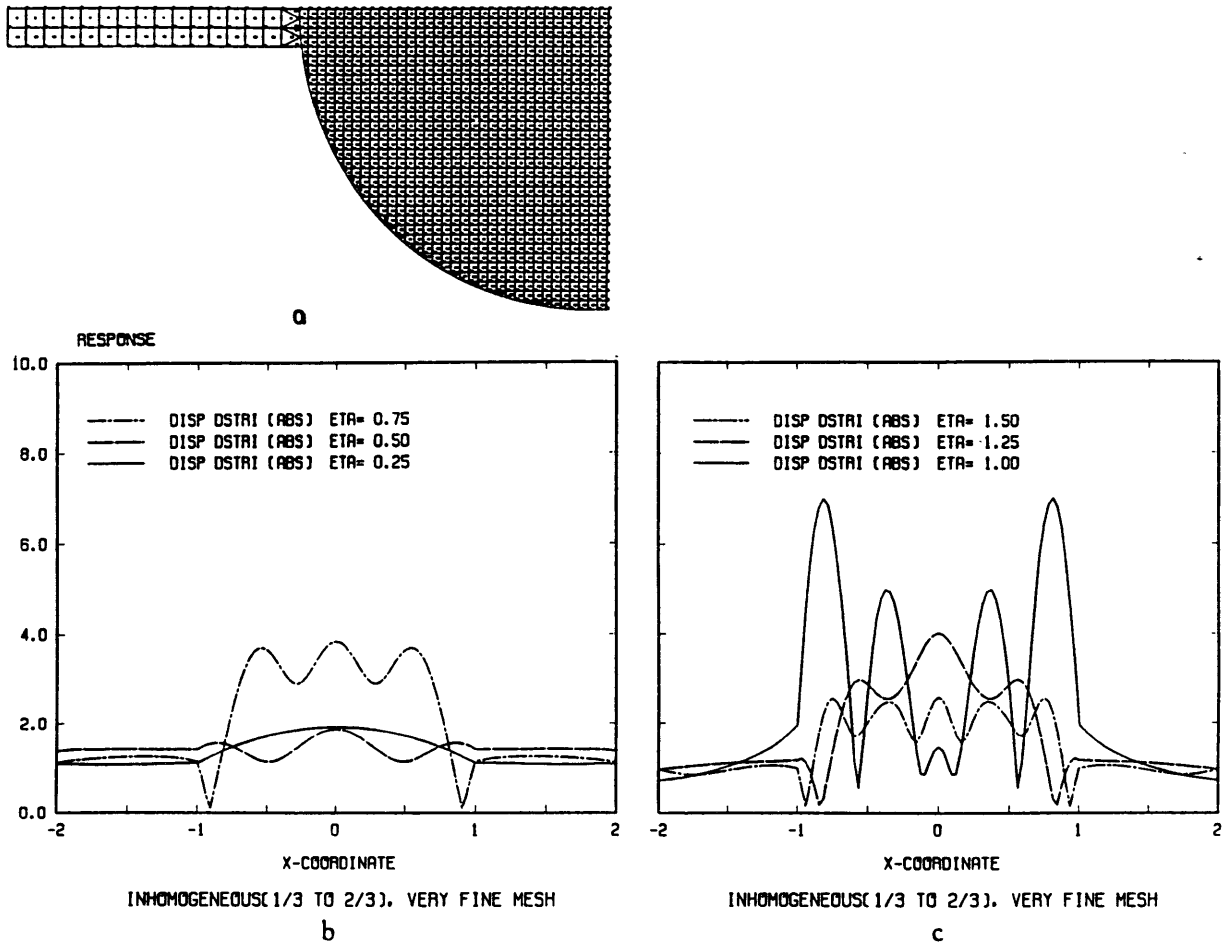

FIGURE 4.22 (a) Finite element mesh of the same inhomogeneous basin as in Figure 4.20. Results in (b) and (c) are to be compared with their corresponding in Figure 4.21 (a) and (b). Such comparison shows that the results by both methods are in good agreement, except for $\eta = 0.75$.

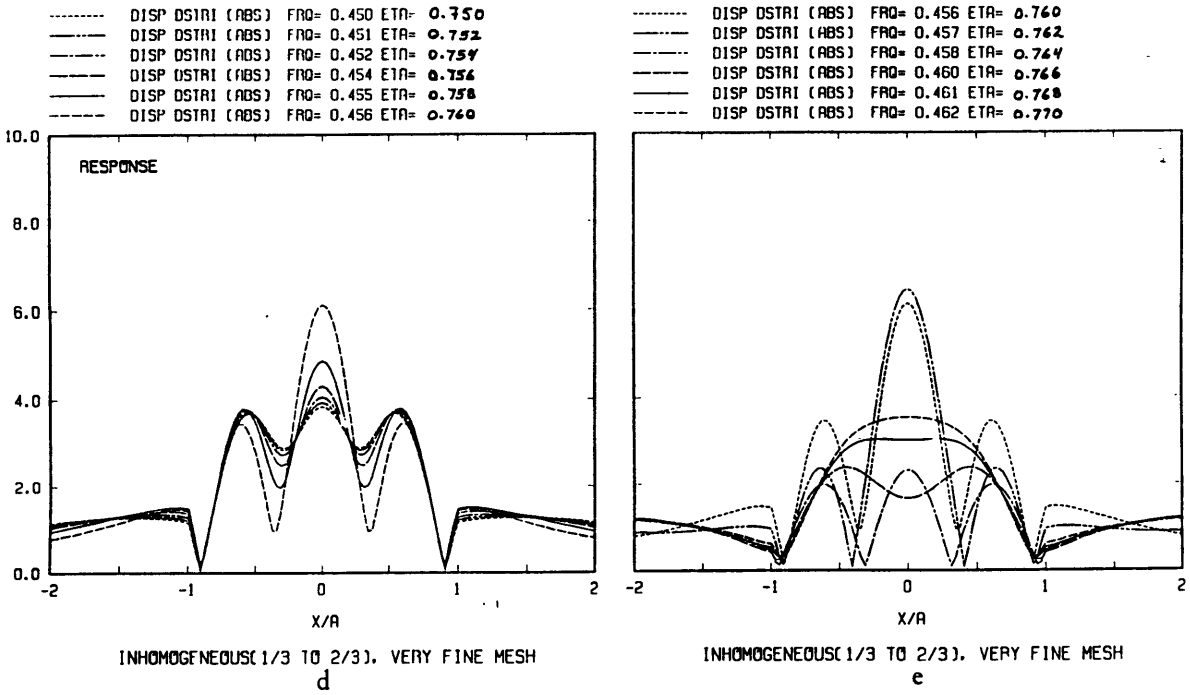

FIGURE 4.22 (d), (e) $\eta = 0.75$ corresponds to a resonance mode of the inhomogeneous basin in Figure 4.20 (a). The corresponding resonance mode for the finite element basin model is $\eta = 0.76$, as demonstrated here by increasing η gradually in 0.001 steps, from 0.750 to 0.770.

to compute the motion at the free- surface. The distribution of velocity with depth is simulated by stepwise velocity variation in a layered structure with homogenous layers, where the velocity of each layer is assigned to be the velocity at the mid-depth of the layer. The values of velocity at the top and bottom of the basin, and that in the half-space are $1, 2$ and 3 units of distance/time, as same as in our case. Results for up to $\eta = 1.5$ are shown in Figure 4.22 (b),(c). Our results in Figure 4.20 are in good agreement with theirs, except for $\eta = 0.75$. However, this disagreement is due to the homogeneous layered structure introduced to simulate the continuous gradient, because η is related to the velocity at a given depth, so that the η's for the layered model mismatches the corresponding values of η for the continuous model. The error due to such mismatch is larger when the selected η is a resonant mode, as it appears to be the case here. This is demonstrated in Figure 4.22 (d),(e), by increasing stepwise the value of η from 0.75 to 0.77. The response computed for $\eta = 0.76$, which gives the largest amplification, is in perfect agreement with our results for $\eta = 0.75$. The above problem can be overcome by increasing the number of layers, although requiring costly computations and cumbersome mesh design.

We also have performed the test of residual traction as introduced in Chapter II and used in the present chapter for the study of inhomogeneous mountain. We found that the fractional residual tractions for the worst case of $\eta = 5$ and gradient $g = 1$ (unit of time)$^{-1}$ when $\beta_0 = 1$ unit of distance/time, is of the order of 10^{-2} at most.

4.6.2 Synthetic seismograms

The appropriate number of sources to represent the wavefield in the basin has to be chosen according to the wavelengths at the free-surface of

the basin, in order to guarantee accurate solution for all frequencies of the incident wave considered in the computation of synthetic seismograms. Using the criterion of 4 sources within a wavelength, we have distributed a total of 120 sources along the free-surface, and enclosing the cylindrical valley. Refering to Figure 4.19 of the basin, the seismograms are synthesized at 160 stations distributed over a distance $10a$, centered at $x/a = 0$ of the basin. These seismograms are $18a/\beta_0$ of duration, computed for the source waveform of Ricker wavelet (Chapter III) with $\lambda_c = 0.6a$. In Figure 4.23 (a) the incidence of the primary wave is vertical, $\beta_0 = 1$ unit distance/time, $\beta_a = 1.001$ unit distance/time, $\beta_H = 3$ unit distance/time and $a = 1$ unit of distance. In (b) the angle of incidence is 30^0, other parameters are kept the same. Since the velocity gradient is small (0.001 (unit of time)$^{-1}$), we consider this as "homogeneous case". In (c) $\beta_0 = 1$, $\beta_a = 1.8$ and $\beta_H = 3$ unit of distance/time, which means that there is less velocity contrast at the bottom interface of the basin with the half-space. As for Figure 4.20, the densities of basin and half-space are uniform, and in the ratio 1/1.5. In both (a) and (b) we observe the smooth delay of the the incident wave passing through the valley, and the reverberations caused by two-dimensional resonance due to trapped waves inside the basin. Similar behavior of the wave propagation inside and outside the basin were obtained by Bard and Gariel (1986) in their study of shallow, medium and deep valleys. Our computation of the total wavefield for this short wavelength allows us to identify the individual reflections taking place in the interference pattern in the basin. We observe stronger attenuation of the waves reflected back-and-forth between the bottom of the basin and the free-surface than those reflected on the sides. Only the first reverberation leaks significant amount

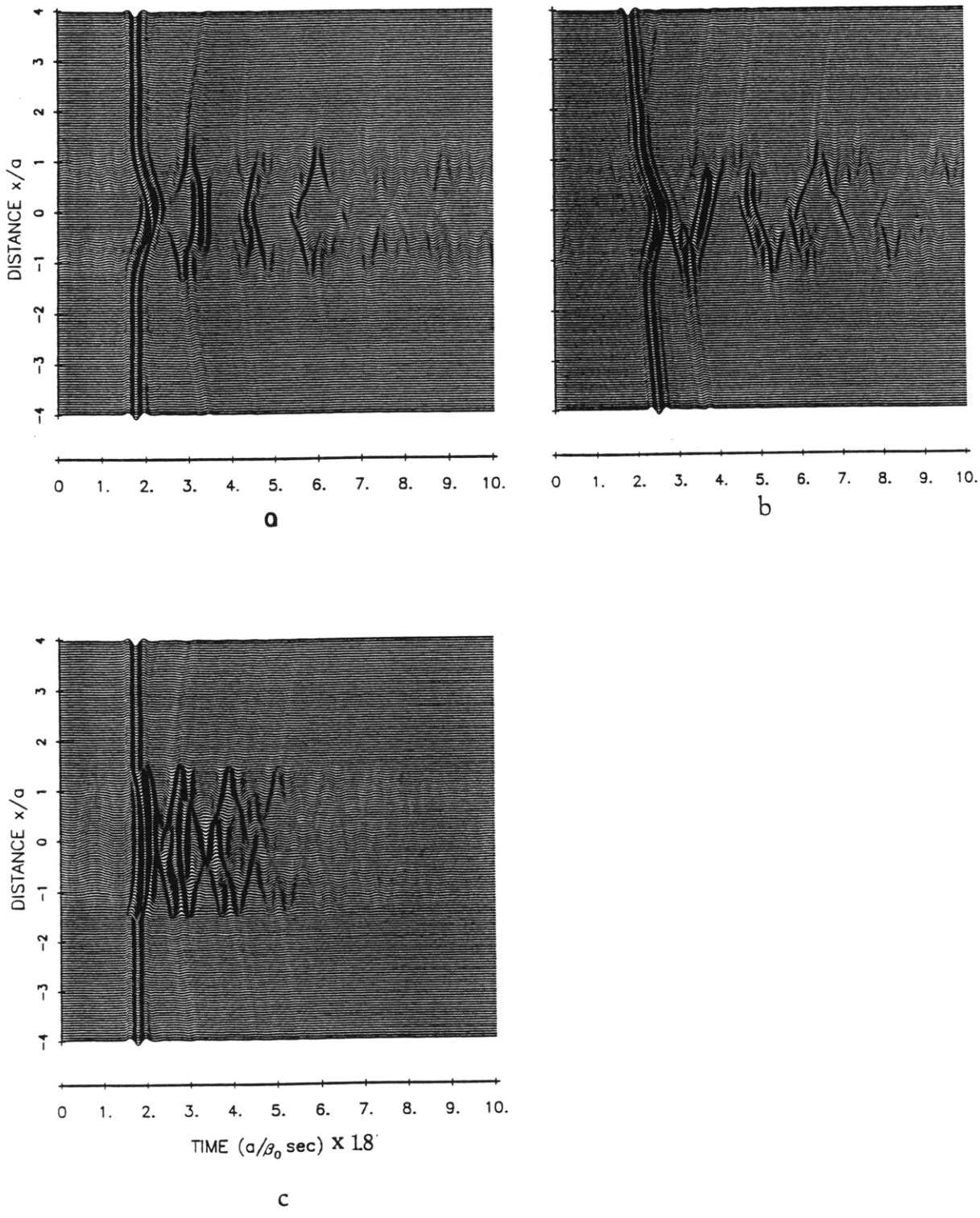

FIGURE 4.23 (a), (b) Synthetic seismograms for the homogeneous basin, and for $\lambda_c = 0.6a$. Velocity of the half-space β_{II} is three times the velocity of the basin β_0. In (b) the incidence angle is 30^0. In (c) the velocity of the bottom of the basin $\beta_a = 1.8\beta_0$.

of energy towards the sides of the basin. In (b), the wave interference inside the basin does not allow reverberation as regularly as in (a). The amplitudes of the reverberating waves appear to attenuate more rapidly in this case. In (c), where velocity gradient is present, two remarkable features emerge. The first is the widening of the amplification zone as compared to the case of homogeneous basin. Second, the reverberations caused by two dimensional resonance have in this case larger amplitudes than those in the case of homogeneous basin, and their time intervals are much shorter due to faster velocity within the basin. The total duration of the seismograms at stations within the basin becomes shorter, due to energy loss carried by waves transmitted back into the half-space. This is more evident in Figure 4.24, where $\beta_a = 2.5$ unit distance/time, keeping β_0, β_H the same as in Figure 4.23(a). In (a) the incidence is vertical, and we observe only one back-and-forth reflection from the sides of the basin having significant amplitude, because of reduced velocity contrast across the interface, and almost no waves are transmitted towards the sides of the basin. In (b) the angle of incidence is 30^0 keeping the value of velocities the same as in (a). In this case we see well defined travel-times of the waves reflected back-and-forth at the sides of the basin, where the impedance contrast is large. The time delay in each reflection suggests that the waves are reflected towards the bottom of the basin, where most of their energy is transmitted into the half-space.

4.7 Discussion

The boundary integral and Gaussian beam methods have provided a new tool to study accurately SH wave propagation phenomena in complex structures by computing the complete waveform for a wide range of

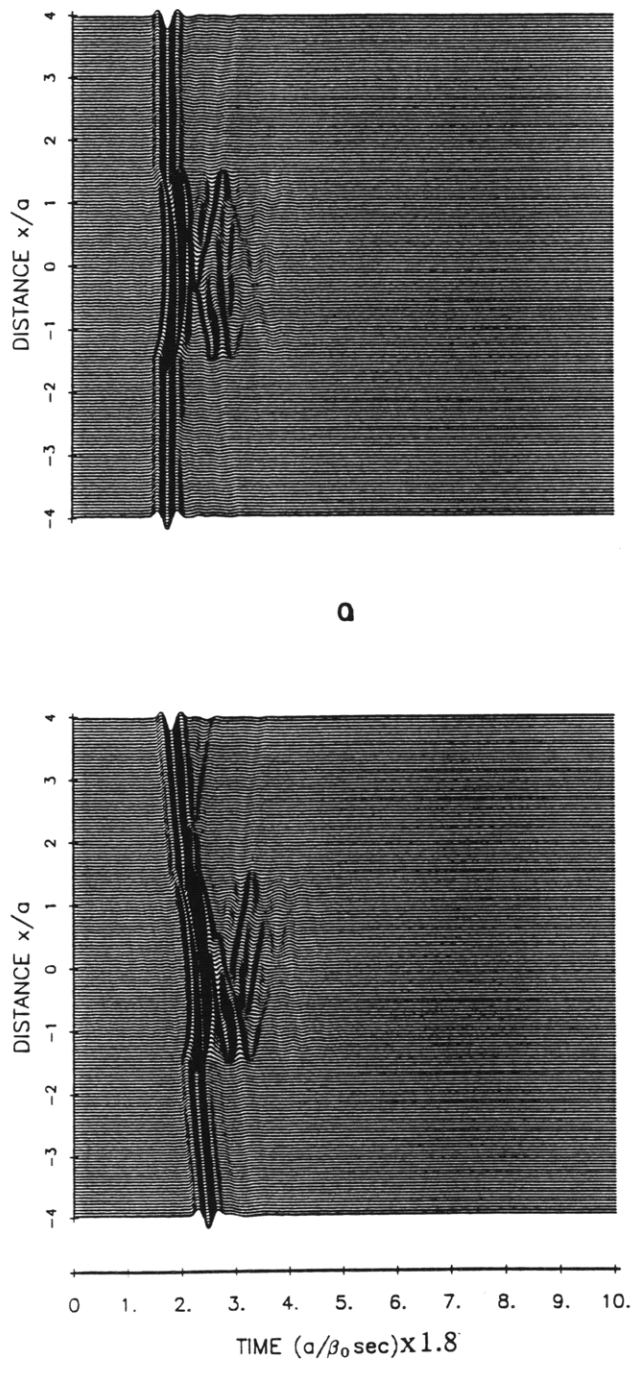

FIGURE 4.24 Synthetic seismograms for the inhomeogeneous basin, when $\beta_a = 2.5\beta_0$, (a) for vertical incidence, (b) for 30^0 incidence angle.

frequencies. We believe that we combined the two methods taking advantages of the strengths of their methods, avoiding their weaknesses. The Gaussian beam method helps to reduce the number of unknowns needed by the boundary integral method to attack a complicated problem. For instance, in media showing smooth spatial variations of velocity and strong boundary irregularity, sources can be distributed along the boundary and Green's function for the smooth media can be constructed by superposition of Gaussian beams, avoiding the task of discretizing the whole medium. In our method, there is no need for the cumbersome calculation of transmission and reflection for Gaussian beams, because the boundary conditions are satisfied globally, by the least squares method. The aim of the present Chapter was to demostrate such advantage, by choosing problems of simple geometry. The validity of the results obtained here are confirmed by using other well stablished methods. Our algorithm to superimpose Gaussian beams is flexible and fast, mainly due to the analytical computation of ray-centered coordinates, although limited to media with linear increase of velocity with depth.

CHAPTER V

MULTIPLE SCATTERING OF SH WAVES IN MEDIA WITH MANY CAVITIES

5.1 Introduction

The problem of scattering of waves interacting with a complex system of heterogeneities was formaly treated for the first time by Foldy (1945) for scalar waves and subsequently studied extensively in several fields of Physics (Lax 1951, Varadan 1980, Kikuchi 1981). In most cases, the difficulty of solving the wave equation under given boundary conditions has forced researchers to look for approximate solutions, using assumptions that simplifies certain aspects of the scattering phenomena. For waves in randomly heterogeneous media, analytical solutions of the wave equation have been restricted to the case of weak scattering, where multiply scattered waves may be neglected (Chernov 1960). The case of strong scattering can be studied only by numerical techniques (Frankel and Clayton 1986) or by the laboratory simulation controlling the size and density distribution of the scatterers as well as source (Matsunami 1989). Unfortunately, numerical techniques such as finite-difference and finite-element methods face the great difficulty of core memory and CPU time limits in dealing with realistic scattering problems, even with state-of-the-art-computers. Moreover, it is not clear whether these techniques can simulate correctly the inhomogeneous (evanescent) waves converted at interfaces with strong velocity contrast and sharp interfaces since their wavelength may turn to be smaller than the size of the mesh used.

In the present chapter, we use the boundary integral method (BIM) to address deterministically the problem of multiple scattering of SH waves in two-dimensional media, where the heterogeneities are distribution of regularly or randomly spaced cylindrical cavities of circular or elliptical cross section. As explained in early chapters, the boundary conditions of the problem are imposed on the integral representation of the wavefield, leading to an integral equation in which the kernel, or Green's function, incorporates the values of the wavefield at the boundaries into the solution for the total wavefield. In general, the integral equation is solved numerically by means of discretization of the boundary. While they share a common foundation, all boundary methods differ in their discretization scheme and the way in which Green's function is evaluated. We use the so-called single layer potential form of the integral representation, described by Ursell (1973), and a discretization based on distribution of point (line) sources along the boundary of the scatterers. Our Green's function is exact (Hankel function for 2-D full-space) and the boundary conditions are imposed in the least-squares sense. A similar scheme has previously been used by Dravinski (1983) to formulate in terms of potentials the complete elastic wavefield in media with many elastic inclusions of arbitrary (smooth) shape, and to compute the ground response of a half-space with one and two elliptical inclusions.

Here we treat cases involving up to 50 cavities in half and full spaces, and for wavelengths larger and smaller than the size of the cavities. Our results are time-domain synthetic seismograms obtained by the inverse Fourier transform of the solution at many frequencies. There are no restrictions on the frequency range of applicability. In fact, the accuracy of

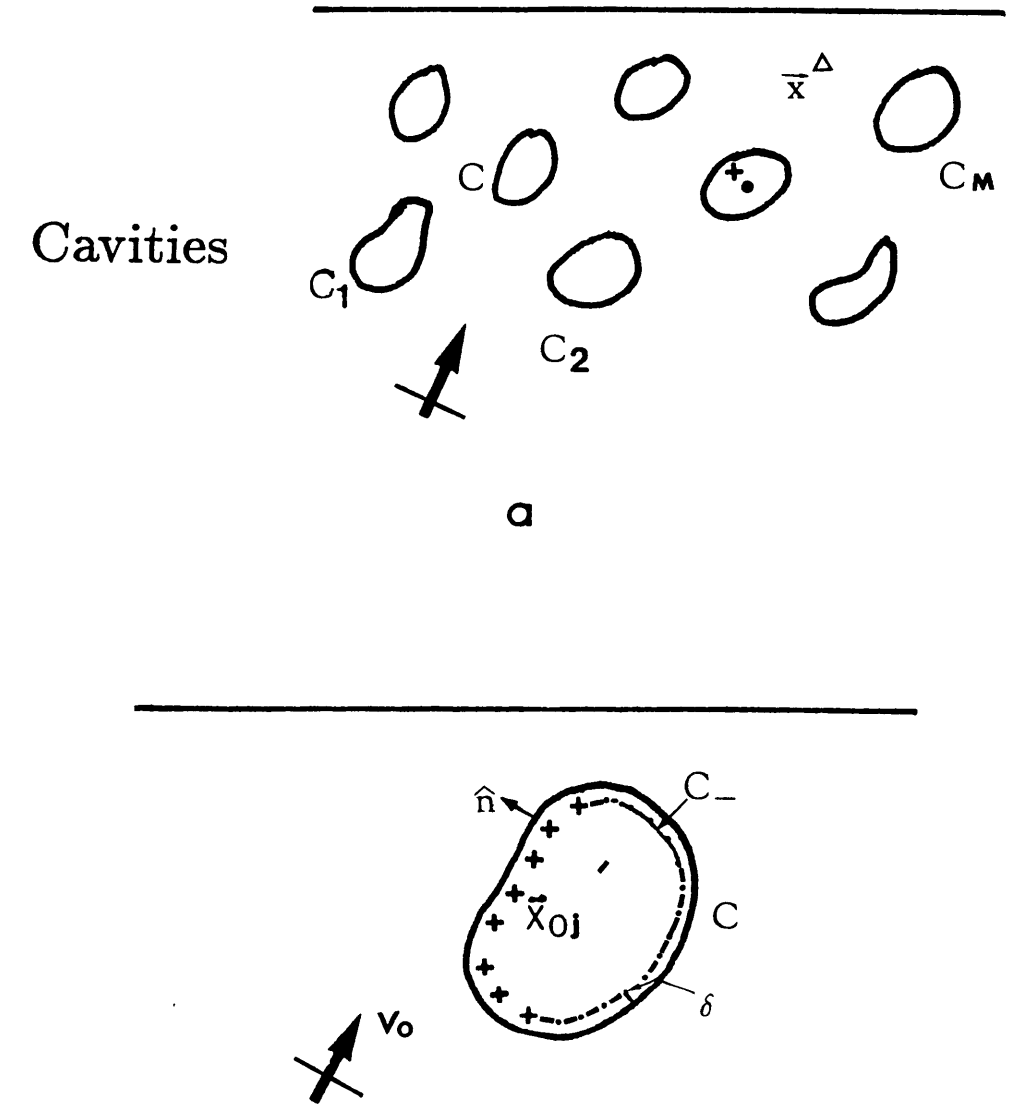

FIGURE 5.1 (a) v_0 is incident upon a collection of M cavities. Upon the incidence of v_0 (plane wave or line source) the total field is measured at the observation point Δ whose vector position is $\vec{x}$. The total field at the observation point is v_0 plus the scattered field contribution from all cavities. (b) a single cavity enclosed by the curve C. Artificial wave sources denoted by '+' are distributed along an interior curve C_-, at a distance δ from C, in order to represent the scattered wave field due to the cavity.

the solution for a given frequency is determined by the number of sources used to satisfy the boundary conditions.

In the following, we first describe the method and check its accuracy in frequency domain. Next, synthetic seismograms along an observation line at $z = 0$ (z positive down) are computed for the cases in which one, two, four, and twelve cavities are regularly distributed in both half and full spaces. The purpose of this exercise is to show the interference patterns that develop in time domain as the number of scatterers increases. Finally we compute the synthetic seismograms corresponding to fifty randomly distributed cavities along with the corresponding quality factor $Q(\omega)$ due to scattering loss for primary waves propagating through the region.

5.2 Basic theory and formulation

The method of integral equations described by Ursell (1973) for the exterior problem of acoustic scattering is used here to derive an expression for the SH wavefield in a medium with many cavities, for the plane wave or line source incidence. According to this method, which was described in our Chapter II, the scattered field due to one cavity can be expressed as the integral of the wavefield produced by a continous distribution of artificial wave sources with unknown strengths along its boundary (see equation (2.1)). In the present chapter, we extend this formulation to compute the total wavefield in the presence of many cavities as the sum of the scattered field due to unknown sources distributed along the boundary of each cavity plus the incident wave.

Referring to Figure 5.1 (a), a plane SH wave v_0 is incident from below (z-positive down), upon a collection of M cavities of arbitrary cross sectional shape. The total wavefield v at an arbitrary observation point P

(position vector $\vec{r}_P$) is given by equation

$$v(\vec{r}_P) = v_0(\vec{r}_P) + \int_{C_1} \sigma_1(\vec{r}_Q) G(\vec{r}_P|\vec{r}_Q) ds_1 + \int_{C_2} \sigma_2(\vec{r}_Q) G(\vec{r}_P|\vec{r}_Q) ds_2 + \ldots$$

$$+ \int_{C_M} \sigma_M(\vec{r}_Q) G(\vec{r}_P|\vec{r}_Q) ds_M$$

or

$$v(\vec{r}_P) = v_0(\vec{r}_P) + \sum_{i=1}^{M} \int_{C_i} \sigma_i(\vec{r}_Q) G(\vec{r}_P|\vec{r}_Q) ds_i \qquad (5.2)$$

σ_i represents the strength of the continuous distribution of wave sources along the contour C_i in cavity i.

$G(\vec{r}_P|\vec{r}_Q)$ satisfies the Helmholtz equation $(\nabla^2 + k^2) G(\vec{r}_P|\vec{r}_Q) = 0$ (omitting the factor $\exp(i\omega t)$), except at $\vec{r}_P = \vec{r}_Q$, at which it has a singularity. The analytical solution obtained for G in a homogeneous full-space, satisfying the radiation condition

$$r^{1/2}\left(\frac{\partial v}{\partial r} - ikv\right) \to 0 \ , \ as \ r \to \infty$$

is

$$G(\vec{r}_P|\vec{r}_Q) = \frac{i}{4} H_0^{(2)}(kr)$$

where $H_0^{(2)}$ is Hankel function of zero order and second kind, $i = \sqrt{-1}$, and $r = \sqrt{(x_P - x_Q)^2 + (z_P - z_Q)^2}$. In evaluating (1) the singularity of $G(\vec{r}_P|\vec{r}_Q)$ can be avoided by distributing the wave sources along a curve C_-, interior to C, whose points are located at a finite distance δ from C (see Figure 5.1(b)). The validity of this approach is demonstrated by Ursell (1973) by constructing Green's function $G(\vec{r}_P|\vec{r}_Q)$ in such a way that it remains bounded as $\vec{r}_P \to \vec{r}_Q$. The construction is in terms of series of Bessel functions that converge for $|\vec{r}_P - \vec{r}_0||\vec{r}_Q - \vec{r}_0| > \delta^2$, where r_0 is the position vector of the center of the cavity.

To evaluate the integral in (5.2) we discretize the boundaries of the cavities following the same discretization scheme described in Chapter II for one scatterer. Although the formulation is quite similar to that in Chapter II, the presence of two indexes, i and j representing cavity and source, respectively, makes it necessary to write the formulas for many cavities explicitly. Let us assume that instead of the continuous wave source distribution we select N points along the boundary of each cavity and assign a line source at each point. The strength σ_i is thus written as

$$\sigma_i(\vec{r}_Q) = \sum_{j=1}^{N} A_{ij}\,\delta(|\vec{r}_Q - \vec{r}_{Q_{ij}}|) \tag{5.3}$$

where $\vec{r}_{Q_{ij}}$ is the vector position of the $j-th$ source in the $i-th$ cavity. Inserting (5.3) in (5.2)

$$v(\vec{r}_P) = v_0(\vec{r}_P) + \sum_{i=1}^{M} \int_{C_i} \sum_{j=1}^{N} A_{ij}\,\delta(|\vec{r}_Q - \vec{r}_{Q_{ij}}|)G(\vec{r}_P|\vec{r}_Q)ds_i$$

$$v(\vec{r}_P) = v_0(\vec{r}_P) + \sum_{i=1}^{M}\sum_{j=1}^{N} A_{ij} \int_{C_i} \delta(|\vec{r}_Q - \vec{r}_{Q_{ij}}|)G(\vec{r}_P|\vec{r}_Q)ds_i$$

$$v(\vec{r}_P) = v_0(\vec{r}_P) + \sum_{i=1}^{M}\sum_{j=1}^{N} A_{ij}\,G(\vec{r}_P|\vec{r}_{Q_{ij}}) \tag{5.4}$$

A_{ij} is a complex constant that represents the strength of the source located at the $j-th$ point on the boundary of the $i-th$ cavity. Since equation (4) is derived for a given ω, it should be written as

$$v(\vec{r}_P,\omega) = v_0(\vec{r}_P,\omega) + \sum_{i=1}^{M}\sum_{j=1}^{N} A_{ij}(\omega)G(\vec{r}_P|\vec{r}_{Q_{ij}};\omega) \tag{5.5}$$

In general, the appropriate number of sources assigned to each cavity may vary according to the shape of its cross-section and to its size relative to the

input wavelength. In this study we assume that all cavities are identical, so that we assign the same number N of sources to each of them.

The problem has been reduced to determine the constants $A_{ij}(\omega)$. This is done by imposing the boundary conditions in the least-squares sense (Sanchez-Sesma and Rosenblueth 1979), i.e. by minimizing the total quadratic error of the values of traction along all boundaries:

$$L = \int_C \left| \mu \frac{\partial v}{\partial \hat{n}} \right|^2 ds \tag{5.6}$$

where $C = C_1 + C_2 + ...C_M$, μ is the shear modulus and $\hat{n}$ the outward normal vector to C at P. The following system of simultaneous linear equations is obtained:

$$\sum_{i=1}^{M} \sum_{j=1}^{N} \Gamma_{mnij} A_{ij} = b_{mn} \tag{5.7}$$

where

$$\Gamma_{mnij} = \int_C \frac{\partial G^*_{mn}}{\partial \hat{n}} \frac{\partial G_{ij}}{\partial \hat{n}} ds$$

and

$$b_{mn} = -\int_C \frac{\partial G^*_{mn}}{\partial \hat{n}} \frac{\partial v_0}{\partial \hat{n}}$$

$(^*)$ stands for complex conjugate, $m = 1, 2, ..., M$, $n = 1, 2, ..., N$ and $G_{\alpha\beta} = G(\vec{r}_P | \vec{r}_{Q_{\alpha\beta}})$. In (5.7) Γ_{mnij} represents the interaction between the $n-th$ source of the $m-th$ cavity and the $j-th$ source of the $i-th$ cavity. Similarly, b_{mn} represents the interaction between the $n-th$ source of the $m-th$ cavity and the incident wave. It is understood that in our calculations the artificial sources will be located at an interior circle C_- whose radius $a_- = 0.8a$, which has been shown to give accurate results (Sanchez-Sesma and Esquivel 1979).

5.3 Test of accuracy

We consider that a fundamental test of accuracy for our method is to check its results with known analytical solutions. We have selected two such problems for this purpose. The first is to compute the scattering pattern, i.e. the pure scattered field after substracting the incident wave, due to one cylindrical cavity in full-space upon incidence of a plane wave. This is done for the range of frequencies that we intent to use in the numerical solution of more complicated problems. In Figure 5.2 we show the comparison of the pattern obtained with both our method (solid line) and the analytical solution (dots) given by Mow and Pao (1971, pp 269) Here the measurement is made at 100 stations located along a circumference of radius equal to 10 times a, the radius of the cavity. The values of the non-dimensional frequency $\eta = 2$ and 20 are equivalent to a and $a/10$, respectively ($\eta = 2a/\lambda$). The second problem is to compute the ground response of a half-space with one cavity totally embedded, also for SH plane wave incidence, and compare our results with those obtained by Lee (1977). We used the exact 2-D Green's function for a homogeneous half-space

$$G(\vec{r}_P|\vec{r}_{Q_{ij}};\omega) = \frac{i}{4}\left[H_0^{(2)}(kr_1) + H_0^{(2)}(kr_2)\right]$$

where

$$r_1 = \sqrt{(x_P - x_{Q_{ij}})^2 + (z_P - z_{Q_{ij}})^2}$$

$$r_2 = \sqrt{(x_P - x_{Q_{ij}})^2 + (z_P + z_{Q_{ij}})^2}$$

(r_2 is the position of the image source corresponding to the source located at $(x_{Q_{ij}}, z_{Q_{ij}})$. The incident wave is the superposition of up-going and down-going (reflected at the surface) SH plane waves, as if there were no

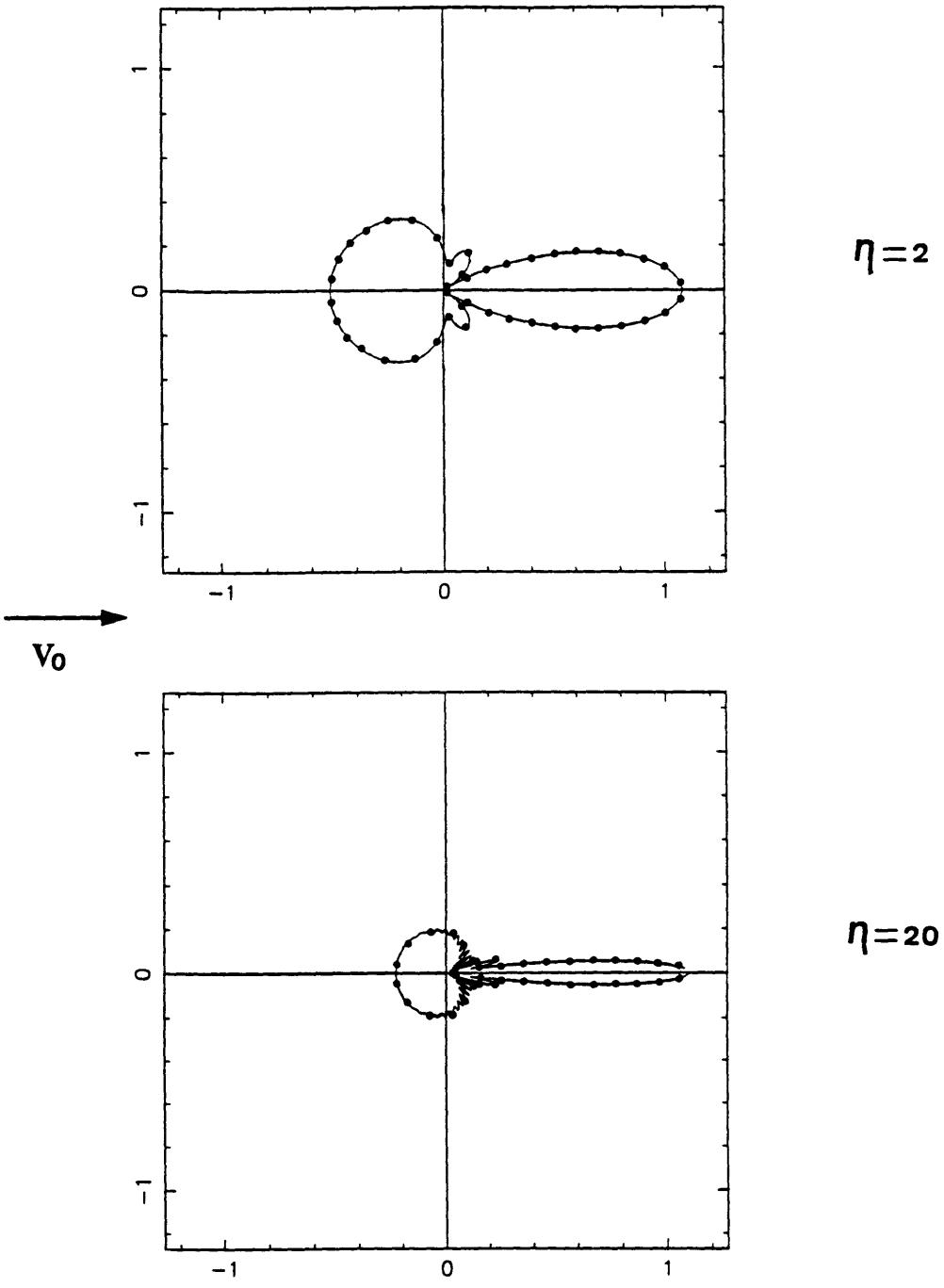

FIGURE 5.2 Scattering radiation pattern due to one cavity, computed for $\eta = 2$ and $\eta = 20$ ($\eta = 2a/\lambda$). Solid lines correspond to the solution given by this method; dots to the exact solution.

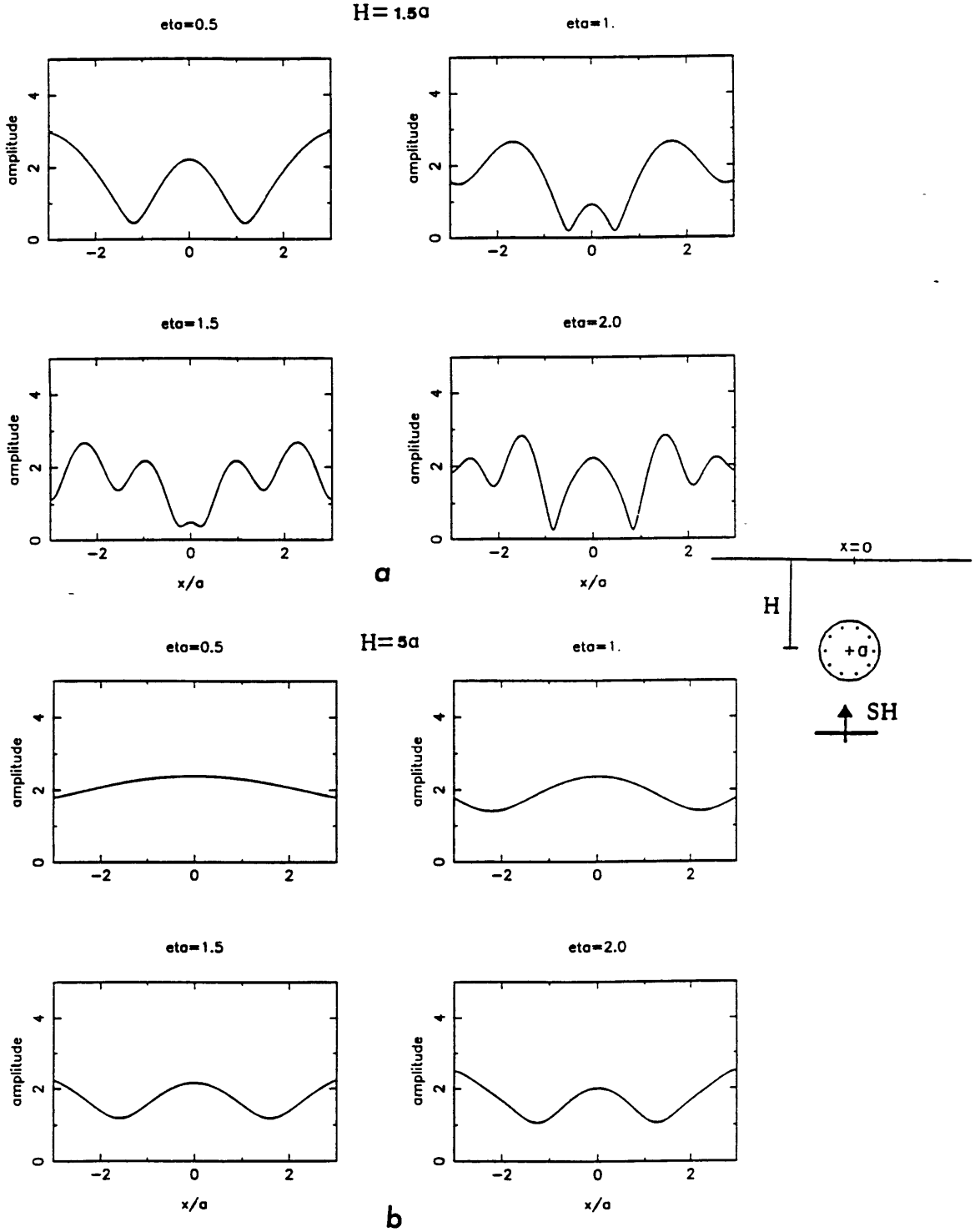

FIGURE 5.3 Solution for the ground motion at the free-surface of a half-space with a cylindrical cavity whose center is at a depth H from the surface. The ground motion is computed for $\eta = 0.5$, 1.0, 1.5, and 2.0. Results in (a), (b) are obtained using the proposed solution; and in (c), (d) using the exact solution (c), (d) modified from Lee (1977)

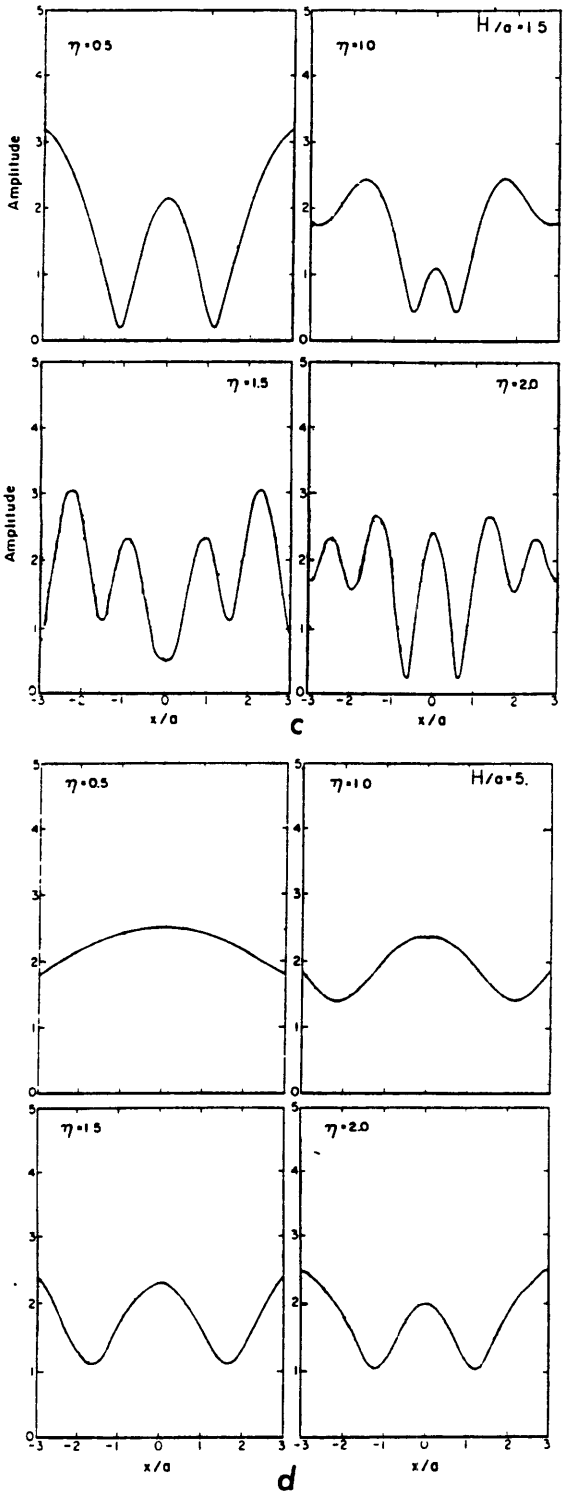

FIGURE 5.3

cavity in the half-space, i.e.

$$v_0(r_P) = \exp(-i\vec{k}.\vec{r}_P) + \exp(i\vec{k}.\vec{r}_P)$$

As shown in Figure 5.3 for $H/a = 1.5$ (a), (c); $H/a = 5$ (b), (d), and for several values of η, the accuracy of our numerical solution is excellent.

The case of two or more cavities is complicated and no explicit analytic results in either frequency or time domains are available. Some closed form solutions based on the wavefield representation by linear superposition of basis functions have been proposed by some authors (Waterman 1969, Kristensson and Ström 1978, Chaterjee et. al. 1978) but in most of these studies results are given for the average value of the physical quantity of interest (displacement for instance) in terms of the probability of finding one cavity within certain spatial interval. The involved algebra and the computation of large polynomial expansions required to compute the scattering for wavelengths comparable or smaller than the size of the cavities made them impractical for our purpose of comparing results. Instead we examine how accurately the traction-free condition along the boundaries of the cavities half-space is satisfied by our solution. A measure of the error in traction at a certain point on the stress free boundary is given by the fractional residual traction (introduced in Chapter II) defined here as

$$Tr_R(a,\theta) = 1 + \sum_{i=1}^{2}\sum_{j=1}^{N} A_{ij}\frac{Tr_{ij}}{Tr_0}(a,\theta)$$

where Tr_{ij} is the traction at this point acting on the plane with normal $\hat{n}$, due to the artificial source j on the boundary of cavity i, A_{ij} are the coefficients obtained after solving (5.7), and Tr_0 is the traction acting on the plane with normal $\hat{n}$ due to the incident wave at the same point, when there

are no cavities. The polar angle θ is measured from the center of the cavity, counterclockwise from the vertical. Thus, the fractional residual traction at the point where the error is estimated is equal to the total traction measured at this point (due to the incident wave plus all artificial sources), divided by the traction due to the incident wave only. This way to check the solution given by a boundary integral method has consistently shown that small residual along the boundaries correspond to an accurate solution of the problem (Benites and Aki 1989), and that the degree of accuracy depends to a large extent on the total amount of artificial wave sources distributed in order to correctly fulfil the boundary conditions. The geometry of our example is shown in the right top of Figure 5.4 The centers of the cavities are separated by a distance D. Our purpose here is to measure the residual traction for each cavity and estimate how sensitive it is to variations of separation distance D. In Figure5.4 (a), (b), (c) we show the results for 30^0 plane wave incidence and $\eta = 2$, using 30 artificial sources; and for D increasing from 1.2 to 2 times the diameter of the cavity. We observe that the values of the fractional residual traction in all cases are of the order of 10^{-3}. As D increases, the distribution of residual along the boundary becomes similar to that obtained for a single cavity ($D = \infty$).

The above example demonstrates not only that the presence of an additional cavity does not affect the accuracy of the solution obtained for one cavity in our first example, for any separation distance D, but also that the traction-free condition is fulfilled to a high degree of accuracy using 30 sources per cavity, as evidenced by the small values of residual normalized traction at the boundary of the cavities. It can be observed in Figure 5.4 that the absolute value of this residual is in no case larger than

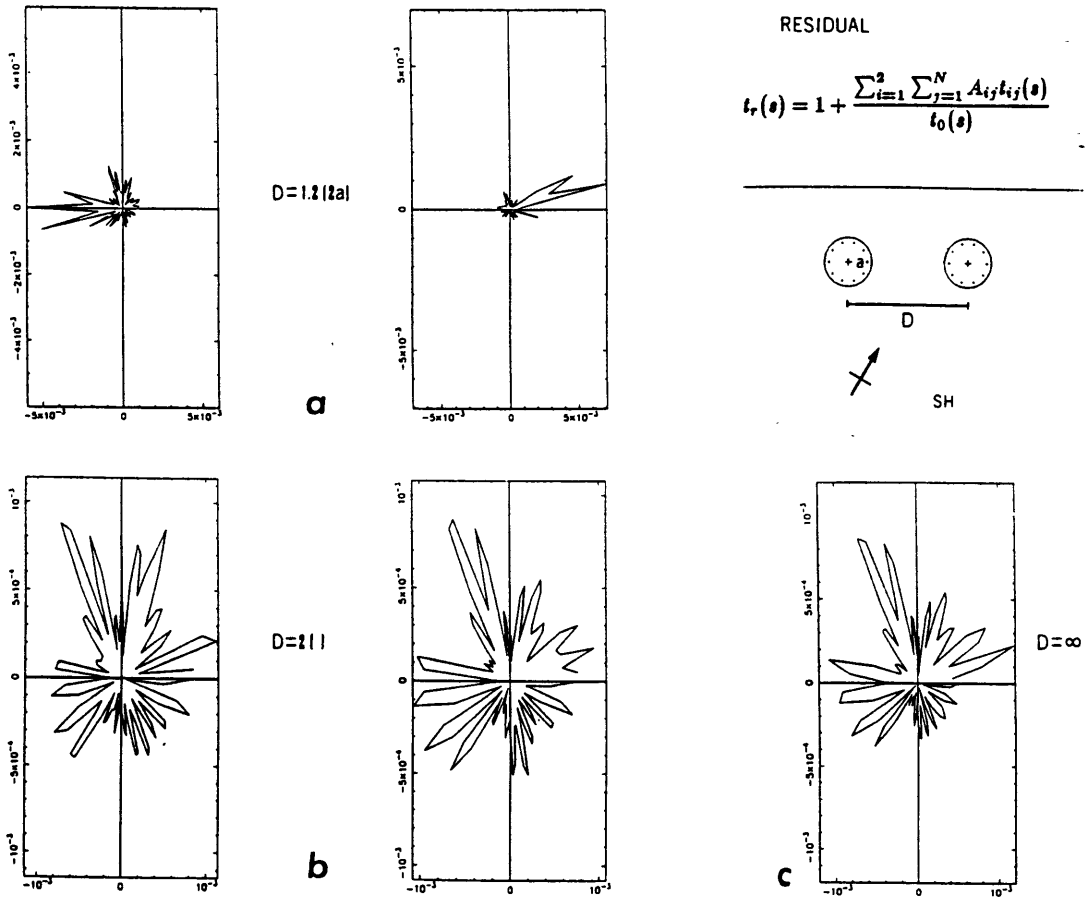

FIGURE 5.4 Residual traction computed along the boundaries of two cavities in a half-space, whose centre are at $1.5a$ depth and separated by a distance D. The angle of incidence of the primary wave is 30^0, measured clockwise from the vertical. In (a) $D = 1.2(2a)$ and in (b) $D = 2(2a)$. (c) corresponds to the residual traction computed for a single cavity. Note that as D increases the residual traction distribution along the boundary of each cavity becomes similar to that of a single cavity.

5×10^{-3}. We conclude that our method gives an accurate solution to the scattering problem for the case of two cavities. The case of any number of cavities can be treated similarly, by distributing a sufficient number of sources around each cavity to correctly satisfy the boundary conditions. For our experience, we select at least four sources per wavelength measured along the boundary in order to represent the external wavefield amplitude. Therefore, if the wavelength is λ, the minimun number of sources required will be $N_s = 8\pi a/\lambda$ for each cavity.

5.4 Multiple scattering in media with many regularly spaced cavities

In this section we analyze in time domain the wavefield generated by one, two, four, twelve and fifty cavities distributed in both half and full spaces, upon the incidence of either plane wave or wave from a point (line) source. This gradual increasing of cavity number is important in order to identify various scattered phases that arrive at the stations of a given seismic observation array, as the number of cavities increases. It is also helpful in understanding the seismograms obtained for more complicated structures, such as those containing a random distribution of cavities.

In the following examples we choose radius $a = 1$ (unit of distance), shear wave velocity $\beta = 1$ (unit of distance/ time). The synthetic seismograms are computed by inverse Fourier transform of the frequency response at 100 frequencies, in the range from $\eta = 0.02$ to $\eta = 2$, where $\eta = 2a/\lambda$ is a non-dimensional frequency. The input source-time function is the symmetric Ricker wavelet, described in Chapter III. We recall that both the real frequency f and η are related by $f = \beta\eta/2a$. For example, for a cavity radius of 100 m in the crust with S-wave velocity 3 km/s, $\eta = 2$ corresponds

to 30 Hz.

We start with computing the synthetic seismograms of the scattering due to one cavity in a homogeneous full-space, upon the incidence of a plane SH wave, shown in Figure 5.5 The seismograms are synthesized at 100 stations, deployed along the line A-A', covering a total range of $8a$. The center of the cavity is located at $x/a = 0$, $z/a = 1.5$. Breadth of the Ricker wavelet is 0.6 a/β seconds, which correspond to a characteristic wavelength of $0.77a$. The main feature observed here is the time-delay and attenuation of the incident wave at stations immediately above the cavity, in the region $|x/a| \leq 1$. The wavefield in this region is due to diffraction of the incident wave at points on the boundary where the incidence direction is perpendicular to the unit normal vector, e.g. the point marked by G in Figure 5.5(b). Upon hitting these points the incident wave creeps around the cavity (Keller 1962), radiating diffracted waves arriving at stations with a time delay proportional to their creeping path along the boundary and their travel path from the boundary to the station, as shown in Figure 5.5 (b). In Figure 5.5(a) we refer to the incident wave and creeping waves as phases d and c respectively, pointed by arrows in the seismogram corresponding to the station at $x/a = 4$. The reflected waves from the cavity boundary, which in turn are referred as phase r , are clearly defined in the seismograms, correctly showing the same polarity as the incident wave. By simple geometrical relations we estimate that their arrival at the farthest stations ($|x/a| = 4$) is about 1.2 a/β after the arrival of the incident wave, also pointed by an arrow in Figure 5.5(a). In order to observe the effect of 15^0 inclined incidence, we have computed the seismogram section shown in Figure 5.5(c). The three phases mentioned

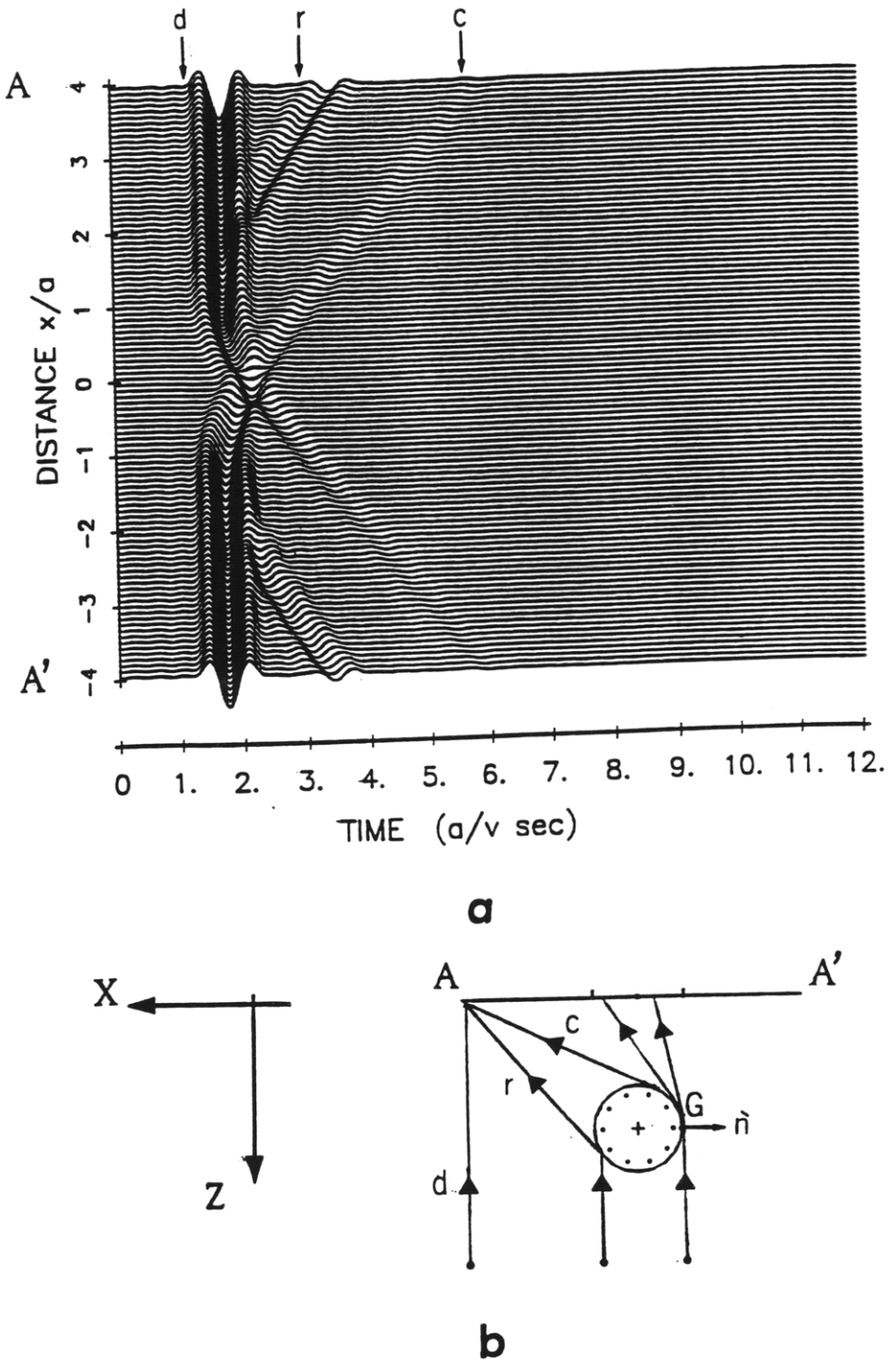

FIGURE 5.5 (a) Synthetic seismograms computed for the scattering due to one cavity in full space, upon the incidence of a plane wave, measured at 100 seismic stations along an observation line $1.5a$ above the center of the cavity. (b) ray diagram depicting the origin of the direct 'd', reflected 'r' and "creeping" 'c' phases observed in the seismograms shown in (a). $|x/a| < 1$ is region of diffraction.

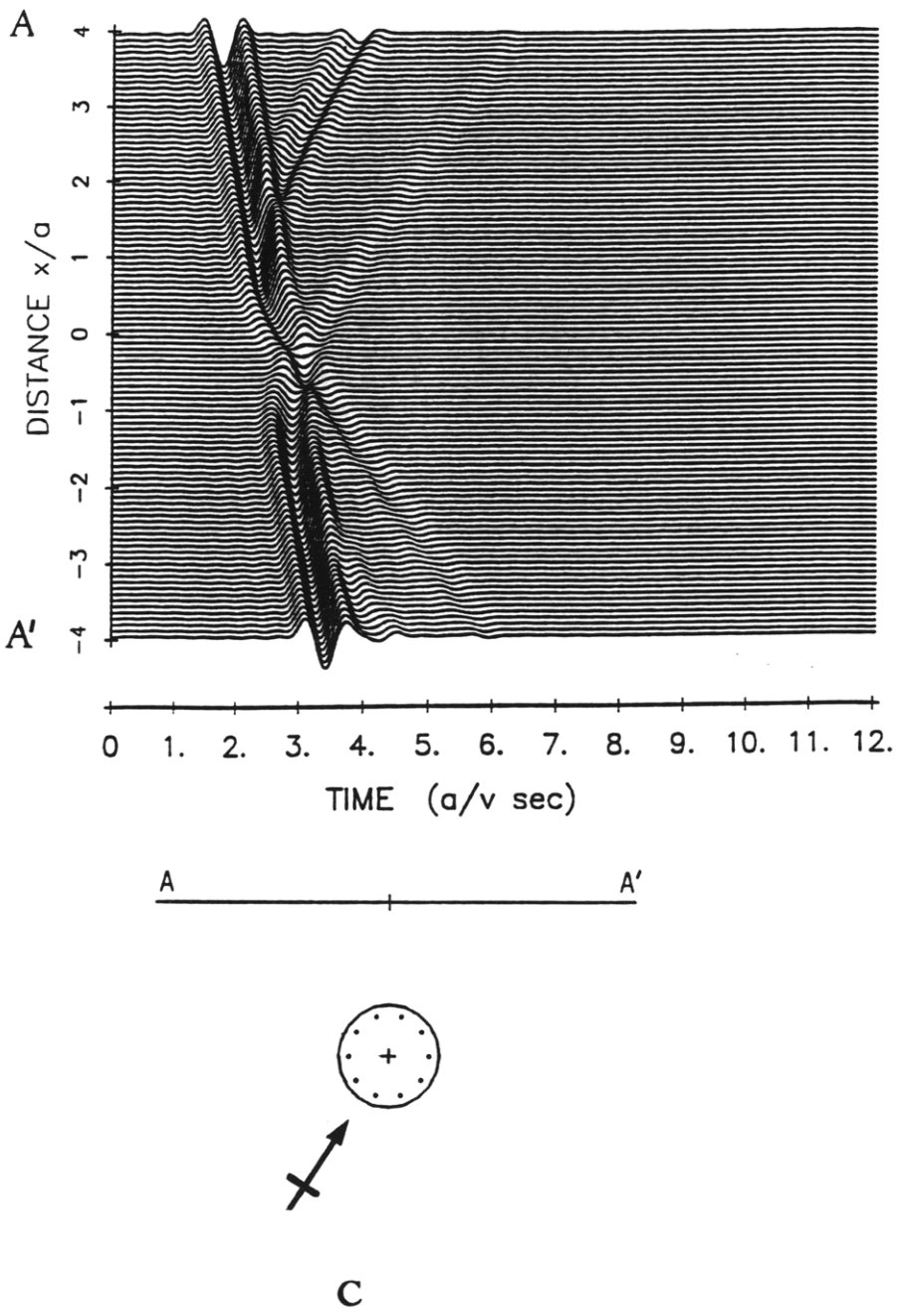

FIGURE 5.5 (c) synthetic seismograms computed when the angle of incidence of the primary wave is 15^0.

above are also clearly identified here, with strong phase r for stations on the side of source wave incidence. The wavefront corresponding to phase c appears as a smooth continuation of phase d beyond $|x/a| = 1$.

In Figure 5.6 we show the case of one cavity in a homogeneous half-space. All parameters are the same as those defined for Figure 5.5. The description of the scattering and diffraction phenomena is similar to the full-space case except for the effect introduced by the free-surface on the amplitude and duration of the seismograms. The amplitude is exactly twice as in Figure 5.5(a), and in addition to phases d, r and c, we observe later arrivals marked as $s1, s2, s3$ at regular time intervals of a/β, corresponding to multiple reflection of trapped waves between the free-surface and the top boundary of the cavity (see ray diagram 5.6(b)).

The case of two cavities in a full space is presented in Figure 5.7. The centers of the cavities are located at $x/a = \pm 1$ and $z/a = 1.5$, i.e., the minimun distance between their boundaries is $2a$. The observation line A-A' is located at $z = 0$. As was described for the case of a single cavity, we observe the arrivals of phases r_1 ,c_1 , r_2 , c_2 due to cavities 1 and 2 respectively (subscript 2 corresponds to the cavity at $x/a = -1$). In addition, we observe the arrival of four phases, r_{21}, r_{12}, r_{121} and r_{212}, separated by intervals of about $2a/\beta$, which correspond to the waves reflected between the boundaries of the two cavities (see ray diagram (b)). The subscripts indicate the order in which each reflection takes place; for instance r_{21} indicates that the wave reflected first by cavity 2 is thereafter reflected by cavity 1 before reaching a particular station. Similarly for r_{121}. We call them "interaction" phases. As we can see, it is quite cumbersome to identify each one of these arrivals in the seismogram section of Figure 5.7

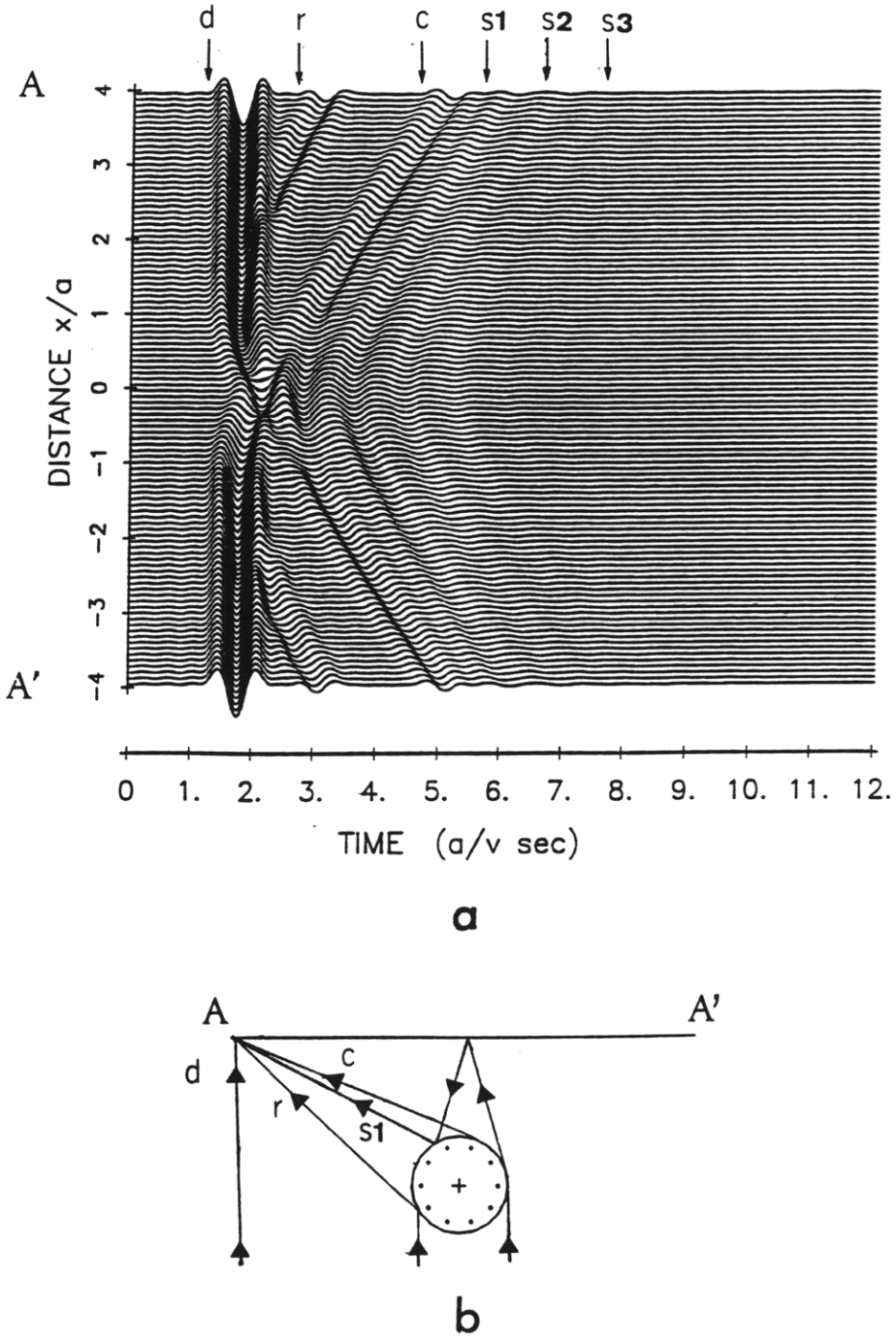

FIGURE 5.6 (a) Synthetic seismograms for the case of a cavity in half-space. Phases s1, s2, s3 correspond to waves reflected one, two and three times back and forth between the free-surface and the boundary of the cavity. In ray diagram (b) only s1 is shown.

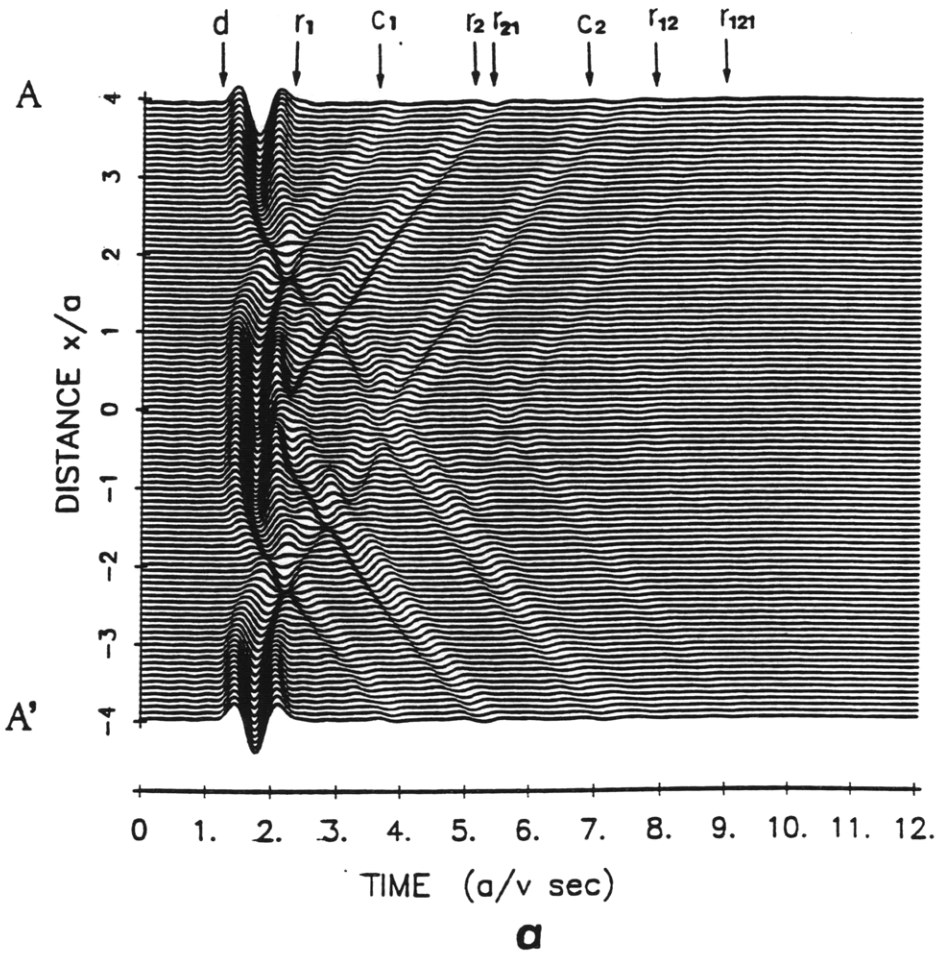

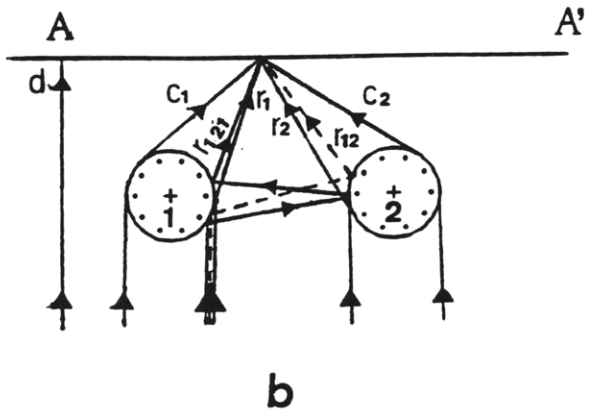

FIGURE 5.7 **Two cavities in full-space, (a) synthetic seismograms, (b) ray diagram. Their centre are separated by a distance equal to 4 a. The observation line is at 1.5 a above the centre. Subscripts indicate the cavity (1 or 2) where the phases originate.**

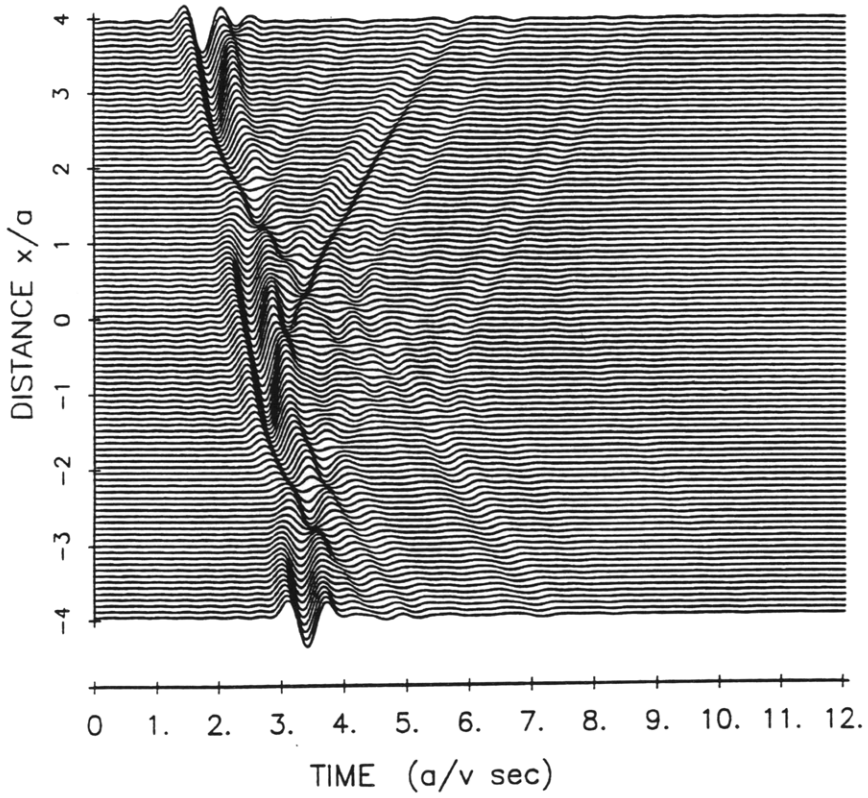

C

FIGURE 5.7 (c) corresponding seismograms for 15^0 incidence.

(a). For most part, they are interfering with the other phases, resulting in their disturbed wavefronts. This situation is not changed in Figure 5.7 (c), where we have computed the effect of 15^0 incidence on the above described phases.

In another experiment, we locate the centres of the cavities at $x/a = \pm 3$, $z = 1.5a$, i.e., the minimum distance between their boundaries is now $4a$. Results are shown in Figure 5.8. In this case the stations are deployed for a range of $10a$. Here we can identify clearly the phases r_{21}, r_{12}, r_{121} and r_{212} arriving at time intervals of about $4a/\beta$ seconds. The ray diagram for this case is similar to that in Figure 5.7 (b). Note that within the region $x/a = \pm 3$, the wavefront of phases r_{21} and r_{12} have the same curvature as r_1 and r_2 respectively (the same we can say about r_{121} and r_{212}). Outside this region their wavefronts merge with those corresponding to r_1 and r_2 respectively.

Summarizing the case of two cavities in a homogeneous full space, we can observe in general (e.g. station at $x/a = 4$ in Figure 5.7 (a)) the arrival of phases r_1 and c_1, due to the closest cavity, plus phases r_2 and c_2 due to the presence of the other cavity, plus the phases r_{21} and r_{121} corresponding to the interaction between them, as marked by arrows in Figure 5.7 (a). In Figure 5.9 we have computed the synthetics for the case of two cavities in a half-space. The geometry and parameters are the same as those for Figure 5.7. Again taking the stations at $x/a = 4$ as an example, we observe the arrivals of phases r_1 and c_1, r_{21}, r_{121}, plus $(s1)_1$, $(s1)_2$, $(s2)_1$ and $(s2_2)$ due to the effect of the free-surface. Note that the seismogram section in this case shows considerably more complexity than the corresponding full space case.

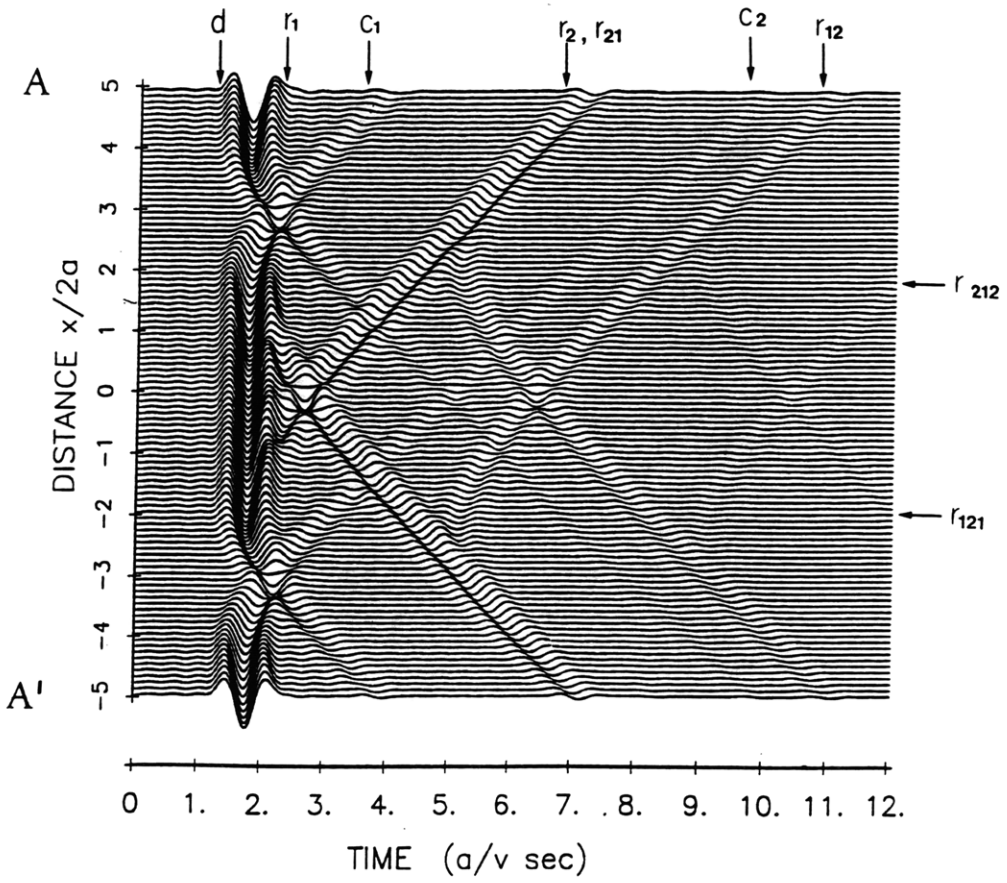

FIGURE 5.8 Two cavities in full-space, their centre separated by a distance 8 a. Phases r_{12} and r_{21} are more clearly defined in this case than in Figure 5.7 (a).

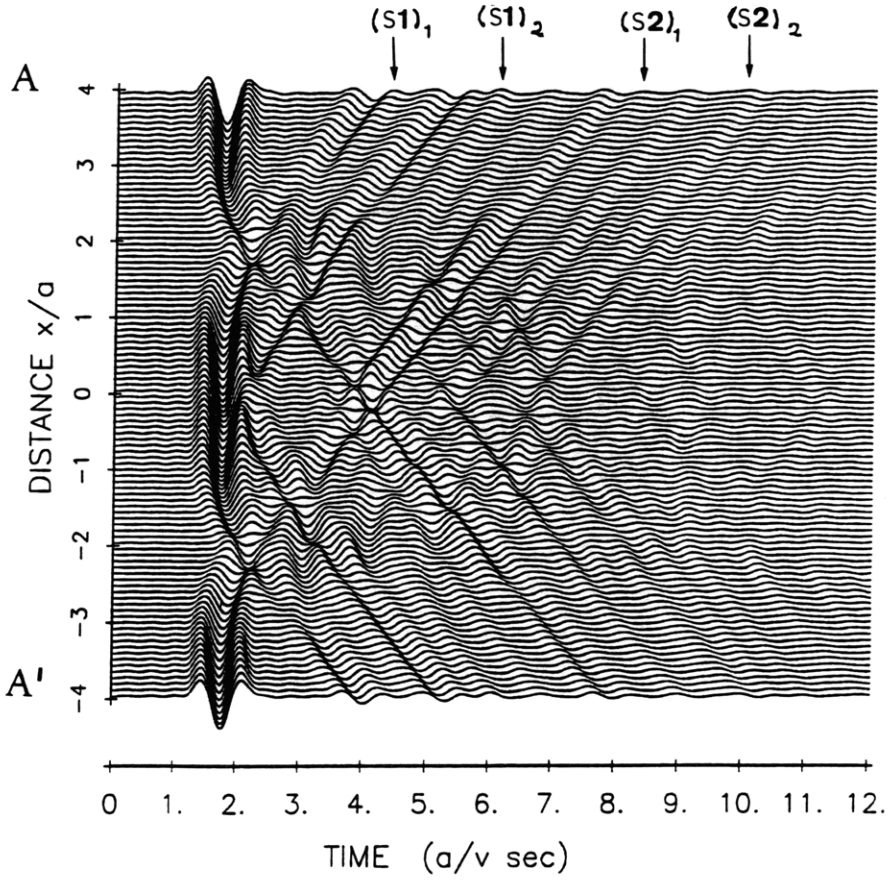

FIGURE 5.9 Two cavities in half-space. Geometry is similar to that in Figure 5.7, the observation line corresponds to the free-surface. s1 ans s2 are phases reflected once and twice back and forth between the free-surface and the boundaries of the cavities. Subscripts indicate the cavity (1 or 2) where the reflection took place, i.e., $(s1)_2$ is the wave reflected once back and forth between the free-surface and the boundary of cavity 2.

Figure 5.10 shows the case of two elliptic cavities in a half-space. The purpose of this exersice is to strengthen the arrivals of phases $(s1)_1$, $(s2)_1$, $(s1)_2$, $(s2)_2$, etc, since the trapped energy between the free-surface and the boundaries of the cavities is larger in this case than that for the case of circular cross-section, due to the stronger reflection from the cavity upper boundary. The cavity centers are located at $x/a = \pm 2a$, $z = 1.5a$, and in both the length of the major axis (horizontal) is a and that of the minor axis is $a/2$. We can observe in Figure 5.10 (a) that these phases have slightly larger amplitudes than when the cross-section of the cavities is circular. They arrive at regular time intervals of $2a/\beta$ seconds, i.e. twice the interval observed in Figure 5.7, since in this case the waves multiply reflected between the free-surface and the top boundary of the ellipse have to travel back and forth over the distance a. Interaction phases r_{12}, r_{21} are also observed here. For instance, the wavefront of r_{12} appears at about $x/a = -1$, and at $t = 4.5a/\beta$ seconds, almost merging the one corresponding to $(s1)_1$. In Figure 5.10 (b) the incident angle is 30^0. Besides the incident wave, the most dominant feature of these seismograms are the phases $(s1_1)$, $(s2_1)$, $(s1_2)$, $(s2_2)$... , whose amplitudes are about twice as those for normal incidence. This is due to the fact that more waves get trapped between the free-surface and the top boundaries of the cavities. We can also observe well defined interaction phases r_{12} and r_{21}. The reflected and creeping phases appear with smaller amplitudes than when the incidence is normal.

In the following examples of scattering by four, twelve and fifty cavities we can observe that the resulting seismograms are composed of superposition of the phases described above, plus the phases due to the mutiple scattering and creeping of these phases for all cavities. Since the complex-

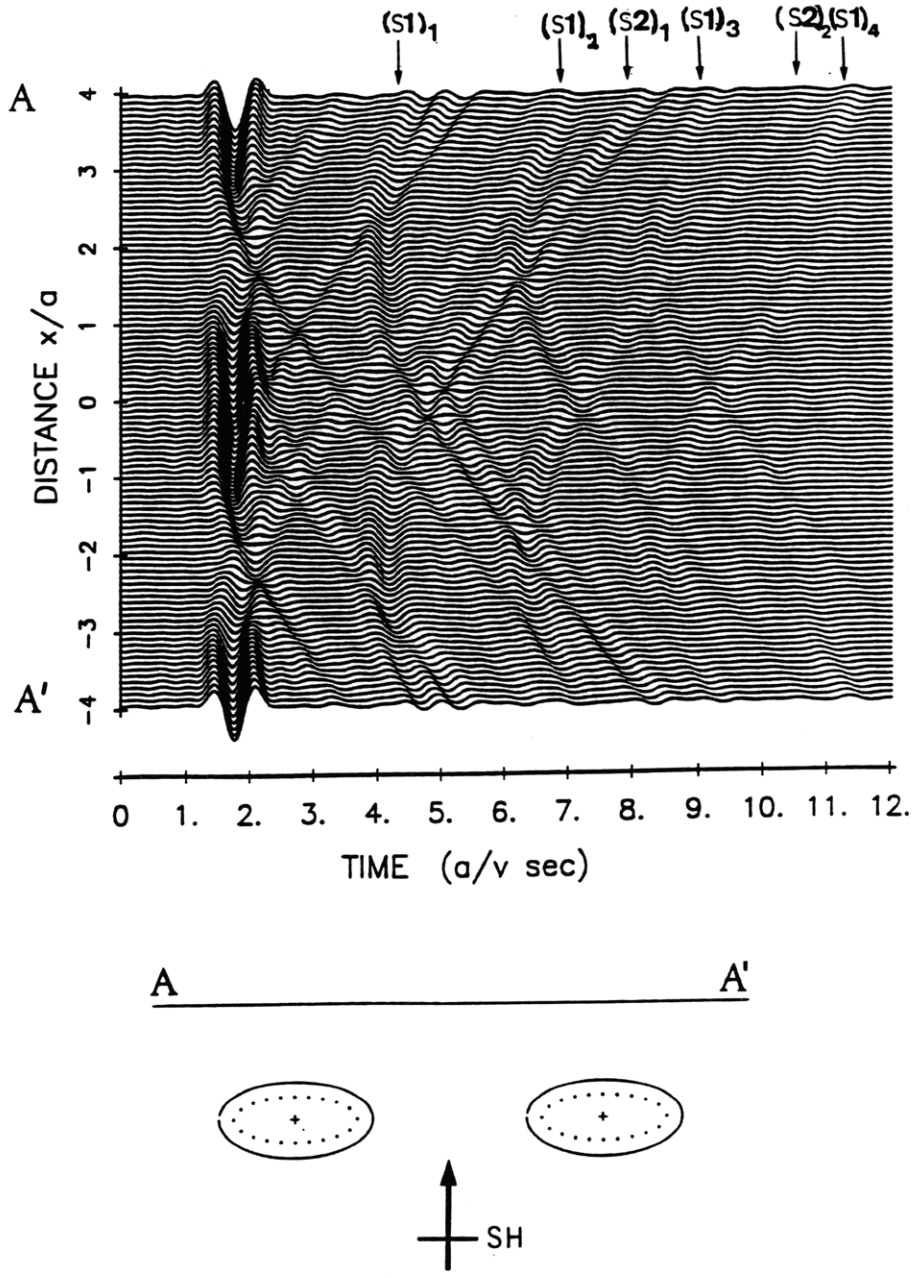

a

FIGURE 5.10 Synthetic seismograms for two elliptical cavities in half-space for (a) normal incidence; and (b) 15^0 incidence. The centre of the cavities are at $x/a = \pm 2$, the lengths of its major (horizontal) axis and minor (vertical) axis are a and $a/2$, respectively.

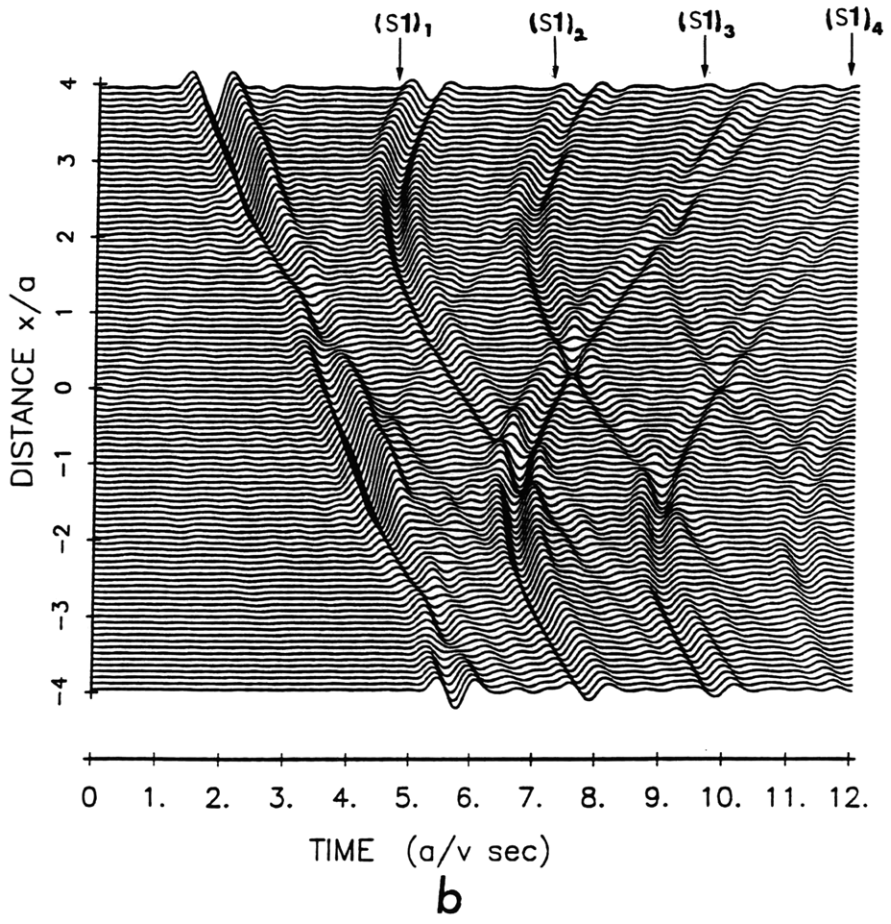
(S1)1
(S1)2
(S1)3
(S1)4
DISTANCE x/a
4
3
2
1
0
-1
-2
-3
-4
0
1.
2.
3.
4.
5.
6.
7.
8.
9.
10.
11.
12.
TIME (a/v sec)
b

FIGURE 5.10

ity of the seismograms makes it very difficult to identify individual phases, we comment only on the observed general feature of scattering.

In Figure 5.11 (a) and (b) we present the case of four cavities in full and half spaces, respectively, for normal incidence. The centre of the cavities are located at $(2a, 1.5a)$, $(2a, 5.5a)$, $(-2a, 1.5a)$, and $(-2a, 5.5a)$. The amplitudes of individual phases are weaker here than those in the corresponding cases of two cavities, because part of the energy of the incident wave has already been lost by scattering at the two deeper cavities before reaching the upper two (energy carried by waves bounced back to the infinity). We observe in general the same arrivals than those in the corresponding cases of two cavities (Figures 5.7 (a) and 5.9 respectively), plus the waves scattered at the deeper cavities, which arrive after $t = 6a/\beta$ at stations within the range $x/a = \pm 2$.

Figure 5.12 shows the scattering due to twelve cavities in half-space, for normal incidence (a) and 30^0 incidence (b). The cavities are distributed as three horizontal rows of four cavities each, whose centre are located at $x = \pm 2a, \pm 6a$. The depths to the center of the cavities in each row are $z = 1.5a$, $5.5a$ and $9.5a$. The seismograms are computed for the Ricker wavelet with breadth $t_b = 1.2a/\beta$, which corresponds to $\lambda_c = 1.5a$. In (a) note that the seismograms of stations located within the range $x/2a = \pm 3$ show more arrivals with relatively larger amplitudes for the duration of $24a/\beta$ than those of stations outside this region. Thus, the seismic signal appear to last longer within the horizontal range of the cavity distribution, due to energy supplied from multiple scattering. The effect of spatial finiteness of the distribution is seen at stations located in the neighborhood of the edges, at $x/a = \pm 3$, particularly clear at times 3.2, 5.2 and $7.2a/\beta$ seconds

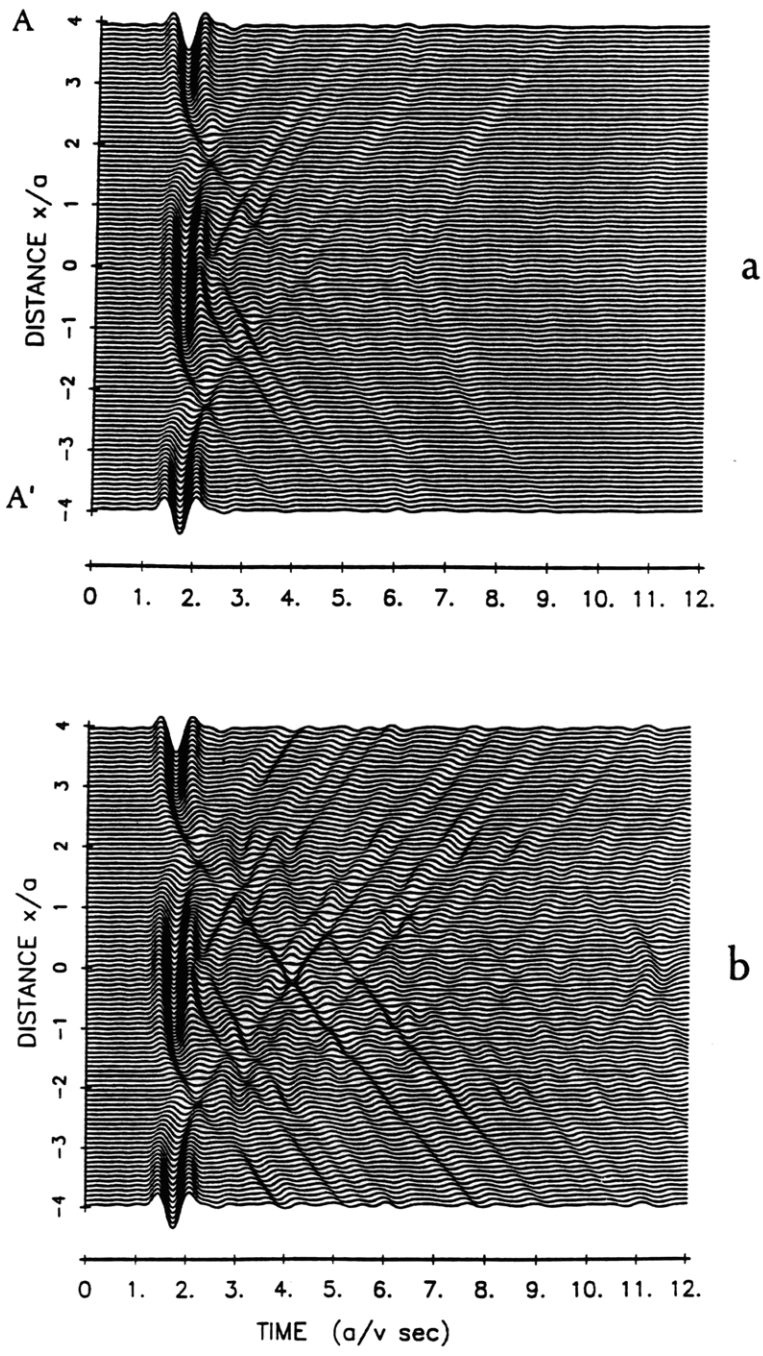

FIGURE 5.11 Four cavities uniformly distributed in (a) full-space, (b) half-space. The position of their centre are at $x/a = -2, z/a = 1.5, x/a = -2, z/a = 5.5, x/a = 2, z/a = 1.5, x/a = 2, z/a = 5.5$.

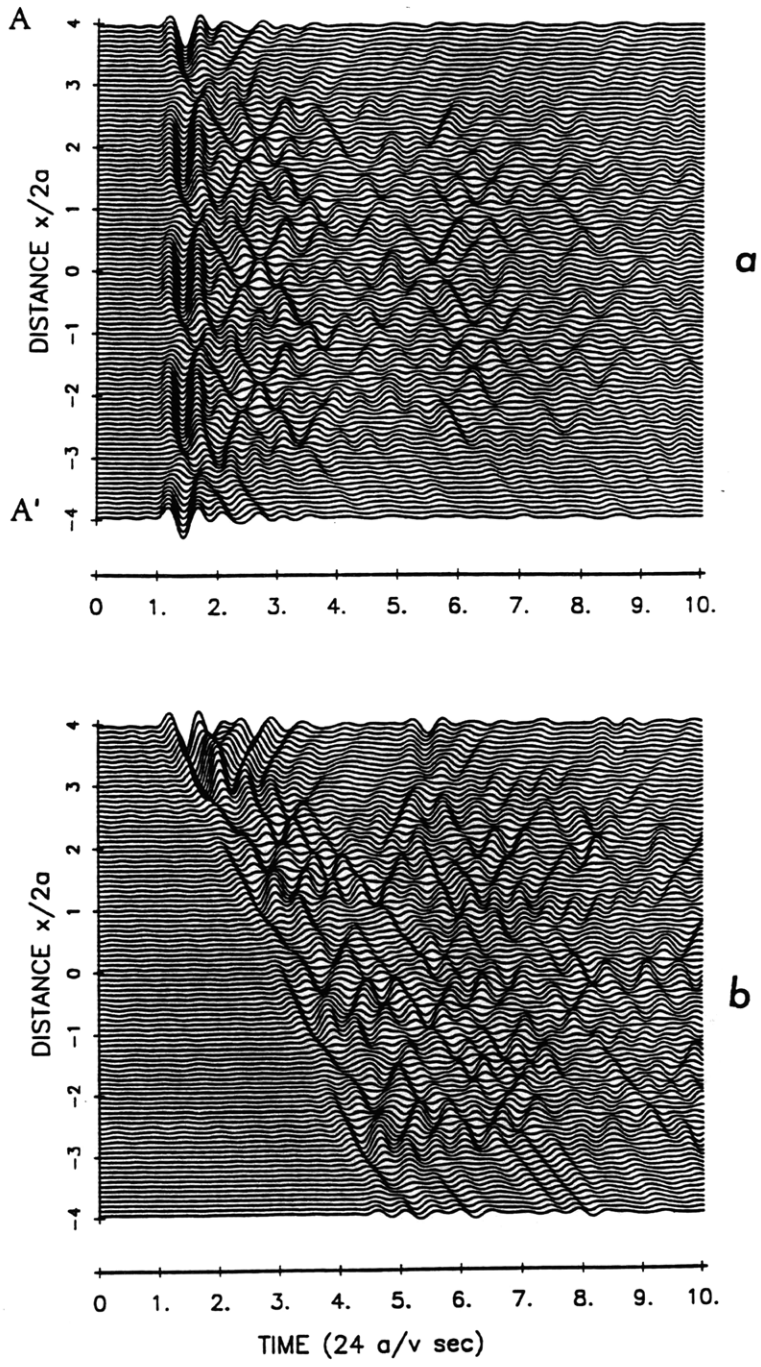

FIGURE 5.12 Twelve cavities in a half-space, arranged in three rows of four cavities each. The centers of the cavities in each row are located at $x/a = \pm 2$, $x/a = 6a$, at depths $1.5a, 5.5a$ and $9.5a$ respectively. (a) corresponds to normal plane wave incidence and (b) to 30^0 incidence.

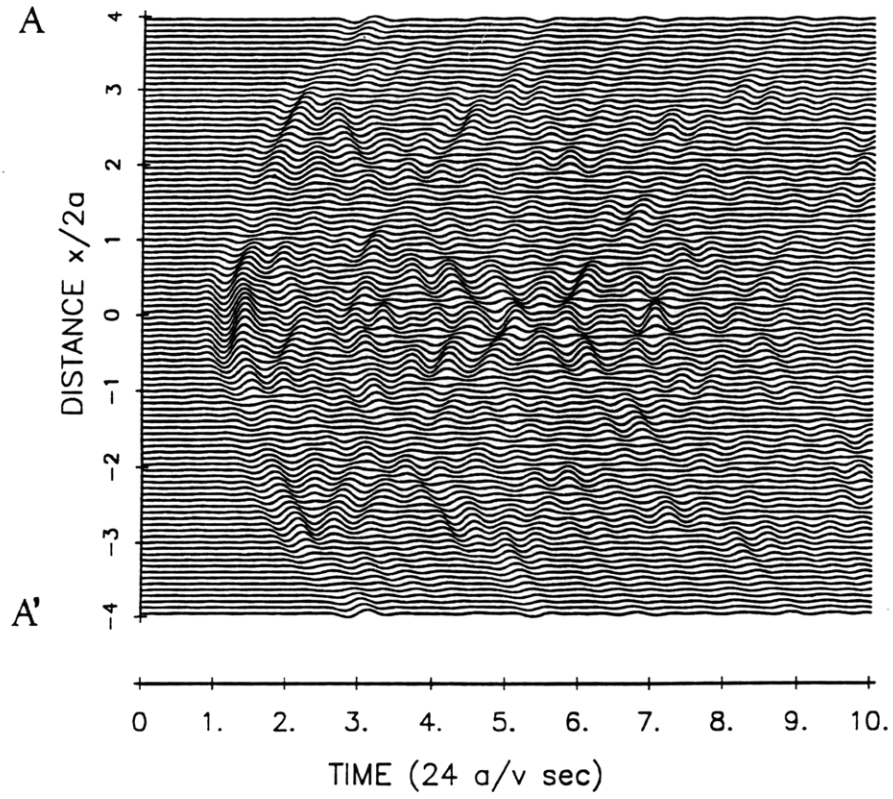

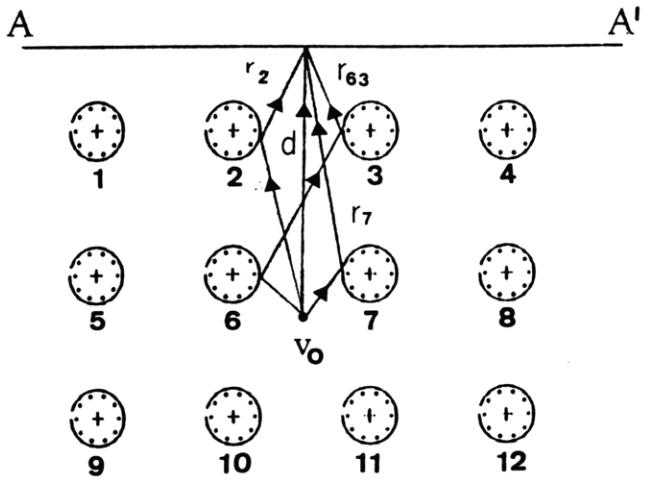

FIGURE 5.13 A line source located at $x/a = 0$ and $z/a = 7$ as incident wave for the case of twelve cavities, described in Figure 5.12. Subscripts indicate the cavity at which the reflection takes place.

. We observe that upon hitting the boundaries of the cavities part of the scattered waves are reflected back into the region $x/a = \pm 3$, while the rest are transmitted (leaked) outside it. The description of the scattering for (b) is similar to that for the normal incidence, except that here the amplitudes of the scattered waves are larger on the side of the incidence than the other side. For comparison, we have computed the synthetic seismograms for the case of these twelve cavities for a line source, located at $x = 0$, $z = 7a$, as shown in Figure 5.13. The input source time function is again a Ricker wavelet. For stations located within the range $x/2a = \pm 1/2$ the first arrivals correspond to waves that travel through the cavity-free path. It is interesting to note that at some stations in the neighborhood of $x/2a = 0$ the amplitude of later arrivals in their seismograms increases with time, being the largest between the time 12 a/β and 16.8 a/β, and decreasing after this interval. Apparently this is a "focusing" effect caused by the contribution of multipath waves that arrive at those stations at the same time. As examples we have drawn (see ray diagram in Figure 5.13) once reflected phases r_2, r_7 at cavities 2 and 7 respectively, which arrive at the same time at $x/2a = 0$. We can construct also r_{63}, r_{632}, and others in a similar manner (the subscripts indicate the cavity at whose boundary they are reflected). This is possible only for uniform distributions. No such phases are identifiable for random media, as we will see in the next section.

5.5 Scattering in media with randomly distributed cavities

In this section we compute the synthetic seismograms corresponding to the scattering of a plane wave in media with many cavities randomly distributed with respect to a certain cartesian coordinate system. Compared to the examples presented in the previous section, here it is much more

difficult to identify specific scattered phases; instead we shall be interested in the average characteristics of the scattering shown in the seismograms, which may in turn reflect the statistical nature of the prescribed random media.

First we consider a half-space with 50 cavities as depicted in Figure 5.14 (a). As in the previous section, all cavities have identical cross-section of radius a and the shear wave velocity of the half-space is 1 (unit of distance/second). The spatial range of the model is $80a$ along the free-surface, and $30a$ in depth. To generate the random distribution of cavities we first generate two independent sequences of fifty random numbers x_i, z_i $(i = 1, ..., 50)$ corresponding to a uniform probability in space defined by $x - z$ coordinates. Each point (x_i, z_i) is the center of a cavity. We must point out that the random generation is such that the cavities do not overlap; in fact we have imposed that the minimum distance between any randomly generated pair of points must be $2.2a$, so that the minimum distance between the boundaries of the two closest cavities of the distribution cannot be smaller than $a/5$. When the points (x_i, z_i) and (x_j, z_j), where $j > i$, do not satisfy this condition, (x_j, z_j) is eliminated and another pair of numbers are generated. The synthetic seismograms are computed for normal incident plane SH wave, with Ricker wavelet source-time function, and for non-dimensional frequencies up to $\eta = 1.6$, which is equivalent to $\lambda_c = 1.25a$. Synthetics are computed at 100 stations along the free-surface, for the duration of $65a/\beta$. The results are shown in Figure 5.14 (b), (c) and (d). In (b) the breadth of the input wavelet is $6.25a/\beta$, which yields $\lambda_c = 8a$. This is the case of long wave scattering, where we observe significative fluctuations in both amplitude and time delay of the first arrivals

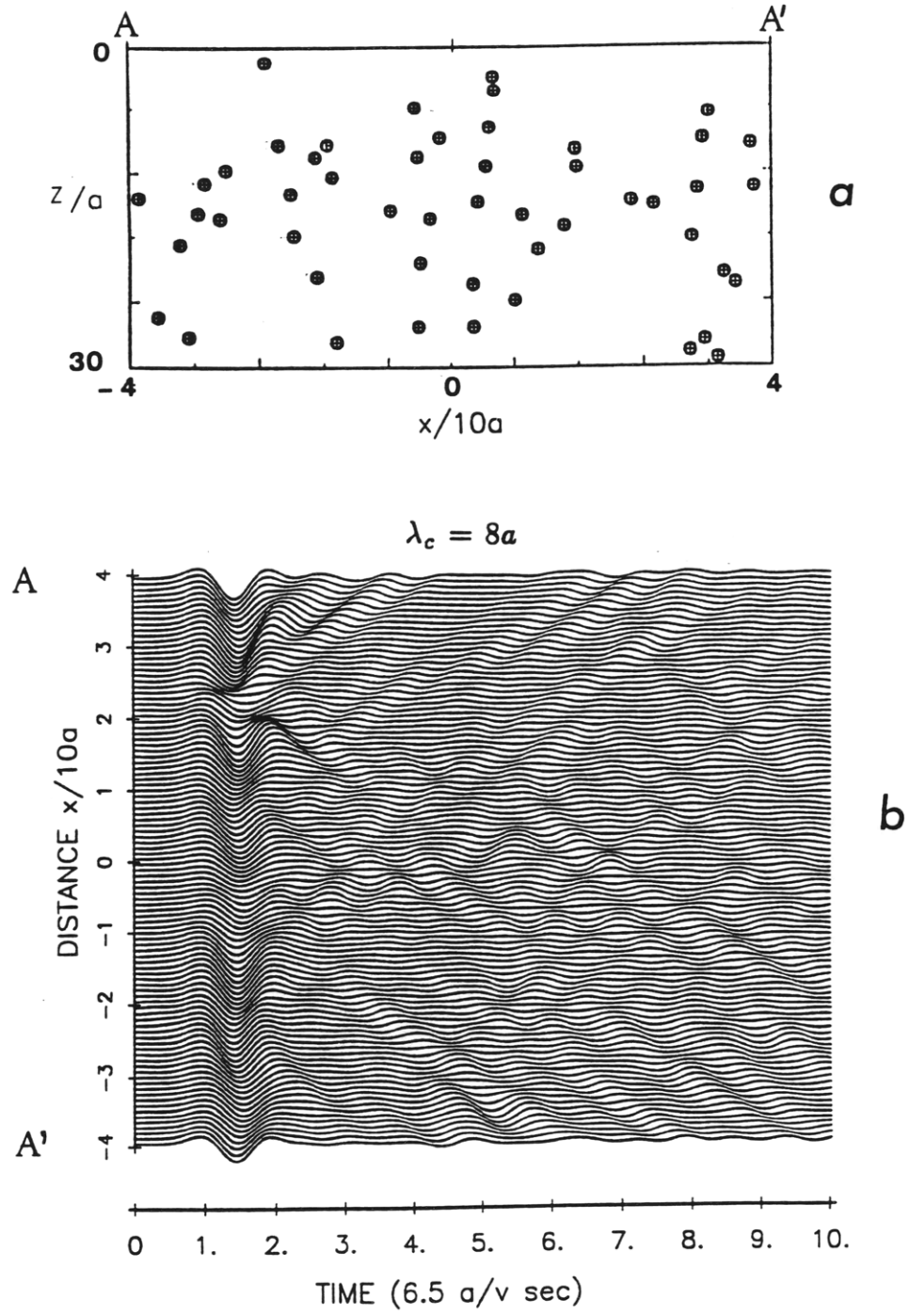

FIGURE 5.14 (a) Fifty cavities randomly distributed in a half-space. The horizontal range of the model is $80a$ and its depth $30a$. In (b) and (c) the synthetic seismograms are computed for characteristic wavelengths equal to 4 and 1.6 times the size of the cavity. In (d) the characteristic wavelength is equal to the size of the cavity.

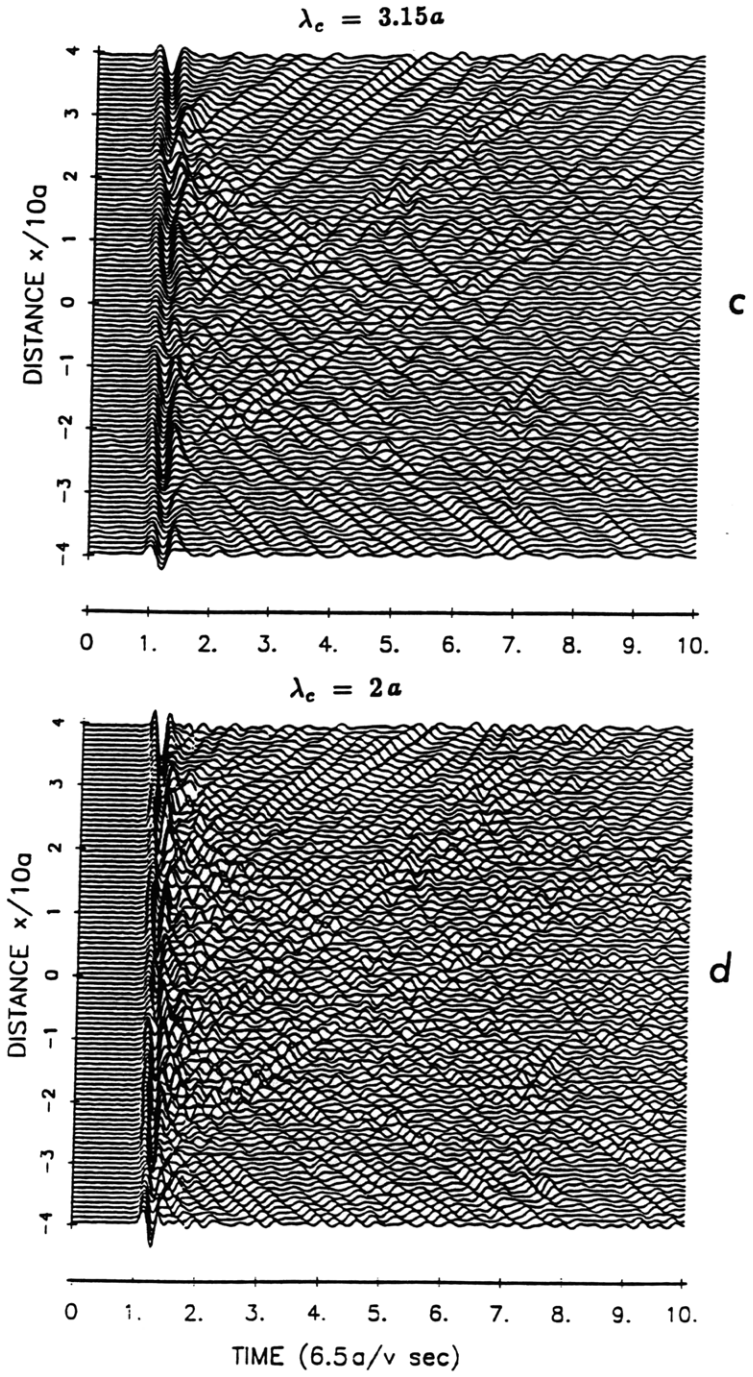
$\lambda_c = 3.15a$
DISTANCE x/10a
4
3
2
1
0
-1
-2
-3
-4
0 1. 2. 3. 4. 5. 6. 7. 8. 9. 10.
c
$\lambda_c = 2a$
DISTANCE x/10a
4
3
2
1
0
-1
-2
-3
-4
0 1. 2. 3. 4. 5. 6. 7. 8. 9. 10.
TIME (6.5a/v sec)
d

FIGURE 5.14

at stations immediately above a cluster of scatterers. The effect of truncation at both ends of the cavity distribution can be seen starting at stations around $x/10a = -3$, after about $32.5a/\beta$ of their seismograms, where waves are transmitted into the homogeneous medium and reflected back into the region of distributed cavities, by the cavities located at the edge of the distribution. They arrive with relatively large amplitudes (comparable to the incident wave). In (c) we have reduced the input breadth to $2.45a/\beta$, or $\lambda_c = 3.15a$ and in (d) to $1.63a/\beta$ or $\lambda_c = 2a$. Note the tremendous complexity of the seismograms that arises as the wavelength becomes smaller, approaching the diameter of the scatterer. We observe that at stations within $|x/10| \leq 2a$ in particular, the seismograms seem to be stationary in time, showing the arrivals of multiply scattered phases with quite large amplitudes for most of their duration shown here. At stations outside this region the seismograms show the side effects due to the truncation of the model, as described above, although the back reflected waves have much less amplitudes for the wavelengths considered here than for the wavelength considered in (b).

For comparison we have computed the synthetic seismograms for identical random distribution of cavities but considering full-space. Results are shown in Figure 5.15 (a) and (b), for $\lambda_c = 3.15a$ and $\lambda_c = 2a$, respectively. We observe that scattered waves arriving earlier than about $35a/\beta$ are similar to those observed for half-space, with amplitudes one half. However, later arrivals do not show such similarity in general. For the half-space case we must consider the backscattered waves caused by the total reflection at the free-surface. This suggests the importance of the free-surface effect (and more generally, of the layered structure) in the study of scattering by

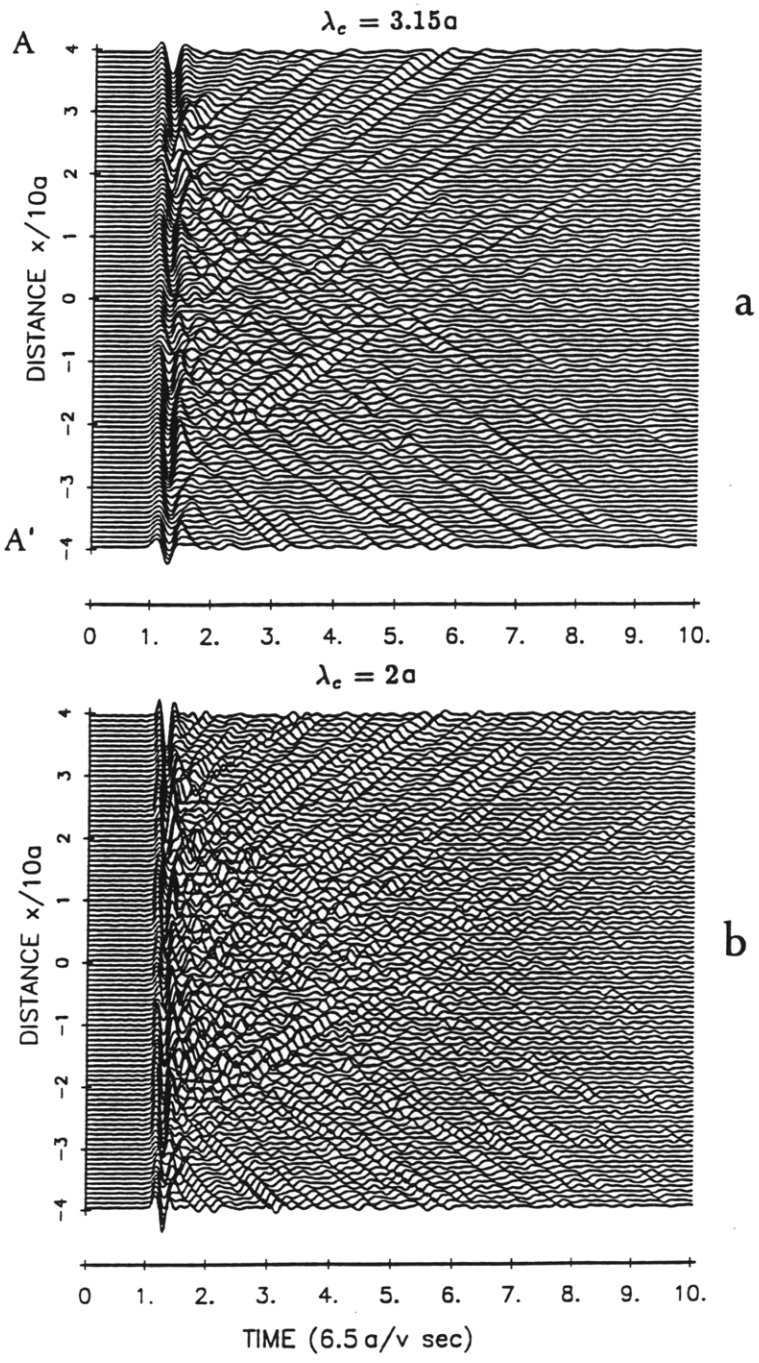

FIGURE 5.15 Synthetic seismograms for the same random distribution of fifty cavities shown in Figure 5.14(a), but here in full-space. Compare the seismograms in (a) and (b) with those shown in (c) and (d) of Figure 5.14. Note the effect on the overall scattering of the waves scattered back from the free-surface.

many heterogeneities in the Earth's crust, in particular when later part of the seismograms are used.

Finally, let us compare the seismograms shown in Figure 5.14 (c) with those obtained for the case in which we consider the same realization of random distribution in half-space, but reduce the radius a of the cavities by one half. In other words, if a' is the radius of the cavities in this model, then $a' = 0.5a$, where a is the radius of the cavities in the model corresponding to Figure 5.14 (c). In Figure 5.16 we have computed the synthetic seismograms for this case, considering $\lambda_c = 3.15a'$, as in the case of Figure 5.14 (c). We observe that although some common arrivals can be observed in both seismogram sections, the overall scattering is significatively different. Most remarkable is that the complexity of the seismograms appears to be homogenized for all stations, i.e. the scattering process becomes spatially uniform in this case. This suggest the possibility that certain nature of heterogeneity distribution may be diagnosed from the observed seismograms.

5.6 Measurement of Q^{-1}

Finally, we measure the attenuation factor Q^{-1} for the amplitude decay of direct arrivals due to scattering. We use the seismograms obtained for the case of a full space with 50 cavities randomly distributed and primary plane wave incident along z-axis (shown in Figure 5.15). We measure the peak amplitude, i.e. the maximum amplitude measured from zero to peak, of the primary wave in the synthetic seismograms of selected stations, obtained after applying a Butterworth band pass filter to the spectrum computed at each station. Let us recall that spectra at all stations were computed for non-dimensional frequencies η up to 1.6 in the present model. We choose

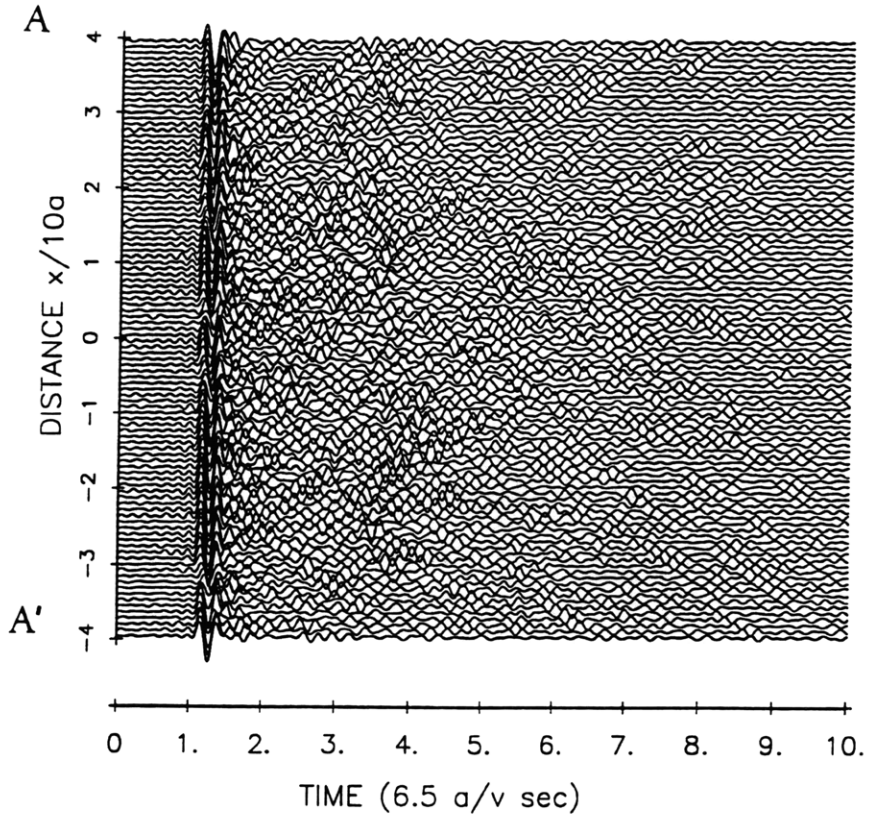

FIGURE 5.16 The cavity distribution in this case is the same as in Figure 5.15 (full-space), but the radius of each cavity is 1/2 times smaller, i.e. $a' = a/2$. The characteristic wavelength is $\lambda_c = 3.15a'$. Compare the scattering shown in the seismogram section with that of Figure 5.15 (c), in which $\lambda_c = 3.15a$. The scattering in this case appears to be more spatially uniform .

five central non-dimensional frequencies, 0.1, 0.15, 0.3, 0.6 and 1.2, and applied the filter with octave bandwidth. These frequencies are equivalent to wavelengths $20a$, $13.33a$, $6.67a$, 3.33, $1.67a$ respectively. Figure 5.17 shows two examples of bandpass filtered seismograms with central frequencies (a) 0.15 and (b) 1.2, respectively. The frequency range lower than 0.1 has been discarded because the corresponding wavelength (over $20a$) is comparable to the total travel distance of the waves (within $30a$), so that there are not enough cycles to properly compute the amplitudes at the different stations. In other words, our measurement for this frequency range may lead to an unstable value of Q^{-1}.

Since there is no geometrical spreading for primary plane waves, the peak amplitudes $A(\omega)$ of the direct arrivals after passing the scattering zone with thickness h can be expressed using the relation

$$A(\omega) = A_0 \exp\left(-\frac{\omega h}{2\beta Q}\right) \tag{5.8}$$

where A_0 is the peak amplitude of incident wave and $\omega = 2\pi f$. In order to avoid the contamination by waves reflected back from the boundaries of the cavities at the end of the distribution, we use the seismograms of 60 stations located around the center $x/10a = 0$ and in the range $x/10a = \pm 2.5$, where these contaminating waves arrive later than $65a/\beta$. In Table I we have listed the values of kd for each characteristic frequency, where $k = \omega/\beta$ is the wavenumber and $d = 2a$ is the diameter of the cavities. By definition, $kd = 2\pi\eta$. Their corresponding values of Q^{-1} and standard deviations computed from the mean of amplitude fluctuations for the chosen 60 seismograms are also listed in Table I:

(over)

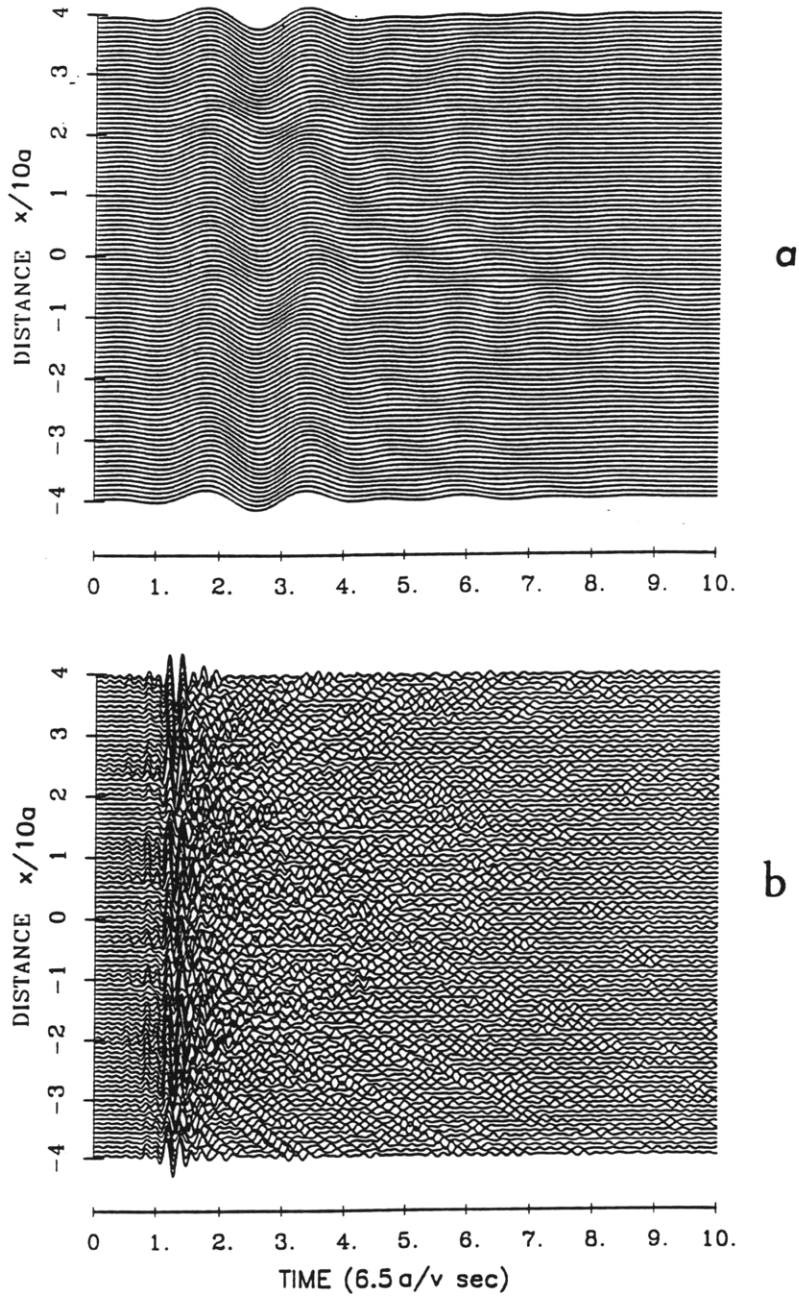

FIGURE 5.17 Examples of synthetic seismograms obtained after a Butterworth band pass filter was applied to the seismograms shown in Figure 5.16. In (a) the central non-dimensional frequency $\eta = 0.15$ ($\lambda_c = 13.3a$) and in (b) 1.2 ($\lambda_c = 1.67a$). The observed noise is due to the effect of the filter.

TABLE I

η	kd	$Q^{-1} \pm \sigma_d$
0.10	0.63	$-3.63 \times 10^{-3} \pm -7.64 \times 10^{-3}$
0.15	0.94	$6.08 \times 10^{-3} \pm 5.93 \times 10^{-3}$
0.30	1.88	$1.53 \times 10^{-2} \pm 1.03 \times 10^{-3}$
0.60	3.77	$1.07 \times 10^{-2} \pm 6.87 \times 10^{-3}$
1.20	7.54	$6.24 \times 10^{-3} \pm 4.34 \times 10^{-3}$

These values (except the first) are plotted versus $\log(kd)$ in Figure 5.18. As mentioned above, the first value is unreliable because the amplitude is measured for extremely low frequency.

As far as the authors know, there are no studies on the direct measurement of frequence dependency of Q^{-1} for randomly distributed cavities for such a high frequency, neither experimental nor numerical. Matsunami (1989) studied scattering attenuation in duralumin plates with randomly distributed holes (2-D) using ultrasonic waves. In his experiments the radius a of the holes was about 2 mm, the S-wave velocity of the material $\beta \simeq 3.0$ mm/μsec and the maximum value of the ratio of the diameter of the holes to the input wavelength (η) was 0.17, i.e. $\lambda = 23.5$, which corresponds to frequency 127.5 KHz. For the same parameters, our value of $\lambda = 2a$ ($\eta = 1$) in Figure 5.15 (b) corresponds to frequency 750 Khz.

Studies of scattering attenuation in random media characterized by autocorrelation function (see Herraiz and Espinoza 1987 for review) have used Born approximation and certain criterion for excluding the forward scattering loss to estimate Q^{-1}. These studies show that Q^{-1} increases proportional to $(ka)^3$ for $ka < 1$ following the Rayleigh scattering (Chernov 1960), peaking around $ka = 1$ (Sato 1982 , Wu (1982), then decreasing as ka

increases (or equivalently, as frequency increases) according to power law, with power depending on random models. For instance, for exponential autocorrelation function Q^{-1} is proportional to $(ka)^{-1}$ for $ka > 1$. Although our model with randomly distributed cavities cannot be compared directly to such stochastic random models characterized by autocorrelation functions, we note that our result on Q^{-1} vs kd (see Figure 5.18) also shows that Q^{-1} is roughly proportional to $(kd)^{-1}$ for $kd > 2$, where d is the diameter of the cavity.

More direct comparison can be made between our results and those of Varadan et. al. (1978) who studied SH waves in composite materials with cylindrical inclusions, using T-matrix formulation and statistical average of the wavefield, and for the scatterer concentration $c(= \pi a^2 n_0)$ from 0.3 to 0.7, where n_0 is the number of scatterers per unit area. In our model $c = 0.07$. They obtained a behavior of Q^{-1} vs kd similar to the one described above. By converting their attenuation coefficient α to Q^{-1} according to $\alpha = \omega(Q\beta)$, where β is the wave velocity, their results show that Q^{-1} peaks at $ka \simeq 1$ and decays sharply for $ka >\sim 1$. The peak value of Q^{-1} increases with the scatterer concentration c, and they also show that it is larger for elliptic cross-sectional shape of the scatterers than for circular one. The extension of the T-matrix formulation and statistical approach to the case of elastic 3-D scatterers (spheres) distributed randomly in a full-space (Varadan and Varadan, 1989) yields similar behavior of Q^{-1} vs ka, for concentration $c = 0.05$. Kikuchi (1981) studied Q^{-1} vs ka for SH waves in a medium with infinitesimally thin cracks, and found similar behavior with the peak at $ka \simeq 1$ to 2, where a is the half-width of the crack.

Observed Q^{-1} for S-waves in the lithosphere has usually peaks around

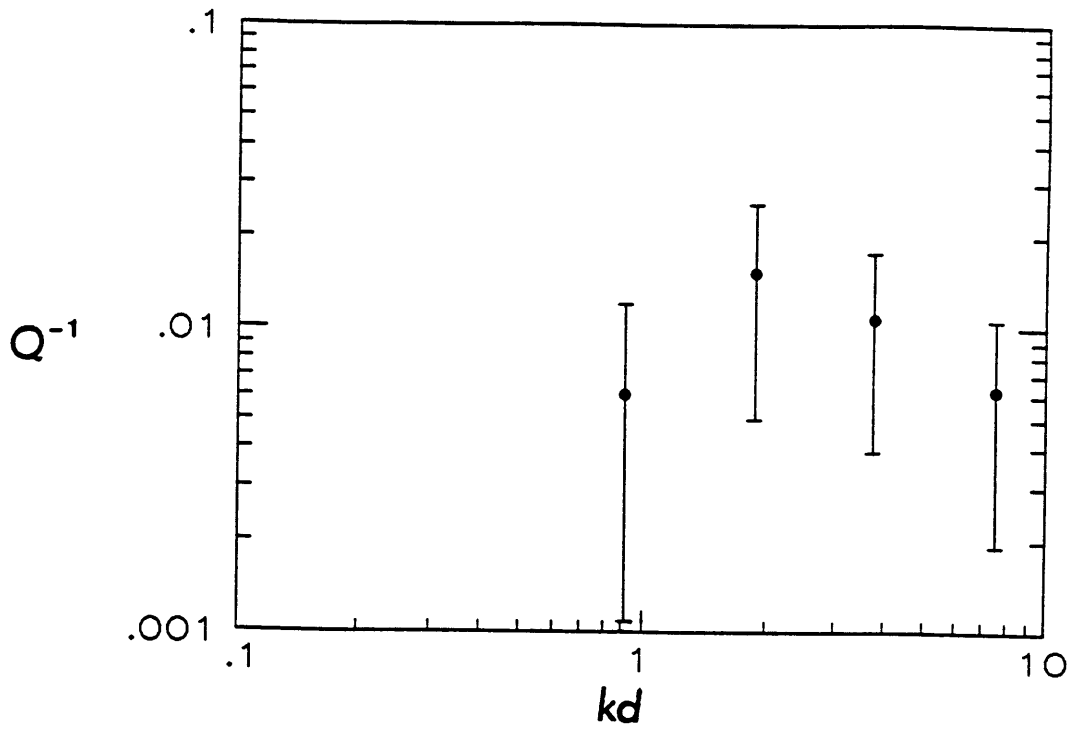

FIGURE 5.18 Q^{-1} vs kd, $d = 2a$. These values of Q^{-1} were computed using the seismograms of 60 stations around the center of the seismic array. Error bars correspond to the standard deviation of first arrival amplitude fluctuations in those 60 seismograms.

0.5 to 1 Hz, and decays proportionally to f^{-m} for higher frequencies with low m ($\sim$ 0.2) for stable area and high m ($\sim$ 1.0) for seismically active areas. Since $k = (2\pi f/\beta) \simeq 1 \sim 2$ km^{-1} corresponding to $f = 0.5 \sim 1$ hz, a for the lithosphere may be 0.5 to 1 km (Wu 1989).

Obviously further work is needed to confirm the general applicability of results on the wavenumber dependency of Q^{-1}. In particular we need to extend our method to treat the scattering of elastic waves in media characterized by random distribution of inclusions and cracks of various shapes.

5.7 Discussions

In this paper we have developed a numerical scheme based on the Boundary Integral Method to calculate the scattered wavefield of SH waves propagating in media containing many inclusions. Our solution includes all reflected and diffracted wave contributions that result from the multiple scattering process. Our immediate goal was to compute accurately the total SH wavefield synthetic seismograms in media with randomly distributed inclusions for wavelengths comparable to the size of the inclusions. The inclusions studied here are a collection of identical cavities of circular cross section, distributed in full and half spaces. The choice of cavities of circular shape was not a necessary imposition but just a convenience for introductory purposes; in fact the method is especially suited to deal with irregular shapes and strong impedance contrast between the inclusions and the surrounded media. Since we used exact Green's function, the accuracy of the wavefield representation was determined only by the discretization of the boundary and the corresponding distribution of wave sources. We have performed several tests that established the satisfactory accuracy of

our solution. First, we solved problems involving one cavity for which exact analytic solutions exist, and found that our results were in excellent agreement with those obtained using the exact solutions. For complicated problems involving more than one cavity we assessed the validity of our solution by estimating the degree of mismatch for the boundary conditions. This was done by assuring minimal traction residuals along the boundary of the cavities.

The first part of our analysis was concerned with identification of various arrivals in terms of scattering ray paths using a small number of scatterers. We studied them one by one, by increasing the number of scatterers gradually, while keeping the scatterers at regularly spaced locations. We started with one cavity, computing the synthetic seismograms measured at a prescribed array of seismic stations and identifying the phases that arrive at these stations. We found that in addition to the waves reflected at the boundary, there are also waves that creep around the cavity yielding a wavefront that appears as a smooth continuation of that of the incident wave. These waves result from diffraction phenomena associated with grazing incidence at the boundary, and have relatively large amplitudes so that they appear as one of the dominant features in the seismograms. Another dominant feature is the observed attenuation and time delay of the direct wave at stations right above the cavity, where the field is basically due to diffraction. In the case of two cavities the seismograms show the same arrivals that we would observe for each without the presence of the other, plus the waves multiply reflected between their boundaries. For the case of half-space with two cavities, the seismograms become more complicated but we still could identify ray path for every phase including those due to

multiple reflection between free-surface and the upper boundary of cavity.

For more than two cavities the computed seismograms became extremely complicated. There appeared in addition multipath phases corresponding to reflection at the boundaries of several neighboring cavities, before reaching a particular station . For the case of twelve cavities and incident wave from a point(line) source located in the region of cavity distribution, it appears that multipath waves cause focusing effect at stations located between two columns of cavities, right above the source. The same effect appears for an inclined incident plane wave. In spite of the complexity of the seismograms, we were able to understand the physics of the wave propagation process, including the gross reflection at the edge of the cavity region distribution.

Next, we computed the scattering of a plane wave for a wide range of frequencies, in media with 50 cavities randomly distributed; the highest frequency corresponding to the wavelength equal to 1.25× the radius of the cavities. Using the seismograms obtained for the full-space case, we computed the scattering attenuation factor Q^{-1} at several frequency bands. Considering the factor kd (wavenumber times the diameter of the cavity) as parameter, we found that the value of Q^{-1} increases with kd in the region where $kd < 2$, peaking at about $kd = 2$ (or $\lambda = 2\pi a$ and decreasing roughly proportional to $(kd)^{-1}$ for $kd > 2$. The proportionality of Q^{-1} with k^{-1} (or f^{-1}) for large ka implies that the scattering loss per unit distance is independent of frequency. This can be easily understood if we consider that for large ka the ray theory may be applicable to the scattering process and hence attenuation due to scattering loss become frequency independent (hence Q^{-1} proportional to ω^{-1}). The observed frequency dependence of

Q^{-1} for shear waves in the lithosphere was explained in this manner by Dainty (1984)

CHAPTER VI

SUMMARY AND CONCLUSIONS

6.1 Boundary integral - Gaussian beam method

In this thesis we have introduced the boundary integral - Gaussian beam method and demonstrated that it is a reliable and versatile numerical technique to accurately compute the full waveform of seismic waves propagating in complex structures expected to be encountered at a shallow part of the Earth. The method is based on the boundary integral representation of the scattered wavefield by irregular shaped boundaries, where artificial wave sources are distributed along the boundaries and the Gaussian beam method is used to compute the wavefield, or Green's function, due to each of those distributed wave sources. We take advantage of strengths of the two methods and avoid their weaknesses. The advantage of the boundary integral method is in economizing the discretization along the boundary surface (line) rather than over volume (surface). The Gaussian beam on the other hand, gives simple, adequate and relatively fast solution of wave equation in smoothly inhomogeneous media. We avoid the cumbersome task of calculating reflection and transmission of the Gaussian beam solution locally at each incidence on a discontinuous boundary, by determining the intensity and phase of wave sources distributed along the boundaries to match boundary conditions globally in the least squares sense.

In Chapter II we described the basic theory on both boundary integral and Gaussian beam methods. We started with the single-layer potential form of the integral representation of the field, following the formulation from the Helmoltz integral equation for exterior and interior problems due

to Mow and Pao 1971. Then we described our discretization scheme based on distribution of point (line) sources to approximate integrals by discrete summations, leading to a system of simultaneous linear equations for the unknown multiplicative complex constants. We then described the geometrical formulation of Gaussian beams following Madariaga (1984), which is more appealing to intuition than the original asymptotic expansion by Červený (1982). One novelty in this chapter is that we developed an expression for the traction field acting on a plane of arbitrary normal vector, by superposition of the same Gaussian beams that represent displacement field, to be used in the boundary integral scheme. The accuracy of our representation of displacement and traction Green's functions for a source - receiver pair was checked using homogeneous media, by comparing them with the corresponding Green's functions calculated analytically. Our use of Gaussian beams to represent Green's functions has an important advantage that they are not singular anywhere. This is important to avoid the need of smoothing matrix elements when the integration path includes the point where the source is located.

One of the main purposes of this chapter was to test the validity of our method, by applying it to problems with known exact solutions, or known approximation solutions obtained by other reliable numerical methods. Selected problems were (1) the problem of semi-cylindrical canyon studied by Trifunac (1973), (2) a mountain with cosine-shaped topography and (3) a semi-cylindrical alluvial valley, for which we computed the ground motion along the free-surface. In all cases the agreement between our solution and the corresponding published one was excellent. Through a parameter sensitivity study of our solution, we also confirmed that the final solution is

insensitive to the choice of the initial beam width of each Gaussian beam.

6.2 Seismological applications

In Chapter III, we applied our method to a comparative study of wave scattering observed at the surface of a half-space containing a soft (lower velocity than that of the half-space) inclusion and a hard (higher velocity than that of the half-space) due to vertically incident plane SH waves. The computed wavefield includes all multiply reflected, refracted and diffracted waves by the boundary of the inclusion. One of the surprising results was that both soft and hard inclusions produced a deamplification of incident waves at the receivers located immediately above the inclusion. Detailed investigation of their spectra in frequency domain and their waveform in time domain revealed that the deamplification is primarily due to the reflection of incident waves at the inclusion boundary. In other words the stations above the inclusion are in its shadow whether the inclusion has higher or lower velocity than that of the half-space. This suggests a highly non-unique inverse problem when the data are only amplitudes.

This Chapter III also demonstrated complementary roles of time domain and frequency domain solutions for understanding the physics of wave phenomena. The time domain solution was useful to identify various transmitted, reflected and diffracted waves. For example, they showed clearly the greater amplitude and longer duration of waves produced and propagated away of the inclusion for a soft inclusion than for a hard inclusion.

On the other hand, the frequency domain solution revealed a distinct difference in spectral shape observed near the inclusion between the two cases. The spectrum for soft inclusion showed narrow peaks clearly associated with modes trapped in the inclusion. We found that the resonance

phenomena are affected by the distance between the free-surface and the top of the inclusion and that this effect decreases as the impedance between half-space and the inclusion increases. Larger impedance contrasts yield narrower resonant peaks, as expected for a trapped mode. The study of resonance by a time domain solution is ineffective because of the need for a long duration for synthetics. The result of this chapter is interesting in view of the discovery of the narrowly peaked spectra observed at stations near the rift zone of Kilauea, Hawaii, for the T-phase from the recent Loma Prieta earthquake. The resonance induced in a magma reservoir by incident waves from distant sources may appear as spectral peaks at nearby stations.

In Chapter IV we applied our method to two problems of fundamental interest to strong ground motion in seismology, namely the effect of ridge topography and that of soft sedimentary basin on the surface ground motion. For the first time we studied these two problems when the seismic velocity changes linearly with depth. We choose the cosine shape for the ridge topography, and semi-cylindrical shape for the sedimentary basin.

Sections 2 and 3 of this Chapter IV are devoted to obtain the Gaussian beam solution in media having linearly increasing velocity with depth, for displacement and traction, respectively. The ray-centered cordinates (s, n) of the observation point are computed analytically, taking the advantage that a ray path in media with linear increase of velocity is an arc of a circle, completely determined by the coordinates of the observation point, source point, and the take-off angle. We gave explicit formulas in terms of these coordinates for the corresponding Dynamic Ray Tracing equation solutions, and for obliquely and vertically incident Gaussian beams, for both

displacement and traction. In section 4 we described the algorithm for superposition of beams, and for the subroutine called INGREEN developed in this thesis to compute displacement and traction Green's functions for any arbitrary pair of source-observer points in a full-space with linearly increasing velocity. We checked the accuracy of the results given by INGREEN in two steps. First we checked the accuracy of computation of the ray-centered coordinates of an observation point with respect to several rays departing from a source point, by computing the points on the rays where their respective normal passes through the observation point (Figure 4.3), for various source-receiver geometries. Then we compared the amplitude and phases for displacement and traction to those obtained from the analytical solution in the case of homogeneous media.

In section 4.5 we solved the problem of ground motion at the surface of an inhomogeneous mountain whose velocity increases linearly with depth, due to an incident plane SH wave. We computed the ground motion for several values of the aspect ratio of the mountain, defined as the ratio of its height h to its half-width a (h/a), for several non-dimensional frequencies $\eta = 2a/\lambda$ (λ wavelength of incident wave) and for four models of linear variation of velocity with depth in which the velocity β_0 at the top of the mountain and the velocity β_h at the bottom of the mountain were related as $\beta_h = 0.001\beta_0$, $\beta_h = 1.1\beta_0$, $\beta_h = 1.5\beta_0$ and $\beta_h = 2\beta_0$, respectively. In general, results show that the well known amplification on the top of the ridge in the homogeneous case, is further increased with the velocity gradient. For example, when $\beta_h = 2\beta_0$, and $\eta = 2$, the amplification at the top of the mountain was 2 times larger than that for the corresponding "homogenous case" ($\beta_0 = 0.001$), which was about a factor of 3 greater

than the incident wave. Therefore, the incident wave at the top of the ridge is amplified by a factor of 6 in this case. This amplification factor of the ground motion helps to explain the discrepancy between the observed amplification of ground motion in ridges and the corresponding theoretical predictions using homogeneous and layered models of mountains (Bard and Tucker 1985). Spectral ratios of the motion at the top of a ridge 30 m high and 100 m wide, with respect to the motion at a nearby tunnel, observed by Tucker et al. (1984), show that the amplification factor at the top of the ridge is between 4 and 8, in the frequency band between 5 and 10 hz. Theoretical models using homogeneous ridges and ridges with a surface low-velocity layer (Bard and Tucker) predicted 4 as the largest amplification factor. We believe that our model can explain these observations, by considering the continuous velocity profile inferred from their study of tunnel effect, i.e. $\beta_0 = 350$ m/sec and $\beta_{2h} = 1300$ m/sec ($2h = 60$ m), for η from 0.4 to 2.5, corresponding to their frequency band.

In section 4.6 the problem of inhomogeneous basin embedded in a homogeneous half-space was solved. In our model, the velocity varied linearly with depth within the semi-cylindrical basin. The velocity at the surface is β_0, and the velocity at the bottom of the basin is β_a, while the velocity β_H of the half-space is assumed to be $3\beta_0$. The density was assumed to be constant in the basin (ρ_0) and in the half-space (ρ_H). ρ_H is assumed to be $1.5\rho_0$. We studied the cases for several choices of the velocity at the bottom of the basin β_a, varying from β_0 to $2\beta_0$. We found that the effect of the velocity gradient on the response of the basin is to widen the area of amplification of the ground motion within the basin, as the gradient increased. For instance, for the homogeneous case and for $\eta = 1$ (see Figure

4.21) the amplification of the ground motion within the basin is larger at observation points close to the center of the basin, than at those at the edges. As the velocity gradient increases, the area of amplification extends towards observation points close to the edges, and finally, for $\beta_a = 2\beta_0$, the ground motion at the edges of the valley is amplified by a factor of 6 with respect to incident wave, twice larger than the amplification at the center of the basin. However, this amplification effect due to increase of velocity gradient is not systematic for all frequencies. For instance, the large amplification as much as a factor of 8 for $\eta = 0.25$ (see Figure 2.12) for the homogeneous basin, disappears when $\beta_h = 2\beta_0$ (see Figure 4.20 (a)).

We checked the accuracy of our method in this case by measuring the fractional residual traction along the free-surface, which turned out to be no larger than 10^{-2} for $\beta_a = 2\beta_0$, and for a wavelength comparable to the half-width of the basin. Also our results for selected values of wavelength showed satisfactory agreement with the corresponding one obtained by other well-established method, illustrated in Figures 4.22. From our synthetic seismograms, we found that the long duration seismograms observed within homogeneous basins due to two-dimensional resonance, are shortened by increasing the velocity gradient, because the impedance contrast at the interface of the basin with the half-space is reduced as β_a increases, allowing energy to leak out of the basin by the waves transmitted to the half-space.

In Chapter V we used the boundary integral method to compute the full waveform synthetic seismogram of multiply scattered SH waves by many cylindrical cavities in homogeneous elastic media. It was not necessary to use Gaussian beams in this problem, because analytical formulas for dis-

placement and traction Green's functions are available for homogeneous media. In section 5.2 we formulated the problem by extending the formulation for the scattered field due to one cavity described in Chapter II to the case of many cavities, and introducing a discretization scheme based on distribution of point(line) sources along the boundary of each cavity. In section 5.3 we checked the validity of this solution by computing the radiation patern due to a single cavity in full-space, which was in perfect agreement with its equivalent analytical solution. We also computed the case of one cavity in a homogeneous half-space, and compared our results with the analytical solution (Lee, 1977). For more than one cavity we checked our solution by computing the fractional residual traction along the boundary of each cavity, which was never larger than 10^{-2}, even for wavelengths equal to one quarter of the radius of the cavity.

To the author's knowledge, sections 5.4 and 5.5 represent the first deterministic computation of the total wavefield due to scattering by many cavities, due to incident plane or line source SH waves with wavelengths as short as the radius of the cavity. In section 5.4 we treated the cases of two, four and twelve cavities, in full and half-spaces, and the case of two elliptical cavities in half-space. In these examples we identified the arrival of the phases with a simple ray diagram, and confirmed that our solution contained all reflected and diffracted waves expected from the physical process involved in the wave propagation. In section 5.5 we applied the method to compute the case of fifty cylindrical cavities, each of radius a, randomly distributed in a region $80a$ wide by $30a$ deep in a half and full spaces for wavelengths of the incident wave comparable to the size of the cavity. The seismograms become extremely complex, and we believe that the absence

of noise due to numerical error guarantees that the computed seismograms reflect correctly the scattering process for such wavelengths. In section 5.6 the value of the attenuation factor Q^{-1} is obtained from the amplitude of the synthetic seismograms calculated for the random distribution of 50 cavities in full-space. We used the decay of the incident wave with distance, for wavelengths in the range from $1.7a$ to $13.3a$. The resulting Q^{-1} as a function of wave number k showed a peak around $kd \simeq 2$ (where d is the diameter of the cavity). The decrease of Q^{-1} toward smaller k or longer wavelength is due to well understood Rayleigh scattering. The decrease toward greater k or shorter wavelength has been predicted by Varadan (1978) for cylindrical inclusions, and by Kikuchi (1981) for cracks, both based on the extended T-matrix method. Dainty (1984) also argued that for Q^{-1} being inversely proportional to frequency on the basis of ray-theoretical loss for shorter wavelengths than the scatterer size. Observed Q^{-1} for S-waves in the lithosphere usually has peaks around 0.5 to 1 hz, and decays proportionally to f^{-m} for higher frequencies with low m ($\sim$ 0.2) for stable area and high m ($\sim$ 1.0) for seismically active areas. Since $k = (2\pi f/\beta) \simeq 1 \sim 2$ km^{-1} corresponding to $f = 0.5 \sim 1$ hz, a for lithosphere may be 0.5 to 1 km (Wu 1989).

6.3 Future work

A natural extension of the present thesis work is to solve the 2-D P-SV problems corresponding to all SH problems studied here. This is not an unrealistic goal using the available computer. In order to extend the boundary integral method to 3-D, the integral representation of the

wavefield (2.1) must be written in a vector form

$$\vec{v}_s(\vec{r}_P) = \int_C \vec{\sigma}(\vec{r}') \cdot \bar{G}(\vec{r}_P \mid \vec{r}_Q) ds$$

i.e., the scattered field is made up of the contributions of a continuous distribution of sources of density $\vec{\sigma}(\vec{r}_Q)$ on C. For fixed $\vec{r}'$, $\bar{G}$ is the displacement Green's dyadic due to a *force* $\vec{F} = (F_1, F_2, F_3)$ applied at $\vec{r}_Q$. Then we would use the appropiate 3-D ray-tracing to compute Green's function by superposition of Gaussian beams, for each component of the field, in a similar way as we did in Chapter IV. This formulation, for the case of irregular topography, is currently being developed.

APPENDIX 1

INHOMOGENEOUS BASIN: BOUNDARY INTEGRAL SCHEME.

In this appendix we shall give explicit expression for the matrix elements Γ_{ij} (equation 2.6).

Let v_{vj} the sources representing the field in the basin, with velocity $\beta_1(z)$, and rigidity $\mu_1(z)$, distributed along the interface (curve C_I). Sources for the half-space are v_{hi}, with velocity $\beta_2(z)$, and rigidity $\mu_2(z)$, distributed along the interface (curve C_E). Let v_{sk} the sources representing the field in the basin distributed along the free-surface (line $\bar{C}_I$). Here, $i = 1, ...NH$, $(j,k) = 1, ...NV$.

Refering to Figure 4.19, and to equations (2.7), the fields inside and outside the basin will be, respectively:

$$v_E(x,z;\omega) = v_0 + \sum_{i=1}^{NH} A_{hi} v_{hi}$$

$$v_I(x,z;\omega) = \sum_{j=1}^{NV} B_{vj} v_{vj} + \sum_{k=1}^{NV} B_{sk} v_{sk}$$

where v_{hi}, represent Green's function for the half-space with point source at the position i in the basin, v_{vj} represent Green's function for the basin with point source at the position j in the half-space, and v_{sk} represent Green's function for the basin with point source at the position k in the free- surface.

The linear system of simultaneous equations obtained from the minimization of the function L in equation (2.7) in order to satisfy continuity of displacement and traction along the boundary, and at the free-surface is

$$\sum_{j=1}^{NV} B_{vj} R_{qj}(1,1) + \sum_{j=1}^{NV} B_{sk} R_{qk}(1,2) + \sum_{j=1}^{NH} A_{hi} R_{qi}(1,3) = S_{q,o}$$

$$\sum_{j=1}^{NV} B_{vj} R_{rj}(2,1) + \sum_{j=1}^{NV} B_{sk} R_{rk}(2,2) + \sum_{j=1}^{NH} A_{hi} R_{ri}(2,3) = S_{r,o}$$

$$\sum_{j=1}^{NV} B_{vj} R_{pj}(3,1) + \sum_{j=1}^{NV} B_{sk} R_{pk}(3,2) + \sum_{j=1}^{NH} A_{hi} R_{pi}(3,3) = S_{p,o}$$

where the R's and the S's are respectively :

$$R_{qj}(1,1) = \int_{\bar{C}_1} \frac{\partial v^*_{vq}}{\partial \hat{n}_1} \frac{\partial v_{vj}}{\partial \hat{n}_1} dl + \int_{C_1} (v^*_{vq} v_{vj} + \frac{\partial v^*_{vq}}{\partial \hat{n}_2} \frac{\partial v_{vj}}{\partial \hat{n}_2}) ds$$

$$R_{qk}(2,1) = \int_{\bar{C}_1} \frac{\partial v^*_{vq}}{\partial \hat{n}_1} \frac{\partial v_{sk}}{\partial \hat{n}_1} dl + \int_{C_1} (v^*_{vq} v_{sk} + \frac{\partial v^*_{vq}}{\partial \hat{n}_2} \frac{\partial v_{sk}}{\partial \hat{n}_2}) ds$$

$$R_{rj}(2,1) = \int_{\bar{C}} \frac{\partial v^*_{sr}}{\partial \hat{n}_1} \frac{\partial v_{sj}}{\partial \hat{n}_1} dl + \int_{C} (v^*_{sr} v_{vj} + \frac{\partial v^*_{sr}}{\partial \hat{n}_2} \frac{\partial v_{vj}}{\partial \hat{n}_2}) ds$$

$$R_{rk}(2,2) = \int_{C_1} \frac{\partial v^*_{sr}}{\partial \hat{n}_1} \frac{\partial v_{sk}}{\partial \hat{n}_1} dl + \int_{C_1} (v^*_{sr} v_{sk} + \frac{\partial v^*_{sr}}{\partial \hat{n}_2} \frac{\partial v_{sk}}{\partial \hat{n}_2}) ds$$

$$R_{qi}(3,1) = -\int_{C} (v^*_{vq} v_{hi} + \mu \frac{\partial v^*_{vq}}{\partial \hat{n}_2} \frac{\partial v_{hi}}{\partial \hat{n}_2}) ds$$

$$R_{ri}(2,3) = -\int_{C} (v^*_{sr} v_{hi} + \mu \frac{\partial v^*_{sr}}{\partial \hat{n}_2} \frac{\partial v_{hi}}{\partial \hat{n}_2}) ds$$

$$R_{pj}(3,1) = \int_{C} (v^*_{hp} v_{vj} + \mu \frac{\partial v^*_{hp}}{\partial \hat{n}_2} \frac{\partial v_{vj}}{\partial \hat{n}_2}) ds$$

$$R_{pk}(3,2) = \int_{C} (v^*_{hp} v_{sk} + \mu \frac{\partial v^*_{hp}}{\partial \hat{n}_2} \frac{\partial v_{sk}}{\partial \hat{n}_2}) ds$$

$$R_{pi}(3,3) = -\int_{C} (v^*_{hp} v_{hi} + \mu^2 \frac{\partial v^*_{hp}}{\partial \hat{n}_2} \frac{\partial v_{hi}}{\partial \hat{n}_2}) ds$$

$$S_{q,o} = -\int_C (v^*_{vq} v_o + \mu \frac{\partial v^*_{vq}}{\partial \hat{n}_2} \frac{\partial v_o}{\partial \hat{n}_2}) ds$$

$$S_{r,o} = -\int_C (v^*_{sr} v_o + \mu \frac{\partial v^*_{sr}}{\partial \hat{n}_2} \frac{\partial v_o}{\partial \hat{n}_2}) ds$$

$$S_{p,o} = -\int_C (v^*_{hp} v_o + \mu^2 \frac{\partial v^*_{hp}}{\partial \hat{n}_2} \frac{\partial v_o}{\partial \hat{n}_2}) ds$$

where $\mu = \mu(z) = \mu_E(z) \div \mu_I(z)$, and dl is an element of distance along the free surface and ds is an element of arc along the interface.

APPENDIX 2

DEPARTMENT OF GEOLOGICAL SCIENCES
TELEPHONE (213) 743-2777

7 November 1986 - MEMORANDUM

TO: Francisco, Hiroshi, and Rafael

FROM: Kei Aki

RE: Wave propagation in heterogeneous media with irregular interfaces

Thanks to our discussion Thursday morning I think I know how to solve the above mentioned problem by the superposition of Gaussian Beams.

Consider an irregular topography, interface and seismic source as shown in Fig. 1. The steps toward the solution are as follows:

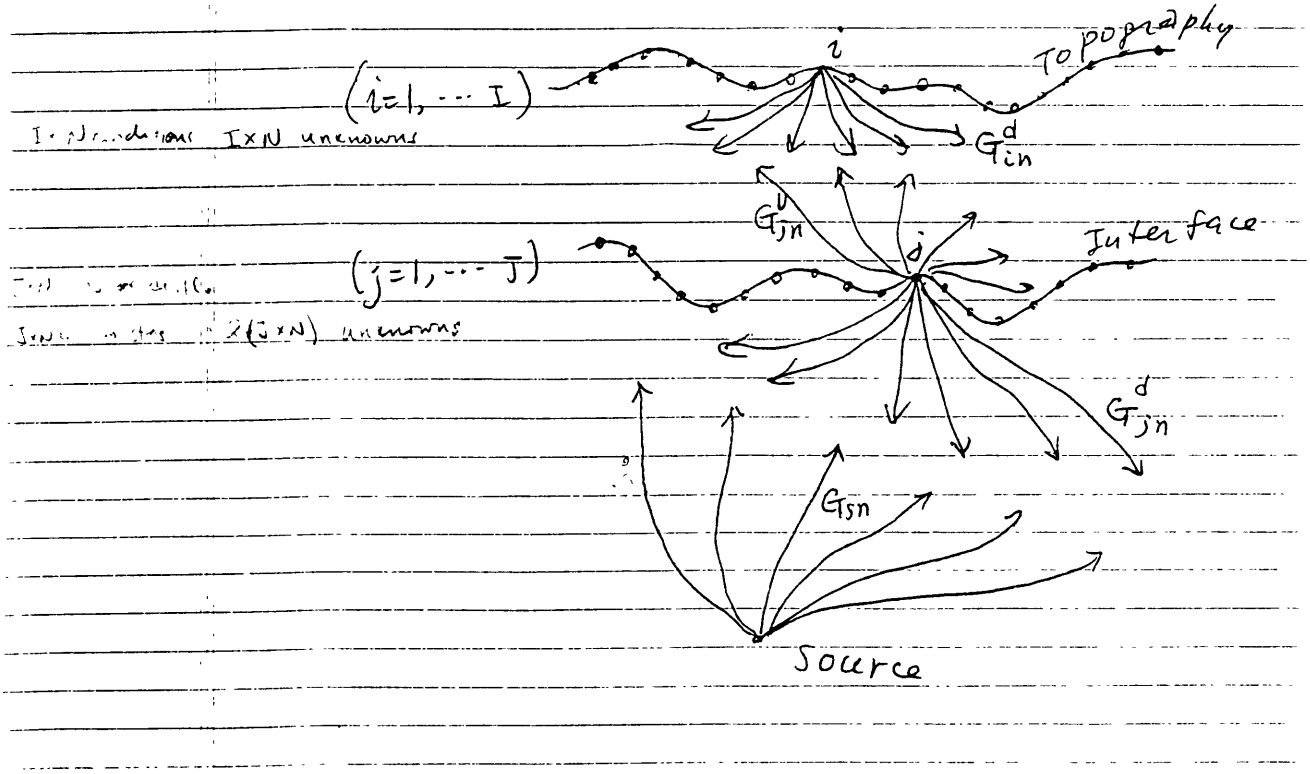

(1) Select points along topography and interface, and let us call them (i=1,2,... I) and (i=1,2,...J), respectively.

(2) Shoot Gaussian Beams from
a) upward from the source,
b) downward from point j,
c) upward from point j, and
d) downward from point i. Let us refer to
a) as G_{sn} (n=1,...N)
b) as G^{d}_{jn} (n=1,...N)
c) as G^{u}_{jn} (n=1,...N)
d) as G^{d}_{in} (n=1,...N)
as shown in Fig. 1.

(3) Each Gaussian Beam is an approximate solution of wave equation, so their sum is also an approximate solution. All we have to do is to find G's which satisfies the boundary condition and interface condition.

(4) G_{sn} are known quantities determined for a given seismic source.

(5) In order to determine unknowns G^{d}_{in}, G^{u}_{jn}, and G^{d}_{jn}, we shall first form the sum of the squares of traction at free surface. For SH waves, for example, we have one component of traction, which is a function of G^{d}_{in} and G^{u}_{jn}. We then calculate the sum $S^{trac.}_{topo}$ of the squares of traction at i=1,2,...I.

(6) Next, we calculate the mismatches in traction and displacement at j=1,2,...J, then the sum of their squares and call them $S^{trac.}_{INT}$ and S^{disp}_{INT}, respectively. They are functions of G^{d}_{in}, G^{u}_{jn}, G^{d}_{jn}, and G_{sn}.

(7) We shall form the weighted sum $S=S_{topo} + S^{trac}_{INT} + \omega S^{disp}_{INT}$ where ω is the weight to take care of the difference in physical unit in order to make the numerical magnitude comparable among the three sums.

(8) We then minimize S with respect to unknowns. We shall have equations of the form

$$\frac{\partial S}{\partial G} = 0$$

as many as the number of unknown G.

(9) Knowing G, we can compute the wave field at any point by suposing Gaussian Beams.

(10) Would any of you try this idea with simple examples?

:jl

REFERENCES

Aki, K., Local site effects on strong ground motion, Proc. Earthq. Eng. and soil dynamics II, GT Div/ASCE, Park City, Utah, June 27-30, 1988.

K.Aki and P. Richards, Quantitative Seismology, Theory and Methods, , W.H. Freeman and Co., San Francisco, California, U.S.A., pp.742 (1980).

Aki, K. and K.L. Larner, Surface motion of a layered medium having an irregular interface due to incident plane SH waves, J. Geophys. Res.,75, pp 933-954, 1970.

Bard, P.Y., Diffracted waves and displacement field over two dimensional elevated topographies, Geophys. J. R. Astr.Soc., 71, pp 731-760, 1982.

Bard, P.Y. and J-C Gariel, The seismic response of two-dimensional sedimentary deposits with large vertical velocity gradients, Bull. Seism. Soc. Am., 76, pp 343-366, 1986.

Bard, P.Y., and B.E. Tucker, Ridge and tunnel effects: comparing observations with theory, Bull. Sei. Soc. Am., 75, pp 905-922, 1985.

Benites, R. and K. Aki, Boundary integral-Gaussian beam method for seismic wave scattering: SH in two-dimensional media, J. Acoust.Soc.Am. 86(1), 1989.

Biswas N.N., S.K. Koyanagi, V. Ferrazzini and K. Aki, Propagation of T-phase across the island of Hawaii from Loma Prieta earthquake, Seism. Res. Lett., 61, 1, p46, 1990.

Boore, D.M., A note on the effect of simple topography on seismic SH waves, Bull. Seismol. Soc. Am. 62, 275-284, 1972.

Brebbia, C.A., The boundary element method for engineers, Pentech Press, London, 1978. Brebbia, C.A. and J. Dominguez, Boundary Elements, an introductory course, Computational Mechanics Publications, McGraw-Hill, 1989.

Bouchon, M., Effect of topography on surface motion, Bull. Seismol. Soc. Am., 63, 615-632, 1973. Bouchon, M., A simple, complete numerical solution to the problem of difraction of SH waves by an irregular surface, J.Acoust. Soc. Am., 77 1-5, 1985.

Brekhovskikh, L.M., Waves in Layered Media, Academic Press, New York 1960, pp 100-117.

Burridge, R., F. Mainardi, and G. Servizi, Soil amplification of seismic plane waves, Phys. Earth Planet. Int., 22, pp 122-136, 1980.

Chapman, C.H. and R.A. Phinney, Diffracted seismic signals and their numerical solutions, in Methods of computational Physics, 12, ed. B. A. Bolt, Academic Press Inc., New York and London, 1972.

Chaterjee, A.K, A.K. Mal and L. Knopoff, Elastic moduli of two-component systems, J. Geophys. Res., 83, 1785-1792 (1978).

V. Červený, M.M. Popov and I. Pšenčik, Computation of wave fields in inhomogeneous media, Gaussian beam approach, Geophys. R. Astr.Soc. 70, 109-128, 1982.

Červený V. and I. Pšenčik, Gaussian beam and paraxial ray approximation in three-dimensional elastic inhomogeneous media, J. Geophys., 53, 1-15, 1983 (a).

Červený, V. and I. Pšenčik, Gaussian beams in two-dimensional elastic inhomogeneous media, Geophys. J. Roy. Astr. Soc., 72, 417-433 1983 (b). V. Červený and I. Pšenčik, Gaussian beam in elastic two-dimensional laterally varying structures by the Gaussian beam method, Geophys. J. Roy. Astr. Soc., 78, 65-91, 1984.

Chernov, L.A., "Wave Propagation in a Random Medium", McGraw-Hill, New York. 1960.

Copley, L.G., Integral equation method for radiation from vibrating surfaces", J. Acoust. Soc. Am., 41, 807-816 (1967).

Dainty, A.M., High-frequency acoustic backscattering and seismic attenuation, J.Geophys.Res., 89, 3172-3196, 1984.

Davis, L.L and L.R. West, Observed effects of topography on ground motion, Bull. Seism. Soc. Am., 63, pp283-298, 1973.

Dravinski, M., Ground motion amplification due to elastic inclusions in a half-space, Earthquake. Eng. and Struct. Dyn, Vol.11, 313-335 (1983).

Dravinski, M., Scattering of SH waves by subsurface topography, J. Eng. Mech. Div., ASCE 108, 1-17 (1982).

Foldy, L. L. ,The multiple scattering of waves, I. General Theory for isotropic scattering by randomly distributed scatterers", Phys. Rev. 67, 107-119 (1945).

Frankel, A. and R.W. Clayton, A finite difference simulation of wave propagation in two-dimensional random media, Bull. Seismol. Soc. Am., 74, 2167-2186, 1984.

Frankel, A. and R.W. Clayton, Finite difference simulations of seismic scattering: Implications for the propagation of short-period seismic waves in the crust and models of crustal heterogeneity, J. Geophys. Res., 86, 6465-6489 (1986).

Fukuwa, N., T. Sato, H. Kawase and S. Nakai, Effects of surface Irregularities on strong ground motion, Proceedings of the 31st Japan Structural Engineering , pp 1-10, Tokyo, Japan, 1985.

George, Th., Une approximation a haute frequence de l'equation des ondes: la sommation de faisceaux gaussiens. Methodologie, tests et applications sismologiques, These de Doctorat de l'Universite Paris 6, France, 1987.

Herraiz, M. and A.F. Espinosa, Coda waves: a review, PAGEOPH vol.125, pp 499-577, 1987.

Idriss, I.M., H.B Bolton Seed, Seismic response of horizontal soil layers, Journal of the Soil Mechanics and Foundation Division, Proceedings of the American Society of Civil Engineers, SM4, pp. 1003- 1030, July 1968.

Jih, R-S, K.L. McLaughlin, and Z.A. Der, Free-boundary conditions of arbitrary polygonal topography in a two-dimensional explicit elastic finite-difference scheme, Geophysics, 53, 8, pp 1045-1055, 1988.

Kawase, H. "Time-domain response of a semicircular canyon for incident SV, P, and Rayleigh waves calculated by the discrete wave number boundary element method", Bull. Seismol. Soc. Am., 78, 1415-1437 (1988).

Keller, J.B., Geometrical Theory of Diffraction, J. Opt.Soc.Amer., Vol. 52, pp.116-130.

Kellogg, O.D. Foundations of potential theory, New York, Dover, 1953.

Kikuchi, M., Dispersion and attenuation of elastic waves due to multiple scattering from inclusions, Phys. Earth Planet. Inter., 25, 159-162 (1981).

Kikuchi, M., Dispersion and attenuation of elastic waves due to multiple scattering from cracks, Phys. Earth Planet. Inter., 27, 100-105 (1981).

Kristensson, G. and S. Ström, The T-matrix approach to scattering from buried inhomogeneities in Acoustic, Electromagnetic and Elastic waves-Focus on the T-Matrix Approach, edited by V.K. Varadan and V.V. Varadan, pp. 135- 167, Pergamon, New York.

Kupradze, V.D. , Three-dimensional problems of the mathematical theory of elasticity and thermoelasticity, North Holland series in Applied Mathematics and Mechanics, 25, p. 300, North-Holland (1979)

Lax, M., Multiple scattering of waves, Revs. Modern Phys. 23, 287-310, 1951.

Lee, V.W., On deformations near circular underground cavity subjected to incident plane SH waves, Proceedings of the application of computer methods in Engineering Conference, Vol. II, University of Southern California, Los Angeles, Calif., 951-962 (1977).

Madariaga, R. and P. Papadimitriou, Gaussian beam modelling of upper mantle phases, Annale Geophysicae, 3, 6, 799-812, 1985.

Madariaga R., Gaussian beam synthetic seismograms in a vertically varying medium, Geophys. J. Roy. Astr. Soc.,79 589-612, 1984.

Matsunami, K., Laboratory tests of the single and multiple scattering models for the generation fo seismic coda waves, sumitted J. Phys. Earth, (1988)

Matsunami, K., Laboratory measuremens of spatial fluctuations and attenuation of elastic waves by scattering due to random heterogeneities, PAGEOPH, Vol. 132 , pp 197-220, 1990.

Morse, P.M. and K.U. Ingard, Theoretical Acoustics, Princeton University Press, 1968.

Morse, P.M. and H. Feshbach 1953, Methods of Theoretical Physics, Part II, New York, McGraw Hill.

Mow C.C and Y.H Pao, The diffraction of elastic waves and dynamic stress concentrations, The Rand Corporation, USA, 1971,pp 279-291.

Nowack and K. Aki, The two-dimensional Gaussian beam synthetic method; testing and applications, J. of Geophys. Res. 89, 7797-7819, 1984.

Popov, M.M. and I. Pšenčik, Computation of ray amplitudes in inhomogeneous media with curved interfaces, Stud. Geophys. Geod. 22, 248-258, 1978.

Sánchez-Sesma F.J. and E. Rosenblueth, Ground motions at canyons of arbitrary shapes under incident SH waves, Earthquake Eng. Struct. Dyn., 7, 441-450, 1979.

Sánchez-Sesma, F.J. and J.A. Esquivel, Ground motion on alluvial valleys under incident plane SH waves, Bull. Seismol. Soc. Am. 69, 1107-1120, 1979.

Sato, H., Amplitude attenuation of impulsive waves in random media based on travel time corrected mean wave formalism, J. Acoust. Soc. Am., 71, 559-564

(1982).

Sato, T., A hybrid approach for theoretical seismograms usin thin layer element and axisymetric finite element, and its application to simulation of earthquake ground motions, Doctoral thesis, Tohoku University, Sendai, Japan, 1989.

Smirnov, V.I., A course in higher mathematics, vol. 4, Pergamon, London (1964).

Takahasi, R., and K. Hirano. Seismic vibrations of soft ground. Bulletin of the earthquake research institute, Tokyo Univ. 19, pp 534-543, 1941.

Toksöz, M. N., and D.H. Johnston (eds), Seismic wave attenuation, Geophysics Reprint Series, No.2, Society of Exploration Geophysicist, 1981.

Trifunac, M.D., Surface motion of a semi-cylindrical alluvial valley for incident plane SH waves, Bull. Seis. Soc. Am., 61,1755-1770, 1971.

Trifunac, M.D., Scattering of the plane SH waves by a semi-cylindrical canyon, Int. J. Earthquake. Struct. Dyn., 1, 267-281, 1973.

Tucker, B.E., J.L. King, D. Hatzfeld, and I.L. Nersesov, Observations of hard rock site effects, Bull. Seis, Soc. Am. 74, pp 121-136, 1984.

Ursell, F., On the exterior problems of acoustics, Proc. Camb. Phil. Soc., 74, 117-125 (1973).

Varadan, V.K., Multiple scattering of acoustic, electromagnetic and elastic waves, in Acoustic, Electromagnetic and Elastic waves-Focus on the T-Matrix Approach, edited by V.K. Varadan and V.V. Varadan, pp. 103- 134, Pergamon, New York.

Varadan, V.K., V.V. Varadan and Yih-Hsing Pao, Multiple scattering of elastic waves by cylinders of arbitrary cross section. I. SH waves, J. Acoust. Soc. Am. 63(5), 1310-1319 (1978).

Varadan, V.K., Y. Ma and V.V. Varadan, "Scattering and attenuation of elastic waves in random media", PAGEOPH, Vol. 131, pp 577-603 (1989).

Waterman, P.C., New formulation of acoustic scattering, J. Acoust. Soc. Am., 45, 1417-1428 (1969)".

Wielandt, E., On the validity of the ray approximation for interpreting delay times, Seismic Tomography, with applications in global seismology and exploration geophysics, Guus Nolet (Ed), D. Reidel Publishing Co., pp 85-98, 1987.

Wu, R-S, Attenuation of short period seismic waves due to scattering, Geophys. Res. Lett., 9, 9-12, 1982.

Wu, R-S, "Seismic Wave Scattering" in The Encyclopedia of Solid Earth Geophysics, Edited by D.E James, Encyclopedia of Earth Sciences Series, Van Nostrand, Reinhold, 1989, pp.1166-1186.

Wu, R-S and K. Aki (eds), Scattering and attenuation of seismic waves, parts I, II, and III, Birkhäuser, 1989.

5121 11